



The University of Manchester

**GRAPHENE-BIOINTERFACE BIOSENSOR PLATFORMS FOR  
BIOMEDICAL APPLICATIONS USING THE QUARTZ CRYSTAL  
MICROBALANCE TECHNIQUE**

A thesis submitted to the University of Manchester for the degree of  
Doctor of Philosophy

2022

Piramon Hampitak

Department of Materials  
Faculty of Science and Engineering

Blank page

# Contents

Contents.....	2
List of Figures .....	6
List of Tables .....	16
Acronyms .....	17
Abstract.....	20
Declaration.....	21
Copyright Statement.....	21
Acknowledgements.....	22
About the Author .....	23
Rationale for submitting the thesis in an alternative format .....	24
Outline .....	25
CHAPTER 1. Introduction .....	28
1.1 Background and Motivation .....	29
1.2 Objectives.....	34
1.3 Scopes .....	34
CHAPTER 2. Literature Review .....	35
2.1 Overview of Biosensors.....	36
2.1.1 Trends in biosensing and limitations .....	38
2.2 Biosensor techniques.....	40
2.2.1 Quartz-Crystal Microbalance (QCM) biosensors .....	41
2.2.2 Field Effect Transistor (FET) .....	43
2.2.3 Electrochemical biosensors.....	45
2.3 Graphene and graphene derivatives.....	48
2.3.1 Properties.....	49
2.3.2 Applications in biosensors .....	53
2.4 Interaction between biomolecules and graphene-family materials.....	55
2.4.1 Properties of graphene-related to biological interactions .....	57
2.4.2 Graphene interaction with proteins .....	59
2.5 Model proteins.....	63
2.5.1 Bovine Serum Albumin (BSA) .....	63
2.5.2 Lysozyme .....	67
2.5.3 Immunoglobulin.....	69
2.6 Antigen-antibody interaction.....	72

2.7	Screening for autoimmune diseases .....	73
2.8	Membranous nephropathy .....	74
2.9	Nanobody technology .....	75
2.9.1	Structure of VHH.....	76
2.9.2	Nanobody Production.....	77
2.9.3	Applications of nanobodies .....	78
CHAPTER 3.	Review of Characterization Techniques .....	80
3.1	QCM technique.....	81
3.1.1	QCM Principle.....	81
3.1.2	Viscoelastic modelling .....	83
3.2	Contact Angle .....	88
3.3	Scanning Electron Microscope (SEM).....	90
3.4	Atomic Force Microscopy (AFM) .....	92
3.5	Fourier Transform Infrared (FTIR) .....	94
3.6	X-ray Photoelectron Spectroscopy (XPS).....	95
3.7	Raman Spectroscopy .....	98
3.8	Dot blot.....	101
CHAPTER 4.	General Methodologies .....	102
4.6	The preparation and handling of biological samples .....	102
4.1	Overall .....	103
4.2	GO preparation.....	104
4.3	Graphene-coated QCM chips preparation .....	104
4.3.1	Cleaning protocol for Au QCM chips .....	105
4.3.2	Coating the sensors with GO .....	106
4.3.3	Thermal reduction of GO-coated chips .....	106
4.4	A general protocol for QCM-D measurement .....	106
4.5	Material characterisations.....	107
4.5.1	FTIR .....	107
4.5.2	SEM.....	108
4.5.3	Contact angle.....	108
4.5.4	AFM.....	110
4.5.5	XPS .....	111
4.5.6	Raman.....	112
4.5.7	Dot Blot approach.....	112
4.6	The preparation and handling of biological samples .....	113
CHAPTER 5.	Publication 1 .....	115

Abstract.....	116
Introduction .....	117
Materials and Methods.....	120
Results and discussion .....	123
1. Characterization of graphene surfaces .....	123
2. Effect of different degree of reduction of the GO .....	125
3. Effect of protein concentration in media.....	126
4. Adsorption mass and thickness .....	129
5. Proposed adsorption model .....	130
6. Specific and non-specific binding studies .....	134
Conclusions .....	138
Arguments and Future Work .....	141
CHAPTER 6. Publication 2. ....	143
Abstract.....	144
Introduction .....	145
Materials and methods.....	148
Results and discussion .....	153
1. Binding studies.....	153
2. Ab12 detection and specificity analysis using QCM-D.....	158
3. Detection of Ab12 using the C-QCM system .....	162
4. Comparison between QCM-D and the C-QCM .....	163
5. Testing with patient serum samples.....	164
6. Comparison with other techniques .....	166
Conclusions .....	167
CHAPTER 7. Publication 3 (In the process of publication) .....	170
Abstract.....	171
Introduction .....	172
Materials and Methods.....	175
Results and discussion .....	180
1. Characterization of graphene coating and functionalization .....	181
2. Exploration of sensing surfaces using QCM-D and selection criteria .....	182
3. Functional surface model and thickness.....	186
4. Lysozyme detection and binding analysis using QCM-D.....	188
5. Specificity studies with other proteins .....	190
6. Quantification of lysozyme in calf serum.....	191
7. Sensing surface comparison .....	193

8. Binding of different nanobodies and comparison with other techniques .....	195
Conclusion .....	199
CHAPTER 8. Publication as the second author .....	200
Abstract .....	201
Introduction.....	202
Materials and methods .....	205
Results and discussion .....	210
1. Characterisation of rGO-coated QCM sensors .....	210
2. Thermal chamber evaluation .....	210
3. Protein adsorption studies with cQCM and QCM-D systems.....	212
4. Discussion .....	215
Conclusions.....	219
CHAPTER 9. Conclusions.....	222
APPENDICES.....	225
Electronic Supporting Information 1. ....	226
Electronic Supporting Information 2. ....	247
Electronic Supporting Information 3. ....	263
Electronic Supporting Information 4. ....	277
<b>REFERENCES</b> .....	<b>299</b>

(Word count: 82461)

## List of Figures

<b>Fig. 2.1</b> Schematic diagram showing the main components for a biosensor including bioreceptor, transducer, electronics for signal processing and display interface.....	36
<b>Fig. 2.2</b> QCM instrument suppliers <b>(a)</b> QSense Analyzer from Biolin Scientific. Source: ref. [43] <b>(b)</b> QCM200 from Stanford Research System (SRS). Source: ref. [44] <b>(c)</b> open-source QCM system from Novaetech S.r.l. Source: ref. [45].....	43
<b>Fig. 2.3</b> Illustration showing construction of bio- and chemical FET sensor with three main components including recognition layer, transducer and electronic system for signal amplifying and processing. Source: ref. [46] .....	45
<b>Fig. 2.4</b> Diagram showing analytical procedure for clinical electrochemical sensors. Analytes are detected by receptors giving electrochemical signal. Then the signal will be processed and displayed in form of analytical signal. Adapted from ref. [49].....	46
<b>Fig. 2.5</b> Schematic of the structure of graphene sheet showing hexagonal carbon lattice. The identical carbon atoms are covalently bonded with the distance between the two carbon atoms of 1.41 Å .....	50
<b>Fig. 2.6</b> Structural model of GO proposed by Lerf-Klinowski. The basal plane of carbon lattice is interrupted by several oxygen functional groups with hydroxyl and epoxy functional groups on the plane and carboxylic acids on peripheral of the graphitic platelets. Source: ref. [59].....	50
<b>Fig. 2.7</b> Illustration of graphene-based sensor showing its potential application for detecting gases, organic and biological matters. The sensing surface can be modified by functionalisation with nanoparticles, DNAs, antibodies, and organic molecules. Source: ref. [69].....	54
<b>Fig. 2.8</b> Example of a microfluidic FET biosensor for detecting glucose made from graphene-based materials. Source: ref. [70] .....	55
<b>Fig. 2.9</b> Related properties of graphene-based materials to colloidal behaviour and biological interaction including surface area, lateral dimension, number of layer and surface chemistry. Adapted from ref. [81] .....	59
<b>Fig. 2.10</b> $\pi$ - $\pi$ interaction (black arrow) in which the gray atoms represent carbon and the orange atoms indicate hydrogen in the case of benzene. Source: ref.[88] .....	61
<b>Fig. 2.11</b> Hydrogen bonding (blue arrow) and $\pi$ - $\pi$ interaction (green arrow) with GO structure. Source: ref. [88].....	61
<b>Fig. 3.1</b> Comparison of frequency and dissipation response during adsorption process of rigid and soft molecules Adapted from ref [171].....	82
<b>Fig. 3.2</b> QCM-D profile analysis for structural properties of adsorbed molecules .....	83
<b>Fig. 3.3</b> Geometry of QCM oscillating in bulk liquid covered by a double layer of viscoelastic film, namely film1 and film 2. Each layer possess its own density ( $\rho$ ), elastic shear modulus ( $\mu$ ) and shear viscosity ( $\eta$ ). The density and shear modulus of the quartz plate are assigned as $\rho_0$ and $\mu_0$ , respectively. X axis represents distance from the centre	

of the crystal; Y axis represents the thickness of each viscous layer assigned as h1, h2 for film 1 and 2 and h3 for the height of bulk liquid. ....	84
<b>Fig. 3.4</b> Workflow and experimental conditions for determining the mass, thickness and viscoelastic properties of adsorbed films on surfaces using Dfind.....	87
<b>Fig. 3.5 (a)</b> Dfind results from viscoelastic modelling including thickness, elastic modulus, viscosity and Chi-square <b>(b)</b> fitting of the experimental results for frequency and dissipation using the theoretical models described in the main text .....	88
<b>Fig. 3.6</b> Contact angle description showing wetting properties of a substrate.....	89
<b>Fig. 3.7</b> Interaction energy and contact angle between DI water and different layer number of graphene substrate. Source: ref. [175].....	89
<b>Fig. 3.8</b> Static water contact angle of the mix of graphene and GO. Source: ref. [176]	90
<b>Fig. 3.9</b> Schematic of electron beam interaction on the surface of the sample .....	91
<b>Fig. 3.10</b> The SEM image of monolayer GO flake on SiO <sub>2</sub> .....	92
<b>Fig. 3.11</b> AFM imaging of suspended graphene membranes a) SEM image of a graphene flake spanning an array of circular holes. The area I shows a hole partially covered by graphene, area II is fully covered, and area III is fractured from indentation b) AFM image of one membrane. The solid blue line is a height profile along the dashed line. c) Schematic nanoindentation on suspended graphene membrane (after [279]) .....	93
<b>Fig. 3.12 (a)</b> Schematic of AFM measurement in liquid phase. Source: ref.[182] (b) AFM images of a graphene transistor surface with and without DNA strands adapted from [183]. .....	94
<b>Fig. 3.13</b> Transmission FTIR spectrum of multilayers GO at room temperature. Source: ref. [188].....	95
<b>Fig. 3.14 (a)</b> Schematic of basic XPS set-up <b>(b)</b> X-ray photon, an excitation source of photoelectrons <b>(c)</b> XPS wide-scan result, the peaks indicate in elements containing in the sample.....	96
<b>Fig. 3.15</b> High-resolution C 1s XPS spectra (a) GO spectra (b)-(f) Deconvoluted peaks with increased temperature. The inset from (c) shows the C/O ratio as a function of the reduction temperature. Comparatively, the inset from (f) shows a reference XPS spectra for raw graphite. After [196].....	98
<b>Fig. 3.16 a)</b> Raman spectra of pristine (top) and defected (bottom) graphene. The main peaks are labelled <b>b)</b> Comparison of Raman spectra at 514 nm for bulk graphite and graphene. They are scaled to have a similar height of the 2D peak at 700 cm <sup>-1</sup> (c) Evolution of the spectra at 514 nm with the number of layers. After [199].....	100
<b>Fig. 3.17 (a)</b> apparatus for dot blot. Source: ref. [204] <b>(b)</b> Construction of an indirect immunoassay used for the dot blot test in this research .....	101
<b>Fig. 4.1</b> Overall process of experimental work in this thesis .....	103
<b>Fig. 4.2</b> Processes for preparing GO and rGO sensors for QCM-D measurement.....	105
<b>Fig. 4.3 (a)</b> QSense Omega Auto (Biolin Scientific®) system <b>(b)</b> eight sensing chip holders and ports .....	107



<b>Fig. 4.4</b> Scanning Electron Microscopy images of <b>(a)</b> GO on SiO <sub>2</sub> with magnification of 132x showing separated flake for determining flake size <b>(b)</b> scans of GO coating on gold substrates with a magnification of 141x.....	108
<b>Fig. 4.5</b> Contact angle plugin interface (a) Selection of 2 baseline points and 3 points on the curvature of the drop-let edge (b) Circle/ ellipse fitting to determine contact angle .....	109
<b>Fig. 4.6</b> AFM mappings and Root-mean-square roughness ( $R_{RMS}$ ) of <b>a)</b> bare Au QCM chip, <b>b)</b> GO coating on Au chip. The height and roughness of gold nanoparticle highly contribute to the roughness of the graphene coating. Source: ref.[207]. .....	111
<b>Fig. 5.1 (a)</b> Tertiary structure of BSA <b>(b)</b> dimensions of BSA molecule <b>(c)</b> tertiary structure of immunoglobulin antibody <b>(d)</b> dimensions of immunoglobulin with specific binding sites. Protein structure images from the RCSB PDB (rcsb.org) .....	120
<b>Fig. 5.2</b> Optical and SEM micrographs from GO coated on Au QCM-D sensor. The working surface is fully covered with the varied number of graphene layers from one to few monolayers.....	123
<b>Fig. 5.3</b> QCM-D profiles of <b>(a)</b> frequency and <b>(b)</b> dissipation upon BSA adsorption on surfaces with different reduction degrees of the GO <b>(c)</b> $\Delta D - \Delta F$ plots of the adsorption. Two-stage adsorption (i, ii) can be seen in rGO2 to rGO4 samples that could correspond to hydrophobic and hydrophilic interactions, respectively <b>(d)</b> the plot of adsorption mass obtained from QCM-D analysis against the level of reduction of GO from zero to five representing GO to rGO5. The adsorbed mass reduces as the degree of reduction increases.....	126
<b>Fig. 5.4</b> QCM-D real-time adsorption monitoring and $\Delta D - \Delta F$ plots of different concentration BSA on <b>(a,b)</b> bare-Au, <b>(c,d)</b> GO coated on Au <b>(e,f)</b> rGO2 coated on Au and <b>(g,h)</b> rGO5 coated on Au .....	127
<b>Fig. 5.5 (a)</b> specific adsorption mass as a function of concentration for Au, GO and rGO. <b>(b)</b> the thickness of BSA film with varied concentrations adsorbed on Au, GO, rGO2 and rGO5 .....	130
<b>Fig. 5.6</b> The proposed models for BSA adsorption on graphene-based materials surfaces with the dependence on the hydrophobic degree and concentration of the protein. 133	
<b>Fig. 5.7</b> QCM-D monitoring of BSA and anti-BSA interaction on <b>(a)</b> GO and <b>(b)</b> rGO5. The protein adsorption on GO can maintain binding functionality to its antibody. The denaturation of protein was found on highly hydrophobic rGO but an additional layer of protein can be created on top of the denatured layer without denaturation .....	136
<b>Fig. 5.8</b> QCM-D results for IgG injection over BSA adsorption on <b>(a,b)</b> GO and <b>(c,d)</b> rGO for investigating non-specific adsorption and denaturation of BSA adsorption on the surfaces. Two concentrations of BSA including <b>(a,c)</b> 10 $\mu\text{g}/\text{mL}$ and <b>(c,d)</b> 1000 $\mu\text{g}/\text{mL}$ were studied. Only the case of 10 $\mu\text{g}/\text{mL}$ BSA-rGO can adsorb high amount of IgG as the thin layer of BSA could be denatured resulting in non-specific adsorption for other proteins. ....	137

**Fig. 5.9** QCM-D monitoring for testing the selectivity of BSA against its antibody on **(a)** GO and **(b)** rGO5 platforms. Both supports show specific adsorption of anti-BSA with comparatively low adsorption of other proteins..... 138

**Fig. 6.1** Photographs and layout of the sensor chip. **(a)** C-QCM instrument setup and cross section schematic of the C-QCM device with a custom-designed microfluidic channel. **(b)** Photograph of a rGO coated QCM sensing chip **(c)** Scanning electron microscope (SEM) image of the rGO coating on a QCM chip..... 154

**Fig. 6.2** Schematic for surface functionalisation using EDC/NHS crosslink **(a)** mechanism of carbodiimide crosslinker using EDC/NHS activation, **(b)** functionalization of rGO surface to detect the antibodies starting with BSA adsorption, activation with EDC/NHS, immobilization of the receptor NC3 (in red) via amine covalent cross-link and blocking with ethanolamine..... 155

**Fig. 6.3** QCM-D monitoring of receptor protein (NC3) immobilisation and anti-PLA2R antibody (Ab12) detection using different sensing surfaces **(a)** Au, **(b)** GO, **(c)** rGO, **(d)** Au-BSA, **(e)** rGO-BSA, **(f)** rGO-BSA, **(g)** Au-SAM, and **(h)** rGO-BSA+EDC/NHS..... 157

**Fig. 6.4** QCM-D study for selectivity test against calf serum of the sensing platform rGO-BSA with EDC/NHS activation. **a)** the detection of the antibody diluted in serum **b)** bare serum (negative control) **(c)** the antibody diluted in PBS and a table for frequency shifts resulting from the detection of the antibody measured during adsorption and after rinsing process ..... 159

**Fig. 6.5** QCM-D results for binding studies **(a)** frequency and dissipation profiles upon detection of varied concentrations of the Ab12 in PBS buffer and **(b)** their  $\Delta D - \Delta F$  plots of the antibody detection. **(c)** QCM-D monitoring of varied concentrations of the Ab12 in calf serum and **(d)** their  $\Delta D - \Delta F$  plots **(e)** comparison of the detection results obtained from varied concentration of the antibody in PBS and calf serum **(f)** QCM-D monitoring of three serum samples including plain calf serum, human sera from a healthy person and a MN patient. .... 161

**Fig. 6.6** Results from Ab12 antibody detection using C-QCM system. **(a)** The whole injection sequence on rGO coated on Au QCM chip **(b)** QCM results for sequential injection of varied concentrations of the Ab12 samples. **(c)** QCM profile for varied concentrations. The starting chip for **(b)** and **(c)** is rGO-BSA+EDC/NHS functionalised with NC3 as a receptor. **(d)** calibration curve obtained from the final frequency shifts against concentration of the antibody. .... 163

**Fig. 6.7** Detection results for the anti-PLA2R antibody in 8 patients' sera using **(a)** the C-QCM system and **(b)** QCM-D system. **(c)** Correlation plot of the final frequency shifts obtained from the C-QCM and the QCM-D **(d)** Comparison of the results obtained from C-QCM measurements and ELISA. .... 165

**Fig. 7.1** The QCM-D measurement for the monitoring of the nanobody immobilisation on different sensing surfaces and the detection of lysozyme ..... 184

**Fig. 7.2** QCM-D results of the five sensing surfaces used as a sensing platform for detecting varied concentrations of lysozyme (a) S.8 PrGO2-EDC/NHS (c) S.9 rGO-BSA-

EDC/NHS (e) S.11 PrGO2-SA (g) S.12 rGO- BiotBSA-SA and the standard curve with the computed KD values of the nanobody on different sensing platforms.....189

**Fig. 7.3** Results for selectivity tests of the functional surfaces **(a)** Selectivity comparison chart of sensing surfaces to different proteins. The S.12- rGO-BiotBSA-SA presents the highest specific detection of lysozyme with zero detection of other proteins. **(b)** QCM-D profiles obtained from the adsorption of plain serum on sensing surfaces. The SA-biotin surfaces (S.11, S.12) functionalised with the nanobody provide much less adsorption from plain calf serum compared to the amine crosslinking system. **(c)** QCM-D profiles for detection of varied concentrations of lysozyme diluted in serum media operated on S.12. The  $\Delta F$  and  $\Delta D$  increase as the concentration increases. **(d)** The plot of  $\Delta F_{Lys\ binding}$  in both PBS and calf serum against lysozyme concentration. The lysozyme in serum media shows higher frequency shifts compared to the sample in PBS due to the serum background. The triangular markers are the frequency shifts of lysozyme in serum after subtracting the serum background.....192

**Fig. 7.4** **(a)** QCM-D results of lysozyme detection using five different nanobodies as receptors, **(b)** the comparative numbers of lysozyme binding and dissociation measured from  $\Delta F_{binding}$  and  $\Delta F_{Dis}$ .....197

**Fig. 7.5** **(a-e)** Kinetic fitting results of lysozyme detection using five different nanobodies as receptors, **(f)** the comparison of KD determined by SPR and QCM-D systems .....198

**Fig. 8.1** Thermally stabilized cQCM laboratory instrument setup showing the openQCM device inside an isothermal chamber, Peltier cooler, temperature and humidity sensors and front panel of the custom-made electronic temperature control. A portable computer captures the QCM data through a custom GUI and controls the 3-channel peristaltic pump for sample flowing. ....204

**Fig. 8.2** **a)** SEM micrograph from rGO coated on Au QCM sensor. The working surface is fully covered with a varied number of graphene layers from one to few monolayers, **b)** Wetting contact angle (WCA) of bare Au and rGO-coated QCM sensors, **c)** Quartz Pro QCM sensors working electrode dimensions. ....209

**Fig. 8.3** Results for long thermal evaluation of the isothermal chamber. Vertical axis expressed the frequency shifts in kHz **a)** Thermal evaluation of the system's self-heating effect under controlled cooling. Temperature reported by the openQCM onboard sensor when controlling the temperature of the chamber upon self-heating, **b)** Temperature dependence of the frequency response of a QCM sensor under controlled cooling. Frequency vs Temperature response curve (•) for the data regions highlighted in (a) and two curve fits, linear and exponential, are shown and discussed in the text. Crystal's fundamental frequency,  $f_0 = 10$  MHz.....211

**Fig. 8.4** Results for the continuous cooling of the openQCM system **a)** QCM frequency response at continuous temperature decrease. Frequency response and temperature evolution over time. Both frequency and temperature present a linear region (in light blue) with change rates of 2.97 Hz/min and  $-0.51$  °C/min, respectively, **b)** Frequency vs temperature (F(T)) characteristic.....213

<b>Fig. 8.5</b> QCM results for the adsorptions of BSA on <b>a)</b> bare Au and <b>b)</b> rGO-coated using the cQCM, <b>c)</b> and <b>d)</b> present the same pair for the QSense system. ....	216
<b>Fig. 8.6</b> BSA mass adsorption densities comparison on <b>a)</b> bare Au and <b>b)</b> rGO-coated sensors. Results for the cQCM instrument are shown in green bars while QSense results correspond to the orange bars. See online version for colour. ....	217
<b>Fig. S1.1</b> Injection sequence for measuring protein adsorption with QCM-D. During the initial stage, a stable baseline must be reached. After stabilizing the QCM chip with PBS, the sample is injected then flowed through the sensor continuously for ~30 mins, then rinsed with PBS to remove loosely bound molecules.....	230
<b>Fig. S1.2</b> Data modelling flowchart showing the conditions for determining mass, thickness and viscoelastic properties of adsorbed films on surfaces.....	233
<b>Fig. S1.3</b> Scanning Electron Microscopy images, showing (a) flake size distribution of GO on SiO <sub>2</sub> , as described in (b), (c) GO, (d) rGO coated on QCM chip (e) and (f) show scans of GO on gold substrates with a magnification of 92x and 141x respectively. In all cases, the accelerating voltage was 5 kV. All measurements are in $\mu\text{m}$ .....	234
<b>Fig. S1.4.1</b> Atomic Force Microscopy images of a) GO spin coating on Au, b) its corresponding height profile c) GO flakes on SiO <sub>2</sub> and d) its corresponding height profile.....	235
<b>Fig. S1.4.2</b> AFM mappings and Root-mean-square roughness (R <sub>rms</sub> ) in nm scale are shown for (a) bare Au b) GO-Au, c) rGO <sub>2</sub> -Au, d) rGO <sub>5</sub> -Au. Scan area in all images is $2 \mu\text{m}^2$ .....	236
<b>Fig. S1.5</b> Wetting contact angles for GO and reduced GO with different reduction conditions including reduction temperature and time.....	237
<b>Fig. S1.6.1</b> (a) Wide scan XPS spectra (b) Atomic percent of C/O obtained from the wide scans and plot against the contact angle (c) detail spectra of C1s and (d) O1s for GO and reduced GO with different reduction conditions characterized by the contact angle. Oxygen content reduces with respect to the increase of contact angle.....	238
<b>Fig. S1.6.2</b> Deconvoluted details of C1s spectra for GO and rGO with various reduction levels. The reduction of GO to rGO via controlled thermal reduction can significantly restore sp <sup>2</sup> carbons.....	240
<b>Fig. S1.7</b> Raman spectra of GO and rGO with different level of reduction.....	241
<b>Fig. S1.8</b> QCM-D data on different surfaces a) BSA adsorption on Au and graphene derivatives b) Dissipation density graph ( $\Delta D$ vs $\Delta F$ ).....	242
<b>Fig. S1.9</b> Repeated results for QCM-D study of BSA adsorption on (a,b) GO and (c,d) rGO (e,f) partially reduced GO. The repeated results show reproducible and similar trends to the main results.....	243

<b>Fig. S1.10</b> (a) frequency and (b) dissipation shift due to BSA adsorption on GO and partially reduced GO with respect to the contact angle of rGO.....	244
<b>Fig. S1.11</b> The QCM-D real-time adsorption monitoring and $\Delta D$ - $\Delta F$ plots of different concentration BSA on (a,b) GO coated on SiO <sub>2</sub> , (c,d) rGO <sub>5</sub> coated on SiO <sub>2</sub> .....	245
<b>Fig. S1.12</b> Dot blot results of different concentration BSA adsorbing anti-BSA antibody in comparison to the denature BSA. Only non-denatured BSA can present the signal of antibody adsorption.....	246
<b>Fig. S1.13.1</b> Possible orientation of IgG antibody.....	277
<b>Fig. S1.13.2</b> QCM-D results for IgG injection over BSA adsorption on (a,b) GO and (c,d) rGO for investigating non-specific adsorption and denaturation of BSA adsorption on the surfaces. Two concentrations of BSA including (a,c)10 $\mu\text{g}/\text{mL}$ and (c,d) 1000 $\mu\text{g}/\text{mL}$ were studied. Only the case of 10 $\mu\text{g}/\text{mL}$ BSA-rGO can adsorb high amount of IgG as the thin layer of BSA was denatured resulting in non-specific adsorption for other proteins.....	227
<b>Fig. S2.1</b> (a) 3D PLA2R NC3 model structure adapted from Ref. [3] (b) tertiary structure of immunoglobulin G (IgG) antibody, image from the RCSB PDB (rcsb.org).....	249
<b>Fig. S2.2</b> the developed QCM system (a) Setup for the system. The laptop image is under the GNU LGPLv3 from [1] (b) custom-made graphic user interface for QCM data logging and visualization.....	249
<b>Fig. S2.3</b> Dot blot results of different concentration of NC3 binding with murine anti-PLA2R antibody (Ab12) in comparison to the denature NC3. Only non-denatured NC3 can present the response of antibody binding.....	253
<b>Fig. S2.4</b> Scanning Electron Microscopy images, showing (a) monolayer GO flake on SiO <sub>2</sub> (b) rGO coating on QCM-D chip from QSense and (c) rGO coating on QCM chip. In all cases, the accelerating voltage was 5 kV. All measurements are in $\mu\text{m}$ .....	255
<b>Fig. S2.5</b> XPS results obtained from bare rGO, rGO-BSA and rGO-BSA+ NHS samples (a) Wide scan spectra with atomic percent. (b) detail spectra of C1s (c) O1s and (d) N1s for all samples. The sample with EDC/NHS activation clearly shows functionalisation of carbon and nitrogen on the surface.....	257
<b>Fig. S2.6</b> Deconvoluted details of C1s spectra for C1s, N1s and O1s spectra of three functional graphene samples (a, d, g) rGO (b, e, h) rGO-BSA and (c, f, i) rGO-BSA with EDC/NHS activation.....	258
<b>Fig. S2.7</b> Raman spectra of (a) three different functional surfaces including bare-rGO, BSA-rGO and rGO-BSA+EDC/NHS. Deconvoluted details of the spectra of (b) bare-rGO (c) BSA-rGO (d) rGO-BSA+EDC/NHS.....	260
<b>Fig. S2.8</b> Desorption study presenting QCM-D monitoring of the protein receptor NC3 adsorption and detection of antibody in human serum and washing-off process on 3	

sensing platforms (a) immobilisation of NC3 on rGO (b) rGO-BSA (c) rGO-BSA with EDC/NHS activation surfaces.....	261
<b>Fig. S2.9</b> QCM results for sequential injection of liquid samples by pipetting DI water and PBS buffer on (a), (b) Au and (c), (d) rGO surfaces, respectively.....	262
<b>Fig. S2.10</b> Correlation plot of the final $\Delta F$ the final and $\Delta D$ value obtained from the test with 8 patients' sera.....	263
<b>Fig. S3.1.</b> Comparison of the dimension and molecular weight of antibody and nanobody with tertiary structure of a nanobody.....	264
<b>Fig. S3.2</b> The measurements of frequency shifts obtained from different adsorption events including the FO7 ( $\Delta F_{FO7}$ ) immobilisation, the lysozyme binding ( $\Delta F_{Lys}$ ), the dissociation ( $\Delta F_{Dis}$ ) and the reabsorbed nanobody ( $\Delta F_{non-specific Lys}$ ).....	267
<b>Fig. S3.3</b> Raman spectra of plain GO and different level of reduction of rGO and the graphene sample with EDC/NHS activation.....	270
<b>Fig. S3.4</b> XPS results obtained from graphene samples. (a)Wide scan spectra with atomic percent. Detail spectra of C1s (b) GO, PrGO2 and their EDC/NHS activation (c) rGO and rGO-BSA-EDC/NHS.....	271
<b>Fig. S3.5</b> Deconvoluted details of C1s spectra for C1s spectra of three bare surfaces (a) GO, (c) PrGO2, (e) rGO and the EDC/NHS activation samples (b) GO-EDC/NHS (d) PrGO-EDC/NHS (f) rGO-BSA with EDC/NHS activation.....	272
<b>Fig. S3.6</b> SEM image of fully-coverage and uniform coating of GO on a QCM-D chip.....	273
<b>Fig. S3.7</b> QCM-D monitoring of the direct adsorption of EDC/NHS solution on (a) GO (b) PrGO1.....	274
<b>Fig. S3.8</b> QCM-D monitoring of the direct adsorption of the SA adsorption on GO, PrGO1 and rGO and the BiotFO7 nanobody binding.....	275
<b>Fig. S3.9</b> (a) QCM-D result of the binding of varied concentrations of lysozyme on the Au-SAMs functionalised with the FO7 nanobody. (b) The standard curve with the computed KD values of the nanobody on the Au-SAMs.....	276
<b>Fig. S3.10.</b> QCM-D monitoring of non-specific protein adsorption on five different functionalised surfaces showing selectivity against serum protein of the surfaces.....	277
<b>Fig. S4.1</b> Instrumentation electronics for openQCM system a) Pierce oscillator where Xtal represents the QCM sensor b) Instrumentation electronics mounted on a shield for an Arduino Micro.....	260
<b>Fig. S4.2</b> Voltage divider for NTC compensation. RNTC is the thermistor resistance, RREF is a reference or compensation resistor. VCC and VOUT are the supply and output	

voltages, respectively. The mathematical expression represents the standard relationship for a two resistors voltage divider to determine $V_{OUT}$ .....	279
<b>Fig. S4.3</b> Arduino Pro Micro pinout. Image taken from Sparkfun Electronics (Jimblom (Sparkfun Electronics), 2020) under the Creative Commons License BY-SA 4.0.....	280
<b>Fig. S4.4</b> ADC readout analysis. NTC Temperature vs ADC Voltage. The top panel shows the full-scale response of the voltage divider. The lower panel covers the range of experimental temperatures and linear trend.....	281
<b>Fig. S4.5</b> Graphical user interface for openQCM data acquisition, baseline calibration and logging.....	284
<b>Fig. S4.6</b> Flow chart for the custom-made data acquisition GUI.....	285
<b>Fig. S4.7</b> Baseline calibration routine subprocess.....	287
<b>Fig. S4.8</b> Schematic of the data acquisition routine.....	288
<b>Fig. S4.9</b> Block diagram for a closed loop system.....	289
<b>Fig. S4.10.</b> Mathematical expression for the PID control theory and its corresponding closed loop block diagram. $T_i$ and $T_d$ are the integration and derivative time, respectively.....	290
<b>Fig. S4.11</b> Complete PID algorithm implemented on the Arduino Microcontroller for controlling the temperature of the chamber.....	291
<b>Fig. S4.12</b> Setup routine for variables, flags and ports initialization. This routine runs only once.....	291
<b>Fig. S4.13</b> Routine for reading voltages from the NTC voltage divider attached to analog channel 0. Samples are averaged on each acquisition cycle.....	291
<b>Fig. S4.14</b> Routine for reading the keyboard of the thermal control. Each subroutine returns the new value for the PID parameters. If the PID flag is active the control algorithm runs otherwise it stops.....	291
<b>Fig. S4.15</b> Full PID computing and Peltier activation routine. The output of the PID algorithm is an equivalent activation time within a window (period) of 5 seconds.....	292
<b>Fig. S4.16</b> Schematic representation of a) continuous PID computing, signal activation conditions and edge change from LO-state to a HI-state b) Timing scheme example the activation and deactivation of the Peltier cell.....	292
<b>Fig. S4.17</b> Possible activation states for a PWM signal of 5 seconds.....	293
<b>Fig. S4.18</b> XPS data for rGO films a) C1s peaks b) Widescan peaks fitting.....	294
<b>Fig. S4.19</b> AFM profile from a) bare Au sensors and b) rGO-coated sensors. Scan area in all images is $2 \mu\text{m}^2$ .....	295

**Fig. S4.20** cQCM and QSense calibration curves. a) cQCM-Au response with Hill fitting. b) cQCM-rGO response and linear fit. c) QSense-Au response with Hill fitting. d) QSense-rGO response curve and linear fit. Inset plots a) and c) show the linear fits from the highlighted regions (rectangle).....297



## List of Tables

<b>Table 2.1</b> Five types of antibodies and their properties and functions.....	71
<b>Table 5.1</b> Summary of properties of GO and various degrees of rGO used in this study. .....	125
<b>Table 6.1</b> The QCM-D results of the adsorption of NC3 (receptor) and Ab12(analyte) on all sensing surfaces for comparison of sensing performance.....	156
<b>Table 6.2</b> Comparison of existing technique for the anti-PLA2R detection .....	166
<b>Table 7.1</b> Sensing surfaces tested in this study including their complete injection sequences for constructing the functional surfaces and investigating the binding and dissociation. ....	179
<b>Table 7.2</b> Surface characterisations of the graphene surfaces and their carboxylic acid activation obtained from contact angle, Raman and XPS techniques.....	182
<b>Table 7.3</b> Summary and justification of the sensing feasibility for the 12 testing platforms based on the selection criteria discussed in the main text.....	183
<b>Table 7.4</b> The models of five selected sensing surfaces and the thickness of the sensing layer of each functional surface.....	187
<b>Table 7.5</b> Comparison of sensing characteristics obtained from 5 sensing platforms used in this research .....	195
<b>Table 7.6</b> $K_D$ values of five nanobodies against lysozyme with different binding strength determined from QCM adsorption profiles compared to reference values from SPR characterisation .....	196
<b>Table 8.1</b> Summary of mean temperature values and frequencies during the selected stabilization ranges .....	212
<b>Table 8.2</b> Summary of sensitivity, limits of detection and linear ranges for the cQCM and QSense systems.....	219
<b>Table S1.1</b> Wetting contact angle (WCA) of DI water droplet of GO and rGO5 coating on Au and SiO <sub>2</sub> substrates.....	237
<b>Table S2.1</b> Comparison of frequency shift results between Au and rGO QCM chip.....	263
<b>Table S3.1</b> The wetting contact angles (WCAs) of Au, SiO <sub>2</sub> and graphene coating QCM-D chips.....	269
<b>Table S3.2</b> The results of calculated thickness of sensing layers from the Sauerbrey equation.....	275

## Acronyms

2-D	2-Dimensional
3-D	3-Dimensional
Ab	Antibody
AFM	Atomic Force Microscopy
Ag	Antigen
ANA	Antinuclear Antibody
BSA	Bovine Serum Albumin
Biot	Biotinylated
CNT	Carbon nanotube
CVD	Chemical Vapor Deposition
CV	Cyclic voltammetry
CLL	Chronic lymphocytic leukaemia
c-QCM	Custom-QCM
CIDP	Chronic inflammatory demyelinating polyneuropathy
D	Disorder Peak (Raman)
D	energy Dissipation (QCM-D technique)
BSA	Denatured BSA
DI	Deionized (water)
$\Delta D$	Dissipation shift
$\Delta F$	Frequency shift
ELISA	Enzyme-linked Immunosorbent Assay
EDC	Ethyl(dimethylaminopropyl) Carbodiimide
FET	Field-Effect Transistor
FTIR	Fourier-Transform Infrared Spectroscopy
FDA	Food and Drug Administration
G-QCM	Graphene-QCM
GC	Glassy carbon

GO Graphene Oxide  
GOx Glucose oxidase  
GUI Graphic User Interface  
GVHD Graft-versus-host disease  
hcAb Heavy-chain Antibody  
Ig Immunoglobulin  
IVIg Intravenous immunoglobulin  
KD Kinetic dissociation  
KD Kawasaki disease  
Lys Lysozyme  
MMN Multifocal motor neuropathy  
MN Membranous nephropathy  
MS Mass spectrometry  
Nb Nanobody  
NHS N-hydroxysuccinimide  
NIR Near infrared  
PBS Phosphate Buffered Saline  
PCR Polymerase Chain Reaction  
PID Proportional Integral Derivative  
PPE Personal Protective Equipment  
PLA2R Phospholipase A2 Receptor  
PrGO Partially reduced graphene oxide  
PS Polystyrene  
PIs Primary immunodeficiencies  
Q Quality Factor  
QCM Quartz Crystal Microbalance  
QCM-D Quartz Crystal Microbalance with Dissipation Monitoring  
QCR Quartz Crystal Resonators  
QED Quantum electrodynamics

rGO	reduced Graphene Oxide
RNA	Ribonucleic acid
S.n	Surface n (n = 1, 2,3...)
SA	Streptavidin
SAMs	Self-assembled Monolayers
SD	Standard Deviation
SDS	Sodium Dodecyl Sulfate
SEM	Scanning Electron Microscope
SPR	Surface Plasmon Resonance
SLE	Systemic Lupus Erythematosus
sdAb	Single-domain Antibody
TEM	Transmission Electron Microscopy
WCA	Wetting Contact Angle
XPS	X-ray Photoelectron Spectroscopy

## Abstract

In this thesis, graphene derivatives were used as a coating material for sensor chips to improve their surface functionalities. There are three main articles presented in this thesis ranging from the study of graphene-biomolecule interactions to real-world applications. In the first publication, the quartz-crystal microbalance with dissipation monitoring (QCM-D) technique was employed to study the interaction dynamics of a typical protein, bovine serum albumin (BSA) and graphene materials of varying degrees of functionalisation. The results present significant differences in molecular orientation and confirmation, mass adsorption and antibody binding function of BSA on different graphene surfaces. The binding function of adsorbed BSA was investigated through the interaction with its anti-BSA antibody counterpart. Based on these findings, highly hydrophobic rGO was selected to develop a sensing platform for immunochemical detection, as presented in the second publication. Both the route to functionalise rGO with a specific receptor protein along with a sensitive and low-cost immunoassay tool based on a customised open-source QCM are also presented. Graphene biointerface QCM sensors (G-QCM) were employed to quantify antibodies in undiluted patient serum. We demonstrate its efficacy for a specific antibody against the phospholipase A2 receptor (anti-PLA2R), a biomarker in idiopathic membranous nephropathy. Furthermore, we have explored using our graphene-QCM sensing tool with single-domain antibodies, also called nanobodies, as receptors for antigen proteins, as presented in the third article (ongoing publication). Methods for the functionalisation of nanobodies on graphene-family materials have been explored based on physical adsorption, amine crosslinking, and streptavidin (SA)-biotin interaction. The nanobody against lysozyme was used as a model protein pair. The QCM-D technique was used to monitor the adsorption of the nanobody on different surfaces, its biomolecular recognition and selectivity against other proteins and animal serum. Altogether, the collected knowledge from a series of systematic studies on the biomolecular interactions with graphene led to the development of graphene-biointerface immunosensing platforms. The prototype of a point-of-care QCM immunosensor was developed and tested with patient serum emphasising the potential to be a real-world disease screening tool.

## Declaration

No portion of the work referred to in the thesis has been submitted in support of an application for another degree of qualification of this or any other university or other institute of learning.

## Copyright Statement

- i. The author of this thesis (including any appendices and/or schedules to this thesis) owns certain copyright or related rights in it (the “Copyright”) and he has given The University of Manchester certain rights to use such Copyright, including for administrative purposes.
- ii. Copies of this thesis, either in full or in extracts and whether in hard or electronic copy, may be made only in accordance with the Copyright, Designs and Patents Act 1988 (as amended) and regulations issued under it or, where appropriate, in accordance Presentation of Theses Policy.
- iii. The ownership of certain Copyright, patents, designs, trademarks and other intellectual property (the “Intellectual Property”) and any reproductions of copyright works in the thesis, for example graphs and tables (“Reproductions”), which may be described in this thesis, may not be owned by the author and may be owned by third parties. Such Intellectual Property and Reproductions cannot and must not be made available for use without the prior written permission of the owner(s) of the relevant Intellectual Property and/or Reproductions.
- iv. Further information on the conditions under which disclosure, publication and commercialization of this thesis, the Copyright and any Intellectual Property and/or Reproductions described in it may take place is available in the University IP Policy (see <http://documents.manchester.ac.uk/DocuInfo.aspx?DocID=24420>), in any relevant Thesis restriction declarations deposited in the University Library, The University Library’s regulations (see <http://www.library.manchester.ac.uk/about/regulations/>) and in The University’s policy on Presentation of Theses.

## Acknowledgements

I want to express my sincere gratitude to my financial sponsor, the Development and Promotion of Science and Technology Talents Project (DPST), for the financial support given throughout my doctoral studies. Also, I greatly thank the staff who worked on every aspect related to the scholarship, especially during the COVID-19 lockdown period.

I gratefully thank my main supervisor, Dr Aravind Vijayaraghavan, for his supports in both academic and working experiences. Furthermore, I am thankful for the trust he put in me in several academic and business events that represented invaluable challenges that broadened my view on technological commercialization.

I acknowledge my co-supervisor, Dr Thomas Jowitt, for his continuous and kind support in the biological knowledge and lab works. I would also like to thank Maryline Fresquet for her impartial help on biological laboratory techniques, like dot blot, that I had never experienced before.

Special thanks to Dr Patrick Hamilton from Manchester Academic Health Science Centre (MAHSC) and Rachel Lennon from the department of Paediatric Nephrology, Royal Manchester Children's Hospital, Manchester University, for their help and supervision on clinical tests with patients' samples.

In the Nano functional Materials Group, I found myself surrounded by precious people. I want to thank the group members: Dr Maria Iliut, Dr Cian Bartlam, Natalie Parsons, Dai Luan, Kaiwen Nie and everyone else who are part of the Nanofunc crew. Special acknowledgement goes to my beloved colleague Dr Daniel Melendrez for his enormous support in the past years. Thank you for the spontaneous help and for physically and mentally encouragement throughout the whole project.

My special gratitude goes to my family in Thailand, Mr Samai and Mrs Niramol Hampitak, for trusting me and for your encouragement to do what I want to do. Also, thanks to my lovely and funny sister, Kamonwan Hampitak, who always help entertaining me when I feel stressed and bored from work.

## About the Author

Piramon Hampitak was awarded her BSc in Physics (2015) from Khon Kaen University, Thailand. Project title: "In-situ XANES Study of MnO<sub>2</sub> Nanostructure for Supercapacitor Electrodes"

Piramon was awarded her MSc in Advanced Engineering Materials (2017) from The University of Manchester, UK. Project title: "In-situ XRD study Of mixed-conductive ceramics-  $Ba_{0.5}Sr_{0.5}Co_{0.8}Fe_{0.2}O_{3-\delta}$  (BSCF 5582) for Solid Oxide Fuel Cells"

Piramon has published two articles as a first author in *Carbon* and *ACS sensors* and one article as a second author in *Analytica Chimica Acta*. She was featured in the 'Introducing our Authors' section from the *ACS sensors* Journal (*ACS Sens.* 2020, 5, 3295–3296)

## Publications

Publication on Q1 scientific Journals

1. Hampitak, Piramon, et al. "Protein interactions and conformations on graphene-based materials mapped using a quartz-crystal microbalance with dissipation monitoring (QCM-D)." *Carbon* 165 (2020): 317-327. <https://doi.org/10.1016/j.carbon.2020.04.093>
2. Hampitak, Piramon, et al. "A Point-of-Care Immunosensor Based on a Quartz Crystal Microbalance with Graphene Biointerface for Antibody Assay." *ACS sensors* 5.11 (2020): 3520-3532. <https://doi.org/10.1021/acssensors.0c01641>
3. Meléndrez, D., Hampitak, P., Jowitt, T., Iliut, M., & Vijayaraghavan, A. (2021). Development of an open-source thermally stabilized quartz crystal microbalance instrument for biomolecule-substrate binding assays on gold and graphene. *Analytica Chimica Acta*, 1156, 338329. <https://doi.org/10.1016/j.aca.2021.338329>



## Rationale for submitting the thesis in an alternative format

With the fast-paced progression of work, the author of the present thesis has been fortunate to publish her research results in peer-reviewed journals. Two significant pieces of research were published in Q1 journals, including *Carbon* and *ACS sensors*. Another part of the work is currently in the process of intellectual property consideration before these results are presented. Furthermore, she contributed in equal proportion to the leading author in the research published in the *Analytica Chimica Acta* journal. These three publications, along with an additional one in progress, link together this Doctoral research as the findings from the first publication provide an intensive understanding of graphene-protein interaction and set the path for the functionalisation of receptor proteins and further developments for the previously discussed graphene-based immunosensor. Moreover, the publications cover all the work from the author's PhD studies. Therefore, it is justified to present them in this thesis in an alternative format.

## Outline

**CHAPTER 1** presents the introduction of the topics covered in this thesis, including the motivation to pursue this doctoral research and the objectives and scopes of this work. First, general highlights about the properties of graphene, graphene derivatives and their most relevant applications in the biomedical research field are described. This is followed by the description of the QCM-D technique and its importance in biomolecular research. Next, a background on graphene-protein interaction is discussed. This is then linked to the motivation for the first project of this PhD: the investigation of the dynamic behaviour of proteins and their interaction with graphene derivatives. This work was published, and it is presented in Chapter 5. The results from the first project sparked the idea for the second one, which proposes a graphene-based immunosensor for antibody detection, as presented in Chapter 6. It aims to bring research into a real-world application: the development of a graphene biointerface. Its applicability was further explored through the functionalization with another innovative bioreceptor called 'nanobody', becoming the idea for the third project. This third project aims to prove the feasibility of using graphene as a platform to functionalize with a wide range of protein receptors.

**CHAPTER 2** reviews the literature for biosensors, applied materials and their biomedical applications. Section 2.1 introduces the overview of biosensors, including their definition and general properties. Section 2.2 exemplifies some biosensor techniques where graphene-based materials can be applied, including QCM, Field Effect Transistors (FETs) and electrochemical biosensors. Section 2.3 is dedicated to graphene and its derivatives. Their properties and applications in biosensors are discussed. A general description of graphene's main characteristics, such as its structural, electronic, mechanical and optical properties, is discussed. Section 2.4 describes the interaction between biomolecules and the family of graphene materials, emphasizing the properties that affect the interaction and the types of chemical bonds involved in the molecular binding on the graphene surface. Section 2.5 provides information about the model proteins used in this research, including BSA, lysozyme and IgG. The structural details, properties and applications of these proteins are presented. Section 2.6 gives

detailed information about the interaction of antigen and antibodies and their applications in biomedicine. One of the crucial applications based on this interaction is screening autoimmune diseases since specific antigens and antibodies are vital biomarkers for diseases of this type. Further details regarding the screening of autoimmune diseases are presented in section 2.7. In section 2.8, details about membranous nephropathy, an autoimmune disease studied in this research, are explained. Finally, the use of nanobody technology that pinpoints the relevance of the studies presented in the current thesis is discussed in section 2.9.

**CHAPTER 3** presents a review of the techniques used in the characterisation of the related materials. Section 3.1 introduces the QCM technique and its mathematical modelling. Section 3.2 describes the wetting contact angle (WCA) as a technique for measuring the hydrophobicity of graphene. The imaging, topographical and spectrographic methods for the characterisation of graphene, including SEM and AFM, are presented in sections 3.3 and 3.4, respectively. The applied chemical characterisation techniques, including FTIR, XPS and Raman, are described in sections 3.5, 3.6 and 3.7, respectively. Finally, section 3.8 briefly presents the description of the dot blot procedure, a technique in molecular biology used to determine the performance of protein pairs.

**CHAPTER 4** gives a general description of the applied experimental protocols and the tools used in the present research. Section 4.1 describes the general experimental process followed throughout this research. Next, section 4.2 explains the preparation of graphene oxide dispersion used in this research, followed by the protocols for coating the QCM chips via spin coating, presented in section 4.3. Next, general protocols for QCM-D measurement are described in section 4.4. Finally, in Chapter 4.5, the characterisations of graphene samples with multiple techniques are described.

**CHAPTER 5** Publication 1 - Hampitak, Piramon, et al. "Protein interactions and conformations on graphene-based materials mapped using a quartz-crystal microbalance with dissipation monitoring (QCM-D)." *Carbon* 165 (2020): 317-327. doi.org/10.1016/j.carbon.2020.04.093

**CHAPTER 6** Publication 2 Hampitak, Piramon, et al. "A Point-of-Care Immunosensor Based on a Quartz Crystal Microbalance with Graphene Biointerface for Antibody Assay." ACS sensors 5.11 (2020): 3520-3532. doi.org/10.1021/acssensors.0c01641

**CHAPTER 7** Publication 3 (in the process of publication)- Binding kinetics and biological recognition of nanobodies functionalised on graphene derivatives for immunosensing applications

**CHAPTER 8** Co-Author Publication Meléndrez, D., Hampitak, P., Jowitt, T., Iliut, M., & Vijayaraghavan, A. (2021). Development of an open-source thermally stabilised quartz crystal microbalance instrument for biomolecule-substrate binding assays on gold and graphene. Analytica Chimica Acta, 338329. doi.org/10.1016/j.aca.2021.338329

In this project, Piramon Hampitak uses the in-house developed QCM instrument to test graphene-protein adsorption monitoring and validation of the instrument. This task corresponds to the work from publication 1.

**CHAPTER 9** concludes this PhD thesis with relevant remarks and opportunities for research and development with the help of the QCM technique coupled with graphene-based sensors.

**APPENDICES** comprises a series of relevant supporting information created for the individual pieces of research from the present thesis.

## **REFERENCES**

## CHAPTER 1. Introduction

Contents:

1.1 Background and Motivation

1.2 Objectives

1.3 Scopes

## 1.1 Background and Motivation

### **Why Graphene?**

In 2010 the Nobel prize in Physics was awarded jointly to two researchers from the University of Manchester, Sir Andre Geim and Konstantin Novoselov “for groundbreaking experiments regarding the two-dimensional material graphene” pioneering its stable isolation and thus kickstarting a new era for 2D materials research [2]. Since then, the field of 2D materials, led by graphene, has gained the attraction of researchers from many areas of science due to their unique properties which can be exploited in a vast range of technological applications. In particular, graphene has been utilised in various sensing applications, including gas, chemical and biological sensors, due to its extraordinary chemical, electronic and mechanical properties. Due to its 2D nature, each atom in the structure of graphene interacts directly with the environment. Moreover, some of the properties of graphene can change during the interaction with the surrounding media, including its conductivity, mass, resonant frequency and even electron density. These changes can be exploited for the design of a wide variety of sensors leading to high sensitivity, selectivity and high signal-to-noise ratio (SNR). Furthermore, graphene and its derivatives have shown outstanding biocompatibility [3], thus, becoming promising materials for biomedical applications, especially biosensors. For example, exfoliated graphene has been widely used for developing FET (Field-Effect Transistor)-based sensors [4], electrochemical and optical biosensors, drug delivery systems, implantology processes [5] and graphene oxide (GO) as a supporting layer for biomimetic lipid membranes [6], [7].

Graphene oxide, a highly oxidised form of graphene, has also shown great potential to be used in biomedical applications due to its high biocompatibility, particular surface chemistry, structural features like large surface area and a relatively low production cost compared to pristine graphene. It consists of single-atom-thick carbon sheets with oxygen functional groups including phenol, hydroxyl and epoxide groups attached to both top and bottom planes and carbonyl and carboxyl groups attached to the edges of the graphene sheets [8]. Specifically, the functional groups located at the edges are hydrophilic, whereas the basal plane groups are predominantly hydrophobic. The latter

renders GO soluble in water, making it easier to process and handle; however, its electrical conductivity is significantly reduced. Therefore, to confer properties comparable to those from pristine graphene, the oxygen-containing groups from GO must be removed by thermal or chemical treatments to form reduced (r)GO, obtaining a significantly more hydrophobic and conductive form of graphene.

### **The Quartz Crystal Microbalance with Dissipation (QCM-D) Technique**

The QCM-D monitoring technique is a high time-resolved instrumental technique based on the piezoelectric effect from quartz crystals. Specifically, AT-Cut quartz crystal sensors are electronically configured in resonant mode then both its frequency overtones and energy dissipation are computed and stored, representing biomolecular events that occur at the sensor's surface. It is useful to assess the adsorption mechanism and the structural conformation of biomolecular events on the underlying substrate. Our group recently established graphene-based Quartz Crystal Microbalance (QCM) as support surfaces with tuneable hydrophobicity to control lipid membrane structures [6]. We used soluble graphene derivatives, like GO, as thin-film coating materials to provide a fast and easy way to achieve a surface with tuneable hydrophobicity through a controlled thermal reduction. Interestingly, the ability to enhance the sensitivity of graphene-based sensors depends on the appropriate functionalisation of the graphene layers. Using graphene as a direct supporting layer or by interfacing graphene with biological systems, we can present a more native environment to biomolecules to interact with sensor's surfaces, thus promoting sensitivity and selectivity. Therefore, this hybrid 2D-material/biomolecules platform could be an effective method to develop graphene-based biosensors.

### **Importance of Graphene-Protein Interactions**

The study of protein-surface interactions is a fundamental step to understanding the processes involved when a foreign material contacts biological fluid. Additionally, the development of a wide range of applications in biotechnology such as implant surfaces [9], biosensors [10], and surfaces for tissue engineering and regenerative medicine [11] depend on the properties of the bio-interface. More importantly, a better understanding of graphene-based materials and their interaction with biological entities

can importantly aid the manufacture of long-term medical implants and bioartificial sensors [12].

Most of the currently available practical biomedical applications are built upon electrochemical or physical events during the biological interactions at the interfaces between blood plasma protein and substrates. In addition, protein adsorption could also negatively affect the performance of biosensors by blocking the specific adsorption, resulting in the reduction of molecular cut-off limits [13]. One of the key factors for developing reliable biosensors is to provide adequate conditions to the biomolecules to retain their biological activity for the biomolecular binding to successfully occur. Such a task is significantly influenced by the specific surface chemistry of the substrate.

Let the discussion presented so far establish the primary theoretical grounds from this thesis. Moreover, these facts and hypotheses constitute the initial motivation for pursuing the present Doctoral research regarding the study of the interactions between graphene derivatives and proteins, like serum albumins.

Bovine Serum Albumin (BSA), a low-cost human-like serum albumin and the most abundant protein in blood plasma, has been used for many years in a wide variety of applications, including as a blocking agent for biosensors and a coating material for implants, as it can increase the biocompatibility of the coated materials [14]–[16]. BSA has also been vastly used for studying the surface affinity of biomolecules [15]. However, to effectively employ any biomaterial, a good understanding of its structural conformation, its ability to adsorb on the solid surface and its behaviour during kinetic adsorption is fundamental. Although some studies have proposed different scenarios on how BSA adsorbs on graphene derivative surfaces [17] [18], the adsorption mechanisms and the structural properties of proteins on surfaces are not yet well understood due to, in part, the limitations from the experimental techniques for molecular monitoring. Therefore, a better quantitative and qualitative description of the physical and chemical processes at the graphene-biomolecules interface will play a key role in the mass use of graphene in biomedical applications.



## Research Topics in This Thesis

This thesis covers three main research topics: 1) the study of the graphene-biomolecule interaction, 2) the development of a biosensor prototype for disease screening, and 3) the functionalisation of the graphene-QCM platform with a novel receptor, known as nanobodies.

During the first year of this PhD project, we employed a graphene-based QCM sensor to investigate the adsorption dynamics of BSA on GO and rGO. With the help of the dissipation monitoring capabilities from the QCM-D system; a factor that quantifies the energy released during the adsorption process, the structural properties of the adsorbed film can be determined by viscoelastic modelling. Additionally, the biorecognition of the protein and its properties after the adsorption process was studied by binding the protein with its respective antibody. The aforementioned experimental technique established the basis for developing graphene-based biosensors through the effective functionalisation of proteins, specifically BSA, with graphene derivatives for biosensing applications.

The second research involves the development of a graphene-based immunosensor for antibody detection. This study was based on the discoveries from the previous graphene-BSA project and the results from a parallel work from our research group regarding the development of a QCM instrument for point-of-care testing. Here, a sensitive and low-cost immunoassay based on a customised open-source QCM coupled with graphene biointerface sensors (G-QCM) was developed to quantify antibodies in patient serum. We demonstrate its efficacy for a specific antibody against the phospholipase A2 receptor (anti-PLA2R), a biomarker in idiopathic membranous nephropathy. A novel graphene-protein bio-interface was constructed by adsorbing a low concentration of denatured bovine serum albumin (dBSA) on an rGO-coated sensor surface. This method was proposed and demonstrated in the first piece of research from the current project. The dBSA film on the rGO surfaces acts as a cross-linker for the immobilisation of the receptor for anti-PLA2R antibodies and prevents the denaturation of the protein receptor.

In the third project of the current thesis, the graphene-QCM platform for immunosensing applications was further explored. Single domain antibody fragments, also known as nanobodies were used as protein receptors. Nanobody is a trademark of Ablynx. They are based on the variable domain of heavy chain-only camelid antibodies (VHH). Nanobodies can also be recombinantly produced in micro-organisms, like bacteria using synthetic libraries coupled to phage display [19]. Novel classes of recombinant antigen-binding proteins, like nanobodies, are on the rise due to their smaller size and ease of production on a large scale compared to full-length antibodies. Although nanobodies are considered effective protein receptors because of their single antigen-binding site and fewer possible orientations compared to the antibody, their bio-interface functionalisation on solid platforms is still challenging due to interference of surface chemistries of the solid substrate. This study explored methods to functionalise nanobodies and graphene-like materials based on physical adsorption, amine crosslinking, and streptavidin (SA)-biotin interaction. The nanobody against lysozyme was used as a model protein pair. The QCM-D technique was used to monitor the adsorption of the nanobody on different surfaces, its biomolecular recognition and selectivity against other proteins and animal serum. Moreover, the biomolecular conformations can be described in more detail by applying advanced viscoelastic models like the Voigt-Voinova. Additionally, the equilibrium kinetics dissociation ( $K_D$ ) factor was determined from the QCM-D results and compared to those from Surface Plasmon Resonance (SPR) for validation. As a result, a simple but effective method for the functionalisation of nanobodies on the graphene surface was proposed.

Regarding all the studies in this thesis, a fundamental understanding of graphene-proteins interaction was achieved. Furthermore, methods for functionalising different kinds of protein receptors have been explored. Finally, the development of a real-world application of the graphene bio-interface sensor has been demonstrated.

## 1.2 Objectives

The overall objectives of this research are: to investigate and describe graphene-protein interactions, understand their properties and mechanisms and finally exploit our discoveries into a real-world application, in this case, a biosensor for disease screening. Additionally, we aimed at developing a working sensor prototype, testing the system under real-world conditions to validate its utility.

## 1.3 Scopes

- Varying degrees of reduction of GO were achieved via thermal reduction only.
- For the study of graphene-biomolecule interactions, only graphene derivatives (GO, rGO) and protein molecules were studied.
- QCM-D is the primary experimental technique for the investigation of biomolecular interaction, binding and recognition events
- The open-source-based QCM electronic instrument was used to develop a point-of-care immunosensing device.
- The graphene-QCM sensors were developed to detect and quantify immune-related proteins only.

## CHAPTER 2. Literature Review

Contents:

2.1 Overview of Biosensors

2.2 Biosensor techniques

2.3 Graphene and graphene derivatives

2.4 Interaction between biomolecules and graphene-family materials

2.5 Model proteins – BSA, Lysozyme, IgG

2.6 Antigen-antibody interaction

2.7 Screening of autoimmune diseases

2.8 Membranous nephropathy

2.9 Nanobody technology

## 2.1 Overview of Biosensors

Biosensors are analytical devices designed for the conversion of the response from biological interaction into an electrical signal. The typical architecture of biosensors mainly consists of biological components to detect an analyte and transducer parts to produce measurable signals. Biosensing technologies have been extensively researched and developed for various applications, including drug delivery and discovery, diagnosis and treatment, food safety, environmental monitoring, and security [20]. In brief, the functional blocks from a biosensor can be described as follows:

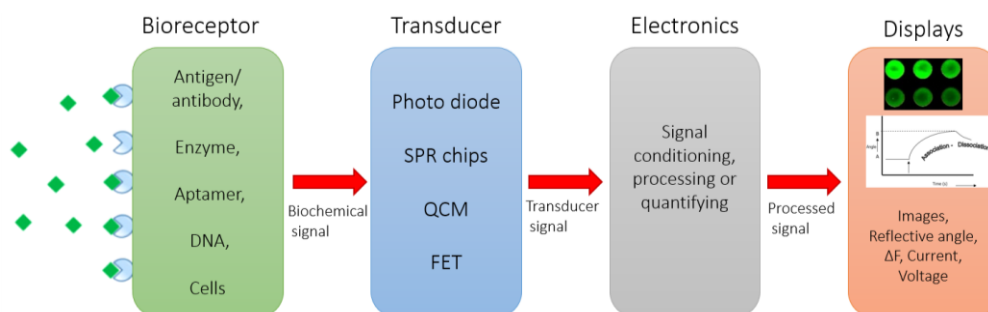
**Analyte:** A substance of interest that needs detection. For example, glucose is the ‘analyte’ for a glucose detector biosensor.

**Bioreceptor:** A molecule that recognizes the analytes such as enzymes, cells, deoxyribonucleic acid (DNA), antibodies, and nanoparticles explicitly. The signal is generated upon the interaction between the bioreceptor and the analyte, known as bio-recognition. For instance, Glucose Oxidase (GOx) is the biological detection entity in a glucose meter.

**Transducer:** An element that converts one form of energy to another; in this case, the bio-recognition event is transformed into a measurable signal. This process of energy conversion is known as signalization.

**Electronics:** A part of a biosensor that transforms the response from the transducer to the displayed signal. It usually consists of complex electronic circuits to process and condition signals such as amplification and conversion of signals from analogue into the digital form.

**Display:** An interpretation system, such as a computer monitor or a direct printed signal understandable by the user. The output signal can be in a number, graph or image.



**Fig. 2.1** Schematic diagram showing the main components for a biosensor including bioreceptor, transducer, electronics for signal processing and display interface.

The performance of the biosensor highly depends on the optimisation of its sensing characteristics, including selectivity, reproducibility, stability, sensitivity, and linearity.

**Selectivity** is the most critical property of biosensors which allows them to detect a single analyte in a mixture of biological entities. For example, the interaction between an antigen and an antibody may be the best indicator of selectivity. Thus, selectivity is the primary criterion for selecting receptors to be used in the construction of a biosensing platform.

**Reproducibility** refers to the ability of a signal to be replicated for a duplicated measurement. This quality is typically dependent on the precision and accuracy of the biosensor's transducer and circuitry. Reproducible signals are critical for a biosensor's dependability and resilience.

**Stability** refers to the sensor's capacity to withstand ambient disturbances during measurement. These disturbances can introduce drift and noise into the output signals, resulting in sensing-related mistakes. Stability may be the most significant issue for monitoring or measuring events that take place over an extended period of time. A stable temperature is a significant component impacting sensing stability, as transducer and electronic responses are frequently temperature-sensitive. Electronics tuning is a frequently used technique for achieving a stable response. Additionally, stability may be dependent on the bioreceptor's affinity. Bioreceptors with a high binding capacity encourage strong electrostatic bonding or covalent coupling with the analyte, which may contribute to the biosensor's stability. Another critical element is the degradation of the bioreceptor during the testing procedure or over the sensor's lifetime. Thus, routine sensing system maintenance is essential to address the difficulty of stability

**Sensitivity** refers to the smallest amount of analyte detected by a biosensor. A detection limit of analyte concentration can be as low as ng/ml or even fg/ml in a variety of medical and environmental monitoring applications to confirm the presence of the analyte in a sample. For instance, a prostate-specific antigen (PSA) value of 4 ng/ml in blood indicates a connection with prostate cancer [299]. The creation of biosensors to achieve high sensitivity is one of the most critical directions for biosensor development.

**Linearity** is the range of analyte concentrations for which the sensing response changes linearly along with sample concentration. Linearity is defined mathematically as the slope of  $y = mc$ , where  $c$  is the concentration of the analyte,  $y$  is the output signal, and  $m$  is the slope. It is related to the resolution of the biosensor. The resolution of a concentration sensor is defined as the smallest change in concentration that results in a change in the sensing signal. Depending on the application, the sensor requires a good resolution for a wide working range of concentration.

#### 2.1.1.1 Trends in biosensing and limitations

In recent years, the demand for biosensors has shown significant growth due to a wide range of applications in medicine and biological studies. Biosensors had a global market value of USD 15.6 billion in 2016, and it was predicted to increase at a 7.9 percent compound annual growth rate until 2020 [21]. The growth is likely to be driven by continuous technological advancements in the biosensor ecosystem, a rise in non-medical applications, lucrative growth in point-of-care diagnostics, the advent of Internet-of-Things (IoT) and Web-capable electronic devices, and an increase in the demand for glucose monitoring. From a business perspective, disposable, cost-efficient, user-friendly, and rapid analytical response biosensors have become attractive and in high demand [21]. Furthermore, from a future perspective, the ability to identify single molecules, cellular and whole living life activities with low detection limits and high accuracy are the most desirable requirements for future biosensors [20].

Biosensor development has frequently been explored employing a variety of biosensing approaches, including electrochemical, bioelectronic, optical, and piezoelectric devices. Integrated sensors that combine multiple technologies ranging from electrochemical, electromechanical, optical and QCM techniques have become increasingly interesting for biological research. For example, combined electrochemical and QCM techniques can simultaneously give information on the quantity of adsorbed mass and electrochemical reactions occurring at the interface. In addition, a combination of nanomaterials and polymers with various types of biosensors can be used to develop both single and hybrid devices to improve sensitivity, accuracy, and stability [22]–[24]. Nanomaterial-based biosensors have shown great potential in clinical diagnosis, food

analysis, process control and environmental monitoring and are expected to become practical in the near future [20]. However, researchers continue to face difficulties in functionalizing nanomaterials or polymers with bioreceptors to obtain high selectivity. For example, building bioreceptors on graphene surfaces to create highly selective and sensitive sensors presents numerous obstacles during functionalisation due to the variety of graphene-based material surface chemistries [25]. Additionally, a limited knowledge on the conformational and interaction dynamics of proteins and graphene precludes the development of such biointerfaces.

Using nanomaterials in biosensors offers opportunities for creating a new generation of biosensors. Nanomaterials can improve the mechanical, electrochemical, optical and magnetic properties of biosensors and aid in developing devices with higher selectivity and sensitivity [20], [23]. For example, the structure of carbon nanotubes and graphene, a 1D and 2D carbon nanomaterials provides great mechanical flexibility, conductivity, and excellent electrochemical stability due to high carrier mobility and surface area [26]. These properties make them very attractive for applications in electrochemical biosensors. An example of nanomaterials that has been attractive for researchers in biosensing fields due to their outstanding optical properties is up-conversion nanoparticles (UCNPs). It is a novel luminescent material that converts near-infrared radiations into visible radiations. It expresses less background noise, higher photostability, and better signal penetration through tissues compared to down-conversion fluorescent materials, like organic fluorescent dyes. The magnetic nanoparticles (MNPs) are integrated into the transducer materials for magnetic-based biosensors to attract analytes in the samples by an external magnetic field. MNPs biosensors have many advantages over the non-magnetic strategy, including improved sensitivity, lower detection limit, less noise, and quicker analysis [27]. However, the MNPs come with a high cost of synthesis materials, poor dispersion abilities and environmental dependence [28].

Since biological molecules possess distinct structures and functions, finding strategies to engineer the materials, fabricating multifunctional bio-sensing applications is challenging. Many aspects of the engineering of materials require a deeper understanding, including characterisation, interface problems, quality, and the



adsorption behaviour and mechanism of the nanomaterials on the surface of electrodes [20]. Therefore, fundamental research to elucidate the interaction mechanisms between nanomaterials and biomolecules is pivotal to promote technological advancements.

Future biosensing technology research and development will focus on developing a new generation of biosensors or upgrading existing technologies by using the advantages of nanomaterials to generate highly precise and cost-effective sensing devices.

## 2.2 Biosensor techniques

Biosensors employ both labelled and label-free detection approaches [29]. A label refers to any foreign molecules chemically or temporarily attached to the target molecule to detect molecular presence or activity. Label-based detection means using labelled molecules to help to detect the target, while label-free detection can be used without labelling. While a label-based sensor is relatively reliable, the procedure of specifying sensing elements can be challenging. Additionally, the act of labelling may modify the molecule's intrinsic features. Fluorescent labelling, chemiluminescent labelling, electrochemical probe labelling, and nanoparticle labelling are just a few examples of label-based detection approaches.

In contrast, label-free techniques including QCM, field-effect transistor (FET), surface plasmon resonance (SPR) and certain electrochemical sensors, allow the detection of target molecules without a complex tagging process. A QCM biosensor for aflatoxin (AF) detection, for example, uses an IgA antibody as a receptor and measures the weight of AF molecules bound to the antibody without the need for sample tagging. [30]. The label-free FET biosensor for DNA or RNA detection measures the hybridization of the DNA through the gate voltage corresponding to the minimum conductance (VCNP) [31]. An SPR biosensor measures the binding between the two molecules from the excitation of surface plasmons at the planar surface using a light source. It is a label-free technique that has been commonly used for protein binding assay. Another example is label-free electrochemical protein sensors. Bioreceptors such as antibodies [32] and aptamers [33] were functionalized on glassy carbon electrodes (GCE). The binding between analytes

and receptors is reflected in the change of electrochemical signals such as DPV, CV, and impedance.

Recently, the label-free technique has paved the path for several sensing strategies with a wide range of biotechnological, medical, and environmental monitoring applications. This section provides an overview of three types of graphene-based biosensors, including QCM, FET, and electrochemical sensors. Quartz-Crystal Microbalance (QCM) biosensors

### 2.2.1 Quartz-Crystal Microbalance (QCM) biosensors

The QCM sensor is based on the formation of acoustic waves during a quartz crystal's resonant mode. It is a highly sensitive platform for detecting and analysing biomolecule adsorptions and interactions. The mass adsorption on the surface can be measured from the changes in frequency of a quartz crystal resonator. The details of the operating principle and applications of QCM are described in section 2.4. This precise measurement of mass adsorption is crucial for developing ultrasensitive sensors for detecting molecules in the gas or liquid phase.

The QCM sensor is a simple, cost-effective and capable instrument able to achieve high measurement with both high resolution and sensitivity, so it has been favourably adapted to be used in a wide range of applications such as molecular detection, environmental monitoring, food science and medicine. A QCM instrument fitted with a Peltier module, has also been employed as a humidity sensor [34]. The QCM sensor can achieve high selectivity by modifying the surface of the QCM chip, for instance, by fabricating a layer film by coating and depositing the receptor. There are several reports on the use of surface-functionalised QCM as gas sensors. Kikuchi (2004) used clay/polyelectrolyte layer-by-layer self-assembled film to develop a QCM sensor for ammonia detection [35]. Sun (2009) synthesized supramolecular Cryptophane-A and crystalized it on the QCM chip surface in order to develop the methane gas sensor [34]. A highly sensitive QCM sensor for medical diagnosis, like diabetes, was proposed with the fabrication method of creating Ag<sup>+</sup>-ZSM-5 Film [36]. Hao (2009) used a QCM sensor for the rapid detection of *Bacillus anthracis* by functionalising it with a monoclonal antibody. Several QCM sensors were developed based on molecular imprinting

polymers (MIPs) for detecting biomolecule and metal ions. Lin (2004) designed a MIP-QCM sensor for determining albumin concentration [37]. Yang (2009) developed a QCM sensor for the determination of Cu(II), Co (II) and Ni (II) ions in a solution based on the MIP technique [38]. Several researchers recently reported functionalised QCM chips with DNA or RNA for virus detection [39]–[41]. The favourable receptors for specific viruses are divided into four main classes based on their nature and virus-binding mechanism: 1) Synthetic antibodies based on molecularly imprinted polymers; 2) natural antibodies; 3) DNA; 4) aptamers; and other biomacromolecular receptors, like proteins [39].

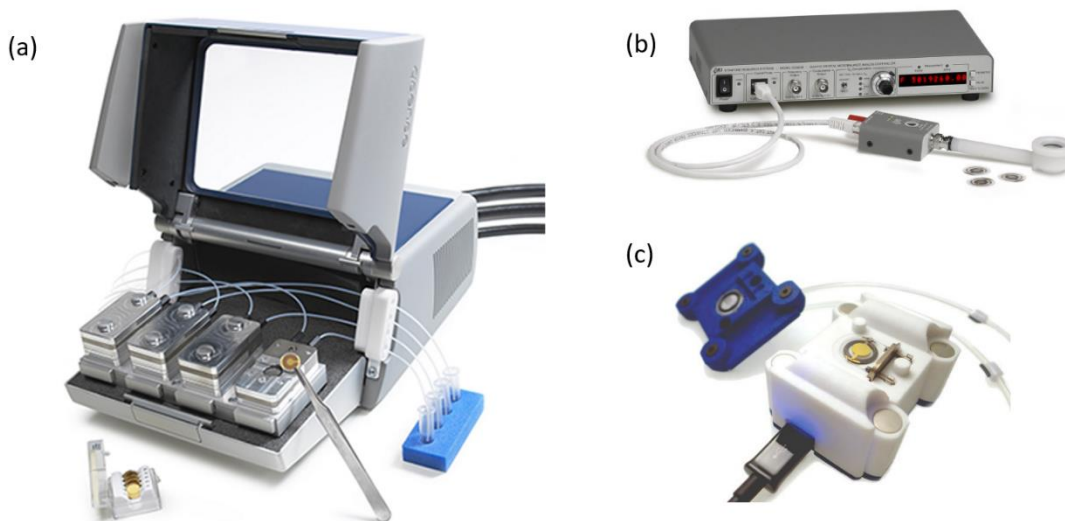
In the commercial segment, many scientific companies supply QCM instruments worldwide, such as Biolin Scientific, Stanford Research System (SRS), Gamry and open-source QCM system from Novaetech S.l.r. A Swedish company, Biolin Scientific, has developed a fully automated QCM-D system making the experimental session more manageable and more repeatable in a controlled environment. The dissipation factor (D) provides insights about the viscoelastic properties of an adsorbed layer. It is therefore helpful for the understanding of the molecular structure during the adsorption processes.

Although the concept of QCM-based sensing has relatively matured and applied in several sensing applications, robust technology is still required to evaluate its benefits and drawbacks compared to other commercially available technologies. So far, many advanced analytical techniques, including SPR-based BIAcore instruments from GE Healthcare, provide significant advantages in large scale applications such as industries, academia, and healthcare [42]. Additionally, microtiter plate immunoassays, for example, enzyme-linked immunosorbent assays, immunoassays, and fluorescent immunoassays, perform high sensitivity and are still extensively used as the standard for disease diagnostics [42]. Nevertheless, using QCM for biomolecular adsorption monitoring, detailed information, especially adsorbed mass of liquid-rich molecules, can be provided.

The QCM-D approach, for instance, can be used to investigate the structural characteristics and orientation of biomolecules adsorbed on surfaces. Since the decay rate is proportional to the oscillator's energy dissipation, the dissipation parameter

refers to the decay of a crystal's oscillation following an excitation near to the resonant frequency. The more water or liquid is adsorbed inside the film, the more impedance and decay of the oscillator. Thus, the dissipation value increases as the viscoelasticity of the adsorbed film increases. A viscoelastic film can originate from the arrangement of the adsorbed molecules that allow more water or liquid to be adsorbed. Information regarding the conformation and orientation of the adsorbed molecules may be derived by integrating the thickness information extracted from the QCM-D profile and the plot of frequency shift ( $\Delta F$ ) versus dissipation shift ( $\Delta D$ ) with the appropriate models of molecular arrangement.

Recently, the development of a combined system, such as QCM and SPR or QCM and electrochemical measurement system, has been demonstrated to provide more sensing information than an individual technique. As a result, the progress of QCM technology has attracted important interest in both research and commercial fields in recent years.



**Fig. 2.2** QCM instrument suppliers **(a)** QSense Analyzer from Biolin Scientific. Source: ref. [43] **(b)** QCM200 from Stanford Research System (SRS). Source: ref. [44] **(c)** open-source QCM system from Novaetech S.r.l. Source: ref. [45]

### 2.2.2 Field Effect Transistor (FET)

A Field Effect Transistor (FET) is a type of transistor that controls the flow of current through a semiconductor by using an electric field. When compared to a bipolar transistor, it includes two significant advantages. First, they provide near-infinite current

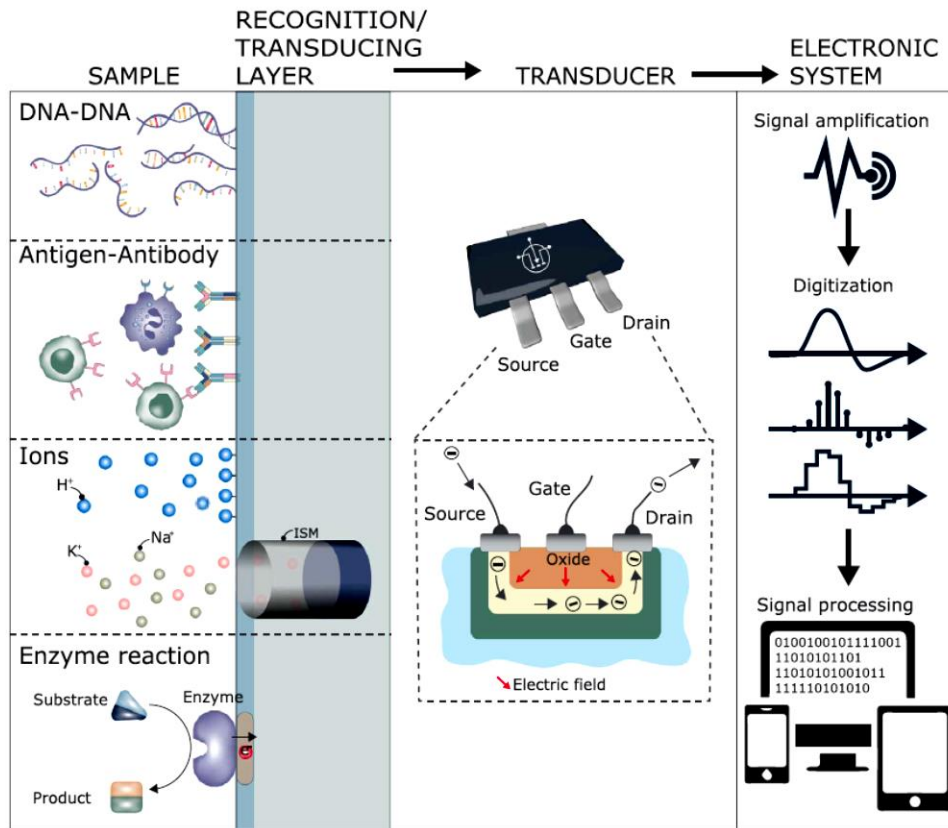
and power increase as a result of their extremely high input resistance. Second, because there are no charge-storage issues, the switching performance, such as digital switching speeds, is significantly better than bipolar switching. The source, gate, and drain terminals of a FET are equivalent to the emitter, base, and collector of a conventional transistor device. Due to their ability to reduce sensor size, parallel sensing, fast reaction time, and ion sensitivity, FETs have proved interesting for sensing applications.

FETs incorporating nanomaterials have become highly promising candidates for next-generation biosensors capable of detecting charged molecules via electrical responses. With bioreceptor functionalisation, a two-dimensional (2D) material, like graphene, has been demonstrated for ultrasensitive sensors used for real-time detection of various bioactive molecules with detection levels ranging from nM to fM. An example of FET construction for a biosensor is shown in **Fig. 2.3**. Graphene-based FET (GFET) has been produced to investigate electrogenic cells [64]. Using FET measuring the conductive signals from beating chicken embryonic cardiomyocytes provides high-quality signals with very low noise than typical values for other planar devices.

Moreover, GFET has been applied in a biosensor to detect proteins, DNA and RNA. GO films have been used in FET biosensors in a thermally reduced pattern on the transistor device [46]. GFET devices have achieved label-free and real-time monitoring of catecholamine secretion from living cells. Xu (2017) revealed the use of a graphene single-crystal domain patterned into multiple channels for measuring time- and concentration-dependence of DNA hybridisation kinetics and affinity with a reliable and sensitive detection limit of 10 pM [4]. These show the potential examples of FET applications in biosensors.

Even though FET is a suitable device for being a low-cost, sensitive and straightforward sensor, every sensing application requires more conditions, particularly sensitivity, to achieve the final commercial device as it is still challenging to reproduce selective sensors from actual samples containing complex mixtures of several biological species. Furthermore, because only a limited number of analytes, such as blood glucose, can be measured directly from the sample, several actual detections require pre-treatment processes to activate the sensor. Furthermore, various factors such as ionic strength, pH

level, temperature, or even light conditions, could influence the uncertainty in the detection. Many entrepreneurs and researchers have put in significant effort to achieve real-world applications overcoming these challenges in the near future.



**Fig. 2.3** Illustration showing a construction of bio- and chemical FET sensor with three main components including recognition layer, transducer and electronic system for signal amplifying and processing. Source: ref. [46]

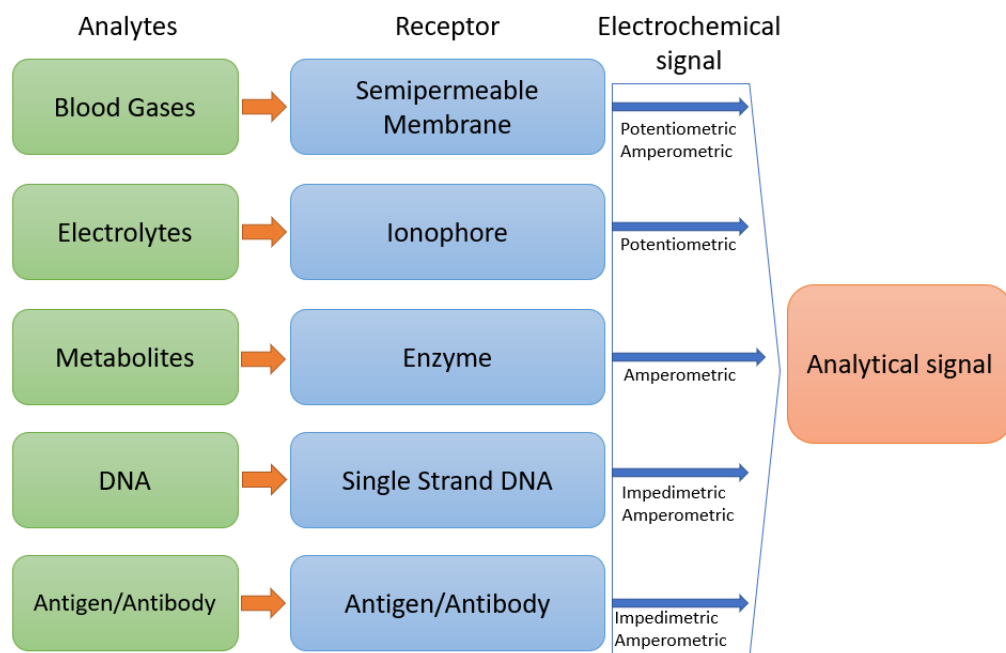
### 2.2.3 Electrochemical biosensors

Electrochemical biosensors utilize a biological transducer to detect electrochemical responses when exposed to different analytes [47]. These electrochemical responses are typically measured in the form of changes in the current (amperometric), the potential (potentiometric), or the impedance (impedimetric) across the electrodes [48].

**Fig. 2.4** summarizes different types of electrochemical signals based on different analytes.

To accurately measure the electrochemical profile on the sensor, a three-electrode setup, consisting of a dedicated reference electrode (in addition to the working electrode and the counter electrode), is typically employed in the system. Generally, all

three electrodes need to be electronically conductive and chemically stable. Nevertheless, the reference electrode has to be especially stable during the entire measurement. Using a separate reference electrode (typically made of Ag/AgCl) provides a stable reference potential while allowing opposite redox reactions to occur at the counter electrode. For the counter electrode, it should be designed to have a large electrochemically active surface area. Otherwise, the counter reaction might limit the overall current in the circuit, thus convoluting the reaction kinetics on the working electrode. The working electrode (also known as sensing or a redox electrode) is one of the most important in the setup since it acts as the main transducer detecting the bio-electrochemical signal in the reaction. Depending on the analyte properties, various materials have been used to make electrochemical electrodes such as platinum, gold, carbon materials, and silicon compounds.



**Fig. 2.4** Diagram showing the analytical procedure for clinical electrochemical sensors. Analytes are detected by receptors giving the electrochemical signal. Then the signal will be processed and displayed in form of an analytical signal. Adapted from ref. [49]

Screen-printed electrodes, which are electrochemical measuring devices made by printing various inks on plastic or other substances are increasingly being manufactured because they are a simple and low-cost fabrication route that is also easy to mass-produce [50]. They are currently being used in the food industry for rapid determination of the triglyceride content of coconut milk [51] and are widely used as personal

glucometers [52]. Apart from the materials mentioned, electrochemical biosensors can be fabricated from conductive polymers such as polyaniline, polypyrene and polystyrene coated on substrates. Typically, the polymers are adsorbed well on gold surfaces leading to a good redox cycle with high stability and easy handling [48]. Gold and other metallic surfaces used in conjunction with conductive polymers can also be modified using self-assembled monolayers (SAMs) of sulphides (thiols) and disulfides. The modification results in the formation of highly ordered and well-organized organic linker structures, which can help with boosting the sensitivity. The polyaniline/gold electrochemical sensor has been demonstrated to be a novel method for glucose determination [53]. Different chemical functional groups are also used as biological recognition elements. For instance, carboxyl groups often aid for antibody immobilisation; esters aid amine and biotin coupling, binding streptavidin and other functionalised-biotin molecules [54].

Graphene is another working electrode material that was reported recently to have outstanding electrochemical characteristics. Graphene has an electric potential window similar to graphite and glassy carbon (GC) electrodes (2.5 V in 0.1 M with pH 7), but its charge-transfer resistance is substantially lower [55]. Also, from cyclic voltammetry (CV) studies, graphene has exhibited well-defined redox peaks with both anodic and cathodic peak currents in the CVs linear with the square root of the scan rate [56]. This study suggested that the diffusion during redox processes is mostly controlled. Furthermore, the peak-to-peak potential separations ( $DE_p$ ) for most one-electron-transfer redox couples are low, close to 59 mV, implying that the reaction can happen quickly. For the reasons stated, graphene-based electrochemical sensors have been widely developed for bioanalysis, environmental examination, and biomolecular detections in which redox reactions can occur, including graphene-based 3rd generation glucose sensors, graphene-based DNA sensors for HIV gene detection, GP-based DNA sensors for HER2 and CD24 detection for breast cancer detection, or Dopamine, Uric Acid, and Ascorbic Acid sensors [57].

Other than the analytes mentioned above, enzymes are also predominantly used as label elements due to their specific binding capabilities and biocatalytic activity. The enzyme acts as a catalyst for specific reactions without significantly altering the charge transferring process across the interface of the electrode. Glucose biosensing is an



example of an enzyme detection-based- electrochemical sensor application in which glucose oxidase is used as a biorecognition for glucose detection. It captures around 70% of the total biosensor market since it is often used by diabetic patients to test their blood sugar levels multiple times throughout the day [58]. However, other biorecognition elements such as nucleic acids, cells and micro-organisms can also be used in an immunosensor and electrochemically binding events monitoring.

Biosensors, medical diagnosis, environmental monitoring, and energy storage are just a few of the applications where the electrochemical approach excels. By reducing the preparation steps and the cost of reagents, the electrochemical approach has increased the performance of various bio and chemical sensors, allowing for the development of low-cost, easy-to-use, and portable analytical instruments. Furthermore, electrochemical biosensors outperform conventional biosensing technologies in terms of their linear response range, detection limits, reproducibility, and overall stability. Electrochemical sensors, on the other hand, still have several drawbacks, such as electrochemically active sample interferences, poor long-term stability, and complicated electron-transfer paths. As a result, the current focus of electrochemical sensor development is on overcoming these issues.

### 2.3 Graphene and graphene derivatives

Graphene is a fascinating material due to its extraordinary properties. It was successfully isolated in 2004 by Prof. Andre Geim and Prof. Kostya Novoselov at the University of Manchester [2]. Graphene is the first two-dimensional (2D) material discovered, as well as the thinnest material ever isolated. Furthermore, this material demonstrates the integration of many outstanding properties such as excellent mechanical, electronic, and optical properties. For these reasons, graphene has been used and studied for a wide range of engineering material applications aimed at improving current technologies and creating new market routes.

Graphene oxide (GO), formerly known as graphite oxide, is a wrinkled two-dimensional carbon sheet with oxygen functional groups on the basal planes and edges. It has a thickness of about one nanometre and lateral sizes that range from a few nanometres to microns. B. C. Brodie developed GO for the first time in 1859. It has grown in

popularity in the scientific and commercial communities because it can be used as a precursor to the production of low-cost, large-scale graphene-based materials [8]. To obtain the graphene-like properties, oxygen contents in GO are required to be removed using heat or chemical treatment to form reduced (r)GO, which shows significantly higher hydrophobicity and electrical conductivity, similar to pristine graphene.

The important properties and applications of graphene and graphene derivatives in biosensors are reviewed in this section.

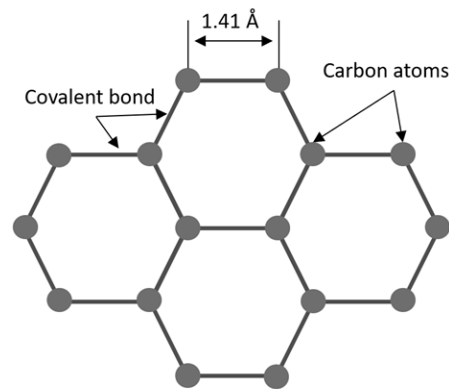
### 2.3.1 Properties

#### 2.3.1.1 Structural properties

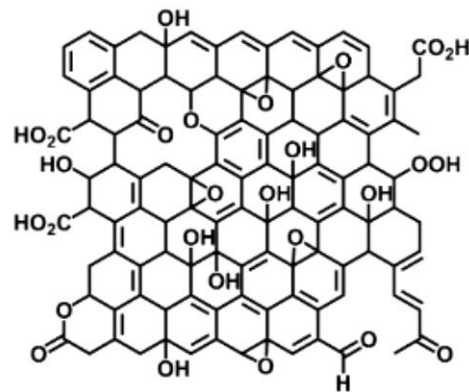
Monolayer graphene has a honeycomb carbon lattice structure. Each layer's carbon atoms are densely packed in a hexagonal pattern. Its unit cell is made up of two identical carbon atoms, but their planes translate from a distance of 1.41 angstroms due to the difference of the initial energy states [2]. **Fig. 2.5** displays graphene structure. In general, a carbon atom contains four valence electrons showing a ground-state electronic configuration of  $2s^2 2p^2$ . In the graphene structure, the hybridized orbitals are generated by the superposition of 2s orbitals called  $sp^2$  hybridization. This phenomenon contributes to the highest electron mobility known to date, which can be applied for future electronic technological developments.

While graphene contains only  $sp^2$ -hybridized carbon atoms, graphene oxide (GO) shows both  $sp^2$  and  $sp^3$  hybridization of carbon atoms. The basal plane of the carbon structure is interrupted by several oxygen functional groups, including hydroxyl (OH), epoxy (C–O–C), carbonyl (C=O) and carboxyl (COOH) contributing to  $sp^3$ -hybridization. The oxidative mechanisms and the precise chemical structure of GO have been considerably debated over a decade, and even until now, no explicit model exists. This is due to several reasons including the complexity of the amorphous material, the variability of samples, berthollide character (i.e. nonstoichiometric atomic composition) and the lack of precise techniques for characterizing the material [59]. However, many structural models of GO have been proposed. Currently, the most well-known and cited model is the one by Lerf and Klinowski [59] (**Fig. 2.6**). The proposed structure of GO is atomically thin, about 0.7 to 1 nm in vertical height, with a semi-aromatic network of  $sp^2$  and  $sp^3$

hybridized carbon atoms. The hydroxyl and epoxy functional groups are dominantly bonded across the basal plane of GO, while carbonyl and carboxyl groups are attached to the edges. The removal of the functional groups via thermal or chemical reaction results in reduced GO (rGO). By removing the oxygen contents from GO, the basal plane of carbon atoms converts from  $sp^3$  to  $sp^2$  hybridization restoring the aromatic system of graphene. Thus, it is believed that the reduction of GO could provide a scalable and low-cost approach for producing graphene-like materials.



**Fig. 2.5** Schematic of the structure of graphene sheet showing hexagonal carbon lattice. The identical carbon atoms are covalently bonded with the distance between the two carbon atoms of  $1.41 \text{ \AA}$ .



**Fig. 2.6** Structural model of GO proposed by Lerf-Klinowski. The basal plane of carbon lattice is interrupted by several oxygen functional groups with hydroxyl and epoxy functional groups on the plane and carboxylic acids on peripheral of the graphitic platelets. Source: ref. [59].

### 2.3.1.2 Electronic properties

In solid-state physics, the first Brillouin Zone or the primitive cell in the reciprocal space of graphene has two inequivalent Dirac points  $K$  and  $K'$ , where a band crossing occurs.

Therefore, the bandgap is zero. The electronic states near Dirac points of graphene are composed of states belonging to the different sub-lattices, and their relative contributions are considered by using two-component wave functions [2]. The linear band structure closely resembles the Dirac spectrum for massless fermions. Thus, the effective Hamiltonian near  $K / K'$  of graphene can be expressed by the Dirac equation with zero mass, shown in the equation below.

$$\hat{H} = \hbar v_F \begin{pmatrix} 0 & k_x - ik_y \\ k_x + ik_y & 0 \end{pmatrix} = \hbar v_F \vec{\sigma} \cdot \vec{k}$$

Where

$\hat{H}$  is the Hamiltonian

$\hbar$  is Planck's constant

$v_F$  is the Fermi velocity

$\vec{k}$  is the momentum of the quasi-particles in graphene

$\vec{\sigma}$  is the 2D Pauli matrix

The two-component explanation of graphene is similar to the spinor wave function in quantum electrodynamics (QED), but the 'spin' index of graphene is referred to as pseudospin ( $\sigma$ ) as it describes the orbital wave function in the sublattice rather than the spin of the electrons in the honeycomb lattice. As a zero-band gap material, graphene performs an ambipolar electric field effect and charge mobilities at room temperature is up to  $15\,000\text{ cm}^2\text{V}^{-1}\text{s}^{-1}$  [60]. For these reasons, graphene has become the highest electrically conductive material at room temperature measured to date.

In contrast, GO is an insulating material at room temperature due to the disruption of the carbon lattice by its oxygen contents. However, it can become more conductive when removing some oxygen-containing material. These features provide a range of applications, including field-effect transistors, polymer composites, sensors, conductive coatings, energy storage and biomedical applications, among others [5], [61]–[63].

### 2.3.1.3 Mechanical properties

Some of the most relevant mechanical properties of the monolayer and a few layers of graphene, including Young's modulus and fracture strength, have been determined. Through experimental investigation, Young's modulus of a few graphene layers was characterised using atomic force microscopy (AFM) with force-displacement mode. It was reported that defect-free graphene exhibits Young's modulus value of 1.0 TPa and fracture strength of 130 GPa [64]. Using a similar AFM method, reduced graphene oxide with a hydrogen plasma displayed a mean elastic modulus of  $0.25 \pm 0.15$  TPa [65]. An average elastic modulus of 32 GPa and the highest fracture strength of 120 MPa has been reported on individual graphene platelets [66]. Moreover, the mechanical properties of GO were improved by introducing chemical cross-linking between individual platelets using divalent ions and polyallylamine [67]. In this aspect of mechanical strength, graphene, GO, and rGO possess outstanding properties and can be used for improving the mechanical properties of other materials by mixing them as composites or as functionalisation entities.

### 2.3.1.4 Optical properties

Pristine graphene is a highly transparent material where only 2.3% of visible light can be adsorbed in each layer [67]. The visible spectrum is between about 3.1 eV to 1.6 eV (400 to 700 nm wavelength). If a material's bandgap is greater than its maximum energy, no light is absorbed and the light simply goes through it. As a result, they appear translucent. Because of the relationship between the increasing bandgap and a decreasing refractive index, the latter may decrease for that transparent material because it is a high bandgap material. When the refractive index is reduced, the transmission value rises. As a result, a larger bandgap will result in better transmission in the visible region, if the bandgap is greater than 3.1 eV.

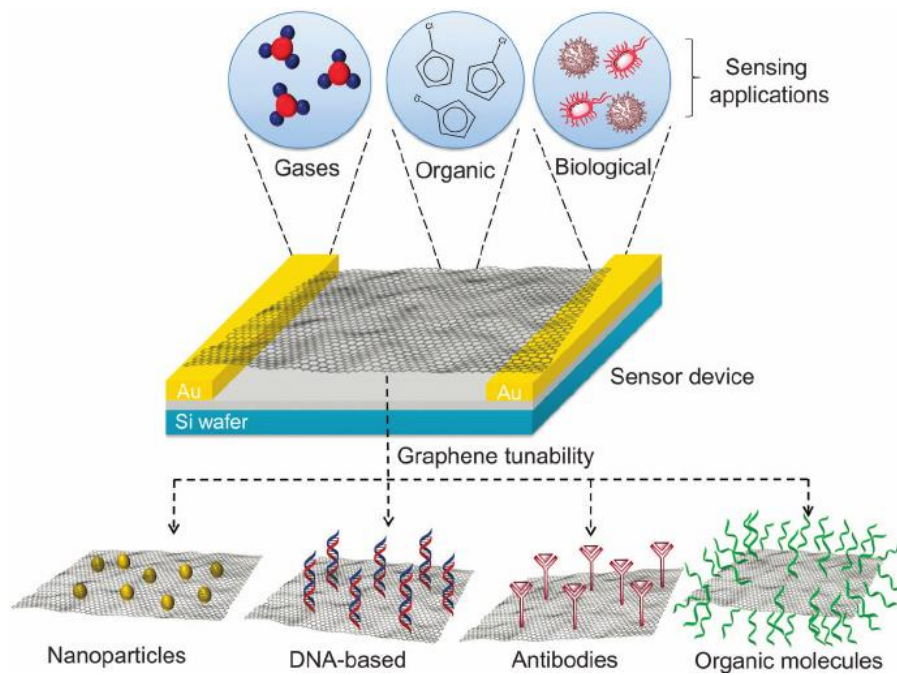
The mentioned process renders graphene transparent, which is advantageous in the development of various optical-electronic devices such as touch screen monitors and optical sensors. GO, on the other hand, exhibits significantly different optical properties than a single- and few-layer graphene. It is usually transparent with high optical

transmittance in the visible spectrum region. The absorption spectrum depends on wavelength. The peaks in the UV/blue edge of the visible spectrum falls towards the near-infrared (NIR). Discernible  $\pi$ - $\pi^*$  and  $n$ - $\pi^*$  transitions arise from the presence of oxygen-containing functionalities also present in its UV absorption range (200–320 nm) [68]. The optical response of GO is significantly sensitive to the degree of oxidation which varies between the different reduction methods depending on residual oxygen group coverage and defects within the carbon sheets.

### 2.3.2 Applications in biosensors

In recent years, graphene has been gaining important attraction from scientists from a wide variety of fields, predominantly from the biomedical and biotechnological sciences for the fabrication of biosensors. Due to its outstanding electronic properties, high surface-to-volume ratio, and biocompatibility, graphene can contribute to the development and enhancement of the analytical performance of sensors. Other graphene-family materials, including graphene oxide (GO) and reduced GO (rGO), are also good candidates. The presence of oxygen functional groups on the GO surface could enhance its solubility resulting in easier functionalization. Through chemical and thermal methods, the oxidation levels of GO can be reverted to obtain a material that resembles pristine graphene, to an extent. Graphene and rGO become highly sensitive to changing environmental conditions as their atomic thickness increases. All carbon atoms can directly interact with the analytes, an important characteristic in sensing applications to promote sensitivity. Graphene can also be easily linked with biomolecules by  $\pi$ - $\pi$  stacking and hydrophobic interactions. Graphene has advantages over other materials due to its simple functionalization, lower noise ratio, solution-processability, and biocompatibility.

Several papers have been published in the last five years describing graphene-based sensors and biosensors functionalized with bioreceptors such as proteins, lipids, antibodies, and DNA[69]. The biosensor fabrication techniques can be varied and cover a range of operation principles, however, the most commonly reported one is mainly focused on chemical, electrochemical and FET-based devices [55], [60], [70].

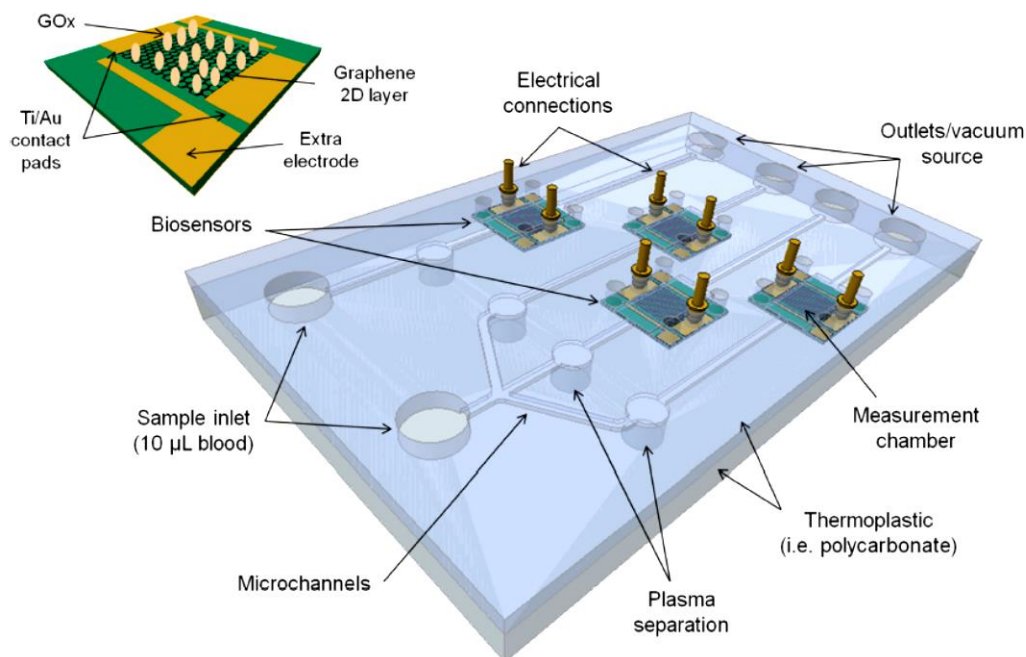


**Fig. 2.7** Illustration of a graphene-based sensor showing its potential application for detecting gases, organic and biological matters. The sensing surface can be modified by functionalisation with nanoparticles, DNAs, antibodies, and organic molecules. Source: ref. [69]

Hirtz (2013) presented the fabrication of lipid membranes onto graphene using the L-DPN technique, showing the precise and selective spatial positioning and pattern shaping of individual lipid molecules [7]. This method enables multiplexed and localized heterogeneous functionalization of lipid membranes on a graphene substrate, which is useful for fabricating platforms for biosensors. Viswanathan (2015) proposed an approach for developing a graphene-based glucometer [70]. It involves modifying enzymes for improving selective performance, developing methods to bind them onto the graphene surface and fabricating a graphene-FET sensor integrated with a microfluidic cell to achieve a point-of-care device. **Fig. 2.7** demonstrates the conclusion scheme for potential applications of graphene platform sensors. The graphene sheet is transferred onto a Si wafer and connected to a metallic electrode at the edges to fabricate the sensing device. The sensing capacity can be tuned by modifying the graphene surface with chemical- and bio-receptors

Although graphene has significant advantages for biosensor applications by increasing the sensitivity, it requires functionalization with biomolecules to make the sensor selective. Understanding how biomolecules interact with graphene-related materials

can lead to the development of a method for fabricating graphene sensors. As a result, research topics involving the interaction between graphene-based materials and biomolecules are particularly intriguing.



**Fig. 2.8** Example of a microfluidic FET biosensor for detecting glucose made from graphene-based materials. Source: ref. [70]

## 2.4 Interaction between biomolecules and graphene-family materials

Graphene-based family materials have been reported in several publications as having potential in biomedical applications such as biosensors, tissue scaffolds, drug delivery carriers, and antibacterial agents due to their high specific surface area, which allows for high-density biofunctionalization or drug loading [71], [11], [72]. For example, Hussien NA, et al. (2018) reported that the anti-cancer medication paclitaxel, which is known to be a cellular hazardous chemical, was delivered via an aptamer-conjugated magnetic Graphene Oxides (MGO) nanocarrier with a reduction in cell death compared to conventional cancer drug delivery. As a result, they are a promising vehicle for cancer treatment delivery [73]. Understanding the fundamental interactions of these ultrathin



carbon forms with biological molecules can significantly help to broaden the design of applications and intelligently exploit the functions of the materials.

Both covalent and noncovalent surface modifications of graphene, GO, and rGO, have been used to connect specific biological molecules to improve biocompatibility and colloidal stability. The most common covalent binding is the conjugation of GO or rGO to hydrophilic polymers via polymerization or amine coupling to carboxylic groups. Hydrophilic polymers such as polyvinyl alcohol (PVA) and polymethyl methacrylate (PMMA) can be incorporated with GO to improve their mechanical properties. The composites of GO/PVA or PMMA have the potential to be used as fillers to repair cartilages, tendons and meniscuses as GO incorporation increase both the tensile strength and elasticity of hydrogels without affecting their potential for osteoblast attachment [74]. As an example of the amine coupling method, GO-chitosan can be synthesized by covalent linkage of the carboxyl groups of GO with the amide groups of chitosan. This composite can be used for medical scaffolds as GO incorporation can reduce the rate of scaffold degradation benefitting the hard tissue regeneration [75].

Noncovalent modifications often rely on hydrophobic forces or  $\pi$ - $\pi$  stacking on the pristine graphene or highly reduced GO surface [76]. The driving force for physisorption is cited as  $\pi$ - $\pi$  interaction and hydrophobic forces in several publications. *Zhang et al.* loaded both Dox and calprotectin (CPT) onto functionalized GO, and cite  $\pi$ - $\pi$  interactions and hydrophobic forces as the driving force on the adsorption [77]. Lipid-coated on graphene and highly reduced GO has been reported to form a monolayer [6], [7], [78] while bi-layer lipid can be formed on hydrophilic GO [6]. The interactions between the lipid and graphene family materials have been claimed to be driven by hydrophobic and hydrophilic forces.

In addition, graphene or rGO can be functionalized with amino acid functional groups via 1,3-Dipolar Cycloaddition of Azomethine Ylide [79]. The 1,3-dipolar cycloaddition is a reaction between a 1,3-dipole and a dipolarophile to form a five-membered ring on graphene planar on the graphene plane. This method can be a promising option to functionalize bio-receptor molecules on graphene for biosensing applications.

In addition, the variation in layer number, lateral dimension, and surface chemistry tend to affect the biological response as well. From these unique biomolecular interactions, the graphene-bio interface has become a challenging area for further scientific research.

The features of graphene-based nanomaterials relevant to biological interactions and specific graphene-protein interactions are described in this section.

#### 2.4.1 Properties of graphene-related to biological interactions

The most relevant properties of graphene-based nanomaterials affecting biological effects include surface area, layer number, lateral dimension, surface chemistry, and purity (refer to **Fig. 2.9** for examples) [80].

##### 2.4.1.1 Surface Area

Surfaces dimension is a crucial factor for the occurrence of biological interaction with nanomaterials. It is mainly because nanoparticles (lower than 10 nm) have a significant fraction of their atoms exposed on their surfaces [80]. Single-layer graphene exhibits an extreme case for the importance of the surface area as every atom lies on the surface giving rise to the theoretical maximum surface area of an  $sp^2$ -hybridized carbon sheet of about 2600  $m^2/g$ . Graphene and its derivatives exhibit surface phenomena such as physical adsorption or catalytic chemical reaction due to their high surface area. This interaction may have a significant impact on the biological response to the materials. Graphene-based materials can become aggregated in an aqueous medium, turning into spherical particles and increasing operative size; however, most surface area is typically retained unless aggregated by sintering, dissolution, or reprecipitation [80]. Especially for GO, it is reported to align effectively during filtration or drying to produce GO papers, and by stacking, the interlayer spaces do not affect accessibility for biological interactions.

##### 2.4.1.2 Layer Number

The number of graphene layers is essential for determining specific surface area and bending stiffness. The specific area ( $m^2/g$ ) is inversely proportional to the number of layers [80]. It has been reported that the adsorptive capacity for biological molecules

will increase significantly inverting the layer count. Furthermore, thin materials, such as single-layer graphene or GO, are relatively deformable by weak forces such as water surface tension; in contrast, multilayer materials may behave as rigid bodies during cell-material interactions [81], [82]. Characterization of layer number typically uses AFM observing the topographical properties of the film on substrates.

#### 2.4.1.3 Lateral Dimension

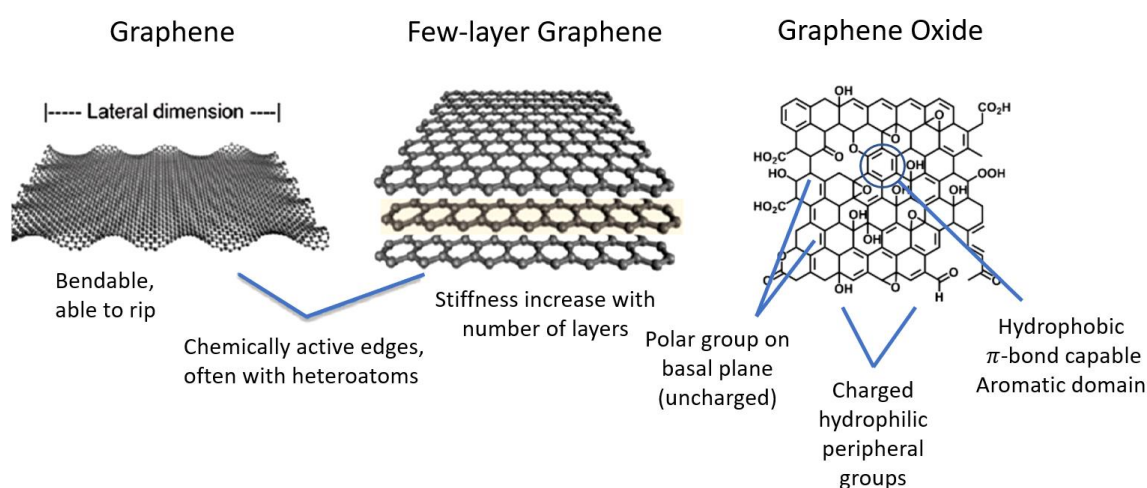
Although lateral dimension has no considerable effect on a specific surface area, it is significant for determining the maximum dimension of the attached material. This factor is highly relevant for biological phenomena that rely on particle size, including cell uptake, renal clearance and blood transport [80]. Lateral dimension should affect the maximum uptaken number of receptors and also the size of the cell. Similar to the number of layers, the lateral dimension also affects deformability, but the lateral dimension is related to the torque applied by cellular forces. Large sheets tend to be more deformable than small ones at equal layer numbers. In this case, SEM or AFM can easily characterize lateral dimensions.

#### 2.4.1.4 Surface Chemistry

GO surface shows the combination of hydrophobic with hydrophilic effects with a typical water contact angle between 40 and 50° [83]. Its structure contains negative charges on the edges and is associated with the carboxylate groups, while the  $sp^2$  plane is hydrophobic with a water contact angle close to 90°. Reduced graphene oxide (rGO) expresses medium hydrophilicity due to remaining functional groups and vacancy defects in the basal plane produced during oxygen removal [84]. GO colloids show relative stability in pure water; however, it is required further functionalization to maintain long-term stability in saline or culture medium [83]. Pristine graphene dispersibility in water is extremely poor and surfactants or other stabilizers are required to develop applications in biological fluids.

### 2.4.1.5 Purity

Typically, graphene and its derivatives do not contain any residual metal catalysts. However, some of them could contain remaining intercalants or chemical additives due to improper washing. There is little knowledge about the effects of impurities in graphene- biological interaction, and thus cautious use and careful characterization are recommended to avoid undesirable biological effects.



**Fig. 2.9** Related properties of graphene-based materials to colloidal behaviour and biological interaction including surface area, lateral dimension, number of layers and surface chemistry. Adapted from ref. [80]

### 2.4.2 Graphene interaction with proteins

Protein adsorption on nanomaterial surfaces has become a popular issue in scientific research in these recent years due to its potential to mediate cellular uptake that can help to address toxic responses [17]. Graphene-based materials are known for their potential to absorb a larger amount of protein due to their higher specific area compared to most other nanomaterials. Proteins can be bound onto graphene-based nanomaterials by both covalent and noncovalent interactions.

#### 2.4.2.1 Non-covalent interaction

Graphene and graphene derivatives that have oxygen-containing functional groups have been shown to bind with a large number of proteins, for instance, bovine fibrinogen (BFG), immunoglobulin (Ig), transferrin (Tf), and bovine serum albumin (BSA) through

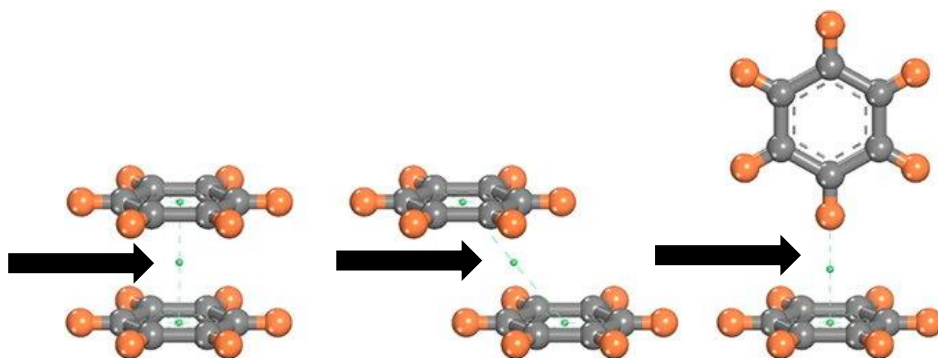
various non-covalent interactions [85]. These non-covalent interactions for graphene and graphene derivative materials are mainly based on van der Waals, hydrophobic interaction, electrostatic and  $\pi$ -stacking [86].

Van der Waals force is the main driving force for stacking graphene or GO flakes on 2D solid surfaces such as graphene coating on gold or SiO<sub>2</sub> and even the stack of carbon lattice in graphite. Van der Waals forces can be formed between graphene or GO flakes and organic molecules for water-insoluble drugs or creates nanocomposites between graphene and polymers that can be further bound to proteins [87]. Graphene is recognized for its hydrophobic properties, graphene derivatives such as GO are only hydrophobic on the basal planes and hydrophilic at the margins. Thus, GO might be less preferable for Van der Waals force compared to graphene or rGO. On the other hand, the electrostatic interactions could be more pronounced on GO.

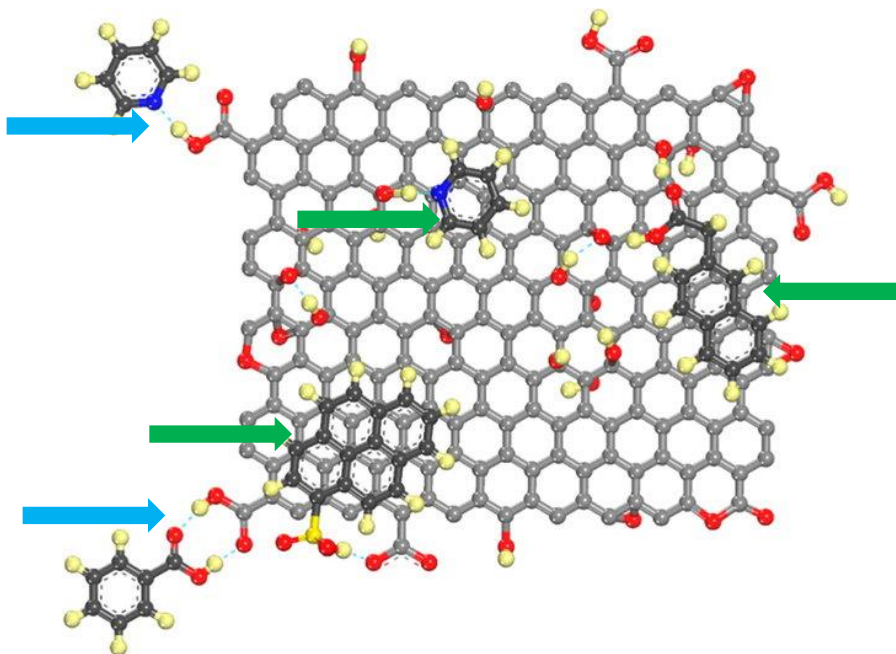
The interaction between protein molecules and GO could be very complicated due to the charge status on the protein surface depending strongly on the environmental conditions, including the pH value, and the ionic strength of the buffer. The protein can be negatively or positively charged, while the GO is typically negatively charged and also varies with the preparation procedure and level of reduction. Based on this, various proteins could interact with GO through electrostatic interaction with different stability.

In general, agglomerated protein molecules tend to form on a hydrophobic surface [88]. It is assumed that the hydrophobic aromatic rings on graphene can promote protein adsorption through hydrophobic interaction. Kamiya et al. studied the adsorption of protein on graphene in an aqueous environment focusing on the influence of surface modification of the support substrates [88]. It was found that high-density clusters of agglomerated avidin molecules are likely to form on a hydrophobic area of graphene substrate rather than in the hydrophilic zone. Also, it is reported a hydrophobic interaction could lead to the structural conformation of protein molecules. Therefore, protein adsorption and its cluster formation can be controlled by the hydrophobicity of graphene. Proteins, which are made up of amino acids, can have both hydrophilic and hydrophobic properties. While the hydrophobic component is responsible for G-to-macromolecular interactions, the hydrophilic part is frequently employed to improve the stability of G/GO compounds in water [86].

Nevertheless, the main interaction found between protein and graphene is mainly  $\pi$ - $\pi$  interaction, which is the interaction between aromatic rings that include  $\pi$  orbitals (shown in **Fig. 2.10, 2.11**)



**Fig. 2.10**  $\pi$ - $\pi$  interaction (black arrow) in which the grey atoms represent carbon and the orange atoms indicate hydrogen in the case of benzene. Source: ref.[86]



**Fig. 2.11** Hydrogen bonding (blue arrow) and  $\pi$ - $\pi$  interaction (green arrow) with GO structure. Source: ref. [86]

At physiological pH, due to its hexagonal aromatic structure, and the negatively charged oxygenated functional groups, the interaction between the 2D material and protein can occur with ease. On the GO surface, weak interactions, including hydrophobic,

electrostatic, and  $\pi$ - $\pi$  stacking, could lead to the immobilization of enzyme proteins on its surface. The basal plane of the GO enriched with  $\pi$  electrons contributes to the possibility for the GO to create  $\pi$ - $\pi$  stacking interaction with proteins. The charge at the surface of GO due to functional groups could lead to hydrophilic interaction. In fact, the interactions between enzyme or proteins molecules and GO could be very complicated as the enzyme become active strongly depending on the environmental conditions, including the pH value and the ionic strength of the buffer [89]. A theoretical study of protein or enzyme noncovalent adsorption onto GO was conducted using molecular dynamics simulation [90]. The result indicated that the  $\pi$ - $\pi$  interaction between the GO backbone and the aromatic residues of the enzymes might be a primary factor for immobilization. Also, the softness of GO could assist the binding by adapting its shape to fit better with the aromatic residues of the protein and form stronger  $\pi$ - $\pi$  stacking. Since the stacking is simple, non-destructive, and reversible, making it is ideal for material engineering applications such as drug immobilization, particular identification, and material construction [91].

Functionalized GO with PEG molecules bearing fluorescent dye-tagged proteins has been studied as examples of  $\pi$ - $\pi$  interaction-based biological drug delivery systems. Proteins that interact with GO material via  $\pi$ - $\pi$  stacking enter cells directly and activate or deactivate the associated pathways, resulting in biological signalling [92]. This method could be employed in cancer treatment, in which the protein-based medicines on the nanosheets could be protected from enzymatic breakdown during the delivery [93].

#### 2.4.2.1 Covalent interaction

The covalent interactions of graphene and graphene derivatives are generally comprised of two pathways; firstly, the formation of covalent bonds between free radicals and secondly, the formation of covalent bonds between amino acid functional groups and the oxygen groups of GO [94].

Most of the time, the covalent binding of a protein to GO is based on chemical interactions between the side groups of amino acid residues on the protein surface and functional groups in graphene derivatives materials. The amine and carboxyl groups on

the surfaces of protein are considered functional molecules that promote protein immobilization by covalent contact [95]. For GO, which contains many functional groups, it can be covalently functionalised with certain proteins. The free amine groups on the surface of the enzyme or protein are typically applied to the carboxylic groups of GO or rGO. Shen et al.(2010) functionalized BSA to GO through diimide-activated amidation [95]. GO–BSA conjugation showed high water-solubility and retained its bioactivity [95].

Reduced GO, can be covalently bonded to polymeric chains that have reactive species like hydroxyls and amines. Shan, C, et al (2009) reported the use of rGO after its functionalization by poly(L-lysine) (PLL) through amidation as a biosensor for hydrogen peroxide ( $H_2O_2$ ). The detector was constructed by immobilizing horseradish peroxidase on the PLL/rGO surface and depositing the resultant nanocomposite onto a gold electrode [96]. Although the cross-linkers are also frequently used to covalently attach enzymes onto GO, the functional groups of GO can directly bind with enzymes or proteins. Li et al. (2016) demonstrated ovalbumin as a model protein that can be absorbed on GO without requiring any additional linker strategy [97]. In addition, they reported that GO nanosheets could spontaneously adsorb proteins by combining a few different interactions. For example, the presence of the hydrophobic aromatic groups on the GO surface could favour hydrophobic adsorption of protein, and the presence of epoxide moieties could allow covalent binding with lysine units.

However, there have been limited studies about graphene-protein or graphene-amino acid interactions due to the complexity of the experimental method for investigation. As a result, the mechanism of adsorption is yet unclear. Many studies are now requiring an understanding of how proteins interact with graphene-family nanomaterials to make it easier to use the materials in a variety of biological and engineering applications.

## 2.5 Model proteins

### 2.5.1 Bovine Serum Albumin (BSA)

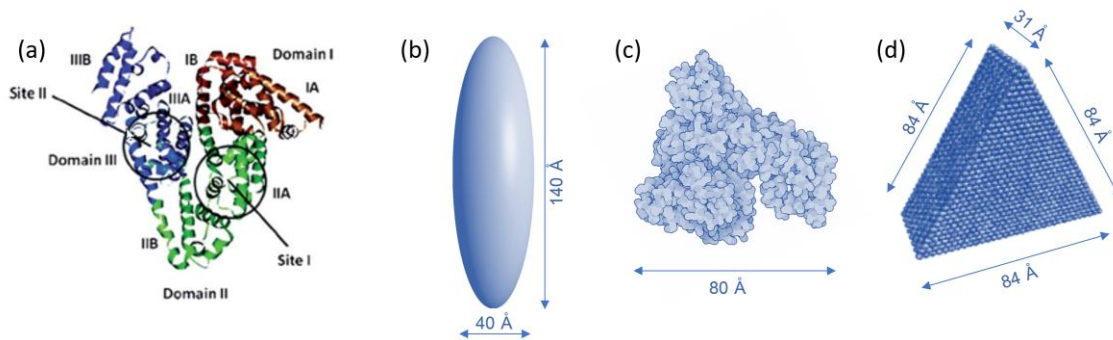
Serum albumin is the most abundant protein in blood plasma. It functions primarily as a carrier protein for various substances, e.g. fatty acids, hormones and steroids. BSA is low-cost human-like serum albumin derived from bovine blood. The composition and folding of BSA are very similar to human serum albumin (HSA). One important difference



is the fact that BSA has two tryptophan residues while human albumin only has a unique one which results in the difference in ligand-binding properties. For its low cost and similarity to HSA, BSA has been widely used as a model protein in a variety of studies on protein adsorption and structural conformation.

### **Physico-chemical properties**

Monomeric BSA is a globular protein with an average MW 66 kDa containing 580 amino acid residues with 17 intrachain disulphide bonds and one free thiol group at residue 34. BSA is negatively charged in PBS pH 7.4. It comprises three homologous domains (I, II, III) divided into nine loops (L1–L9) by seventeen disulfide bonds. Each domain is formed of two subdomains (A and B). The main regions of ligand binding sites in BSA are located in two hydrophobic pockets in sub-domains IIA and IIIA, namely site I and site II [98]. There are two Tryptophans (Trp) around its binding site – firstly, Trp134 is outside of the pocket, surrounded by the polar environment and secondly, Trp212 is inside the hydrophobic pocket. The molecule contains three binding domains specific for metal ions, lipids, and nucleotides, respectively [15]. Serum albumin is in the soft proteins class, which can easily change its structure and conformation. Despite various physico-chemical studies for the determination of its tertiary structure and solution conformation, its three-dimensional molecular structure has remained largely unclear [99], [100]. Three models have been suggested to represent its molecular conformation: 1) as a prolate ellipsoid (cigar-shaped) with dimensions of 140x40x 40 Å and the axial ratio of ~3.5 [101]–[103]; 2) as a heart-shaped molecule with a diameter of 80 Å [104], [105] and 3) a prism shape with optimized dimensions of 84 × 84 × 84 × 31.5 Å [99]. These models are supported by different experimental results, and they might be reconciled as the flexible tertiary structure of the protein in solution could adopt a folded conformation within the crystalline solid [99]. In addition, another key factor that might contribute to the discrepancy in model results could be the use of albumin in different studies. Commercially available BSA contains variable proportions of monomer, dimer and higher oligomers, thus, monomeric and oligomeric forms of albumin in solution could express [100].



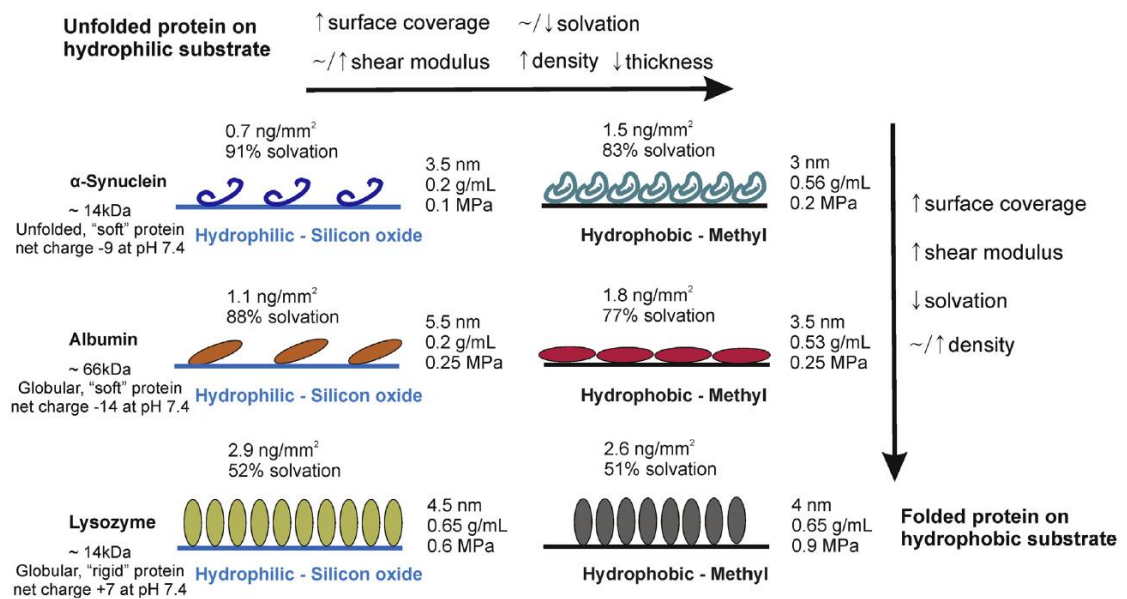
**Fig. 2.12** (a) Ribbon diagram of BSA showing domains, sub-domain (b) BSA conformation in prolate ellipsoid model with dimension label (c) heart-shaped molecule of BSA adapted from PDB 3v03 (d) prism-shape model of BSA conformation adapted from [106]

For studies of serum albumin adsorption on solid surfaces using AFM, QCM-D and ellipsometry technique, several publications have reported the use of the prolate ellipsoid model due to the simplicity of interpretation and calculation of its thickness [106]–[109].

### Adsorption of BSA on Solid Substrates

BSA has been used for many years to study protein–substrate affinity due to its structural similarity to HSA and its importance in biochemical applications. The adsorption of BSA on different surfaces has been extensively studied [15]. On a charged surface, the electrostatic interaction is a major driving force between the surface and the functional groups containing opposite charges along the polypeptide chain of the BSA. On the non-polar surfaces, protein absorption is driven by hydrophobic attraction between the non-polar parts of BSA and the surface. BSA adsorption is typically restricted to a monolayer. However, when the concentration or incubation time increases, BSA molecules could be forced to adsorb more within the monolayer resulting in a variety of several conformations due to the inherent flexibility of the BSA molecule [106]. Higher concentrations of BSA molecules were assumed to form 2D aggregates by partially unfolding the tertiary structure and reducing the R-helical or random coil contents [106]. Due to the high binding efficiency of phosphate to BSA molecules, BSA molecules adsorb more compactly when using phosphate buffer, exhibiting a stable conformation. The reduction of the R-helical structure revealed that BSA molecules were denaturing during adsorption on hydrophilic surfaces. Furthermore, the molecules were discovered to be oriented parallel to the surface, allowing for several electrostatic

interactions with the hydrophilic surface. The methyl groups of BSA are oriented randomly on a hydrophobic surface, and it was reported that more molecules were adsorbed than on a hydrophilic surface. [110], [111]. The models of BSA adsorbed on the hydrophobic and hydrophilic surface were studied using QCM-D and dual-polarization interferometry (DPI) technique and reported as seen in **Fig. 2.13** [112]. It is suggested that BSA changes its orientation and packing arrangement on the hydrophobic surface, inducing the formation of more compact and less hydrated layers.



**Fig. 2.13** Properties and orientation of adsorbed proteins on the hydrophilic and hydrophobic substrates. Adsorbed proteins on hydrophilic and hydrophobic surfaces have different surface coverage and layer characteristics. Although Lysozyme and α-Syn have comparable molecular weights, their affinity for substrates and layer characteristics differs due to structural differences. Source: ref. [112]

Recently, Vilhena et al. (2016) used molecular dynamics simulations with an explicit solvent condition to determine the adsorption behaviour of the BSA on bilayer graphene [113]. They found that BSA can preserve the majority of its binding sites' structural properties. Seredych (2018) presented an experimental assessment of the adsorption properties of expanded graphite with different functional groups and graphene nanoplatelets towards BSA [17]. The proposed interaction between BSA and graphene derivatives is through π-π stacking, hydrophobic interaction and covalently binding with functional groups. Although some studies of BSA adsorbed on the graphene surface have been conducted, the adsorption mechanisms and the structural properties of

proteins on surfaces are not well understood due to the limitations of molecular monitoring experiments.

### **Biological functions**

Albumin is a critical protein for maintaining the oncotic pressure required for proper fluid balance between the blood vessels and the bodily tissues. Without albumin, the arteries' high blood pressure would force more fluid into the tissues. One of the most important properties of albumins is their capacity to bind to a variety of different substances reversibly. It acts as a carrier for numerous hydrophobic steroid hormones and fatty acids in the plasma. The protein frequently increases the solubility of hydrophobic drugs in the plasma improving blood circulation and efficacy of drugs [20], [26] Excessive or insufficient serum albumin might be hazardous. For instance, the presence of albumin in the urine typically indicates the presence of renal disease.

BSA possesses discrete binding sites with different specificities. The most important ones are referred to as site-I and site-II located in hydrophobic cavities of subdomains IIA and IIIA, respectively [20]. Site markers are small molecules that have specific binding to the active sites of albumin including warfarin, phenylbutazone, dansylamide and iodipamide for site I and ibuprofen, flufenamic acid and diazepam are site-II [32] They are often used in studying the interaction of different ligands with the protein.

#### 2.5.2 Lysozyme

Lysozyme (N-acetylmuramic-hydrolase) is an enzyme with antibiotic properties abundantly found in secretions like saliva, tears, mucus, and egg white [114]. It was discovered in 1922 by Alexander Fleming when he demonstrated that his nasal mucus presented the ability to inhibit the growth of a certain bacteria in culture [115]. Lysozyme damages microbes by attacking their cell walls made of peptidoglycan, which consists of the repeating amino sugars, namely N-acetylglucosamine (NAG) and N-acetylmuramic acid (NAM), crosslinked by peptide bridges. Lysozyme disrupts the bond between NAG and NAM by hydrolysing them. This process increases the permeability of bacteria and causes them to burst. Lysozyme has been widely used in the food and pharmaceutical industries due to its bacteriostatic and bactericidal properties.

### **Physico-Chemical Properties**

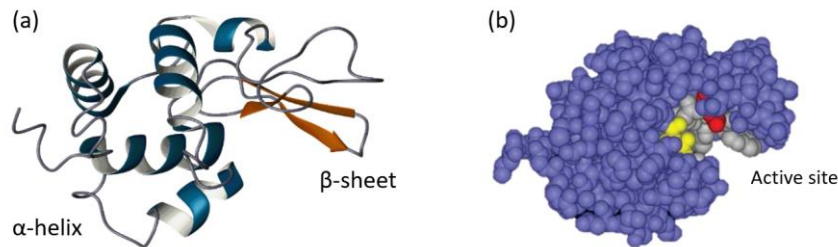
In nature, lysozyme is found mainly as a monomer possessing a molecular weight of 14.3 kDa. The primary structure of lysozyme is a single polypeptide conformed of 129 amino acid residues [116]. The structure consists of two domains linked by a long  $\alpha$ -helix which acts as the active site of the enzyme [117]. The first domain (residues 40 to 88) is composed mostly of the antiparallel  $\beta$ -sheet, whereas the second domain (residues 1 to 39 and 89 to 129) is made up of large  $\alpha$ -helix (**Fig. 2.14**). Lysozyme is a highly stable enzyme as it contains four disulfide bonds of the single polypeptide chain. At least two of the -S-S- bonds must be intact to maintain its enzymatic activity. Lysozyme folds into a compact globular structure with a long cleft on the protein surface under physiological conditions. This cleft is the active site that can bind to the carbohydrate chain at the bacteria cell wall and subsequently break it.

Lysozyme has been commonly chosen as a model protein for protein interaction studies due to its small size and simple molecular structure [118]. For example, hen egg lysozyme (HEL) is a well-studied model for investigating antibody-antigen interactions [119]. It maintains biological activities in a large range of pH 6-9 and behaves positively at neutral pH [120]. The interaction between anti-HEL antibody and HEL involves hydrogen bonds and van der Waals interactions predominantly, as the antibody binding site contains an uneven number of aromatic residues [121]. The kinetics of association and dissociation of anti-HEL with HEL depend on a variety of conditions including pH, temperature and viscosity of the medium [122]. It is also reported that the association reactions are insensitive to ionic strength [122].

### **Antimicrobial Roles**

Lysozyme is a natural preservative due to its potent antimicrobial properties, particularly against Gram-positive bacteria. The enzyme hydrolyses a variety of structurally similar substrates, most notably the polysaccharide copolymers including NAG and NAM found in many bacterial cell walls. The enzyme catalyses the hydrolysis reaction of the glycosidic  $\beta$  (1-4) linkage between NAG and NAM, resulting in the breakdown of the cell wall. The antimicrobial activity of the lysozyme monomer is limited to Gram-positive bacteria since their cell walls consist mainly of a peptidoglycan layer. Gram-negative bacteria, on the other hand, are less likely to be attacked by this enzyme due to their

more complex envelope structure. The composition and sequence of N-acetylamino sugars in the bacterial cell wall may influence lysozyme's bacteriostatic, bacteriolytic, and bactericidal activities[123].



**Fig. 2.14** Crystal structure of lysozyme (a) Ribbon structure showing two domains-domain 1 (N-terminal) contain mostly  $\beta$ -sheet and domain 2 is mainly  $\alpha$ -helix; source: PDB 1DPW ref. [124] 2 contain a majority of  $\alpha$ -helix. (b). A molecular model of hen egg-white lysozyme where key residues in the binding site are highlighted - Asp 52 (red); Glu 35 (yellow); some of the other residues (grey) source: ref. [125]

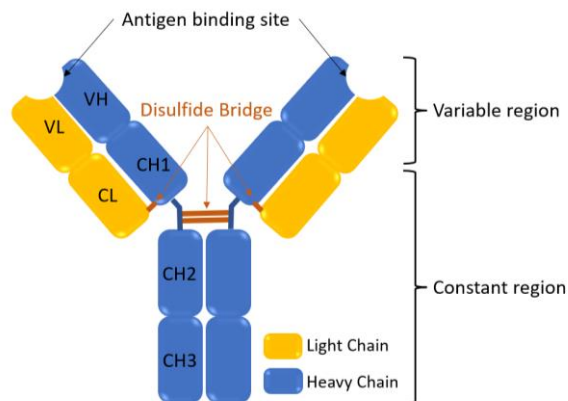
### Medical applications

Since human lysozyme is considered as 'body's own antibiotic', it is used as a biomarker in a variety of medical diagnostics, including bacterial infection, coronary artery disease, sarcoidosis, and breast cancer. [120], [126], [127]. Arterial plasma lysozyme levels are measured to identify patients with varying degrees of coronary artery disease, observed in separate cohorts of patients using a cut-off value of 1.5  $\mu\text{g}/\text{mL}$  [126]. The sensitivity of serum lysozyme for predicting sarcoidosis lies between 69% and 80%; the serum lysozyme level also demonstrated a significant tendency to increase with the number of organs involved [128]. In some cancers, like myelomonocytic leukaemia, excessive levels of lysozyme can be produced by cancer cells leading to kidney failure and low blood potassium [129].

#### 2.5.3 Immunoglobulin

An immunoglobulin (Ig), also known as an antibody (Ab), is a Y-shaped protein produced by white blood cells as a part of the immune system. The overall structure of immunoglobulin antibodies is assembled from two identical heavy-chain (CH) and two identical light-chain polypeptides (CL), see **Fig 2.15**. The heavy and light chains are composed of both constant and variable regions. The variable domains comprise the different sequences of the N-terminal domain of the H and L polypeptide chains, called

as VH and VL. This region contains a binding site which is a characteristic of each antibody.



**Fig. 2.15** Schematic structure of an antibody presenting constant and variable regions. Heavy chains and light chains are in blue and yellow. The antigen-binding site is at the tip of variable regions.



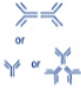


The Ig can capture and neutralize foreign objects that infiltrate mammalian bodies, such as pathogenic bacteria and viruses. Each tip of the "Y" of an antibody contains a paratope (analogous to a lock) that can recognize a unique epitope (analogous to a key) of the pathogen, also known as an antigen, allowing a precise binding mechanism. Antigen-binding sites at both tips of each antibody can adapt to capture the specific epitope, allowing it to recognize millions of different antigens.

The structure of the antibody is classified into five classes, including IgA, IgD, IgE, IgG and IgM. This classification is based on differences in amino acid sequence in the constant region (Fc) of the antibody heavy chains involved in the interactions with other immune system components. The class also determines the function that an antibody performs after binding to an antigen. Antibodies from different classes, for example, differ in their releasing location in the body and the stage of an immune response. IgG and IgA are also further identified into subclasses (isotypes), e.g., in human IgG1, IgG2, IgG3, IgG4, IgA1 and IgA2, are based on slight differences of the amino acid heavy chain sequences. In short, the Ig classes and isotopes differ in their biological features, structure, target specificity and distribution. As a result, determining the Ig isotype can provide valuable insights into the complex immune response.

An immunoglobulins blood test may be used to help diagnose a variety of conditions, including bacterial or viral infections, certain types of cancer like multiple myeloma

[130], immunodeficiency, which is a condition that reduces the body's ability to fight infections, and autoimmune disorders such as lupus and nephrotic syndrome, which cause the immune system to mistakenly attack healthy cells, tissues, and/or organs [131], [132].

**Table 2.1** Five types of antibodies and their properties and functions

	IgG	IgM	IgA	IgE	IgD
					
Heavy Chain	Y	μ	α	ε	δ
MW (kDa)	150	900	385	200	180
Number of antigen binding sites	2	10	4	2	2
% of total antibody in serum	80%	6%	13%	0.002%	1%
Fixes complement	Yes	Yes	No	No	No
Distribution	Intra & extravascular	Mainly intravascular	Intravascular and secretions	Basophils and mast cells (saliva & nasal secretions)	Lymphocyte surface
Function	Main blood antibody, neutralizes toxins	Primary response, B cell receptor	Secreted into mucus, tears and saliva	Allergic antibody and anti parasitic activity	B cell receptor

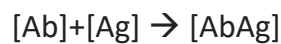
Furthermore, due to its ability to fight infections as well as its anti-inflammatory and immunomodulating effects, immunoglobulin is being increasingly demonstrated as a treatment for a wide range of medical conditions [131]. Clinical indications for intravenous immunoglobulin (IVIg), licensed by the US Food and Drug Administration (FDA), include: (1) treatment of primary immunodeficiencies (PIs), (2) prevention of bacterial infections in patients with hypogammaglobulinemia and recurrent bacterial infection due to B-cell chronic lymphocytic leukaemia (CLL), (3) prevention of coronary artery aneurysms in Kawasaki disease (KD), (4) prevention of infections, pneumonitis, and acute graft-versus-host disease (GVHD) following bone marrow transplantation, (5) reduction of severe bacterial infection in children who infected with HIV, (6) increasing platelet count in idiopathic thrombocytopenic purpura to prevent or control bleeding,



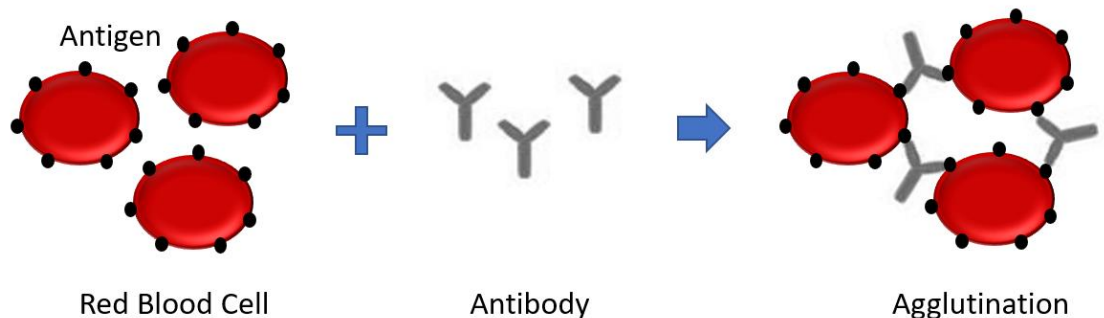
and (7) treatment of chronic inflammatory demyelinating polyneuropathy (CIDP) and multifocal motor neuropathy (MMN) [131], [133], [134].

## 2.6 Antigen-antibody interaction

Antigen-antibody (Ag-Ab) interaction refers to the chemical interaction that occurs between antibodies and antigens during an immune response. A high-affinity binding interaction is similar to a lock and key. The antigen is the key that allows the antigen to enter a cell and infect it, whereas the antibody is the lock that captures and locks the key, preventing it from infecting cells. The process of combining antigens and antibodies is called agglutination, **Fig 2.16**. A dynamic equilibrium exists for the binding. For example, the reaction is a reversible one and can be expressed as:



where [Ab] is the antibody concentration and [Ag] is the antigen concentration, either in free ([Ab],[Ag]) or bound ([AbAg]) state.



**Fig. 2.16** Representation of agglutination reaction between blood group antigens and antibodies forming a clumping of erythrocytes

The specific association between Ag and Ab is essentially based on non-covalent bonds including hydrogen bonds, hydrophobic interactions, electrostatic forces, and Van der Waals forces. The dissociation or association could also be influenced by liquid medium parameters such as surface tension, pH, ionic strength, dielectric constant and temperature [135]. It is proposed that the binding between Ag and Ab will be effective and reliable under optimal conditions. For example, red cell antigen–antibody reactions occur in the pH range of 6.0 to 8.0; results become unreliable outside of this range. [136].

Additionally, the interfacial water molecules might influence the non-covalent interactions between Ag and Ab, resulting in cross-reactivity. This situation occurs when a single antibody recognizes antigens from two distinct pathogens or one pathogen and proteins from non-pathogens [137]. This process can produce allergies when identical carbohydrate structures cross-react with unrelated proteins from the same or different species. Moreover, cross-reactivity has implications for flu vaccination due to a large number of the strains, while antigens produced in response to one strain may involve the protection of other strains [138]. Cross-reactivity can also occur between non-closely related viruses, such as the cross-reactivity between influenza virus-specific CD8+ T cells and hepatitis C virus antigens [139].

In blood, the antigens are specifically and with high affinity bound by antibodies to form an antigen-antibody complex. The immune complex is then transported to cellular systems to be destroyed or deactivated. In a clinical laboratory, the principles of specificity and cross-reactivity of the antigen-antibody interaction are used for diagnostic purposes. One common application is determining the ABO blood group. It can also be used as a disease screening technique for pathogens like HIV, microbes, helminth parasites, and autoimmune diseases. Nonetheless, the actual nature of antibody-antigen interaction in autoimmune disease is unknown. [140], [141].

## 2.7 Screening for autoimmune diseases

Autoimmunity is a condition of losing normal immune homeostasis in which the organism produces an abnormal response to its own tissue. In general, antibodies can detect and distinguish between foreign and self-molecules produced within the body. Typically, self-molecules are ignored by the immune system. However, antibodies recognize self-molecules as antigens in certain conditions (antinuclear antibodies) and cause unexpected immune responses that are always harmful and sometimes fatal. Symptoms differ depending on the disease, but they may include rashes, swelling, arthritis, or fatigue. In general, the presence of self-reactive T cells, autoantibodies, and inflammation that attacks healthy cells is a sign of an autoimmune disease. Depending on the type of antigens and antibodies involved, these unexpected immune responses cause a variety of autoimmune disorders. For example, some autoimmune diseases only affect one organ such as Diabetes type 1 affects the pancreas while other diseases, such

as systemic lupus erythematosus (SLE), affect the entire body. The early stages of autoimmune diseases can be screened by detecting these unusual antibodies (ANA test).

Although the ANA is traditionally used to make a serologic diagnosis of SLE, it is also found in the majority of other autoimmune diseases either. Methods for disease screening employ immunofluorescence testing of the patient's serum at various dilutions with a cell-substrate, like ELISA methods. An ELISA test provides high sensitivity but lacks specificity. Results are reported as either the dilution of serum that suggests a positive response level or the degree of positivity measured using the specific testing procedure [142].

The exact causes of the immune-system misfire have not yet been determined. However, some people are more prone to developing an autoimmune disease than others. Multiple laboratory tests are generally needed for the diagnosis of autoimmune diseases, including basic studies like a complete blood count, comprehensive metabolic panel, acute phase reactants, immunologic studies, serologies, flow cytometry, cytokine analysis, and HLA typing [143]. When symptoms suggest an autoimmune disease, the antinuclear antibody (ANA) test is frequently one of the tests used for detection. A positive test indicates that one of these diseases may be present, but it is not a confirmation.

Immunofluorescence is particularly useful as an initial screening test for those suspected patients of having SLE, Sjögren syndrome, RA, mixed connective tissue disease, scleroderma, and polymyositis/dermatomyositis [143]. However, one crucial caution regarding the interpretation of the presence of ANA is that it is also found in non-rheumatic diseases, including Hashimoto thyroiditis, Graves' disease, autoimmune hepatitis, primary autoimmune cholangitis, primary pulmonary hypertension, and various infections and malignancies. Besides, the presence of low-titer ANA occurs more frequently in elderly populations. Therefore, complementary clinical tests are required to confirm the diagnosis.

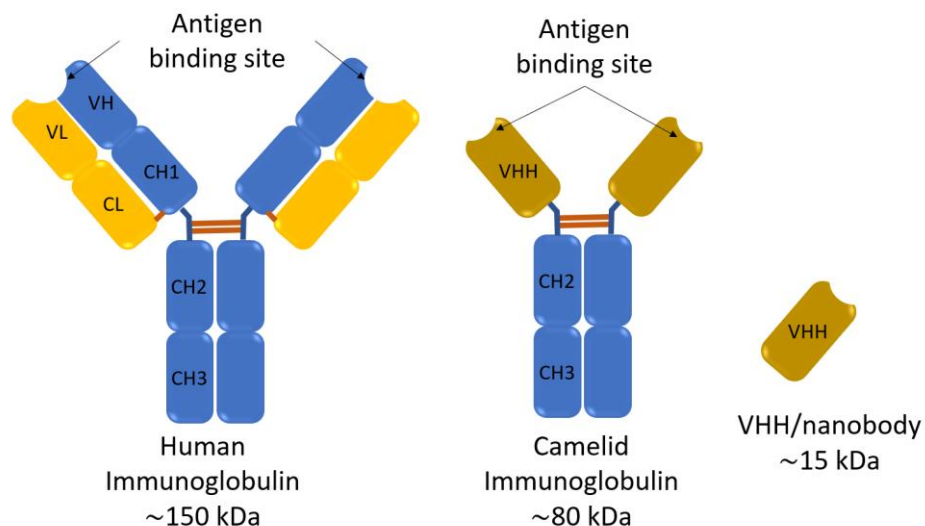
## 2.8 Membranous nephropathy

Nephrotic syndrome (NS) is kidney disease with typical symptoms of nephrotic range proteinuria, hypoalbuminemia, oedema and hyperlipidaemia [144]–[146]. The

syndrome can be characterised by the rise of glomerular permeability [144]. Membranous nephropathy (MN) is a common cause of NS in adults. Idiopathic membranous nephropathy (iMN) is found in 80% of MN patients affecting 10 to 12 cases per one million population [147], [148]. The important discovery in 2009 that circulating antibodies to phospholipase A2 receptor (PLA2R) present in 70% of patients with iMN identified the autoimmune nature of this pathologic abnormality [149]. As ~80% of patients show proteinuria in the nephritic range, identifying some patients with proteinuria is a conventional physical examination [150]. However, performing an invasive renal biopsy for all suspected cases is infeasible, resulting in its delayed diagnosis. Although MN displays a slow progression, and some patients enter a spontaneous remission phase, 30 to 40% of patients eventually develop end-stage renal disease or die [150]–[152].

## 2.9 Nanobody technology

A nanobody (Nb) is a registered trademark of Ablynx, referring to a single-domain antibody (sdAb). It is a binding domain of heavy-chain antibodies (HCAbs) found abundantly in camelid sera. The structure of HCAbs is noticeably different from conventional mammalian IgG structure as it lacks L-chain polypeptides and the first constant domain (C<sub>H1</sub>). Its H chain contains only a variable domain (VHH) that serves as an antigen-binding site at the N-terminal region. **Fig. 2.17** presents the difference between conventional immunoglobulin (IgG) and heavy-chain antibodies with a derivation of a single domain VHH or a nanobody. Nanobodies, like antibodies, can selectively bind to specific antigens, but the nanobody molecule is much smaller. A nanobody has a molecular weight of 12–15 kDa, whereas a typical antibody has a molecular weight of 150–160 kDa, which is 10 times larger. Aside from being smaller and having a less complex structure than antibodies, many nanobodies can be produced on a large scale using eukaryotic and prokaryotic cells. [19].

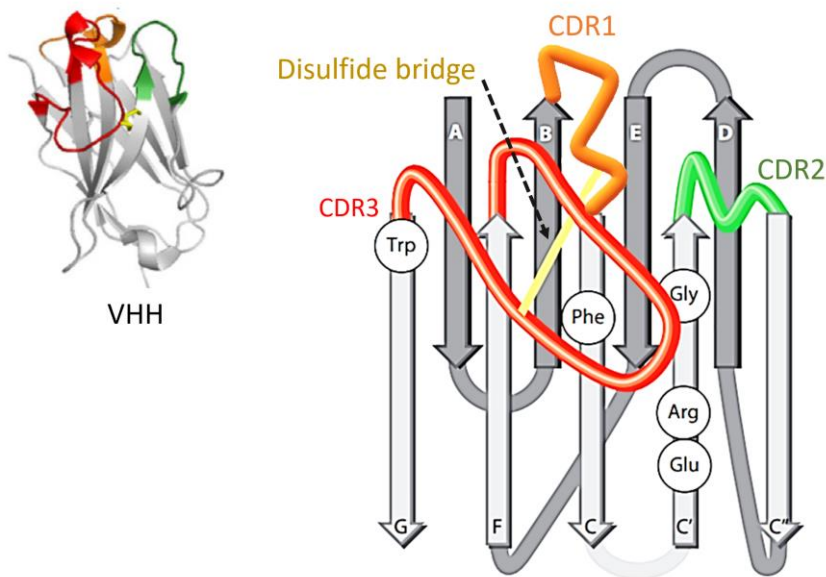


**Fig. 2.17** Schematic of conventional immunoglobulin (IgG) and heavy-chain antibody (HCAs) derived from camelid sera and a VHH part of HCAs or a nanobody with the antigen recognition region.

### 2.9.1 Structure of VHH

The structure of the VHH domain is similar to the VH with a few distinguished differences including complementarity-determining regions (CDRs) and framework 2 (FR2). It contains three hypervariable (HV) regions surrounded by more conserved FR regions and longer CDR3 than that of VH [153]. In the FR2 region of VHH, the critical hydrophobic amino acids expressed in VHs (Val47, Gly49, Leu50 and Trp52), which are normally participating in the interaction with the VL domain, are frequently substituted by the more hydrophilic residues, called hallmark residues which are mostly Phe42, Glu49, Arg50, and Ph52 [154]. With this replacement of amino acids, VHHs become more soluble and independent of the VL.

**Fig. 2.18**, the folded variable domain of VHH comprises from nine  $\beta$ -strands (A, B, C, C', C'', D, E, F, G), arranged in a four-stranded  $\beta$ -sheet in the back (A, B, E, D) and a five-stranded  $\beta$ -sheet in the front (C, C', C'', F, G) [154]. These groups of the back and front  $\beta$  structures are connected by loops and a disulfide bridge between Cys23 and Cys94, packed against a conserved Trp. The fold and disulfide bond help stabilise the whole structure of the domain.



**Fig. 2.18** Ribbon structure of a VHH (PDB:1JTT) and the schematic representing the VHH structure and its key amino acids that are substituted in a VHH are shown with three-letter codes. The A, B, E, and D  $\beta$ -strands of one sheet in the back and the G, F, C, C' and C'' strands in the front sheet.

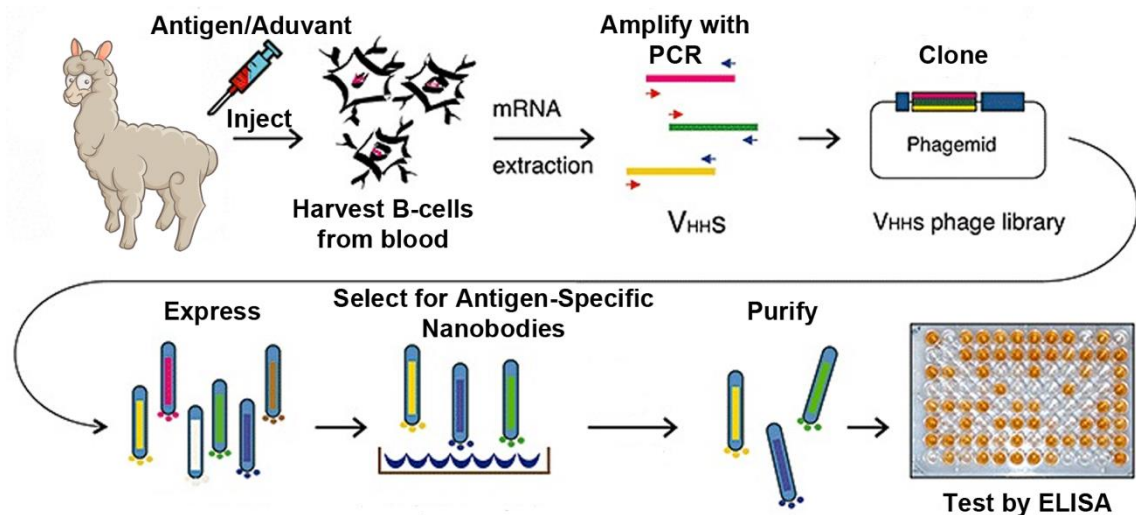
### 2.9.2 Nanobody Production

Nanobodies or immunoglobulin-based recombinant antigen-binding proteins can be generated by immunising the particular animal with the target antigen or evolving existing Naïve libraries [155].

For the immunizing method, a camelid animal is immunized with the protein of interest, then the produced pool of nanobody cDNAs will be amplified by PCR before the process of cloning to get a phagemid library. The library will be then screened by expression against the target protein. Positive clones are sequenced and confirmed the specific binding using ELISA. Finally, nanobodies against the protein are produced and purified from *E. coli*, **Fig. 2.19**. For the naïve library, the process of immunising the animal can be skipped. Naïve libraries can produce satisfactory VHHs within 1-2 months and are especially applicable for toxic, lethal, transmissible, low immunogenic antigens or nonimmunogenic small molecular compounds.

The nanobodies, for which the sequence is available in the library, are suitable for engineering and expression in eukaryotic and prokaryotic systems. The trend in nanobody production is toward simpler but more reliable bacterial-based methods that

can substitute for the more difficult processes required when using eukaryotic systems. However, when the final immune constructs require features that cannot be obtained in prokaryotic cells, the eukaryotic method will be used.



**Fig. 2.19** Process for nanobody production by the immunizing method. Begin by exposing an interesting antigen to llamas and then harvesting B-cells for mRNA extraction. VHH is amplified by PCR and then cloned for optimal antigen selection. The selected nanobodies will be purified and their specificity and sensitivity will be determined using the ELISA method. Source: ref. [155]

### 2.9.3 Applications of nanobodies

Nanobodies have the potential to be next-generation tools for antigen-recognition applications where conventional antibodies are ineffective. Because full-length antibodies can be difficult to generate, produce, functionalize, and apply intracellularly due to their structural and chemical complexities, novel classes of recombinant antigen-binding proteins, such as nanobodies, are on the rise.

The antibody has a complicated structure in terms of its size and chemistry. Conventional IgGs contain six single domains with a highly conserved loop length for the antigen-binding domain, which has evolved to bind convex paratopes, thus limiting the scope of potential antigens [156]. Regarding the chemistry, the antibodies contain inter- and intramolecular disulfide bonds. These bonds make the molecules vulnerable to environmental changes, the reductive milieu of the intracellular environment and increase adsorption of non-specific molecules. Nanobodies, on the other hand, have a

much simpler physical structure and chemistry than antibodies. A nanobody is made up of only a peptide chain of about 110 amino acids. These peptides have a similar affinity to antigens as whole antibodies but are more heat-resistant and stable towards detergents and concentrated urea. Furthermore, the lack of a disulfide bond results in instability in a changing environment.

Nanobodies are frequently used in basic research due to their compact structure and high stability, ranging from sophisticated imaging and mass spectrometry to the delivery of nanobodies into living cells for the visualization and manipulation of intracellular antigens. [157]. Furthermore, their ease of functionalization opens the way towards the development of promising diagnostic and therapeutic applications [158]–[160]. For example, several publications have reported promising clinical data of nanobody-based molecular imaging in cancer diagnosis, such as ovarian cancer [161] and breast cancer [162], [163]. Very recently, Xiang et al. developed nanobodies that can bind to the receptor-binding domain (RBD) of SARS-CoV-2 spike protein within picomolar to femtomolar affinities [164].

Since nanobodies are smaller molecules than monoclonal antibodies, they can penetrate more deeply into difficult-to-reach tissues to reach the target antigen, attracting the development of novel therapeutic strategies. For example, a nanobody-based therapy for influenza A virus H5N1 was tested with infected mice. The nanobody was directed against hemagglutinin, suppressing the replication of the H5N1 virus in vivo and reducing morbidity and mortality [165]. Additionally, the conjugation of nanobody recognizing antigen, presenting in cells, has been successfully used for tumour detection [121] and boosts strong immune response [166].



## CHAPTER 3. Review of Characterization Techniques

Contents:

3.1 Quartz Crystal Microbalance (QCM) technique

3.2 Contact Angle

3.3 Scanning Electron Microscope (SEM)

3.4 Atomic Force Microscopy (AFM)

3.5 Fourier Transform Infrared (FTIR)

3.6 X-ray Photoelectron Spectroscopy (XPS)

3.7 Raman Spectroscopy

3.8 Dot Blot

### 3.1 QCM technique

#### 3.1.1 QCM Principle

The quartz crystal microbalance (QCM) is a mass sensitive technique used for measuring the mass adsorbed on the surface of the QCM chip. This technique is based on the piezoelectric properties of quartz crystals. Upon applying alternating electric fields to an AT-Cut quartz crystal's gold electrodes, mechanical deformation of the crystal lattice occurs, generating an oscillating signal with a frequency equal to its characteristic resonant frequency. . QCM sensors are commonly used in aqueous media, where the crystal is left to oscillate until a stable signal with no noticeable drift is obtained, then the final frequency is registered as a baseline. When a mass adsorption event on the surface occurs, a shift in the frequency due to the mass loading will follow. The amount of adsorbed mass can be determined using the Sauerbrey equation [167], (Eq 1)

$$\Delta m = \frac{-A\sqrt{\rho_q\mu_q}}{2f_0^2} \Delta f \quad (1)$$

Where

$f_0$  is the resonant frequency (Hz)

$\Delta f$  is frequency change (Hz)

$\Delta m$  is mass change (g)

$A$  is Piezoelectrically active crystal area (area of a working electrode, cm<sup>2</sup>)

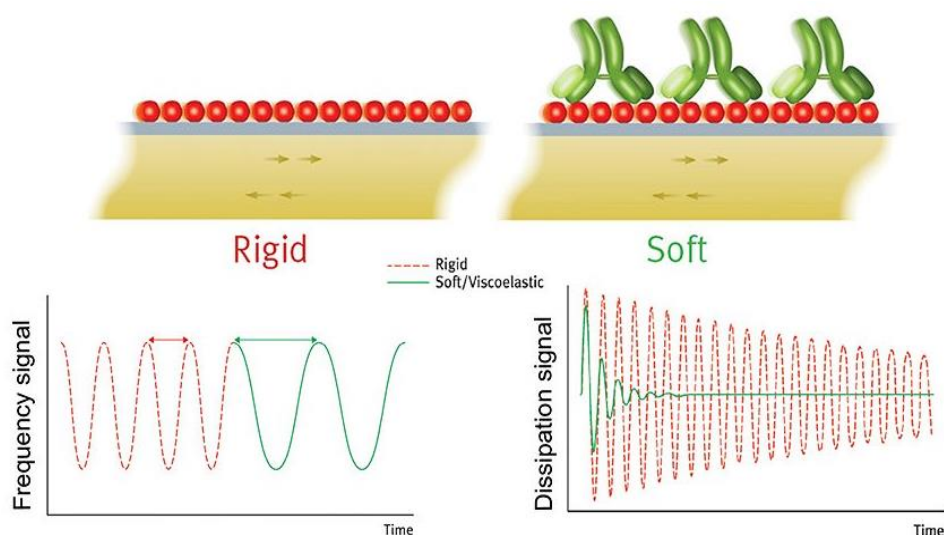
$\rho_q$  is density of quartz ( typically 2.648 g/cm<sup>3</sup>)

$\mu_q$  is shear modulus of quartz for AT-cut crystal ( typically  
2.947x10<sup>11</sup> g·cm<sup>-1</sup>·s<sup>-2</sup>)

Interestingly, the Sauerbrey equation establishes a linear relationship between the change in frequency ( $\Delta f$ ) and adsorbed mass ( $\Delta m$ ). Therefore, by measuring the frequency shift, the adsorbed mass can be calculated. However, the Sauerbrey model presents some limitations and involves some assumptions. First, the adsorbed mass must be small relative to the mass of the quartz crystal. Second, the model applies only to rigid films since its viscoelasticity is not considered and thus the calculation will not be precise. Lastly, the adsorbed mass should be distributed evenly over the active surface of the sensor with no predominant adsorption regions. Initially, the QCM

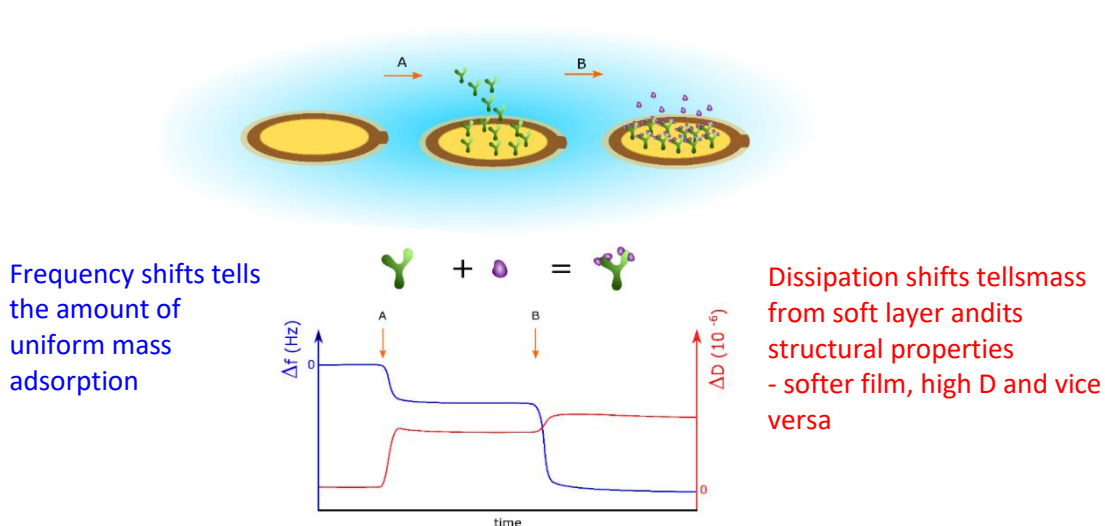
technique with Sauerbrey mass computation was almost solely used in vacuum or gas phase monitoring which overcame those limitations. However, the QCM technique can be used in the liquid phase when the molecules adsorbed on the surface tend to form a rigid film. To overcome the intrinsic limitations of the conventional QCM instrument, an advanced technique in which the energy dissipated during the adsorption event is measured in real-time and has been vastly used in biomolecular studies for the past 25 years.

The Quartz Crystal Microbalance with Dissipation monitoring (QCM-D) can simultaneously measure the frequency and energy dissipation of the oscillating quartz crystal after the excitation stage. The energy dissipation, measured in the form of a damped sinusoid, is the sum of the total energy losses in the system in an oscillation cycle and it is defined as the lost energy divided by the total energy stored,  $E_{\text{loss}}/E_{\text{total}}$ . In a QCM-D system, the dissipation parameter is measured every time after the excitation signal is disconnected and the exponentially decaying oscillations are measured at half amplitude. This is known as the ring-down method. The Molecules forming a soft film on the quartz crystal tend to deform during the oscillations, producing high energy dissipation. In contrast, a rigid film attached to the crystal usually creates low dissipation due to lower molecular deformations (see **Fig. 3.1**).



**Fig. 3.1** Comparison of frequency and dissipation response during adsorption process of rigid and soft molecules Adapted from ref [168].

In general terms, the QCM-D technique outperforms conventional QCM systems as it not only can provide relevant information about conformational changes, structural properties and softness but also regarding the rigidity or viscoelasticity of the molecules attached to the surface **Fig. 3.2** shows a typical QCM-D profile and presents basic descriptions for both frequency and dissipation changes for molecular adsorption.

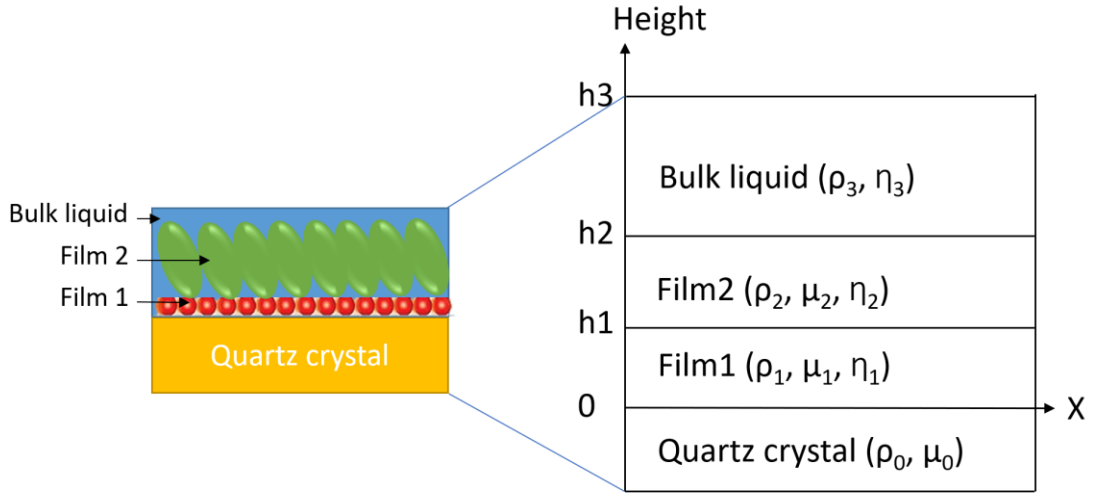


**Fig. 3.2** QCM-D profile analysis for structural properties of adsorbed molecules

### 3.1.2 Viscoelastic modelling

To extract relevant information like mass or the thickness and viscoelasticity, of a viscous film the QCM-D profiles must be fitted using an adequate physico-mathematical model. In this research, the modelling of the viscoelasticity for all of the presented QCM-D profiles is achieved by employing the Voigt-Voinova model [169].

The modelling begins after a quartz sensor is completely coated with a viscoelastic, thin and homogenous layer after being fully immersed in an aqueous media, regarded as the bulk liquid. Under these conditions, the quartz sensor will generate acoustic bulk shear waves propagating through the different layers. **Fig. 3.3** displays the geometry of a QCM sensor covered by double-layer viscous films in the bulk liquid.



**Fig. 3.3** Geometry of QCM oscillating in bulk liquid covered by a double layer of the viscoelastic film, namely film1 and film 2. Each layer possesses its own density ( $\rho$ ), elastic shear modulus ( $\mu$ ) and shear viscosity ( $\eta$ ). The density and shear modulus of the quartz plate is assigned as  $\rho_0$  and  $\mu_0$ , respectively. X axis represents distance from the centre of the crystal; Y-axis represents the thickness of each viscous layer assigned as  $h_1$ ,  $h_2$  for films 1 and 2 and  $h_3$  for the height of the bulk liquid.

The wave equation for the shear waves that propagate in the viscoelastic medium is shown as eq. 2 [169].

$$\mu^* \frac{\partial^2 u_x(y,t)}{\partial y^2} = -\rho \omega^2 u_x(y,t) \quad (2)$$

Where  $\mu^*$  is the complex shear modulus ( $\mu^* = \mu + i\omega\eta$ );  $U_x$  is the displacement in the x-direction;  $\omega$  is the angular frequency.

The viscoelastic layer is modelled as a Voigt element, in which the elastic response is connected in parallel with a response from a viscous layer. Regarding the Voinova modelling, equations for different cases, including viscoelastic layers in a vacuum and bulk liquid, have been solved to obtain a simplified form of  $\Delta f$  and  $\Delta D$  [170][171]. In this research, we use only the cases of viscoelastic layers immersed in a Newtonian bulk liquid. The simplified equations of  $\Delta f$  and  $\Delta D$  are shown in equations 3 and 4.

$$\Delta f \approx -\frac{1}{2\pi\rho_0 h_0} \quad (3)$$

$$\Delta D \approx \frac{1}{2\pi f \rho_0 h_0} \quad (4)$$

Where  $\rho_0$  and  $h_0$  represent the density and shear modulus of the quartz crystal;  $\eta_3$  and  $\delta_3$  represent viscosity and viscous penetration depth of the bulk liquid;  $\mu_j$ ,  $\eta_j$  and  $h_j$  are the elastic shear modulus, the shear viscosity and the thickness of a viscoelastic layer  $j$ , respectively.

From equations 3 and 4, the adsorbed film is relatively small compared to the acoustic response from the bulk liquid. However, the thin film with finite thickness will produce a different response depending on the ratio between the viscosity and the elasticity of the film.

In QSense Dfind, the QCM-D modelling software developed by Biolin Scientific®, the propagating wave equations are used in a simpler form resulting in better outcomes. Furthermore, as the simple Voigt elements can be a proper model only for a few materials, Dfind has included the possibility to use elastic shear modulus and viscosity, which are frequency dependent. This modelling method is more realistic; however, more computationally heavy.

To accurately describe the response of  $\Delta f$  and  $\Delta D$ , the required conditions for the mathematical models implemented in Dfind are as follows:

- Each layer covers the whole active area of the QCM-D sensor.
- Each layer has a uniform thickness.
- Each layer is homogenous.
- All layers' viscoelastic properties can be described by Voigt viscoelastic representations.
- The medium in which the sensor is resonating is a bulk Newtonian fluid (like air or water).
- All layers are stress-free, i.e., the layers present no internal stress.

Therefore, in the present thesis, the modelling of the QCM-D signals was carried out using QSense Dfind Biolin Scientific in order to determine the adsorbed film's mass, thickness and viscoelasticity.

QSense Dfind is a proprietary graphical and intuitive software for QCM-D profiles. It is a useful tool for data visualization and extracting the most relevant information such as mass, thickness and viscoelastic properties of a film formed during a biomolecular event.

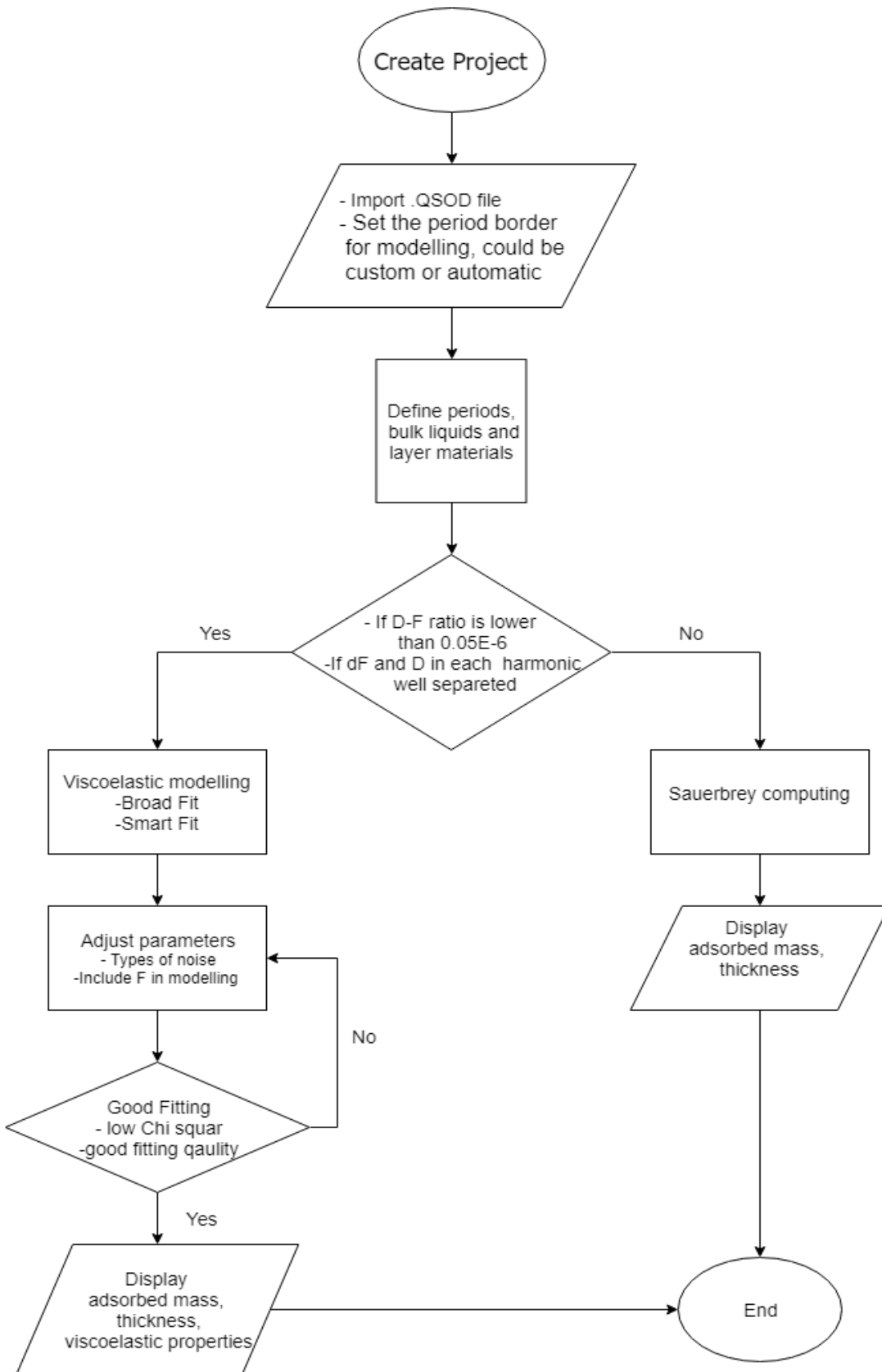
With particular attention, the software provides computational methods to determine the mass adsorbed on QCM sensor surface, including Sauerbrey; calculated from only the shift of frequency and viscoelastic modelling based on Voigt-Voinova model. A typical workflow and conditions for extracting information from QCM-D profiles using this software are shown in **Fig. 3.4**.

Briefly, to process native '.QSOD' files containing QCM-D profiles they must be imported to Dfind Then initial configuration parameters are set before starting the computational processing. Choosing the right model is crucial for determining accurate adsorbed mass, thickness, and viscoelastic. If there is no considerable spreading between its harmonics group from the frequency shifts and no significant magnitude for the D shifts, it is recommended to use the Sauerbrey model. On the other hand, the viscoelastic modelling with Smart Fit or Broad Fit should be selected if the measurement contains high dissipation or the frequencies harmonics present spreading.

The fitting process works by first calculating the output values for a model with an arbitrary set of input parameters then it must be adjusted until the output values match as close as possible with the original signals. To achieve a good fit for the viscoelastic modelling, Chi-square and fit quality values are considered. Chi-square is the most common criterion for minimizing  $\chi^2$  and it is defined as:

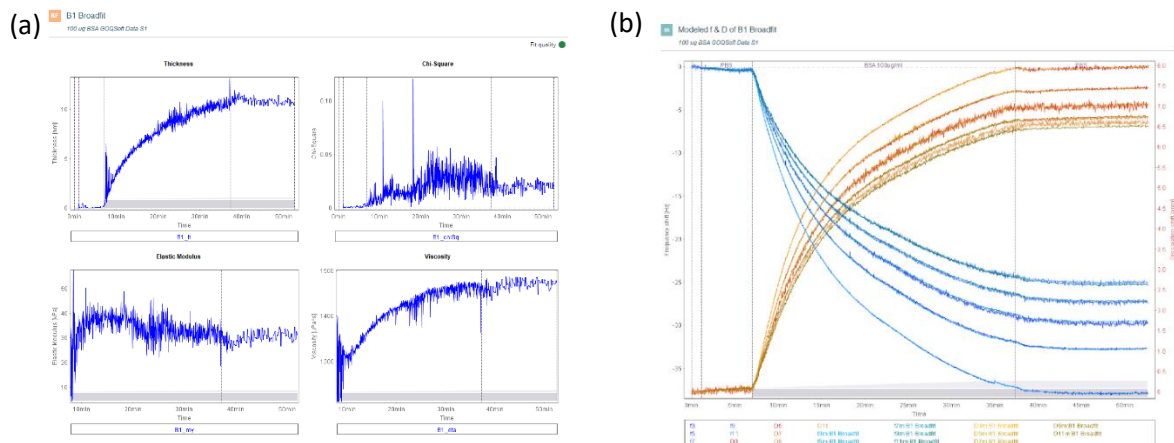
$$\chi^2 = \sum_i \left[ \frac{Y_{theory,i} - Y_{exp,i}}{\sigma_i} \right]^2$$

where  $\sigma_i$  is the measurement error or standard deviation of the data point 'i',  $Y_{theory,i}$  and  $Y_{exp,i}$  are the calculated and experimental Y-values, respectively.  $1/\sigma_i$  is the weight of each measured point. Chi-square should be as small as possible. The fit quality is the sum of chi-square throughout the data. Fitting quality is shown with a coloured circle above the modelling **Fig.**, see **Fig 3.5 (a)**. The colour scale varies from red, yellow to green, where green indicates a good fit. An example of a typical fitting graph is presented in **Fig. 3.5 (b)**.



**Fig. 3.4** Workflow and experimental conditions for determining the mass, thickness and viscoelastic properties of adsorbed films on surfaces using Dfind



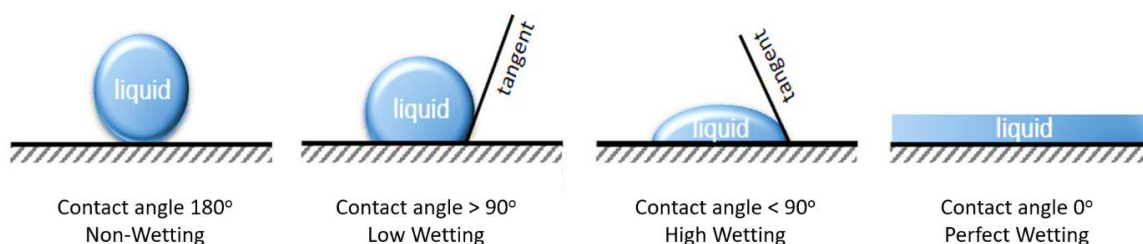


**Fig. 3.5 (a)** Dfind results from viscoelastic modelling including thickness, elastic modulus, viscosity and Chi-square **(b)** fitting of the experimental results for frequency and dissipation using the theoretical models described in the main text

### 3.2 Contact Angle

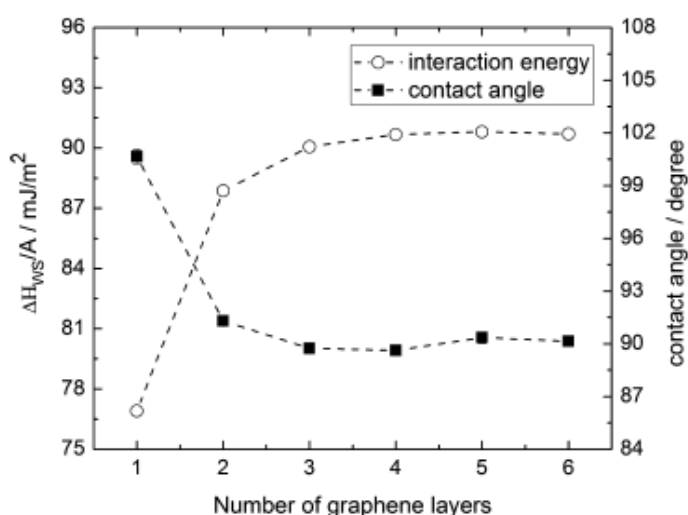
When a liquid droplet, typically deionised (DI) water, contacts a material's solid surface an angle will be formed between the surface plane and the droplet edge. This angle is related to both the solid and the liquid properties, generating attractive and repulsive forces between the liquid and the solid where the three-phase interface properties (gas, liquid and solid) are involved. Those interactions are called *adhesion* and *cohesion* which are intermolecular forces. Cohesive forces originate from similar molecules, such as the interaction between liquid molecules, i.e., hydrogen bonds and Van der Waals forces, while adhesive forces are created between different molecules, such as the interaction between liquid and solid molecules, i.e., mechanical and electrostatic forces. The balance between adhesive and cohesive forces at the interface will determine the contact angle. The smaller the contact angle refers to weaker cohesive forces than adhesive forces, and molecules of the liquid tend to interact more with solid molecules than liquid molecules. On the other hand, the larger the contact angle, the stronger the cohesive forces are while the adhesive forces are significantly weaker. As a result, the liquid molecules tend to interact more with each other than with the solid molecules. It has been conventioned that a surface is hydrophobic when its static water contact angle  $\theta$

is higher than  $90^\circ$  and becomes hydrophilic when  $\theta$  is less than  $90^\circ$ . This is schematically presented in **Fig. 3.6**.



**Fig. 3.6** Contact angle description showing wetting properties of a substrate

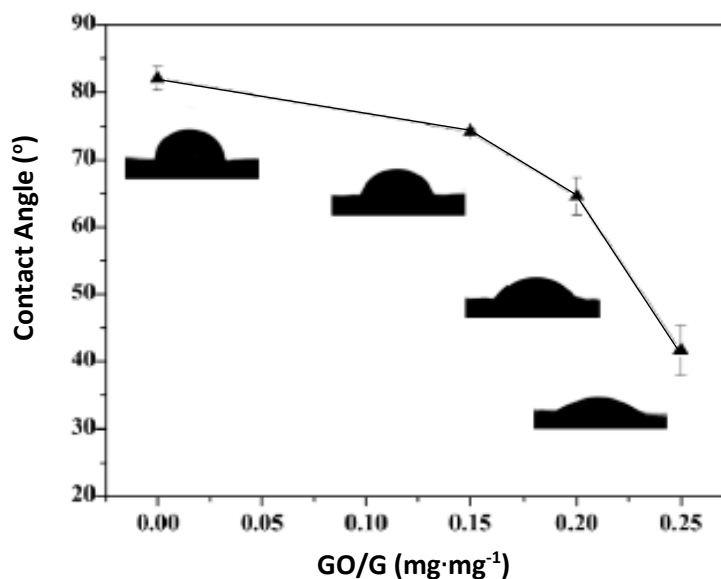
Graphene has been recognized as a hydrophobic material due to its  $sp^2$  hybridized carbon structural property. Many publications have reported that the contact angle of DI water on a monolayer of graphene is of the order of  $95\text{--}100^\circ$  and could be up to ideally  $127^\circ$ [172]. However, Fereshte (2013) reported that the contact angle of graphene also depends on the number of the graphene layers where the mono-layer graphene shows a relatively high contact angle of about  $90^\circ$  while two or more layers show a dramatic decrease in the contact angle [172], as seen in **Fig. 3.7**.



**Fig. 3.7** Interaction energy and contact angle between DI water and different layer number of the graphene substrate. Source: ref. [172]

In contrast, graphene oxide (GO) is composed of an aromatic carbon lattice interrupted by oxygen functional groups, e.g. epoxides, hydroxyls, ketone carbonyls, and carboxylic

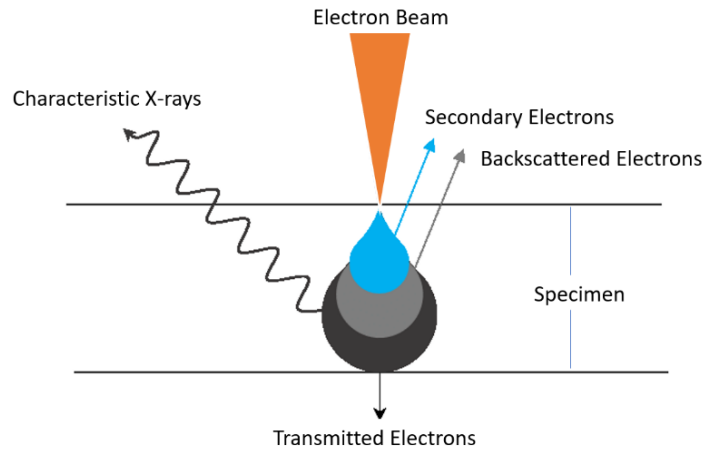
groups. The hydroxyls and carboxylic groups give GO an excellent hydrophilic property. Yang (2016) reported that with the mix of graphene and graphene oxide, the hydrophobicity measured by contact angle could be tuneable depending on the mixture ratio (see **Fig. 3.8**) [173]. Based on the latter examples, the contact angle, therefore, is considered to be a reliable method to determine the degree of hydrophobicity of the graphene family of materials.



**Fig. 3.8** Static water contact angle of the mix of graphene and GO. Source: ref. [173]

### 3.3 Scanning Electron Microscope (SEM)

A scanning electron microscope (SEM) works by focusing an electron beam over a surface to create an image of its topography. The electrons from the beam that interacts with the sample can produce signals from which relevant information about the surface topography and composition can be extracted. During the interaction between electrons and the sample, secondary electrons, backscattered electrons, and characteristic X-rays are created (see **Fig. 3.9**). In a typical setup, one or more detectors collect these signals to form the images to be displayed on the screen. The penetration depth of electrons into the sample is about a few microns depending on the accelerating voltage and the sample density.



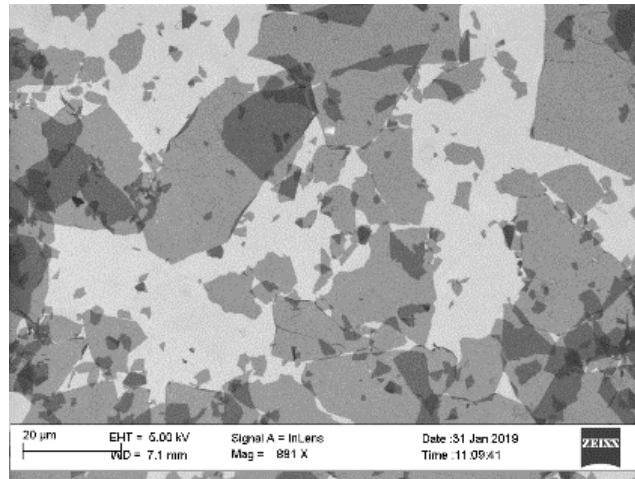
**Fig. 3.9** Schematic of electron beam interaction on the surface of the sample

The maximum resolution obtained from SEM depends on multiple factors such as the electron spot size and interaction volume of the electron beam and the sample. Typically, modern full-sized SEMs offer resolutions between 1 to 20 nm. Two types of signals, including the backscattered electrons (BSE) and the secondary electron (SE), are usually detected and used for surface morphology characterisation.

The BSE signals originate from a wide region within the interaction volume due to elastic collisions of electrons with atoms causing a change in the electrons' trajectory. In contrast, secondary electrons originate from the surface or the near-surface regions of the sample. The latter is due to inelastic interactions between the primary electron beam and the sample. It contains lower energy than the backscattered electrons that are beneficial for the inspection of the topography of the sample's surface.

For the past decade, the use of SEM imaging has been continuously growing as it is a rapid, non-invasive and effective method for characterising the morphologies of graphene films [8]. Due to the fact that various electronic applications of graphene require uniform and defect-free graphene in large sheets. SEM has the advantage of detecting impurities, ruptures, folds, voids and the quality of synthesized or transferred graphene on different substrates. However, SEM imaging of graphene faces some difficulties mainly due to its intrinsic limitation in its resolution and also as a result of the transparency from ultra-thin graphene layers making the images easily display the morphologies of the underlying substrate rather than the graphene itself. Moreover, graphene films sometimes are too smooth to generate enough contrasts for SEM

imaging. In this project, SEM was used to observe GO and rGO flakes on Au and SiO<sub>2</sub> substrates. As a result, the morphology, flake size and number of graphene layers can be observed.



*Fig. 3.10 The SEM image of monolayer GO flake on SiO<sub>2</sub>*

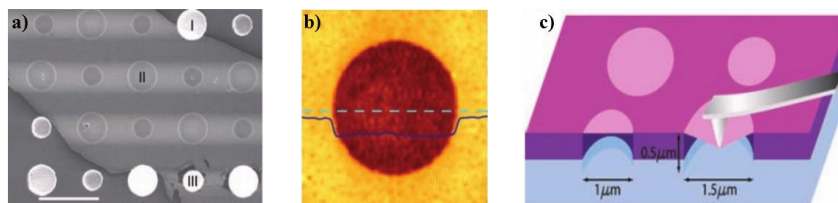
#### 3.4 Atomic Force Microscopy (AFM)

Atomic force microscopy is a scanning probe technique that can extract information on the mechanical properties, surface topology, roughness, thickness and uniformity of sample material. During operational mode, a tiny tip is connected to a cantilever and scanned over the sample's surface, resulting in a topological image with altitude profiles (on the Z-axis). The cantilever may be deflected due to fluctuations in the topography of the surface.

AFM in tapping mode (intermittent contact) is commonly used for measuring the thickness of graphene flakes on substrates; however, the accuracy of the measured thickness as well as counting the number of layers remains challenging [174]. The final measured thickness of a graphene flake could be influenced by electrostatic interactions between the AFM tip and the graphene sample, moisture and incorrect experimental parameters on the system. Raman spectroscopy is often used as a second characterization to correlate the measured thickness and number of layers to complement the benefits of AFM imaging. The usual thickness of monolayer graphene ranges from 0.4 to 1.7 nm [175]. Novoselov et al. measured graphene platelets with thicknesses of 1-1.6 nm [176]. The average thicknesses of GO sheets have been reported

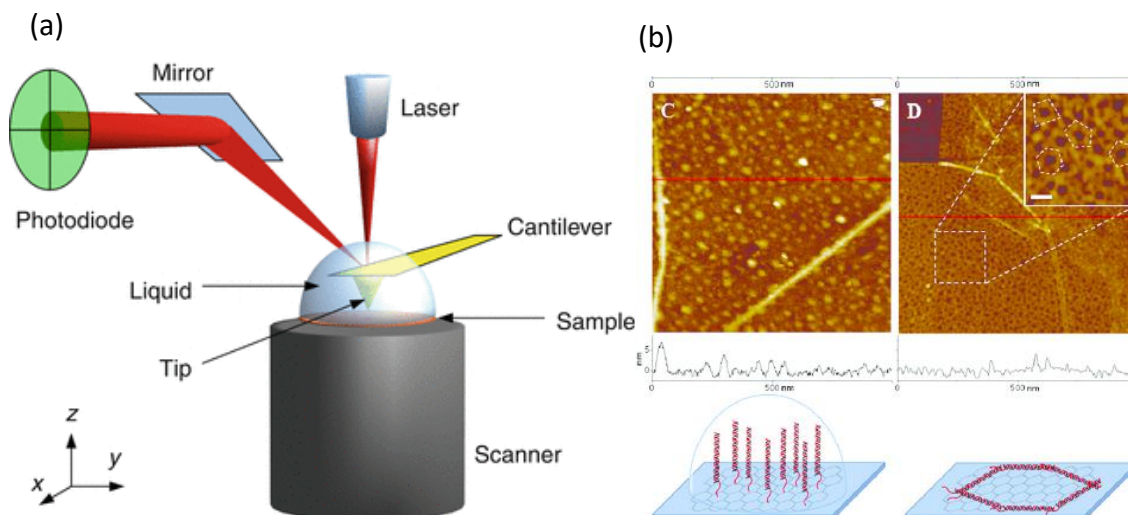
ranging from 0.9-2.3 nm[177], [178], which are slightly higher than that of monolayer graphene. This increase could be due to surface functionalities protruding from the basal plane of the flakes, the quality of the GO sheets and the manufacturing conditions of the GO samples.

By using AFM in nanoindentation mode, the local mechanical properties of the target specimen can be quantitatively characterized. In this special mode, an AFM indentation tip is pressed against a sample surface until the surface is deformed. The relationship between applied force and the sample deformation provides information on the mechanical properties, including hardness and Young's modulus. AFM nanoindentation offers precise control of the sample deformation in the nanoscale and can be applied on a wide range of materials, including thin film coatings, metals, polymers, and biomaterials. Moreover, the stiffness of thin-film suspended graphene can be probed using this technique, **Fig. 3.11**.



**Fig. 3.11** AFM imaging of suspended graphene membranes a) SEM image of a graphene flake spanning an array of circular holes. The area I shows a hole partially covered by graphene, area II is fully covered, and area III is fractured from indentation b) AFM image of one membrane. The solid blue line is a height profile along the dashed line. c) Schematic nanoindentation on suspended graphene membrane (after [279])

Liquid-phase AFM is a special case of the application of AFM in an aqueous environment, in which both the surface of a specimen and an AFM tip is immersed in liquid during scanning. An example from this AFM set-up is shown in **Fig. 3.12 (a)**. It features a cantilever that has a sharp probe tip at the end. The radius of the tip is in the nanometer scale and it is brought into proximity of a sample surface to scan its profile through mechanical contact force. The sample is placed on a piezoelectric scanner that facilitates precise movements of the sample in the micrometre scale. A laser is reflected over the top of the cantilever and reflected on a mirror into a photodiode. With this reflection approach, vertical (z) and horizontal (y) deflection signals can be measured.



**Fig. 3.12** (a) Schematic of AFM measurement in a liquid phase. Source: ref.[179] (b) AFM images of a graphene transistor surface with and without DNA strands adapted from [180].

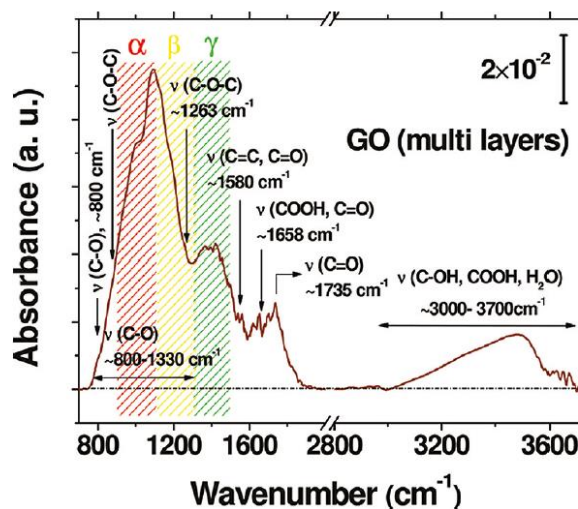
Due to its high resolution and signal-to-noise ratio (SNR), the AFM imaging technique has become one of the most helpful tools for studying biological materials. With this technique, three-dimensional topographical images, biomolecular structural formation, and thicknesses of samples in a solution can be observed and measured. A wide range of biological objects such as DNA and RNA [181], [182], membrane proteins [183] and cells [184] have been visualized and characterised.

### 3.5 Fourier Transform Infrared (FTIR)

FTIR is one of the most preferred methods of infrared spectroscopy. Its principle of operation can be explained as follows. In short, when infrared (IR) radiation is passed through a sample, some of the incident radiation is absorbed by the specimen, and some are transmitted so that the detector can detect the signal. The detected spectrum signal represents a molecular fingerprint of the sample as different chemical structures (molecules) produce specific spectral fingerprints. The principle of FTIR is based on the fact that most molecules absorb light in the infra-red spectrum. This absorption corresponds specifically to the bonds present in the molecule. The frequency range is shown as wave numbers, typically between 4000 and 600  $\text{cm}^{-1}$ . The subsequent spectrum originated from the natural vibration of the bonds at specific frequencies

indicating the presence of several chemical bonds and functional groups. Therefore, FTIR is predominantly beneficial for identifying organic molecules and compounds as the wide range of functional groups, side chains, and cross-links vibrate in the infra-red range of the electromagnetic spectrum.

For graphene oxide (GO)-related research, FTIR is an extensively used technique as GO contains several functional groups such as hydroxyl, carboxylic acid and epoxy. **Fig. 3.13** shows the transmitted infrared absorbance spectrum of multilayer GO at room temperature with various functional groups. For reduced-GO, the amount of these functional groups is lower. Acik et al (2011) used FTIR to observe the structural evolution of GO when reduced at a different temperature[185]. Their observations suggest that the reduction efficiency is related to the concentration of carbonyls at annealing temperatures of about 200 °C. The thermal reduction can form oxygen free radicals mainly at the edges of the sheet rather than on their basal plane.



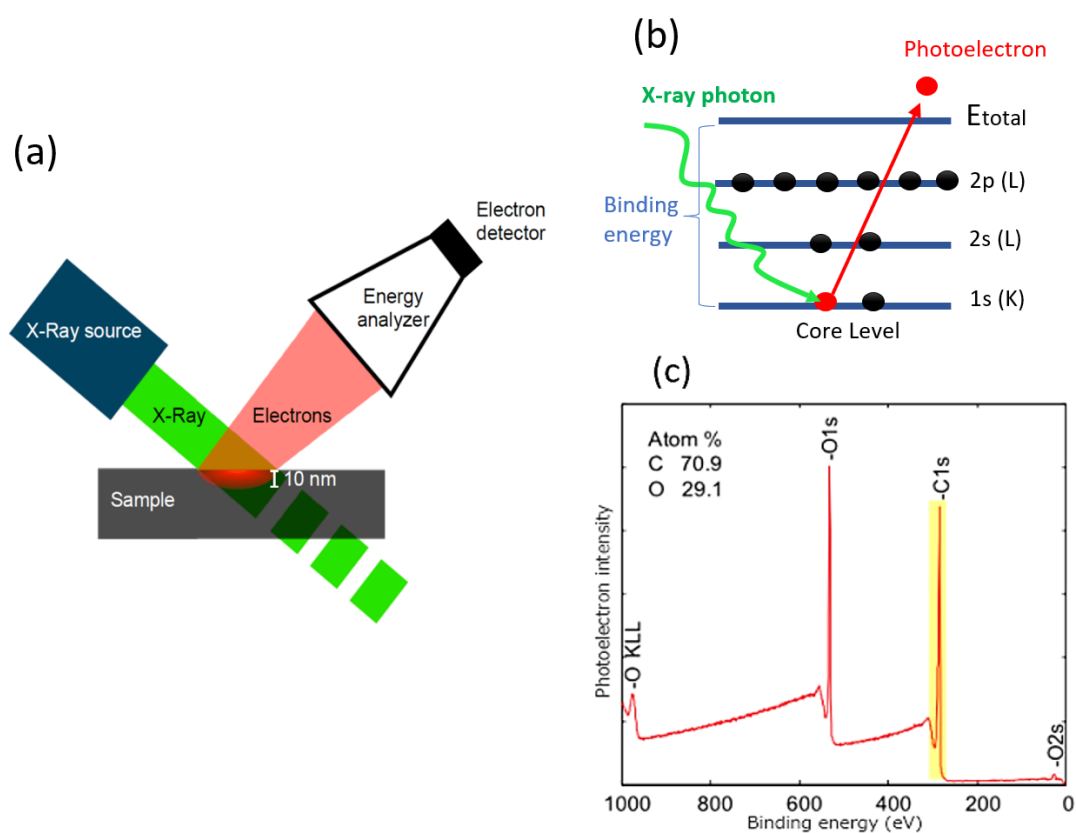
**Fig. 3.13** Transmission FTIR spectrum of multilayers GO at room temperature. Source: ref. [185]

### 3.6 X-ray Photoelectron Spectroscopy (XPS)

X-ray photoelectron spectroscopy (XPS) is a technique for analyzing a material's surface chemistry. It can measure the elemental composition and the chemical oxidation states of the elements in a sample [186]. This technique is based on photoemission spectroscopies in which photoelectron population spectra are probed after irradiating a



material surface with a beam of X-rays, **Fig. 3.14 (a)**. The average depth of analysis for an XPS measurement is approximately 10 nm. **Fig. 3.14 (b)** presents the mechanism of electron excitation. The X-ray photons from the X-ray source excite and remove electrons from core levels. The kinetic energy that drives the electron to escape the binding energy is determined from the photon energy minus the binding energy of the core electron and the work function of the spectrometer. By analysing the binding energy and intensity of a photoelectron peak, the elemental identity, chemical state, and quantity of a detected element can be determined, as seen in **Fig. 3.14(c)**.



**Fig. 3.14 (a)** Schematic of basic XPS set-up **(b)** X-ray photon, an excitation source of photoelectrons **(c)** XPS wide-scan result, the peaks indicate in elements containing in the sample.

The XPS technique is importantly used in the characterization of carbon-based systems[187]. The primary XPS energy level region of carbon is the 1s located at 285 eV. The most common chemical states, like C-C, C-O-C and O-C=O, are located at the binding energies of 284.8 eV, 286 eV and 288.5 eV, respectively. However, the shapes of XPS peaks can be varied and relatively broad due to the contribution of different factors, i.e., instrumental and thermal broadening and excited-state lifetime. Therefore, the analysis

of XPS spectra invariably involves fitting specific peaks to peak-shape functions such as Lorentzian, Gaussian Curves and the Voigt function, which combine both Lorentzian and Gaussian Curves[188], [189].

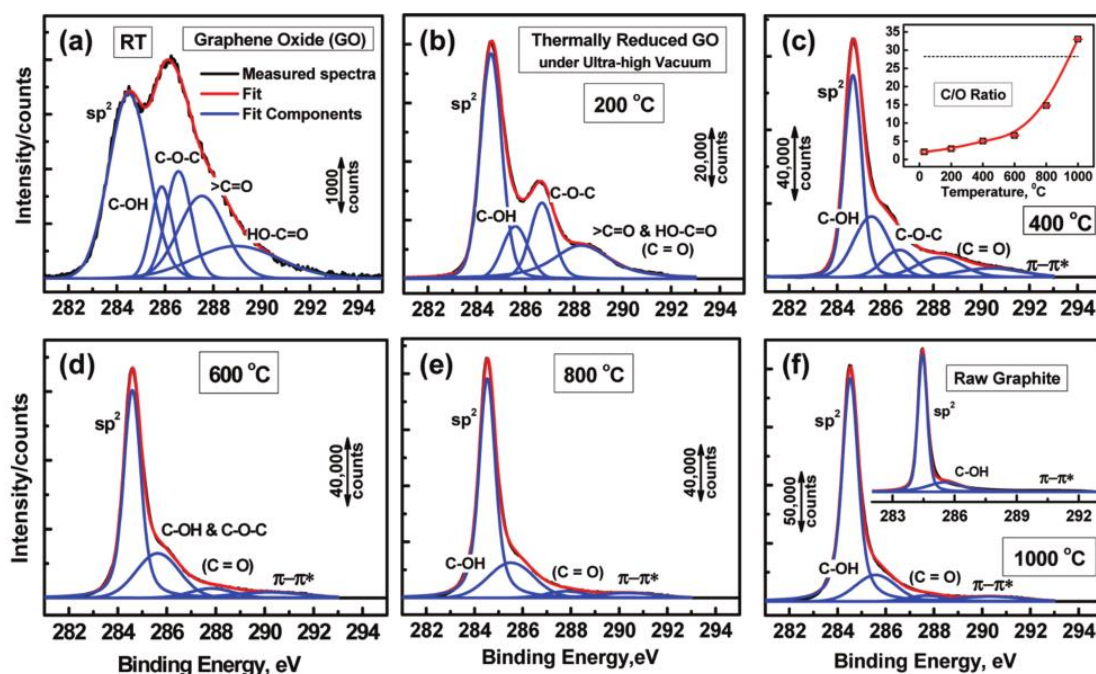
For graphene-family materials, the C1s line, especially in GO sp<sup>2</sup> carbon line, shows an asymmetric shape oriented towards higher energies[189]–[192] arising from the excitation of electron-hole pairs at low energy levels but appearing as higher binding energy levels events [189]. The C 1s spectrum can be fitted with different synthetic components that represent the signatures from each bond, e.g., sp<sup>2</sup> carbon, carbonyl, carboxyl, epoxy, etc. Another parameter for characterizing the degree of oxidation in GO is the sp<sup>2</sup> carbon fraction, estimated by dividing the area under the sp<sup>2</sup> peak by that of C 1s peak-area.

In general, the XPS spectrum of GO powder shows two broadened and overlapped peaks with its centres at around 284 and 286 eV that correspond to sp<sup>2</sup> carbon and oxidized carbon, respectively[8]. As the evolution of oxygen functional groups can be quantitatively and qualitatively analyzed from the fitting peaks, the reduction of GO can be evaluated using this technique [193]. Moreover, the C/O ratio changes with the reduction process of GO. After the reduction, the C 1s deconvolution also shows an increasing peak of C-C=C (sp<sup>2</sup> carbon) and C-C, C-H (sp<sup>3</sup> carbon) while C-OH (hydroxyl group) and C-O-C (epoxy group) decreases.

To exemplify this, **Fig. 3.15** displays high-resolution XPS spectra for the thermal deoxygenation of GO, reported by Ganguly et al.[193]. The evolution of the thermal reduction of GO with controlled temperatures ranging from 200 °C to 1000 °C under ultra-high vacuum is presented. The C1s peaks were fitted using Voigt functions with 80% Gaussian and 20% Lorentzian components. The component at 284.49 eV is attributed to sp<sup>2</sup> graphite. Other four broad components describe the overlapping curves with the peaks at 285.86 eV, 286.55 eV, 287.54 and 288.94 eV attributed to C atoms bonded to oxygen in hydroxyl (C-OH), epoxide group (C-O-C), carbonyl (C=O) and carboxyl groups (COOH or HO-C=O), respectively.

Nevertheless, adequate XPS spectra fitting and interpretation will also depend on many factors: e.g., sample type, quality, preparation, contamination level, substrate type. In

terms of its data processing - background type, a number of synthetic components and the fitting shapes may also affect the results. For a more comprehensive understanding of the materials, the XPS technique should be combined with other spectroscopic methods to characterize graphene, and its derivatives, like Raman and FTIR.



**Fig. 3.15** High-resolution C 1s XPS spectra (a) GO spectra (b)-(f) Deconvoluted peaks with increased temperature. The inset from (c) shows the C/O ratio as a function of the reduction temperature. Comparatively, the inset from (f) shows a reference XPS spectra for raw graphite. After [193]

### 3.7 Raman Spectroscopy

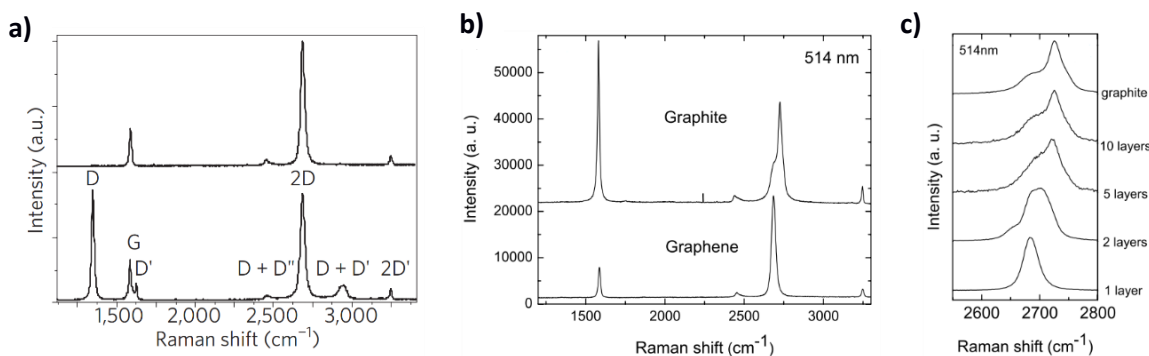
Raman spectroscopy is a spectroscopic technique that provides detailed information about the chemical structure, morphology, disorder level and crystallinity of materials. It relies upon the interaction between a monochromatic light source, typically a laser, and the chemical bonds from a material creating inelastic scattering of photons, known as Raman scattering. In general, the scattered light is very weak (about 0.0000001%) and is comprised of different wavelengths depending on the chemical structure of the analyte. A specific molecular bond, the atomic structure and electronic properties of a material can be identified from the Raman spectra.

Specifically, the Raman technique is one of the most common techniques for the characterization of disordered and amorphous carbons, fullerenes, nanotubes, diamonds and carbon chains [194]. It is particularly beneficial for pristine graphene as the absence of a band-gap makes all wavelengths of incident radiation resonant; thus, the Raman spectrum, including peak shift and shapes, can be significantly distinctive [195]. It is widely used to determine the number and orientation of layers, the effects of external perturbations such as electric and magnetic fields, doping and defects on the lattice.

The Raman spectrum of graphite and multilayer graphene consists of two fundamental peaks, known as the D and the G peak and overtone peaks like the 2D peak, which is the D-peak overtone, as seen in **Fig. 3.16(a)** [196]. The three most prominent Raman peaks for carbon materials are the following.

1. The G peak at  $1580\text{ cm}^{-1}$
2. The D peak at  $1350\text{ cm}^{-1}$
3. The 2D peak at  $2700\text{ cm}^{-1}$

The G peak is due to the high-frequency  $E_{2g}$  phonon [197] originating from in-plane vibrations of the  $sp^2$  bonded carbon atoms. The 2D and 2D' peaks are the D-peak and the D' peak harmonic, respectively. The 2D peak is a secondary D peak and has pronounced the largest intensity in single-layer graphene. The 2D band is also an indicator of the number of graphene layers if it is a sharp peak. It broadens into multiple peaks. The reduction in its intensity corresponds to multi-layer graphene.



**Fig. 3.16 a)** Raman spectra of pristine (top) and defected (bottom) graphene. The main peaks are labelled **b)** Comparison of Raman spectra at 514 nm for bulk graphite and graphene. They are scaled to have a similar height of the 2D peak at 700 cm<sup>-1</sup> **(c)** Evolution of the spectra at 514 nm with the number of layers. After [196]

**Fig. 3.16 (b)** compares the 514 nm Raman spectra of graphene and bulk graphite. There is no D peak observed in the centre of graphene layers proving the absence of significant defects. The most intense features are the G peak at 1580 cm<sup>-1</sup> and a 2D band at 2700 cm<sup>-1</sup>, since it is the second most prominent peak always found in graphite samples [198].

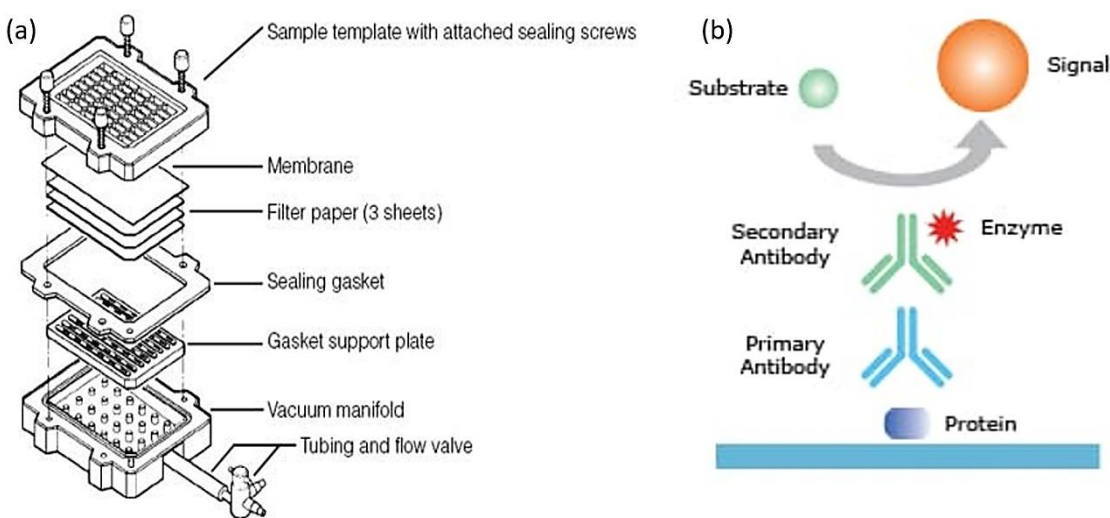
**Fig. 3.16 (c)** displays the evolution of the 2D band as a function of layers. The peak shift can indicate the number of the graphene layers; the higher value of the shift, the higher the number of layers. Thus, a bilayer has a much broader and up-shifted 2D band concerning graphene layers. This band is also significantly different from bulk graphite; however, with ten layers of graphene, the shape and the position of the 2D band is similar to graphite.

In contrast, only the D peak and the G peak are the characteristic peaks of graphene oxide, as GO has a defective lattice due to the presence of oxygen-containing groups. As a result, the ratio between sp<sup>2</sup> and sp<sup>3</sup> hybridization by means of the D and G intensities is commonly used to characterize the flakes in a GO dispersion, expressed as I<sub>D</sub>/I<sub>G</sub>. It is often used for determining the level of stacking and disorder [177], [199] or to characterize the level of reduction in reduced GO [200]. The oxidation conditions for the production of GO will induce changes in the integrity of the aromatic structure of the resulting material reflecting different values of the I<sub>D</sub>/I<sub>G</sub> ratio.

### 3.8 Dot blot

A dot blot (or slot blot) is a biomolecular technique used to detect proteins of interest or to prove the specific binding of pair proteins. It simplifies the western blot method since the detected proteins are not required to be first separated by gel electrophoresis or chromatography. Instead, the sample is applied directly on a membrane in a single spot and then the blotting procedure is conducted. As chromatography and the complex gel-based blotting are eliminated, the technique offers significant savings in time and is easier for larger volumes or quantitative measurements. However, dot-blot systems cannot provide molecular weight information due to no process of gel electrophoresis to separate biological molecules by size. As a result of this limitation, dot blots can be used only if the specificity of the antibody is already known.

Dot blot is conventionally performed on a nitrocellulose or PVDF membrane with a dot blot apparatus that give uniform-size dots, as shown in **Fig. 3.17 (a)**. The series of dots allows the comparison of the intensity of staining. A general dot blot protocol involves spotting 1–2 microliters of samples onto the membrane and air drying it. First, the membrane is sequentially incubated in blocking buffer to prevent non-specific binding, then a primary antibody followed by a detection antibody or a primary antibody conjugated to a detection molecule. After antibody binding, the membrane is incubated with a chemiluminescent substrate and finally imaged.



**Fig. 3.17 (a)** apparatus for dot blot. Source: ref. [201] **(b)** Construction of an indirect immunoassay used for the dot blot test in this research

## CHAPTER 4. General Methodologies

Contents:

4.1 Overall

4.2 GO preparation

4.3 Graphene-coated QCM chips preparation

4.4 General protocol for QCM-D measurement

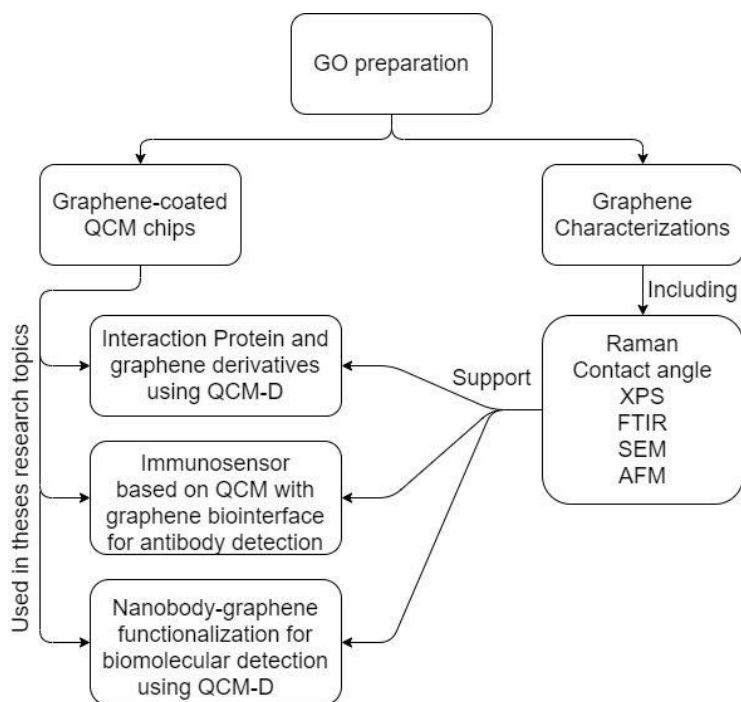
4.5 Material characterisations:

FTIR, SEM, contact angle, AFM, XPS, Raman and Dot blot

4.6 The preparation and handling of biological samples

## 4.1 Overall

The experimental process to accomplish all studies in this thesis is presented in **Fig. 4.1**. It started with graphene oxide (GO) preparation. All the chemical modifications on graphene were performed on a single batch made at the beginning of the present PhD research. Subsequent samples for all experiments were taken from this original modified graphene batch. GO dispersion was prepared by following the modified Hummers method [202]. The stock solution of GO with a final concentration of 10 mg/mL was prepared and saved for use in all graphene-based QCM experiments and its characterisation. Graphene-coated QCM chips were used in three main research topics, including 1) Study of the interaction between proteins and graphene derivatives using the QCM-D technique, 2) Immunosensors based on the QCM technique with a graphene biointerface for antibody detection, and 3) Nanobody-graphene functionalisation for biomolecular detection. The results from other material characterisation techniques, including Raman, wetting contact angle (WCA), XPS, FTIR, SEM and AFM, supported the three studies. The types of graphene samples employed in each study were chemically different; however, they were all prepared using the same GO stock solution for coating a thin layer on QCM sensors by following the same spin-coating conditions.



**Fig. 4.1** Overall process of experimental work in this thesis



The samples coated with graphene derivatives, including rGO and partially reduced GO (PrGO) (i.e. with different degrees of reduction) were made through a thermal reduction of the initial GO coating under controlled time and temperature conditions. More details on the preparation of materials and individual experimental procedures are explained in later sections of this chapter.

## 4.2 GO preparation

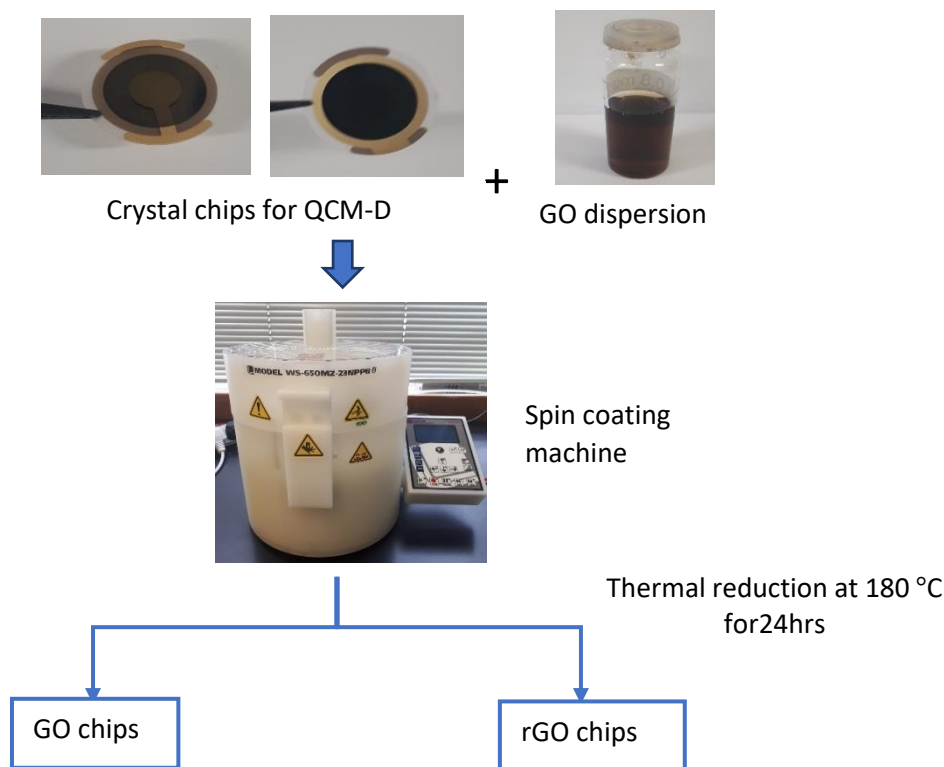
GO dispersion was prepared by the modified Hummers method [202], followed by exfoliation and purification. Initially, graphite flakes of 50 mesh (1g) and  $\text{NaNO}_3$  (0.9 g) were mixed in concentrated  $\text{H}_2\text{SO}_4$  (35 ml) and left overnight to intercalate. Then, the mixture was cooled down in an ice bath before being slowly added with 4.5 g  $\text{KMnO}_4$  during stirring. After that, the mixture was left for five days at room temperature to allow graphitic oxidation. As a result, the brown slurry was gotten and diluted by slowly adding 5%  $\text{H}_2\text{SO}_4$  solution (100 ml). The final dispersion was again diluted with a 100 ml mixture of  $\text{H}_2\text{SO}_4$  and  $\text{H}_2\text{O}_2$  with a concentration ratio of 3% and 0.5%, respectively. The homogenisation and complete exfoliation of graphite oxide was carried out using a vertical stirrer at a low speed for  $\sim 1$ h. The final graphite oxide dispersion was washed repeatedly with dilute  $\text{H}_2\text{SO}_4$ , then DI water until the pH got close to neutral.

To be used in the experiment in this research, the stock solution of GO (10 mg/mL) was diluted to a concentration of 0.8 mg/mL, which this the effective concentration for creating a thin film on the QCM chips.

## 4.3 Graphene-coated QCM chips preparation

Quartz crystal sensors with the gold surface (QX-301) were purchased from Biolin Scientific. To prepare the sensors for studying the adsorption of biomolecules on graphene derivatives surfaces, the QCM chips were clean, following the instruction based on protocol provided by QSense. Then, the chips were coated with GO using a spin coating to get the GO chips and get rGO chips. The GO chips were thermally reduced to be rGO at controllable conditions, specific for each study. The overall process can be seen in **Fig. 4.2**.

The procedure for cleaning and coating the QCM sensors is described below. The graphene-derivatives coated chips were used in the QCM-D measurements. This cleaning process was carried out inside a fumes hood, wearing adequate PPE.



**Fig. 4.2** Processes for preparing GO and rGO sensors for QCM-D measurement

#### 4.3.1 Cleaning protocol for Au QCM chips

The cleaning process is described as follows:

1. Wash the crystals by soaking them in a cleaning solution including 10% Decon 90 or 2% SDS and/or 2% Hellmanex to remove contamination, then acetone to remove graphene dirt and isopropanol, sonicating for 10-20 mins each step, use DI water between each solution to rinse well the surface.
2. Treat the crystals under UV/ozone atmosphere for 10 minutes or 80% power of oxygen plasma for 2 mins
3. Wash with the 75 °C cleaning solution for gold ( $\text{H}_2\text{O}_2$ :  $\text{NH}_3$ : DI water= 1:1:5) 5 mins.
4. Rinse with MilliQ water, keep the sensor surface wet after ammonium-peroxide immersion until rinsing
6. Dry with nitrogen gas and save them in a clean crystal box.

#### 4.3.2 Coating the sensors with GO

GO dilution (0.8 mg/ml) was pipetted on clean QCM crystals making sure that the working electrode area was fully covered. The solution was left to settle for 30 seconds before starting the spin-coating machine (Laurell technologies Corp. WS-650MZ-23NPPB). The coating parameters used are: speed = 3500 rpm, acceleration = 350 rpm/sec, time = 2 mins. With these parameters, a uniform and thin GO film were formed on the Au substrates.

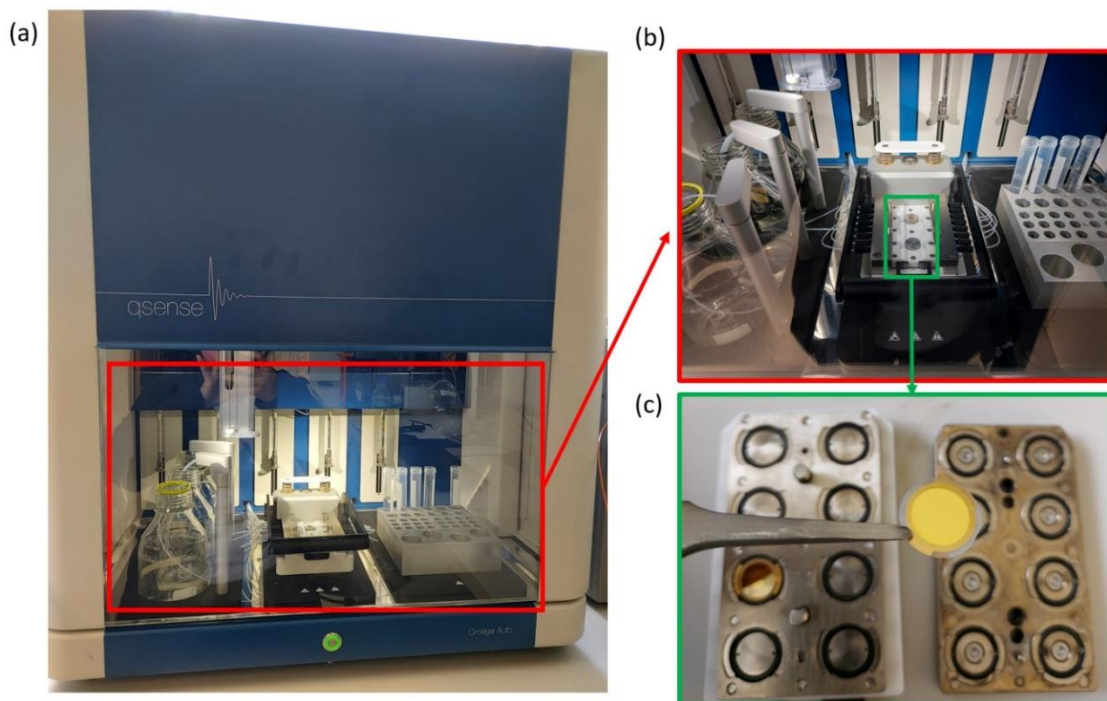
#### 4.3.3 Thermal reduction of GO-coated chips

To obtain rGO chips, freshly GO-coated QCM chips were thermally reduced in a vacuum oven at controlled temperature and time conditions depending on the objectives of the experiment. Two temperature conditions were used, including 80 °C and 180 °C. More specific details about rGO sample preparation can be found in the experimental section of each study.

#### 4.4 A general protocol for QCM-D measurement

The QCM-D measurements for protein adsorption on Au and Au-coated with graphene were carried out using a QSense Omega Auto (Biolin Scientific AB, Sweden) system. The system consists of eight sensing ports which are automatically fed through customized scripts. Before any experimental routine, the ports and sensors holder must be primed using maintenance sensors following the protocol described below. The temperature of the system is set at 20°C to avoid any effects of thermal drift on the response. Then, the maintenance chips are swapped for the sensors for the final measurements loading them into the sensor holder. Before starting the actual measurement, the sensors need to be primed by continuously injecting PBS buffer at a constant flow rate until a stable baseline is obtained. The priming process is important for removing trapped bubbles, checking the sensor's quality, and obtaining a stable baseline for reliable results. Once stability is reached, the programmed measurement can be started. A flow rate of 10 µl/min was used for every measurement. The 3<sup>rd</sup>, 5<sup>th</sup>, 7<sup>th</sup>, 9<sup>th</sup> and 13<sup>th</sup> harmonics are measured and acquired. In theory, there are also resonances at even multiples of the Eigen frequency (the fundamental tone), however, they can only be excited mechanically without showing a response.

After the measurement script is completed, it is suggested to run a washing routine to clean the sensors, syringes and tubing using diluted surfactants like Hellmanex and/or SDS and finally rinsed with MilliQ water. It is recommended to leave the chamber clean and dry before subsequent experiments to avoid contamination.



**Fig. 4.3** (a) QSense Omega Auto (Biolin Scientific®) system (b) eight sensing chip holders and ports

## 4.5 Material characterisations

### 4.5.1 FTIR

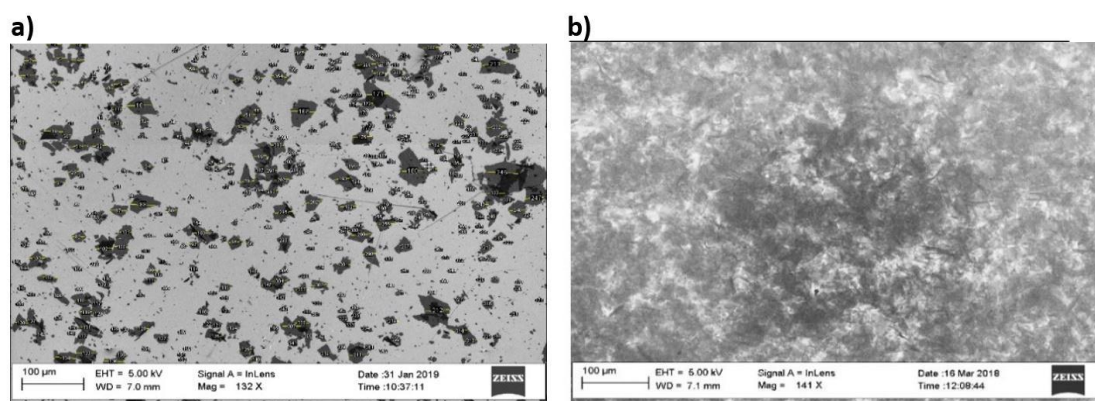
FTIR technique was used to investigate functional groups containing graphene derivatives such as hydroxyl, carboxylic acid and epoxy. The results can support the proof of reduction from GO to rGO. Bulk FTIR spectra were obtained by using an ATR FTIR spectrometer (Nicolet iS50 spectrometer, Thermo Scientific) with a germanium crystal. For each spectrum ( $700\text{-}4000\text{ cm}^{-1}$ ), 64 co-averages has been collected, with a resolution of  $4\text{ cm}^{-1}$ .

#### 4.5.2 SEM

SEM was used to observe the surface morphology of graphene derivatives coated on the Au surface. It was performed on a SEM Zeiss Ultra setup with secondary electron imaging mode using an accelerating voltage of 5 kV at a working distance of 5-8 mm.

Typically, to observe the flake size and size distribution of GO, the sample is imaged with magnification scales ranging from 130x to 140x, see the example in **Fig 4.4(a)**. The sample was prepared by spin coating the GO dispersion (0.2 mg/ml) on a small Si wafer (1x1 cm) using a speed of 1800 rpm, an acceleration of 300 rpm/min during 2 mins. The Si wafer should be cleaned and treated with oxygen plasma 100 W for 5 min. The size distribution was computed using the ImageJ software.

The SEM images of spin-coated GO on QCM chips were taken with a magnification ranging from 90x to 145x (**Fig 4.4(b)**) to observe the coverage and uniformity of the coating on the surface. A higher magnification scale of approximately 900x was used for detailed observation of the graphene flakes and the overlapped distribution as a result of the coating technique.



**Fig. 4.4** Scanning Electron Microscopy images of **(a)** GO on SiO<sub>2</sub> with the magnification of 132x showing separated flake for determining flake size **(b)** scans of GO coating on gold substrates with a magnification of 141x.

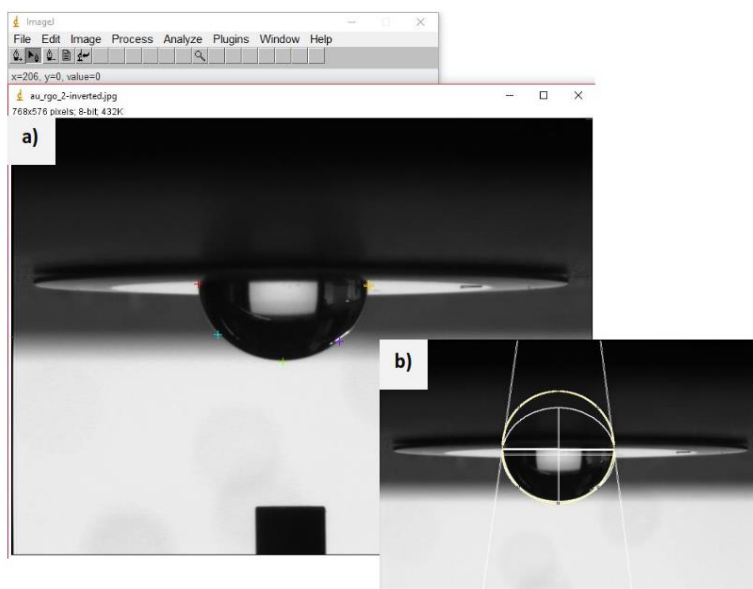
#### 4.5.3 Contact angle

The degree of reduction was also characterised by measuring the wetting contact angle measurement of sessile drops of DI water using the Kruss DSA100 system. The resolution

of the system's camera is  $640 \times 480$  px. All graphene derivative samples for contact angle measurement were prepared by spin coating on Au and  $\text{SiO}_2$  QCM chips following the coating procedure described in section 4.3.2. A manually- controlled syringe was used to cast sessile drops ( $5 \mu\text{L}$ ) of DI water over the substrates of interest.

To successfully measure the contact angle, the image must clearly show a sharp dome-shaped water droplet. The clarity of the image can be adjusted in terms of its magnification, contrast, light intensity and depth of field. The motorized stage was adjusted slightly tilting it (when needed) to align the baseline. If the stage is tilted too far towards the camera, the viewpoint of the droplet could be set too high and the angle measurement will be less accurate.

Manual circle-ellipse fittings were computed using a software plugin for ImageJ developed and published by Marco Brugnara [203]. The software works on pre-captured high contrast images of sessile drops which are processed by first inverting the image upside down, namely, the water droplet must be pending from the top of the image, then two points on a droplet image were selected to be the baseline, and added three points on the curvature are chosen to complete the calculation.



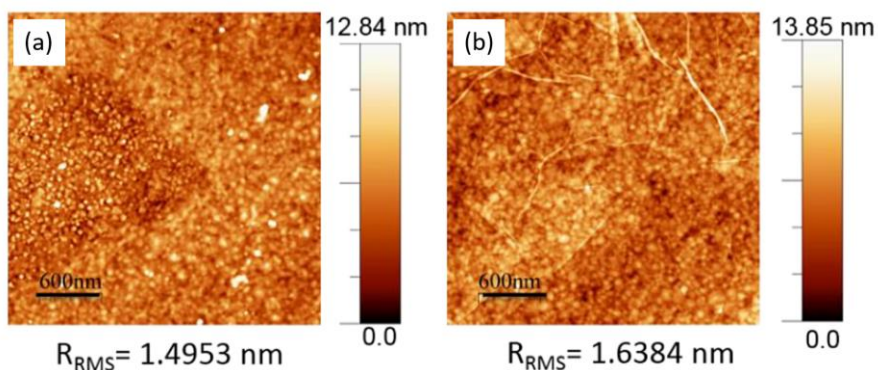
**Fig. 4.5** Contact angle plugin interface (a) Selection of 2 baseline points and 3 points on the curvature of the droplet edge (b) Circle/ ellipse fitting to determine contact angle

#### 4.5.4 AFM

The topography of graphene derivatives coatings was characterized using the atomic force microscopy (AFM) imaging technique. AFM images of the GO- and rGO-coated substrates was performed to measure the thickness of the thin film, to obtain graphene flake characteristics (e.g. flake thickness and thus film height, lateral size, etc.) and to investigate surface roughness. The tips used for the surface scanning were aluminium coated silicon FastScan-A tips (Bruker Alpha) with a spring constant of 18 N/m. The AFM measurement was operated in contact mode on air using a Bruker Dimension FastScan probe microscope. In contact mode, the scan rate decreases as the scan size are increases. Scan rates of 0.5–1.0 Hz were used for large scans on samples with tall features. High scan rates help reduce drift making it suitable for flat samples with small scan sizes. A scanning area of  $10 \times 10 \mu\text{m}^2$  was selected to cover the flake size and overlap.

To measure the thickness of GO flakes, the sample was prepared by spin coating the GO dispersion (0.2 mg/ml) on a Si wafer using a speed of 2000 rpm, an acceleration of 350 rpm/min for 2 mins. Under such coating conditions, GO flakes are separated and distributed over the Si wafer, as confirmed via optical microscopy.

The height profiles and surface roughness was directly performed on GO- and rGO-coated Au QCM crystals. The thickness of the coating was measured by making a gentle scratch on the GO film without damaging the QCM substrate using a clean plastic tweezer. The exposed substrate was used as a height reference by scanning the AFM tip over that specific area. The analysis of AFM images including thickness and roughness measurements was performed using Gwyddion software. The surface roughness is interpreted in terms of the root-mean-square roughness ( $R_{\text{RMS}}$ ) which is an average of the height difference of a surface's microscopic peaks and valleys. However, the roughness of the graphene coating is significantly affected by the roughness of the gold substrate as the graphene layer is extremely thin compared to the size of the sphere-shaped gold particles from the working electrode of the QCM chips



**Fig. 4.6** AFM mappings and Root-mean-square roughness ( $R_{RMS}$ ) of **a)** bare Au QCM chip, **b)** GO coating on Au chip. The height and roughness of gold nanoparticle highly contribute to the roughness of the graphene coating. Source: ref.[6].

#### 4.5.5 XPS

The X-ray photoelectron spectroscopy XPS technique is used to characterize a surface's elemental composition and the chemical oxidation states of the elements in a sample. The XPS samples were prepared by drop-casting the dispersion of GO on a clean Si/SiO<sub>2</sub> substrate and drying it at room temperature in a vacuum oven to achieve a film thickness of not less than 10 nm. The GO samples were then thermally reduced at controlled conditions to achieve different levels of hydrophobicity according to their contact angle.

XPS data were collected on a SPECS custom-built system composed of a Phobios 150 hemispherical electron analyser with the 1D detector. The X-ray source is a microfocus monochromate Al K-alpha (1486.6 eV) source. All spectra were collected with a pass energy of 20 eV. The combined ultimate resolution as measured from Ag 3D is 0.5 eV with an X-ray source and 20 eV pass. The XPS data processing was done using CasaXPS software (version 2.3.16 PR 1.6). The calibration of the C1 spectrum was performed using the sp<sup>3</sup> carbon (C-C, C-H) as a reference at 284.8 eV peak position, and the background type used was spline Tougaard. The C1s spectrum fitting was performed using seven synthetic components ascribed to different chemical species and a satellite peak. The sp<sup>2</sup> C component is represented by an asymmetric line shape of A(a,b,n)GL(p) type (CasaXPS version 2.3.16 Manual) where A(0.3,0.8,40)GL(45); the other synthetic components are represented by a symmetric line shape of GL(p) type where GL(30)



(Gaussian/Lorentzian mix with 30% Lorentzian). The constraints applied were the FWHM constrain (0.9-1.1) and the position constraints (between max  $\pm 1$  eV to min  $\pm 0.1$  eV). XPS C 1s region was fitted with the synthetic components to minimise the total square error fit (0.91) and to match with the reported publications [189], [204], [205].

#### 4.5.6 Raman

Raman spectroscopy was used for the characterization of disordered and amorphous GO and rGO. Raman spectra were taken on a Renishaw Raman system equipped with a Leica microscope and a CCD detector. Raman spectrum was recorded using 532 nm laser line, Cobolt Samba™ continuous-wave diode-pumped solid-state laser, 20 mW. The laser power was kept below ten  $\mu\text{W}$  to avoid thermal degradation of the samples. The relative intensity ratio ( $I_D/I_G$ ) was measured from the averaged acquired spectra, ten spectra per sample. Two main peaks, including graphitic (G) and defect (D), occur at  $\sim 1580\text{ cm}^{-1}$  and  $\sim 1350\text{ cm}^{-1}$ , respectively.

#### 4.5.7 Dot Blot Approach

Dot blot was carried out for testing the binding function of an antibody toward its antigen. In this thesis, this technique was used for confirmation of the specific binding of two pairs of immunoprotein—first, BSA and anti-BSA antibody and second, NC3 and anti-PLA2R antibody.

The tests were carried out by blotting varied concentrations of the antigen protein and its denatured samples by boiling protein with SDS. If the protein is denatured, the antibody will not bind specifically with the molecules resulting in no fluorescent signal.

The protocol used in this research is described as follows

1. Prepare a nitrocellulose membrane, cut it into the size that fits in the dot blot apparatus. Draw a grid by pencil to indicate the blotting regions.
2. Spot 50  $\mu\text{L}$  of protein samples onto a nitrocellulose membrane and let it dry in the air.
3. Block non-specific binding by incubating the membrane in Odyssey blocking buffer for one hour
4. Incubate the membrane with a dilution of the primary antibody in PBS with tween 0.05% (PBS-T), ratio 1:2000, for one hour at room temperature.

5. Wash three times with TBS-T (3 x 5 min).
6. Incubate with secondary antibody conjugated with a chemiluminescent anti-rabbit (for anti-BSA), anti-mouse (for anti-PLA2R) diluted with PBS-T (ratio 1:10000), for one hour at room temperature.
7. Rinse the membrane with MilliQ water and keep it in a dark place
8. Take fluorescent imaging using Odyssey® CLx Imaging System from LI-COR Biosciences with a wavelength of 700 nm.
9. Compare the signal from the denatured and non-denatured samples. There should be a minimal fluorescent signal in denatured samples.

#### 4.6 The preparation and handling of biological samples

When handling biological samples, universal safety precautions should always be aware. Appropriate personal protective items including gloves, lab coats should be worn. Biohazard specimens must be treated with respect and appropriate precautions. They should not be handled with bare hands. In this research, no specimen with potential pathogens has been used.

##### **Preparation of protein samples**

Protein samples including BSA, lysozyme and IgG have been used in this research. Their stock solutions were prepared by dissolving the crystalline protein in PBS buffer pH 7.4 to obtain a concentration of 10 mg/ml. Aliquots of stock solution (10 µl) were kept in the freezer at -20 °C.

The stock solution of animal serum from calf was aliquoted at 50 µl and kept in the freezer -20 °C. When using the sample, the aliquots can then be thawed and diluted to any desired volume.

##### **Specific antibody handling**

Antibodies used in this research include anti-BSA antibody from rabbits and anti-PLA2R produced in mice. All of them had already been produced and kept in form of stock solution in a buffer. In some cases stabilizer, like glycerol, was used. The stock solution was sealed with parafilm and preserved in the freezer at a temperature of -20 °C. To use

the sample, the stock solution must be slowly thawed in an icebox then diluted to obtain the required concentration.

### **Nanobody handling**

The nanobodies used in this project were previously produced by a member of our research group. Their stock solutions were aliquoted and preserved in -80 °C freezer. The aliquots were thawed inside an icebox and then diluted to the required concentration. The remaining stock in aliquot tubes should not be refrozen for reuse.

### **Human Serum handling**

Human serum samples used in the research were provided by the National Institute for Health Research (NIHR). The serum specimens were collected from the patients across the Northwest region of the UK involved in the PRISM trial [206]. They were already aliquoted to 50 µl in vials and kept in the freezer with temperature -20 °C. To prepare the final sample, the sera were thawed at room temperature then diluted to obtain the required dilution.

## CHAPTER 5. Publication 1

Protein interactions and conformations on graphene-based materials mapped using quartz-crystal microbalance with dissipation monitoring (QCM-D)

Hampitak, Piramon, et al. "Protein interactions and conformations on graphene-based materials mapped using a quartz-crystal microbalance with dissipation monitoring (QCM-D)." *Carbon* 165 (2020): 317-327.

Available at <https://doi.org/10.1016/j.carbon.2020.04.093>

### **Authors contributions:**

**Piramon Hampitak** prepared the QCM sensors and carried out all the QCM-D experiments. She prepared all samples for material characterization including samples for SEM, Raman, contact angle, AFM and XPS. She analysed and interpreted SEM, Raman, XPS and AFM results. She carried out contact angle measurement and dot blot and performed the analysis.

P. Hampitak and D. Melendrez jointly carried out Raman spectroscopy.

D. Melendrez and T. Jowitt supervise on QCM-D analysis and interpretation.

M. Iliut prepared and purified GO dispersions.

M. Fresquet provided chemicals for performing dot blot and supervised how to experiment.

N. Parsons carried out SEM imaging.

B. Spencer performed XPS measurement.

T. Jowitt and A. Vijayaraghavan conceived the study. P. Hampitak, D. Melendrez, T. Jowitt and A. Vijayaraghavan designed the experiments. T. Jowitt, A. Vijayaraghavan, D. Melendrez and M. Iliut helped P. Hampitak in the writing of the manuscript. All authors read and approved the final manuscript.

## **Protein interactions and conformations on graphene-based materials mapped using quartz-crystal microbalance with dissipation monitoring (QCM-D)**

Piramon Hampitak<sup>1</sup>, Daniel Melendrez<sup>1</sup>, Maria Iliut<sup>1</sup>, Maryline Fresquet<sup>2</sup>, Natalie Parsons<sup>1</sup>, Ben Spencer<sup>1</sup>, Thomas Jowitt<sup>2</sup>, and Aravind Vijayaraghavan<sup>1,\*</sup>

<sup>1</sup>*Department of Materials and National Graphene Institute, Faculty of Science and Engineering, The University of Manchester, Oxford Road, Manchester M13 9PL, UK.*

<sup>2</sup>*School of Biological Sciences, Faculty of Biology Medicine and Health, The University of Manchester, Oxford Road, Manchester M13 9PL, UK.*

### **Abstract**

Graphene-based materials have shown significant potential for biomedical applications including biosensors, cell scaffolds and drug delivery. However, the interaction of complex biomacromolecules like proteins with graphene and its derivatives, graphene oxide (GO) and reduced (r)GO, remains poorly understood. Here, we demonstrate that the quartz-crystal microbalance with dissipation monitoring (QCM-D) technique can be used to systematically study the interaction dynamics of a typical protein, bovine serum albumin (BSA), with graphene materials of varying degrees of functionalisation. We find significant differences in molecular orientation and conformation, mass adsorption and antibody binding function of BSA on different graphene surfaces, determined by both the population of functional groups of GO and the protein concentration. The dominant forces during the adsorption of biomolecules onto GO and rGO are shown to be hydrophilic and hydrophobic interactions, respectively. The GO surface yielded higher BSA adsorption than both rGO and control standard gold electrodes due to the high density of functional groups. The binding function of adsorbed BSA was investigated through the interaction with its anti-BSA antibody counterpart. BSA on GO can retain its binding sites while, in contrast, a denatured ad-layer of BSA could form on the rGO followed by further binding of active BSA molecules, depending on the concentration of the protein. Intermediate conformations are observed for partially-reduced GO. These results also suggest that QCM-D is a viable readout technique for graphene-based biosensors. This QCM-D approach could be further extended to study the interaction of a host of biomolecules and their assemblies, including whole cells, with 2-dimensional materials.

**Keywords** graphene, graphene oxide, protein, BSA, QCM-D

## Introduction

An understanding of the interaction of complex biomolecules with nanomaterial surfaces underlies the biocompatibility and potential biomedical applications of new nanomaterials. The interaction of proteins with nanomaterials can be exploited to develop implants [9], biosensors [10], and scaffolds for tissue engineering and regenerative medicine [11], [72]. In particular, the adsorption affinity of the protein to the nanomaterial and its conformation and antibody binding function in the adsorbed state determines the feasibility of these applications [207].

Recent studies suggest that graphene-based materials are promising candidates for the development of medical implants, drug delivery and biosensors [65], [72], [113], [208], [209] due to their excellent mechanical properties [2], [66], biocompatibility [210], high specific surface area [2], and ease of functionalization [211]. Graphene oxide (GO), a derivative of graphene with oxygen-containing functional groups, is significant for these applications due to its long-term stability in water-based formulations. On the other hand, the extensive covalent functionalisation in GO renders it an electrical insulator limiting its applicability in electronic devices like field-effect transistors (FETs) for biosensor applications. To partially recover the conductivity of graphene, such oxygen-containing functional groups in GO could be removed by thermal or chemical treatment to form reduced (r) GO, which also makes it significantly hydrophobic.

Graphene-based materials need to be functionalised with specific receptor biomolecules in order to selectively detect their binding counterparts [13], [113], [212]. On the other hand, protein adsorption on the graphene surface could deteriorate the sensing performance by blocking adsorption sites, or narrowing the membrane pores that lower the efficiency of hemofiltration and haemodialysis [13]. The success of such applications significantly depends on biological interactions at interfaces between proteins, like blood plasma protein, and graphene substrates [212]. In mammalian systems, serum albumins are the most abundant proteins in blood plasma, hence among the first proteins to be adsorbed onto substrates. Moreover, they act as carrier proteins for many substances such as fatty acids, hormones and drugs [113]. The structural changes of this type of proteins could affect their binding functions and stability.

Consequently, albumins have been used as model proteins for studying protein-substrate affinity [15]. Bovine serum albumin (BSA) was selected for this study as a low-cost human-like serum albumin. Monomeric BSA is a globular protein with a molecular weight (MW) of 66.430 kDa, based on the amino acid sequence. A BSA molecule may adopt the approximate shape of an elongated ellipsoid with given dimensions of 4 nm x 4 nm x 14 nm in an aqueous medium [101]–[103]. Several publications have reported the use of this model with a range of orientations between two orthogonal extremes: side-on and end-on for the protein adsorption on solid surfaces [106]–[109] (**Fig. 5.1**).

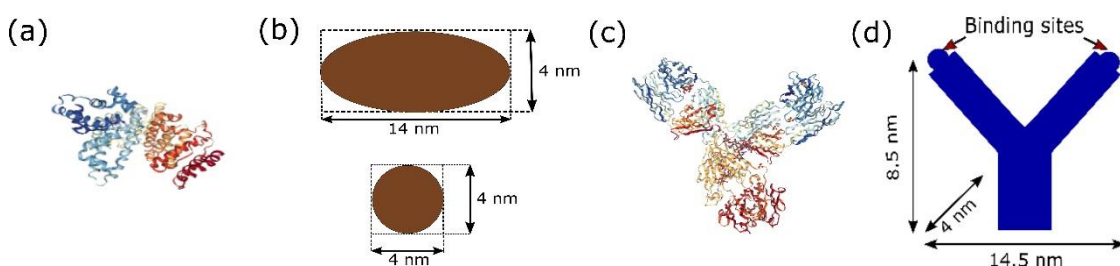
Protein adsorption on a surface is strongly influenced by the polar nature of the scaffold material since the amino acids contained in proteins contain both hydrophilic and hydrophobic moieties. Graphene is known to be a hydrophobic material [213], [214], whereas GO contains nanoscale hydrophilic and hydrophobic domains[215], overall exhibiting a hydrophilic nature[78]. The basal plane of graphene can promote protein adsorption by  $\pi$ – $\pi$  stacking and hydrophobic interaction, while on the GO surface hydrogen bonding and other electrostatic interactions as well as  $\pi$ – $\pi$  stacking could assist the immobilization of proteins [216]. The complex structure of GO, rGO and various intermediate degrees of functionalisation necessitate that the interaction of any biomacromolecule with graphene should be mapped across this range of materials as well as a range of molecule concentrations to understand the conformation and interaction dynamics, prior to any relevant applications of the system. In a recent theoretical study on the adsorption behaviour of BSA on bilayer graphene, it was reported that BSA can adsorb on graphene through  $\pi$ – $\pi$  stacking and the protein can preserve the structural properties of the majority of its binding sites [113]. Seredych *et al.* presented an experimental evaluation of the adsorption properties of expanded graphite with different functional groups and graphene nanoplatelets towards BSA using UV absorbance [17]. They found that protein molecules effectively adsorb to the expanded graphite through hydrophobic interaction, while the incorporation of -O or -N functional groups promote specific binding of protein molecules to the surface and improve the adsorption capacity. However, adsorption dynamics which can reveal the mechanism of the adsorption have not been assessed due to the limitation of the technique. Sengupta *et al.* reported that the formation of protein corona is sensitive to

the defects of carbon nanomaterials (CNMs), like GO, graphene, carbon nanotube, and is accompanied by both charge-transfer and protein unfolding. Both experimental and computational methods including photoluminescence (PL), infrared spectroscopy (IR), electrochemistry, and molecular dynamics simulations were used to assess the adsorption [18]. Nevertheless, the effect of protein concentration on adsorption has been overlooked. These aforementioned experimental techniques can only quantify the mass adsorption of protein at the endpoint while assessments of qualitative information including dynamics and structural properties of the adsorbed protein are beyond their competence. Furthermore, in the studies to date, the adsorption of BSA across the tuneable range of functionalisation between the graphene and GO extremes has not been considered.

Here, we describe how graphene-based sensing chips can be used in a quartz-crystal microbalance with dissipation monitoring (QCM-D) to elucidate the interaction dynamics of proteins, in this case, BSA on graphene with varying degrees of functionalisation. QCM-D is a real-time monitoring system based on the piezoelectric properties of AT-cut quartz crystals. Real-time monitoring of protein adsorption with high mass and time resolution can comprehensively reveal conformational changes and adsorption mechanisms. It can provide both qualitative and quantitative information about biological phenomena in the nanoscale. The mass adsorption, thickness, adsorption mechanism and structural conformation of biomolecules on the crystal surface can be assessed through the real-time monitoring of the shifts in resonance frequency and damping. In comparison with UV vis, PL and IR, the QCM-D technique provides a higher resolution that could result in a more comprehensive interpretation [217]. Recently, Melendrez *et al.* developed graphene-based QCM sensors as support surfaces with tuneable hydrophobicity to control the formation of phospholipid self-assemblies [6]. The aqueous dispersion of GO was used to produce thin-film coatings on QCM crystals, followed by controlled thermal reduction to yield tuneable functionalisation levels. This novel platform is useful not only for monitoring biochemical events but could also serve as an effective route to the development of graphene-based biosensors.



In this work, we measure and discuss the adsorption dynamics of BSA protein onto graphene-based surfaces with varying degrees of functionalisation, and propose adsorption models for BSA on tuneable graphene surfaces, which takes into account the nature of the substrate as well as the protein concentration in the media. Orientations of the protein on the graphene-based surfaces which could affect binding sites, thickness and viscoelasticity of the adsorbed film are also proposed based on QCM-D results. We also investigate the functionality or denaturing of the adsorbed BSA using an anti-BSA antibody, which can specifically bind with the endogenous levels of total BSA protein. Additionally, the selectivity of the graphene-bound BSA toward anti-BSA was studied by observing the adsorption of competing proteins in the assay. The method presented here could be extended to mapping the phase diagram of a diversity of other biochemical interactions of biomacromolecules with 2-dimensional (2-D) materials. Our results not only provide a detailed description of the protein-graphene interaction but could also help design graphene-based biomaterials and biosensing platforms.



**Fig. 5.1** (a) Tertiary structure of BSA (b) dimensions of BSA molecule (c) tertiary structure of immunoglobulin antibody (d) dimensions of immunoglobulin with specific binding sites. Protein structure images from the RCSB PDB ([rcsb.org](http://rcsb.org))

## Materials and Methods

### 1. Materials

GO dispersion was prepared by a modified Hummers' method [202] followed by exfoliation and purification. Briefly, graphite flakes of 50 mesh (1g) and  $\text{NaNO}_3$  (0.9 g) were mixed in concentrated  $\text{H}_2\text{SO}_4$  (35 mL) and left overnight to intercalate. The mixture was cooled down in an ice bath before slowly added with 4.5 g  $\text{KMnO}_4$  during stirring. The mixture was left for 5 days at room temperature to allow graphitic oxidation. The brown slurry was diluted by slowly adding 5%  $\text{H}_2\text{SO}_4$  solution (100 mL), then diluted

again with 100 mL mixture of 3% H<sub>2</sub>SO<sub>4</sub> and 0.5% H<sub>2</sub>O<sub>2</sub>. The homogenisation and complete exfoliation of graphite oxide were carried out using a vertical stirrer at a low speed for ~1h. The final GO dispersion was washed by repeated centrifugation and dilution with diluted H<sub>2</sub>SO<sub>4</sub>, then DI water until the pH was close to neutral.

Albumin, monomer bovine (A1900), and phosphate buffered saline, PBS, (P4417) were purchased from Sigma-Aldrich, UK. The PBS solution, pH 7.4, was filtered and degassed before use. BSA stock solution was prepared with a concentration of 5 mg/mL. Serial dilutions of BSA solution were prepared from the stock solution. Anti-BSA antibody produced from rabbit immunoglobulin G (IgG), polyclonal clone (SAB4301142) (Sigma-Aldrich) was diluted to 50 µg/mL to be used in the affinity experiments.

## 2. Surface modification and characterisation

The stock dispersion of GO was diluted to a concentration of 0.8 mg/mL. QCM sensors with the gold surface electrode (5MHz fundamental frequency, QSX-301, Biolin Scientific) were conditioned following the protocol provided in Melendrez *et al.* [6], then coated with GO via spin coating (speed: 3000 rpm, acceleration: 350, 2 mins) to form a GO film on the chips. A controlled thermal reduction of GO chips was performed in a vacuum oven, Townson+Mercer EV018, with the temperature of 80 °C and 180 °C and varied reduction time from 5 mins to 28 hours to achieve a range of functionalisation levels, see ESI 1.5 for reduction condition. Scanning electron microscopy (SEM) was performed on a Zeiss Ultra using an accelerating voltage of 5 kV with secondary electron imaging to characterize the surface morphology of graphene coatings on Au surfaces. The degree of reduction was characterised via wetting contact angle (WCA) measurement of sessile drops of DI water (Kruss DSA100) in combination with X-ray photoelectron spectroscopy (XPS) using SPECS custom-built system composed of a Phobios150 hemispherical electron analyser with 1D detector. The XPS data were analysed using CasaXPS software (version 2.3.18).

## 3. QCM-D measurement of protein adsorption

The QCM-D measurements for BSA adsorption on bare Au, GO and rGO were carried out using the Q-Sense Omega Auto (Biolin Scientific) system. The temperature of the QCM-D system was stabilised at 20 °C to avoid the effects of thermal drift on the response.

The system was used to monitor the adsorption kinetics of the protein on bare Au and graphene-coated sensors. The generic procedure for the protein adsorption study started with a baseline stabilisation regime in which PBS is flowed until stability is reached and the signal drift is negligible, then the sample was injected and continuously flowed through the sensor, before rinsing with PBS to remove loosely bound molecules. A full protocol for the protein adsorption study is provided in ESI 1.1. The flow rate used for this experiment was 10  $\mu\text{L}/\text{min}$ . The frequency and dissipation values of the 3rd to the 13th harmonics were recorded as they are reported by the QSense Pro system and are necessary for viscoelastic modelling. For simplicity, we report the value for the 5th overtone of both frequency and dissipation which is a typical overtone for computing mass adsorption from Sauerbrey equation [218]. Computational modelling of QCM-D signals was carried out in order to determine mass, thickness and viscoelasticity of the adsorbed films using QSense Dfind software provided by Biolin Scientific. The software provides computational methods to determine the mass adsorbed on the sensor's surface including the Sauerbrey equation, calculated from the frequency shift and viscoelastic modelling, based on the Voigt-Voinova model [169]. The theory of QCM-D as well as procedure and conditions for extracting information from QCM-D profiles using Dfind are showed in the ESI 1.2. To ensure statistical significance, all adsorption results were repeated at least three times, (see ESI 1.7). The orientations and adsorption models of BSA onto the graphene surfaces here proposed are based on the computed thicknesses of the adsorbed protein films and their respective adsorption dynamics.

#### 4. Antibody binding

To check if the BSA denatures upon adsorption on graphene, anti-BSA antibody, which can specifically bind with the endogenous level of total BSA protein, was injected following the adsorption of BSA on graphene. The ability of the antibody to bind specifically to non-denatured BSA was tested using the dot blot technique, which detects proteins and the selectivity of antibodies [219], see ESI 1.12. The injection sequence of the QCM-D measurement for the study of the functionality of BSA is presented in **Fig. 5.7**. This process starts with the adsorption of BSA, rinsing, then anti-BSA, rinsing and finally the repeat adsorption of fresh BSA to confirm the orientation of the antibody. Moreover, the selectivity of BSA adsorbed on graphene-coated chips

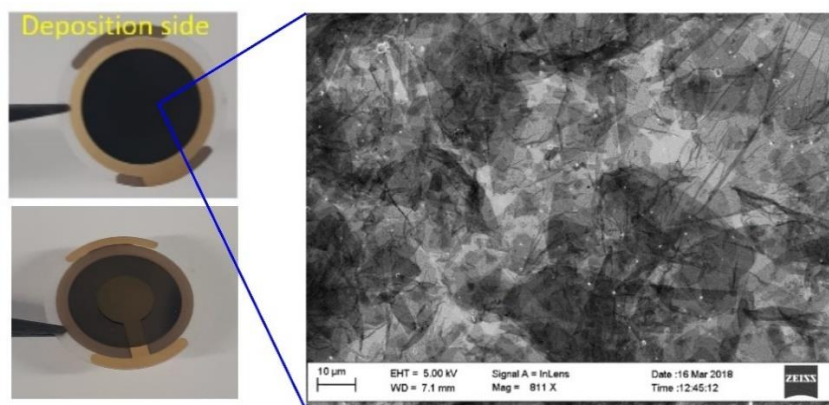
toward anti-BSA was tested by through the evaluation of the adsorption of other proteins including lysozyme and immunoglobulin G (IgG). The adsorption of non-specific proteins over the BSA layer should not occur if BSA molecules uniformly cover the surface and the protein does not suffer a denaturation process [220].

## Results and discussion

We first discuss the properties of the different graphene surfaces, as revealed through SEM, XPS and contact angle measurements. We then report on the adsorption of BSA protein on the graphene surfaces using the QCM-D technique and investigate the effect of varying graphene chemistry and protein concentration on the adsorption dynamics. We go on to establish the biosensor functionality of the adsorbed BSA through its interaction with the corresponding antibody.

### 1. Characterization of graphene surfaces

SEM imaging reveals that the optimised spin-on graphene coatings on the Au surface of QCM-D chips comprise of a continuous film of overlapping flakes covering the entire surface, with film thickness varying from one to few monolayers (**Fig. 5.2**). The coated chips are uniformly full coverage with graphene film on all samples studied (ESI 1.3). The graphene flakes are 100% monolayer with a lateral flake size distribution of  $12.1 \pm 8.7 \mu\text{m}$  (ESI 1.3). Since both GO and rGO surfaces show similar surface morphology on SEM images, here we only present the results from GO.



**Fig. 5.2** Optical and SEM micrographs from GO coated on Au QCM-D sensor. The working surface is fully covered with the varied number of graphene layers from one to few monolayers.

Graphene derivatives, like GO and rGO, form a tuneable hydrophobicity system achieved through the controlled thermal reduction of GO to rGO to obtain different degrees of functionalisation. The conditions for the thermal reduction and corresponding WCA are presented in ESI 1.5. We label this system as rGO#, with increasing reduction levels progressing from rGO1 to rGO5. Water contact angle (WCA) measurements reveal that hydrophilic GO (WCA = 21°) containing various polar oxygen-containing functional groups turns increasingly hydrophobic (WCA = 28° to 84°) as these groups are removed. The extent of deoxygenation is revealed in the corresponding XPS spectra. The ratio of atomic percentage (at %) of carbon and oxygen was obtained from the wide-scan XPS spectra. Table 5.1 shows the C/O ratio corresponding to samples with different WCAs and Raman spectroscopy characterization. The C/O ratio is seen to increase as the WCA increases, corresponding to the removal of the oxygen groups. This trend is also observed in the C1s peak, where the ratio of C-C component intensity to C-O component intensity increases with increasing WCA. Complete wide and narrow scan spectra are included in ESI 1.6. Raman spectra of all samples were measured to obtain information about the number of layers and lattice defects, see ESI 1.7. Two main peaks including graphitic (G) and defect (D) occur at  $\sim 1580\text{ cm}^{-1}$  and  $\sim 1350\text{ cm}^{-1}$ , respectively. The relative intensity of D to G ( $I_D/I_G$ ) provides an indicator for determining the in-plane crystallite size or the amount of disorder in the sample. The  $I_D/I_G$  value of GO is 1.01 which is slightly higher than that of rGO samples. rGO samples with different reduction levels show similar  $I_D/I_G$  value in between 0.97 to 0.98. Our results are consistent with previous reports [6], [221] that thermally reduced rGO materials are only slightly less defective compared to GO.

**Table 5.1** Summary of properties of GO and various degrees of rGO used in this study.

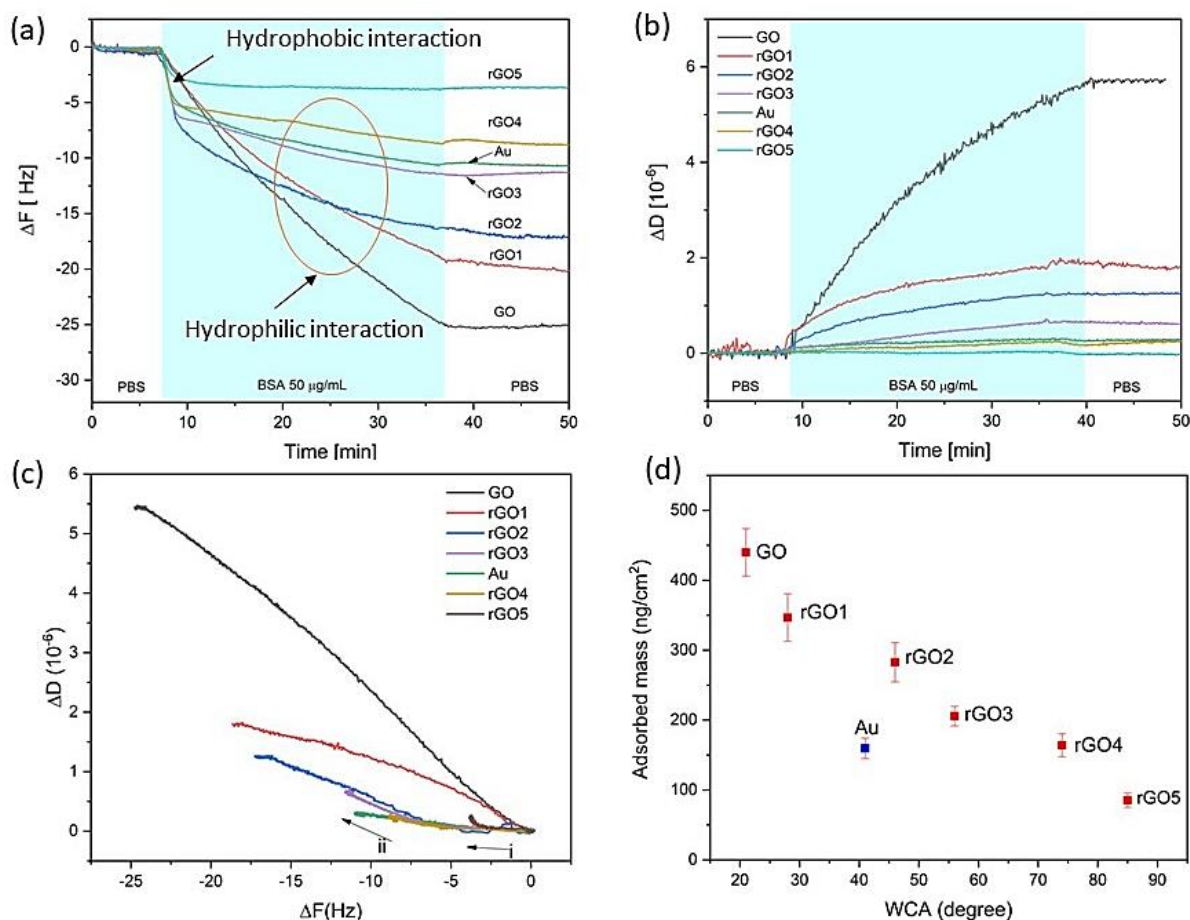
Sample name	Water contact angle (WCA)	XPS peak intensity ratios		Raman peak intensity ratios
		C/O	C-C/C-O	I <sub>D</sub> /I <sub>G</sub>
GO	21°±2°	2.59	0.71	1.0112
rGO1	28°±3°	2.62	0.71	0.9709
rGO2	46°±3°	2.64	0.71	0.9776
rGO3	56°±2°	2.67	0.77	0.9785
rGO4	74°±1°	4.98	4.04	0.9886
rGO5	85°±1°	5.71	4.36	0.9811

## 2. Effect of different degree of reduction of the GO

We first study the adsorption of BSA of a fixed concentration of 50 µg/mL, which is within a linear range for a protein standard assay [222], [223]. The protein was flowed for 30 mins over the graphene surfaces (GO, rGO1 to rGO5); bare gold sensors were used as controls for each experiment. **Fig. 5.3(a)** shows the frequency shift ( $\Delta F$ ) during the BSA adsorption and subsequent PBS rinse steps. The GO surface shows the highest total frequency shift at the PBS rinse stage, which is seen to decrease as the degree of reduction of the GO increases. We also observe that for the two most functionalised surfaces, GO and rGO1, the rate of change of frequency is relatively constant (constant slope), whereas the more reduced graphene (more hydrophobic) demonstrates 2-stage adsorption characterised by a short, fast adsorption step followed by a slower rate of adsorption.

**Fig. 5.3(b)** shows the dissipation shift ( $\Delta D$ ) during the BSA adsorption and rinsing process. The total dissipation shift significantly decreases after the reduction of GO and goes down to around  $0.1 \times 10^{-6}$  at the highest level of reduction of the GO. According to the  $\Delta D$ - $\Delta F$  plot in **Fig. 5.3(c)**, the GO surface presents the highest slope or dissipation density while rGO1 shows lower slope resulted during the adsorption process. However, the slopes from both cases are relatively constant. In contrast, the more reduced graphene samples, rGO2 to rGO5, show two obvious slopes, lower (i) and higher (ii) slopes, during adsorption process. The plot of adsorbed mass against the level of

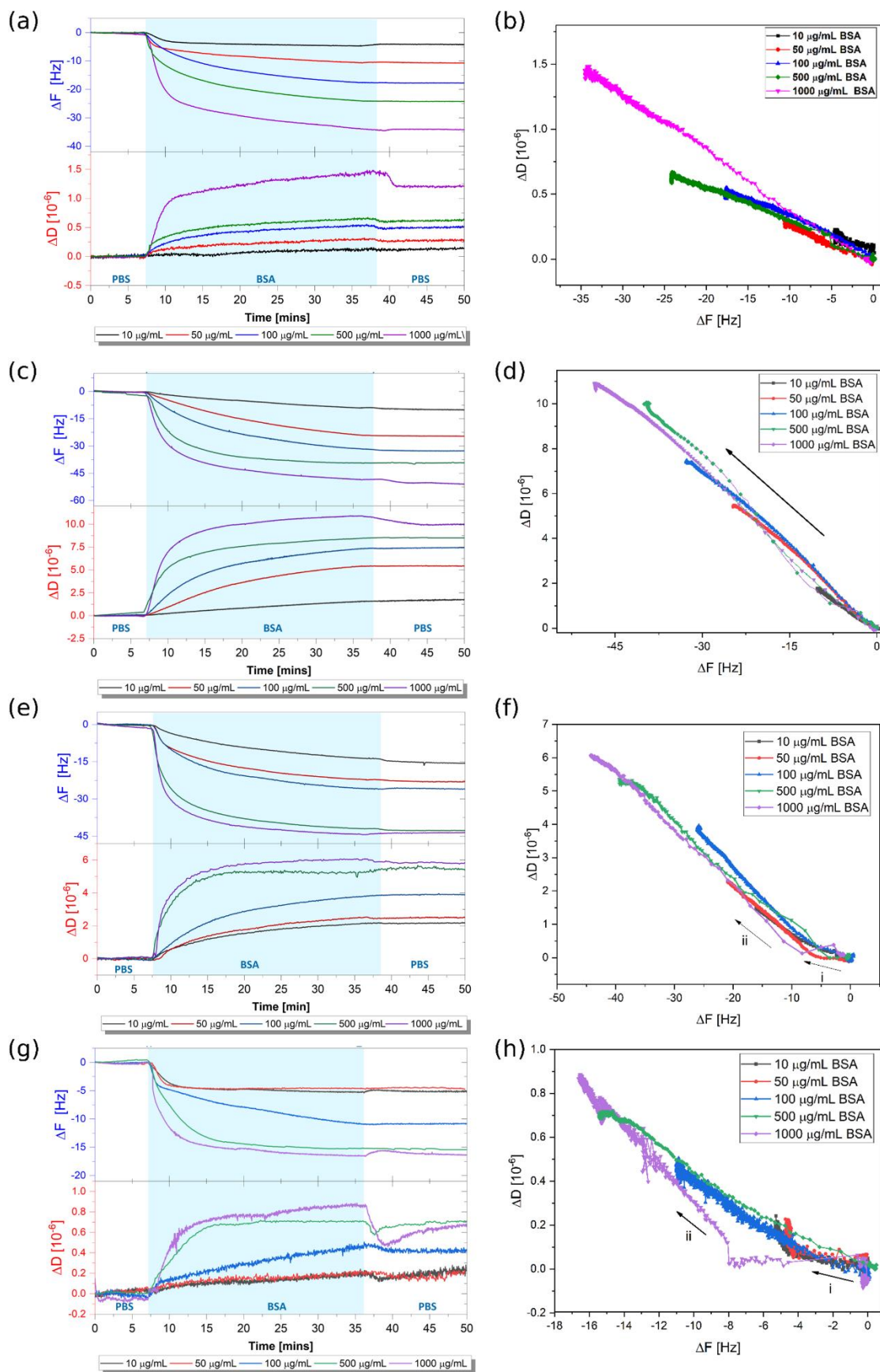
reduction of GO is shown in **Fig. 5.3(d)**, where the reduction level of GO is zero. Here, the mass adsorption decreases as the reduction level increases.



**Fig. 5.3** QCM-D profiles of **(a)** frequency and **(b)** dissipation upon BSA adsorption on surfaces with different reduction degrees of the GO **(c)**  $\Delta D$  -  $\Delta F$  plots of the adsorption. Two-stage adsorption (i, ii) can be seen in rGO2 to rGO4 samples that could correspond to hydrophobic and hydrophilic interactions, respectively **(d)** the plot of adsorption mass obtained from QCM-D analysis against the level of reduction of GO from zero to five representing GO to rGO5. The adsorbed mass reduces as the degree of reduction increases.

### 3. Effect of protein concentration in media

The adsorption of different protein concentrations, from 10  $\mu\text{g/mL}$  to 1000  $\mu\text{g/mL}$ , on graphene-coated QCM-D surfaces were monitored in real-time. Three different graphene samples including GO, rGO2 and rGO5 were used for studying the adsorption. Bare gold sensors were used as controls for each experiment. All measurements were repeated three times (refer to ESI 1.9).



**Fig. 5.4** QCM-D real-time adsorption monitoring and  $\Delta D$ - $\Delta F$  plots of different concentration BSA on (a,b) bare-Au, (c,d) GO coated on Au (e,f) rGO2 coated on Au and (g,h) rGO5 coated on Au



**Fig. 5.4(a)** shows that both the frequency and dissipation during BSA adsorption on bare gold shift increasingly with respect to the degree of protein concentration. The dissipation results are in the range of 0.2 to  $1.5 \times 10^{-6}$ . From **Fig. 5.4(b)**, for the concentrations ranging from 10 to 500  $\mu\text{g/mL}$  the slopes of the  $\Delta D$ - $\Delta F$  plot indicate similarities on the adsorption process, however, the higher slope obtained from 1000  $\mu\text{g/mL}$  could point at distinctive conformation.

**Fig. 5.4(c)** presents the adsorption of BSA on GO showing the shifts of frequency and dissipation increase as the concentration increases, similar to bare gold. Higher adsorption kinetics are observed at higher concentrations. Interestingly, the adsorption on GO shows relatively high dissipation compared to other surfaces, in the range of 2 to  $10 \times 10^{-6}$ . From the  $\Delta D$ - $\Delta F$  plot (**Fig. 5.4(d)**), the slopes from all concentrations present similar values.

On the rGO2 surface, the adsorption of BSA increases as the concentration increase, observed from the shift of frequency in QCM-D profiles from **Fig. 5.4(e)**. However, for BSA concentrations 500  $\mu\text{g/mL}$  and 1000  $\mu\text{g/mL}$ , the frequency shifts at the final regime are similar due to possible saturation of the surface with protein. The total dissipation shift from the rGO2 surface is within the range of 2 to  $6 \times 10^{-6}$  which is comparatively lower than that of GO but much higher than rGO5. From the  $\Delta D$ - $\Delta F$  plot (**Fig. 5.4(f)**), there are two slope values for all concentration profiles, one for each adsorption stage (i and ii). This two-slope characteristic is also seen in the  $\Delta D$ - $\Delta F$  plot of rGO5 surface, see **Fig. 5.4(h)**.

On the rGO5 surface, the protein concentration significantly affects the adsorption behaviour as observed from the change of frequency and dissipation (**Fig. 5.4(g)**). For low concentrations of BSA (10, 50  $\mu\text{g/mL}$ ), the adsorption shows a similar trend: fast adsorption rate at the initial stage followed by no further adsorption after a few minutes, as evidenced by the flat frequency shift. The energy dissipation from both cases is relatively low, less than  $0.3 \times 10^{-6}$ , indicative of the adsorption of a rigid layer. Additionally, the dissipation values keep rising despite no change on the frequency or additional adsorbed mass being observed (**Fig. 5.4(h)** black and red profiles). In contrast, with BSA concentrations higher than 100  $\mu\text{g/mL}$ , the graphs show 2-stage adsorption with different adsorption rates. The initial stage presents fast adsorption with a

frequency shift of about  $-5\pm 2$  Hz during the first few minutes, then the adsorption rate decreases and the frequency changes homogeneously. The dissipation values are relatively low ranging from 0.2 to  $0.8 \times 10^{-6}$ . From the  $\Delta D$ - $\Delta F$  plot, the two-step adsorption characteristic profile can be seen for both rGO2 and rGO5 in the cases of protein concentrations ranging from 100  $\mu\text{g/mL}$  to 1000  $\mu\text{g/mL}$ .

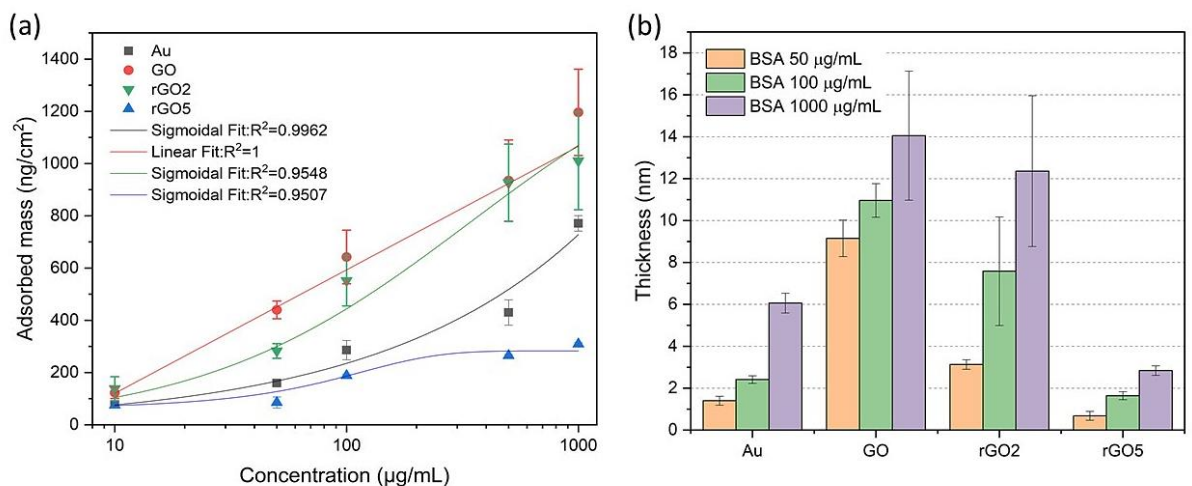
#### 4. Adsorption mass and thickness

The thickness of an adsorbed layer is crucial to determine the orientation of protein molecules on a specific surface and to assess the eventual denaturation of the molecules [107]. In this study, the adsorbed mass and thickness of BSA adsorbed film on bare gold, GO, rGO2 and rGO5 were determined through the modelling of QCM-D results using the software 'Dfind' (Biolin Scientific). On bare gold and rGO5 surfaces, the dissipation from QCM-D was relatively low and the responses from different harmonics did not diverge. It can be inferred that the adsorbed film tends to be rigid, thus enabling the use of the Sauerbrey equation to calculate the thickness of the adsorbed film. On the other hand, the adsorption onto GO and rGO2 surfaces show significantly high dissipation and the QCM-D profile of each harmonic split indicating that the adsorbed films possess viscoelastic properties. Therefore, Voigt-Voinova viscoelastic modelling was used to determine the mass and thickness of the BSA film on GO-coated surfaces.

For predicting the mass adsorption behaviour, the plot of adsorption mass versus concentration was fitted with a linear or sigmoidal function depending on the quality of the fitting ( $R^2$ ) as shown in **Fig. 5.5(a)**. The linear adsorption model has been one of the most applied tools for defining the fitting as it can quantify the distribution of adsorbates and verify the consistency of adsorption isotherm model [224], whereas a sigmoidal function is the most commonly used for biochemical ligand binding theory [225]. Koa *et al* studying the adsorption of globular protein on hydrophobic surfaces reported that the plot of QCM response against the serum albumin concentration fits well with sigmoidal function with  $R^2 > 0.99$  [226]. The mass adsorption on bare gold was fitted to a sigmoidal function ( $R^2 = 0.9962$ ). It can be seen that the adsorption on the gold surface did not reach a saturation condition within the range of concentrations used in this report. For GO, the BSA mass adsorption for all concentrations was fit to a linear function

( $R^2 = 1$ ) on a logarithmic scale. This linear adsorption could be used to predict adsorbed mass within the range of concentrations used. For the rGO2 and rGO5 surfaces, the mass adsorption as a function of BSA concentration fits well with Sigmoidal model. It is possible to divide this function into three sections: slow rise, then accelerated rising that approaches a saturation over time, following its characteristic S shape. However, the curve fitting for rGO2 shows a significantly taller S-shape than that of rGO5 as a result of a higher amount of absorbed mass.

**Fig. 5.5(b)** shows the thicknesses of BSA film generated from concentration 50  $\mu\text{g/mL}$ , 100  $\mu\text{g/mL}$  and 1000  $\mu\text{g/mL}$  adsorption on different surfaces. The thicknesses of BSA on all surfaces increase with respect to the protein concentration. BSA films on GO show the highest thickness in all concentrations following by those on rGO2, bare gold and rGO5. The thickness values of BSA on GO are in a range of 8 nm to 17 nm while on rGO2, the thickness values are slightly lower, in a range of 3 nm to 16 nm. On rGO5, the thickness ranges from 0.6 nm to 3 nm. The different thickness values could be the result of different quantities and/or different orientations of BSA molecule adsorption on the surfaces, which will be discussed in the next section.



**Fig. 5.5 (a)** specific adsorption mass as a function of concentration for Au, GO and rGO. **(b)** the thickness of BSA film with varied concentrations adsorbed on Au, GO, rGO2 and rGO5

## 5. Proposed adsorption model

BSA molecules can adsorb onto a surface at various orientations between two extremes: side-on and end-on [107], (**Fig. 5.1(b)**). Dissipation shift and thickness are the main

criteria to distinguish between side-on and end-on adsorbed layers. We propose and verify that a low dissipation value (less than  $1 \times 10^{-6}$ ) would correspond to the side-on orientation that creates a more rigid film while the single end-on layer shows significantly high dissipation, around  $10 \times 10^{-6}$ . It becomes evident that the molecular adsorption of the protein on the surfaces depends on the hydrophobic level of the GO and concentration of BSA protein, see **Fig. 5.6**. The models proposed here are subsequently verified by anti-BSA and IgG binding studies.

We propose that BSA attaches on GO with an 'end-on' or vertical orientation, but can be tilted when the coverage is low, resulting in lower thickness. When the coverage is higher, it packs closely and is oriented vertically, thus achieving the maximum thickness for one layer of  $\sim 14$  nm which corresponds to the thickness obtained from QCM-D measurement of  $1000 \mu\text{g/mL}$  BSA. In water-based solutions, protein molecules are likely to fold the hydrophobic part into the core structure to minimize exposure of their intrinsic hydrophobicity, while the hydrophilic part will be outside to form hydrogen bonds with water molecules [227]. It was reported that BSA displays higher polar at end-on region compared to the side-on one [106]. Therefore, we conclude that the hydrophilic interaction between functional groups in BSA and GO could be the predominant driving force. The concentration of BSA solution mainly affects the adsorption kinetics. Higher concentration shows faster adsorption rate as reported previously [228]–[230]. With an increase in concentration of the protein, the adsorption mass increases but the slopes from  $\Delta D$ - $\Delta F$  plot still present similar values indicating that a single adsorption event occurs within this concentration range. This implies that the BSA molecules pack denser with the same orientation on GO as higher concentration is adsorbed. several publications reported that GO could induce conformational and activity changes in serum albumin [231], [232]. Ding *et al.* studied the interaction of GO with human serum albumin (HSA) through fluorescence quenching measurements [231]. They suggested that GO may block protein active sites or destroy the protein structure. Similarly, Zhang *et al.* used UV-vis and fluorescence quenching measurements to study the adsorption of BSA on GO [232]. They also reported that GO may decrease the binding capabilities of BSA. However, both reports studied BSA-GO interaction in an

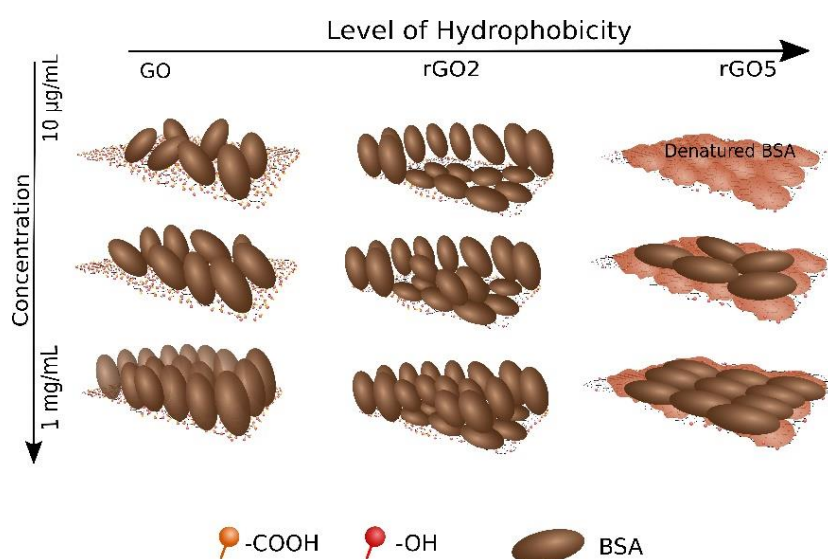
aqueous environment which differs from our study in which we investigated BSA adsorption on a solid GO platform.

On rGO2, as the reduction level of the GO increases, the adsorption mass goes down and a 2-step adsorption process is observed from the different adsorption rates, which is likely the result of both hydrophobic and hydrophilic mechanisms, respectively. In this case, the hydrophobic sites on the graphene plane allow BSA molecules to orient side-on toward the surface due to hydrophobic interaction whereas remaining oxygen functional groups on rGO2 interact with the hydrophilic part of BSA. The hydrophobic sites are adsorbed first, then followed by hydrophilic ones. We propose that the initial fast adsorption rate is due to strong  $\pi$ - $\pi$  stacking and a hydrophobic interaction between the hydrophobic amino acids of albumin; containing aromatic rings, and carbon aromatic rings of graphene while the slower adsorption originates from a hydrophilic interaction with the functional groups. We assume that the  $\pi$ - $\pi$  stacking and hydrophobic strength from rGO surface could directly attract the hydrophobic amino acids in BSA molecules, whereas the hydrophilic parts of BSA need to overcome their hydrogen bond with water media to interact with the functional groups of rGO; as a result, the hydrophobic interaction occurs faster than the hydrophilic one.

With this low hydrophobic degree of GO, the BSA molecules might not be denatured on the hydrophobic domain as the force is not strong enough to flatten and denature the protein. The evidence from **Fig. 5.3(a)**, partially reduced GO (rGO1 to rGO4) shows higher frequency shift in the hydrophobic region of the graph compared to rGO5. It is assumed that the hydrophobic interaction might be too weak to flatten BSA, thus, more BSA molecules can be adsorbed on remaining hydrophobic region. As a higher concentration of the protein is used, the adsorption mass increases. The higher protein concentration, the more BSA molecules can adsorb on the remaining hydrophilic space of rGO2.

The highest hydrophobicity coating, corresponding to rGO5, shows the lowest mass adsorption and a peculiarly fast saturation. In theory, non-denature BSA with side-on orientation should present the thickness of 4 nm [107]. The significantly thin film of BSA on rGO5 with the thickness of  $\sim 0.68$  nm occurred on the adsorption of low concentration of BSA (less than 50  $\mu\text{g}/\text{mL}$ ). This likely results from protein spreading and

denaturation on the surface. It is widely accepted that several proteins undergo conformational changes after adsorption as they contain numerous flexible chains [230]. By interacting with the surface, proteins try to optimize the binding energy by impelling themselves to maximize the surface contact through conformational rearrangements. In this case, we assume that BSA molecules need to orient the hydrophobic region from the aromatic rings of certain amino acids to bind with the hydrophobic region of rGO, resulting in the flattened molecules on the surface. With the concentration of BSA higher than 100  $\mu\text{g/mL}$ , another layer of BSA with side-on orientation was generated as the QCM-D profile displays two adsorption kinetics (**Fig. 5.4(g, h)**). In high concentration environments, a higher amount of the protein is assumed to be adsorbed over the denatured layer of BSA. This could reduce the available spaces for binding and limits the extent of the structural rearrangements. The intermolecular interactions could be preferable to protein-surface interactions [229]. The last model of BSA on rGO shows the close-packed side-on adsorption over the denatured layer of BSA with the total thickness of  $\sim 3$  nm, which fairly corresponds to the thickness of side-on orientation.



**Fig. 5.6** The proposed models for BSA adsorption on graphene-based materials surfaces with the dependence on the hydrophobic degree and concentration of the protein.

We have also investigated the adsorption of protein on GO and rGO5 coating onto a QCM chip substrate with different physicochemical characteristics; a  $\text{SiO}_2$  sensing chip. The results display similar adsorption mass and kinetics to those on gold, as observed from the shift frequency and dissipation as well as the  $\Delta D$ - $\Delta F$  plot, as shown ESI 1.11.

Thus, we conclude that the underlying QCM chip substrate does not influence the protein adsorption process on the graphene surface.

## 6. Specific and non-specific binding studies

The interaction of the adsorbed protein with its antibody was studied to confirm the proposed orientations, functionality and denaturation of the protein. Protein denaturation can occur due to the disruption of disulphide linkages results in unfolding peptide chains and conformational changes including the primary, secondary, tertiary and quaternary structures of a protein due to the exposure of hydrophobic groups [233]. If the protein can specifically bind with its antibody, it can be inferred that the protein is not denatured and binding functionalities are still preserved. The antibody is a large Y-shape protein with MW  $\sim$ 150 kDa and with dimensions of approximately  $14 \times 10 \times 4$  nm [234], shown as **Fig. 5.1(d)**. The antibody is comprised of two fragment antigen-binding (Fab) regions and a fragment crystallizable region (Fc). In case of antibody detection assay, the ideal orientation of the antibody is “head-on” in which both Fab sites bind with antigen on a substrate, however, random orientations of the antibody including “side-on,” or “lying-on”, in which the antibody orients a Fab and Fc sites toward or flatten on the surface respectively, may occur due to various surface properties and orientation of an immobilized antigen [235], see ESI 1.13 for the schematic of the antibody orientation. Another possible orientation of antibody is “end-on” in which the Fc stands on the substrate happening in a non-specific binding case.

In this experiment, the binding ability of anti-BSA antibody was tested with BSA and denatured BSA using dot blot technique, see the results and discussion on ESI 1.12. QCM-D measurement was carried out to monitor the adsorption of anti-BSA after interacting with BSA adsorbing on GO and highly hydrophobic rGO5 surfaces. Binding affinity was determined using a fixed concentration of anti-BSA at 50  $\mu$ g/ml. The concentrations of BSA used in this experiment include 10  $\mu$ g/ml and 1000  $\mu$ g/ml as these two concentrations show significantly different BSA adsorption process and molecular arrangements according to the proposed adsorption model. The adsorption mass of BSA and anti-BSA were computed from viscoelastic modelling and Sauerbrey equation.

**Fig. 5.7(a)** shows the real-time monitoring of anti-BSA and BSA interaction on GO. Low concentration of BSA on GO (density:  $\sim 325 \text{ ng/cm}^2$ ) adsorbed approximately  $410 \text{ ng/cm}^2$  of anti-BSA (step C). After reinjecting BSA, some molecules were adsorbed (step E) possibly due to the mixed orientations of the antibody e.g. side-on and head-on. On the other hand, a high concentration of BSA on GO (density:  $\sim 925 \text{ ng/cm}^2$ ) adsorbed relatively higher amount of anti-BSA with  $\sim 1440 \text{ ng/cm}^2$  (step C). There was no BSA adsorption in step E as the antibody attached to BSA in the correct orientation, thus, no affinity for BSA to additionally adsorb.

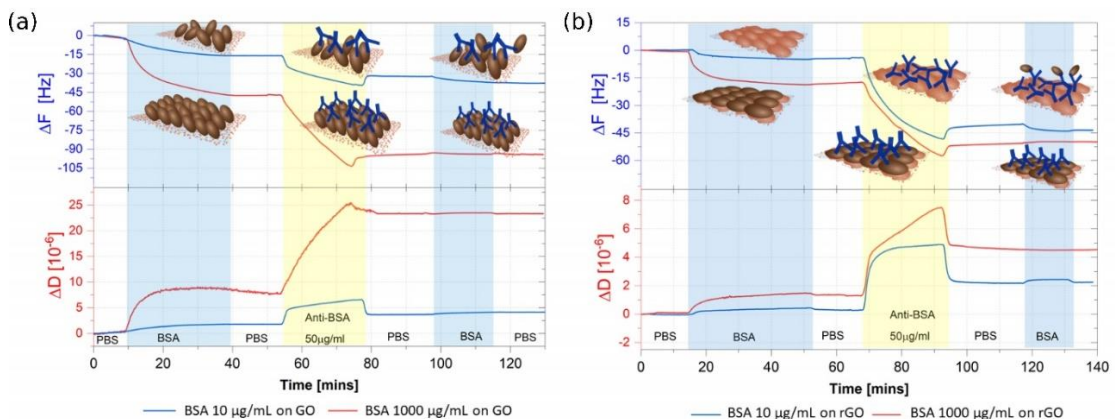
**Fig. 5.7(b)** shows the interaction of anti-BSA and BSA on rGO5. The adsorption densities of BSA with the concentration  $10 \text{ }\mu\text{g/mL}$  and  $1000 \text{ }\mu\text{g/mL}$  are about  $78 \text{ ng/cm}^2$  and  $455 \text{ ng/cm}^2$  respectively. Both cases show that BSA bound with a similar amount of anti-BSA with  $\sim 630 \text{ ng/cm}^2$ , observing from similar frequency shift after the adsorption of antibody (step C). The dissipation shift after rinsing (step D) obtained from the low concentration case is much lower than that from the higher concentration one. Also, the adsorption of BSA occurred during the process of reinjecting BSA (step E). According to these, we assume that the antibodies might not orient the specific binding site on BSA but rather shown the random orientations (non-specific adsorption) in the case of low concentration BSA. This could result from the denaturation of BSA on rGO5. On the other hand, the specific adsorption of the antibody seems to present on the high concentration of BSA adsorption possibly because the added layers of BSA on rGO was created and the top layer was still functional.

As we know the adsorption mass and molecular weight of BSA ( $MW_{\text{BSA}} = 66 \text{ kDa}$ ) and anti-BSA ( $MW_{\text{anti-BSA}} = 150 \text{ kDa}$ ), the number of adsorbed molecules can be calculated. On the flat surface, the theoretically maximum amount of BSA for end-on and side-on orientations should be  $\sim 774 \text{ ng/cm}^2$  or  $7.06 \times 10^{12} \text{ molecules/cm}^2$  and  $\sim 221 \text{ ng/cm}^2$  or  $2.02 \times 10^{12} \text{ molecules/cm}^2$  respectively. Our calculated amount of BSA for a side-on orientation corresponds to a recent report on the saturation of close-packed avidin molecules (which present similar size to BSA) on a surface of  $\sim 320 \text{ ng/cm}^2$  measured by dual polarisation interferometer (DPI) [236]. It is also suggested that if the adsorption amount is above the aforementioned saturation value, additional layers can be formed [236]. This is in line with our description regarding the adlayer for the case of rGO5.



In theory, one antibody can capture two antigens, in this case, therefore, one anti-BSA can bind with two BSAs. In GO case, the number of BSA molecule extracted from adsorption mass for low concentration case is  $2.97 \times 10^{12}$  molecules/cm<sup>2</sup> binding with  $1.65 \times 10^{12}$  molecules/cm<sup>2</sup> of the antibody, while in high concentration case,  $1.20 \times 10^{13}$  molecules/cm<sup>2</sup> of BSA bind with  $5.78 \times 10^{12}$  molecules/cm<sup>2</sup> of the antibody. In both cases, the number of BSA molecules are about double of the number of anti-BSA indicating that BSA molecules remain binding functionality. The number of BSA molecules in high concentration case supports the assumption that BSA adsorption on GO with end-on orientation as it is comparable to the theoretically maximum number of end-on BSA molecules. The higher binding in GO case could be due to the roughness of the surface.

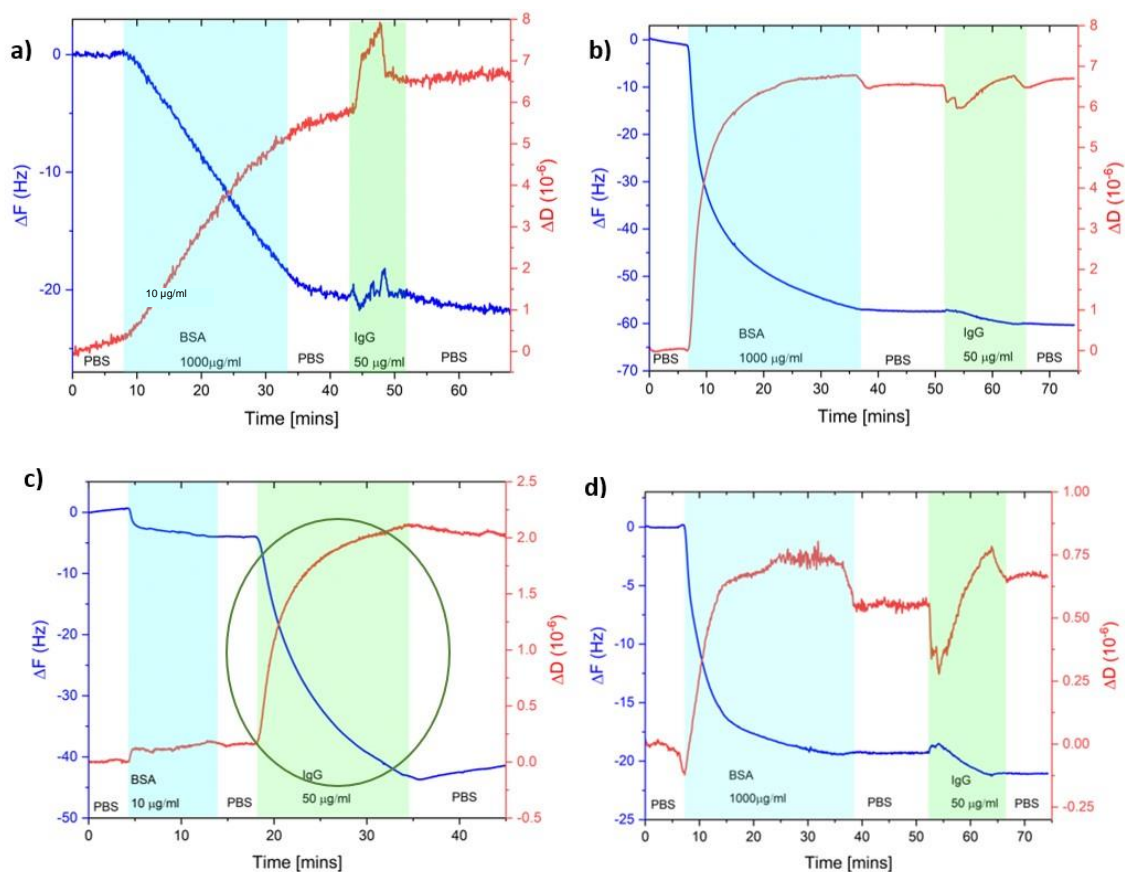
In low concentration of BSA adsorption on rGO case, only  $7.20 \times 10^{11}$  molecules/cm<sup>2</sup> of BSA adsorbed on the surface while, in high concentration case,  $4.18 \times 10^{12}$  molecules/cm<sup>2</sup> adsorption on the surface. Strangely, both cases show similar adsorption amount of anti-BSA, approximately  $2.53 \times 10^{12}$  molecules/cm<sup>2</sup>. The amount of the antibody on the case of low concentration BSA is too much for specific adsorption on BSA molecules. This could be the result from non-specific adsorption of anti-BSA occurring on denatured BSA layer.



**Fig. 5.7** QCM-D monitoring of BSA and anti-BSA interaction on **(a)** GO and **(b)** rGO5. The protein adsorption on GO can maintain binding functionality to its antibody. The denaturation of protein was found on highly hydrophobic rGO but an additional layer of protein can be created on top of the denatured layer without denaturation

To support the assumption about denaturation of BSA, we introduced the adsorption of immunoglobulin G antibody (IgG) over BSA adsorption layer. IgG has the same structure and molecular weight to anti-BSA but non-specific to BSA. If the adsorbed BSA

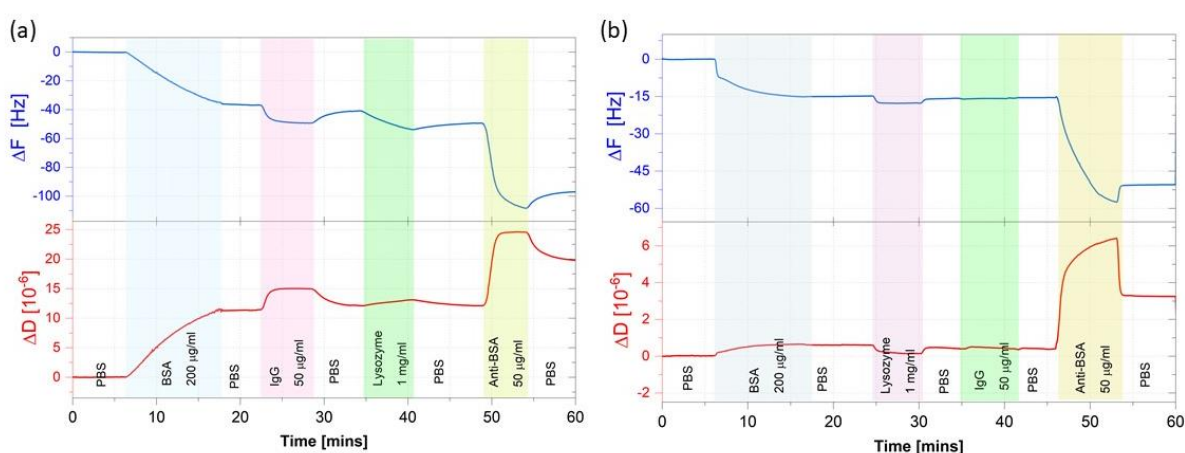
denatured on the surface, it could adsorb IgG with similar quantity to the adsorption of anti-BSA due to non-specific adsorption. **Fig. 5.8** presents the adsorption of IgG over BSA-graphene derivative platform (see the green highlighted band for IgG). Two concentrations of BSA including 10  $\mu\text{g}/\text{mL}$  and 1000  $\mu\text{g}/\text{mL}$  were used for this study. The results present that both 10  $\mu\text{g}/\text{mL}$  and 1000  $\mu\text{g}/\text{mL}$  BSA on GO can adsorb very small amount of BSA, with frequency shift less than 5 Hz similar to the case of 1000  $\mu\text{g}/\text{mL}$  BSA on rGO5. Only low concentration BSA-rGO platform can adsorb high amount of IgG, with the shift of frequency similar to that of anti-BSA adsorption ( $\sim 45$  Hz). This case clearly shows the non-specific adsorption of the protein. It is believed that IgG formed the adlayer over the thin layer of BSA could be denatured on the rGO surface resulting in the adsorption of other proteins over it through non-specific adsorption.



**Fig. 5.8** QCM-D results for IgG injection over BSA adsorption on (a,b) GO and (c,d) rGO for investigating non-specific adsorption and denaturation of BSA adsorption on the surfaces. Two concentrations of BSA including (a,c) 10  $\mu\text{g}/\text{mL}$  and (c,d) 1000  $\mu\text{g}/\text{mL}$  were studied. Only the case of 10  $\mu\text{g}/\text{mL}$  BSA-rGO can adsorb high amount of IgG as the thin layer of BSA could be denatured resulting in non-specific adsorption for other proteins.

All these results support our proposed adsorption models and also suggest that highly hydrophobic rGO could denature the globular protein during adsorption process in the case of low concentration protein but with higher concentration environment, the added layer of the protein will be created without denaturation.

Finally, we evaluated the selectivity of BSA-graphene platforms toward its antibody observing the adsorption of other proteins including lysozyme and IgG. **Fig. 5.9(a)** and **(b)** present the selectivity of BSA on GO and rGO platforms, respectively. Both supports show that BSA can specifically detect anti-BSA as observed from the frequency shift of around 35 to 40 Hz after the adsorption of the antibody with comparatively lower adsorption values of other proteins. However, the signal after injecting other proteins onto the rGO platform presents higher stability compared to the one obtained for GO. This event could happen due to the particular orientation of BSA on rGO that promotes a close-packing with a side-on arrangement, resulting in the prevention of non-specific binding of other molecules. Regarding these results, it is suggested that the rGO platform performs better than GO in terms of its selectivity. Therefore, it stands as a suitable platform for the development of a simple graphene-based immunoassay.



**Fig. 5.9** QCM-D monitoring for testing the selectivity of BSA against its antibody on **(a)** GO and **(b)** rGO5 platforms. Both supports show specific adsorption of anti-BSA with comparatively low adsorption of other proteins.

## Conclusions

The dynamic organisation and interaction of BSA protein on graphene-based materials has been systematically investigated using the QCM-D technique. We report significant differences in orientation, mass adsorption and functionality of BSA on graphene

surfaces relative to the degree of functionalisation and hydrophobicity of the surfaces and the concentration of the protein. Our results suggest that the hydrophilic GO surface containing various oxygen functional groups shows a great affinity for protein adsorption. This result is in agreement to studies which suggested that GO can readily adsorb protein through noncovalent forces, such as electrostatic, hydrogen bonds and van der Waals, without any cross-linking reagents [231], [232], [237]. In terms of the dissipation monitoring, a viscoelastic adsorption behaviour occurs on GO supports while the adsorbed BSA film on rGO tends to be more rigid. Moreover, the mass adsorption decreases as the level of hydrophobicity increases. We reason that these events are a consequence of the immobilization of BSA on graphene-based materials with different orientations that depend on the hydrophobic degrees of the surface. We propose that BSA is flattened by the highly hydrophobic rGO, creating a denatured layer spreading out over the surface, presenting a thickness of less than 1 nm. Such strong hydrophobic interaction could compress the protein structure interacting with hydrophobic amino acids present in the interior of the protein. In contrast, BSA molecules orient end-on onto the GO surface resulting in a thickness of  $\sim 14$  nm. Reduced GO with an intermediate level of hydrophobicity (rGO2 to rGO4) could exhibit a mix of both side-on and end-on orientations since the surface loses certain oxygen functional groups, thus, presenting both hydrophilic and hydrophobic domains, as demonstrated by the XPS analysis. The interaction between rGO and the proteins originates from hydrophobic or aromatic amino acids creating a hydrophobic interaction and  $\pi$ - $\pi$  stacking with the aromatic rings of graphene [113], [238].

Protein concentrations significantly affect the adsorption behaviour on graphene derivatives. On the GO surface, higher concentrations show higher adsorption rates. The adsorption kinetics in all cases were similar, as observed from the similar value of the slope from the  $\Delta D$ - $\Delta F$  plots. On rGO, in contrast, the adsorption mechanisms are different in both the adsorption kinetics and the total adsorbed amount when using different concentrations. On the one hand, with low concentrations of BSA solution (10 to 50  $\mu\text{g}/\text{mL}$ ), the orientation of BSA molecules could occur due to the highly hydrophobic interaction between BSA and rGO. With higher concentrations (100 to 1000  $\mu\text{g}/\text{mL}$ ), an added layer of BSA could be generated on top of a denatured layer as

the QCM-D profile shows two adsorption kinetics and the top layer remains both functional and selective to the antibody.

The functionality of adsorbed BSA was investigated by interacting it with the anti-BSA antibody. BSA adsorption on GO can retain its specific binding sites with antibody; therefore, we conclude that the BSA did not unfold or denature on the GO platform. It is reasoned that the biological activity and the performance of BSA when adsorbed on GO in solution significantly differs from interaction occurring at a solid platform. A denatured layer or double layers of BSA were presented on hydrophobic rGO depending on the concentration of the protein. Highly hydrophobic rGO could flatten the globular protein during the adsorption process creating a denatured layer on the surface. With higher concentration environment, however, an added layer of protein could be created without denaturation. Interestingly, the top layer of BSA on rGO appears to remain functional as it can specifically bind with its antibody and also prevent non-specific adsorption from other proteins.

More broadly, our investigation and the discussed results shed light on the effects of both surface polarity and protein concentration on the adsorption kinetics and protein arrangement that led to specific and unique molecular conformations on graphene-based surfaces. It is clear that GO possesses high affinity for protein adsorption. More importantly, the adsorbed protein retains its binding affinity to its corresponding antibody pair. This result highlights the importance of GO as a potential candidate for biomedical applications such as drug sensing or delivery systems and implant surfaces that require high protein adsorption densities on a solid support [72], [239]. Protein denaturation was distinctively obtained on highly hydrophobic rGO, however, an additional layer of protein can be adsorbed on top of the denatured layer without subsequent denaturation showing high binding selectivity. Therefore, it is proposed that hydrophobic rGO supports could also serve as potential biotechnological platforms such as biosensing and bioelectronic systems. These results emphasise the great diversity of biomolecular interactions that can occur on graphene surfaces, and the importance of systematic mapping of different regimes before the implementation of any new graphene-based biosensor, drug-delivery or cell scaffold platform.

## Arguments and Future Work

In this section, a discussion of the applied reasoning for focusing on both hydrophobic and hydrophilic interactions between graphene and BSA as the primary driving forces for molecular adsorption is given. Moreover, further characterizations are proposed as future work to confirm protein orientations and denaturation.

Based on the observed adsorption results, the number of binding sites increases with the presence of the oxygen groups present on the GO surface. It might be assumed that the binding mechanism could be driven by the attraction between the surface charges from graphene and BSA. However, the oxygen groups on the graphene surface present an overall negative charge given that GO is less negative when it is reduced, while the BSA is negatively charged at neutral pH (PBS buffer pH 7.4). Based on this fact, GO should adsorb fewer molecules due to charge repulsive forces. Our adsorption results show the opposite, GO presents the highest adsorption density. Therefore, we do not believe that the binding between GO to BSA is driven by an opposite charge attraction.

A polar bond could be involved in the interaction since reduced oxygen contents in PrGO could lead to lower binding occupancies of the BSA resulting in reducing the overall thickness of the adsorbed layer. However, the QCM-D profiles of rGO and PrGO clearly show a two-step adsorption mechanism, as observed in the  $\Delta D - \Delta F$  plots for the adsorption (Fig. 5.3 (c), Fig. 5.4 (f), (h)). The slope of the dissipation density plot ( $\Delta D$  vs  $\Delta F$ ), reveals regions of different adsorption behaviours in terms of the viscoelastic structure of the adsorbed material. A lower slope value indicates the formation of a more rigid film while steeper slopes point at viscoelastic films being formed. The plot of the adsorption kinetics for the PrGO sample (Fig. 5.4 (f)  $\Delta D - \Delta F$ ) shows an initially low process (step 1) before rising monotonously (step 2). The two dissipation densities could result from two adsorption mechanisms between the protein and the surface, where the polar bond might not be a single dominant interaction. Therefore, we infer that the adsorption mechanism is primarily driven by hydrophobic and hydrophilic interactions.

In this research, we also proposed possible orientation scenarios for BSA on GO and rGO. In addition, we suggested that BSA might be flattened by the highly hydrophobic rGO, creating a denatured layer that spreads out over the surface. To confirm these claims,

other characterisation techniques such as AFM imaging in a liquid phase and/or ellipsometry could be used to measure the thickness of the protein layer. Additionally, changes in the chemistry of BSA after the adsorption event could be characterized using the AFM-IR technique.

### **Acknowledgements**

P.H. acknowledges the financial support of the Development and Promotion of Science and Technology Talents Project (DPST), Thailand. D.M. acknowledges The National Council for Science and Technology (CONACyT), Mexico for the financial support. A.V. acknowledges the Engineering and Physical Sciences Research Council (EPSRC) grant EP/L01548X/1. We acknowledge the support of the Biomolecular Analysis Core Facility, Faculty of Biology Medicine and Health, The University of Manchester.

## CHAPTER 6. Publication 2

A point-of-care immunosensor based on quartz crystal microbalance with graphene bio-interface for antibody assay

Hampitak, Piramon, et al. "A Point-of-Care Immunosensor Based on a Quartz Crystal Microbalance with Graphene Biointerface for Antibody Assay." *ACS sensors* 5.11 (2020): 3520-3532.

Available at <https://doi.org/10.1021/acssensors.0c01641>

### **Authors contributions:**

**Piramon Hampitak** prepared the QCM sensors and carried out all the QCM-D experiments. She prepared all samples for material characterization including samples for SEM, Raman and XPS. She analysed and interpreted SEM, Raman and XPS results. She carried out a dot blot and performed the analysis. She also designed and fabricated the fluidic cell for QCM immunoassay.

D. Melendrez designed QCM data acquisition software and interface.

D. Melendrez and T. Jowitt supervised on QCM analysis and interpretation.

K. Nie and D. Melendrez jointly carried out Raman spectroscopy.

M. Iliut prepared and purified GO dispersions.

M. Fresquet provided chemicals and antibodies for performing dot blot.

P. Hamilton provided patients' sera samples and perform ELISA.

B. Spencer performed XPS measurement.

T. Jowitt, R. Lennon and A. Vijayaraghavan supervised P. Hampitak on conceptualization and experimental design. T. Jowitt, A. Vijayaraghavan, R. Lennon, P. Hamilton, D. Melendrez and M. Iliut helped P. Hampitak in the writing of the manuscript. All authors read and approved the final manuscript.



## **A point-of-care immunosensor based on quartz crystal microbalance with graphene biointerface for antibody assay**

Piramon Hampitak<sup>1</sup>, Thomas A Jowitt<sup>2</sup>, Daniel Melendrez<sup>1</sup>, Maryline Fresquet<sup>2</sup>, Patrick Hamilton<sup>3,4</sup>, Maria Iliut<sup>1</sup>, Kaiwen Nie<sup>1</sup>, Ben Spencer<sup>1</sup>, Rachel Lennon<sup>3,5</sup>, and Aravind Vijayaraghavan<sup>1,\*</sup>

<sup>1</sup> *Department of Materials and National Graphene Institute, Faculty of Science and Engineering, The University of Manchester, Oxford Road, Manchester, UK.*

<sup>2</sup> *School of Biological Sciences, Faculty of Biology Medicine and Health, The University of Manchester, Oxford Road, Manchester, UK.*

<sup>3</sup> *Wellcome Centre for Cell-Matrix Research, Division of Cell-Matrix Biology and Regenerative Medicine, School of Biological Sciences, Faculty of Biology Medicine and Health, The University of Manchester, Manchester Academic Health Science Centre, Manchester, UK.*

<sup>4</sup> *Manchester Academic Health Science Centre (MAHSC), The University of Manchester, Manchester, UK*

<sup>5</sup> *Department of Paediatric Nephrology, Royal Manchester Children's Hospital, Manchester University Hospitals NHS Foundation Trust, Manchester Academic Health Science Centre, Manchester, UK.*

### **Abstract**

We present a sensitive and low-cost immunoassay, based on a customized open-source quartz crystal microbalance coupled with graphene biointerface sensors (G-QCM), to quantify antibodies in undiluted patient serum. We demonstrate its efficacy for a specific antibody against the phospholipase A2 receptor (anti-PLA2R), which is a biomarker in idiopathic membranous nephropathy. A novel graphene-protein bio-interface was constructed by adsorbing a low concentration of denatured bovine serum albumin (BSA) on the reduced graphene oxide (rGO) sensor surface. The BSA film prevents the denaturation of the protein receptor on the rGO surface and serves as the cross-linker for immobilization of the receptor for anti-PLA2R antibodies on the surface. The detection limit and selectivity of this G-QCM biosensor were compared with a commercial QCM system. The G-QCM immunoassay exhibited good specificity and high sensitivity toward the target, with an order of magnitude better detection limit (of 100 ng/ml) compared to the commercial system, at a fraction of the cost and with considerable time-saving. The results obtained from patient sera compared favourably with those from enzyme-linked immunosorbent assay (ELISA), validating the feasibility of use in clinical applications. The multifunctional BSA-rGO platform provides a promising bio-functionalization method for universal immunoassay and biosensors. With the advantages of inexpensive, rapid and sensitive detection, the G-QCM sensor and instrument form an effective autoimmune disease screening tool.

**Keywords** Quartz Crystal Microbalance, Graphene, Immunoassay, Membranous Nephropathy, Biosensor

## Introduction

Graphene-based materials are promising candidates for the development of drug delivery vectors and biosensors [65], [72], [113], [208], [209] due to their high specific surface area [2], and ease of functionalization [7], [211]. The hydrophobicity of unmodified graphene materials and high sensitivity to charges and electrical fields, however, results in strong and nonspecific molecular adsorption which leads to poor selectivity for biological analytes when operating in an aqueous environment [240], [241]. It has been reported that the hydrophobic nature of graphene could cause conformational changes or denaturation in soft proteins leading to the loss of the binding function as their tertiary structures are disrupted [200], [242], [243]. This is result in poor sensitivity and detection limit for the biosensors. Several methods have been reported to functionalize graphene-based materials with protein receptors [4], [86], [244], [245] such that their tertiary structure and binding sites are preserved and presented. Noncovalent linkers, such as 1-pyrenebutanoic acid succinimide ester, N-hydroxy succinimide (NHS) ester tripod, bovine serum albumin (BSA), and pyrene butyric acid (PBA) have been successfully used to construct a biointerface in graphene-based biosensors to detect glucose [70], DNA [4], proteins [245], [246], and other biomolecules [247], [248]. Harnessing BSA as a biointerface layer offers various advantages including preventing non-specific binding [61], [246], improving biocompatibility [14], ease of use [249] and low cost [246], [249]. Zhou *et al.* suggested a one-step method using thermally denatured BSA activated with EDC/NHS to construct graphene field-effect transistor (GFET) for detecting a cancer biomarker, carcinoembryonic antigen [249]. However, FET biosensors suffer from lack of reproducibility of the signal when experimenting in concentrated biological samples like serum due to the high sensitivity to charges in the solutions [46], [250], [251]. Furthermore the manufacturing complexities of graphene FETs remains a major challenge to mass-market adoption as a medical diagnostic device [60], [245], [250].

We have developed a new biosensor instrument and technique based on a customized quartz-crystal microbalance (QCM), coupled with graphene biointerface sensing chips

[6], [200], and demonstrate it as an immunoassay tool for detecting antibody biomarkers. QCM is a commonly used piezoelectric transducer for biosensing; it is a highly sensitive weighing device based on measuring the change in mechanical resonance of the quartz crystal corresponding to the change of mass adsorption according to Sauerbrey's equation [252]. This mechanism allows for sensitive, label-free, rapid detection of analytes and a reproducible response. Compared to QCM, other label-free transducers like surface plasmon resonance (SPR) sensors rely on optical detection of the molecules on the gold-coated sensor chip. SPR has become a global pharmaceutical and clinical research standard [253], however, it requires expensive equipment and complex fabrication of sensors to accomplish high efficiency for biosensing compared to QCM transducers [42], [251], [254]. The most widely adopted method for the determination of immunochemical markers is enzyme-linked immunosorbent assay (ELISA) which is available as the first choice in most clinical laboratories. Due to its extremely high sensitivity, specificity, precision, and throughput, ELISA has served as the gold standard for various analytes [219], [255]. The main challenges for ELISA assays include high cost, testing duration and complexity owing to the many steps required to complete the assay [255] and the semi-quantitative nature of the assay which is based on a duplicate standard sample. For these reasons, specialized laboratories and highly skilled operators are required, resulting in the high costs of instrument and operation. With advantages of low-cost, high sensitivity, rapid detection and portable size, the QCM device described here shows promise as a point-of-care immunoassay tool, especially for remote locations or low and middle income (LMI) communities.

Nephrotic syndrome (NS) is kidney disease with typical symptoms of nephrotic range proteinuria, hypoalbuminemia, oedema and hyperlipidemia [144]–[146]. The syndrome can be characterized by the rise of glomerular permeability [144]. Membranous nephropathy (MN) is a common cause of NS in adults. Idiopathic membranous nephropathy (iMN) is found in 80% of MN patients affecting 10 to 12 cases per one million population [147], [148]. The important discovery in 2009 that circulating antibodies to phospholipase A2 receptor (PLA2R) present in 70% of patients with iMN identified the autoimmune nature of this pathologic abnormality [149]. As ~80% of

patients show proteinuria in the nephritic range, identifying some patients with proteinuria is a conventional physical examination [150]. However, performing an invasive renal biopsy for all suspected cases is infeasible resulting in its delayed diagnosis. Although MN displays a slow progression, and some patients enter a spontaneous remission phase, 30 to 40% of patients eventually develop end-stage renal disease or die [150]–[152].

Fresquet *et al.*, (2014) identified variably sized constructs of PLA2R reacting with anti-PLA2R under denaturing conditions (Western blotting) and non-denaturing conditions (native blotting) [145]. They found the dominant epitope of PLA2R was within the ricin-like N-terminal domain which competed effectively for the binding of autoantibodies in approximately 90% of the tested patient sera, confirming the presence of a major epitope within the N-terminal fragment of the receptor. As a result, NC3, which is the N-terminal to CTLD3 fragment, was used as a receptor in this study.

We have previously demonstrated the development and use of graphene-coated (G-) QCM chips to study interactions between biomolecules and graphene surfaces [6], [200]. We reported a simple method to obtain a film of denatured BSA (BSA) on rGO [200]. By physical adsorption BSA from a low-concentration solution in phosphate buffered saline (PBS) on to highly hydrophobic rGO at room temperature, a denatured ad-layer of BSA can be formed on the rGO. This method is a simple, fast and cost-effective way to employ BSA on graphene as an inert, biointerface for immobilizing specific protein receptors in graphene biosensors.

In this work, we first use a commercial QCM with dissipation monitoring (QCM-D) system (QSense Pro, Biolin Scientific) to establish the immuno-sensing performance of the G-QCM chip by studying the binding interactions between the receptor NC3 and murine anti-PLA2R antibody (Ab12). With QCM-D measurements, the interaction dynamics between the receptor and analyte can be systematically investigated, as the frequency parameter provides information about the mass adsorbed and film thickness while the dissipation parameter can provide mechanical information such as viscoelasticity of the adsorbed film on underlying surfaces [256], [257].

One of the main disadvantages of the commercial QCM-D system for use as a point-of-care instrument is its high cost. This in turn leads to slow test times as samples will need

to be sent to specialist laboratories. Here, we have developed a customised open-source-based QCM instrument where the openQCM system (Novaetech S.r.l., Italy) is the core sensing device [258], hereafter referred to as the C-QCM. In contrast to the QSense system, in which low fundamental frequency crystals (5 MHz) are used in a flowing fluid, our C-QCM employs crystals with a fundamental frequency of 10 MHz in a static fluid configuration, which provides higher sensitivity. Both systems were used to quantify the antibody in buffer solutions and patient sera samples. The results obtained from patient sera measured by both systems were compared with each other and validated against results from ELISA tests. We demonstrate that our C-QCM instrument coupled with G-QCM crystals is capable of highly sensitive, quantitative and reproducible immunoassay measurements in buffer and human serum, making it suitable for biological research, therapeutics development as well as point-of-care clinical diagnostics.

## Materials and methods

### 1. Materials and reagents

GO dispersion was prepared by a modified Hummers' method [202] followed by exfoliation and purification. Briefly, graphite flakes of 50 mesh (1 g) and  $\text{NaNO}_3$  (0.9 g) were mixed in concentrated  $\text{H}_2\text{SO}_4$  (35 ml) and left overnight to intercalate. The mixture was cooled down in an ice bath before slowly adding 4.5 g  $\text{KMnO}_4$  while continuously stirring. The mixture was left for 5 days at room temperature to allow graphitic oxidation. The brown slurry was diluted by slowly adding 5%  $\text{H}_2\text{SO}_4$  solution (100 ml), then diluted again with 100 ml mixture of 3%  $\text{H}_2\text{SO}_4$  and 0.5%  $\text{H}_2\text{O}_2$ . The homogenisation and complete exfoliation of graphite oxide was carried out using a vertical stirrer at a low speed for  $\sim 1$  h. The final GO dispersion was washed by repeated centrifugation and dilution with diluted  $\text{H}_2\text{SO}_4$ , followed by DI water, until the pH was close to neutral.

Albumin, monomer bovine (A1900), and phosphate buffered saline (PBS) tablets (P4417) were purchased from Sigma-Aldrich, UK. The PBS tablet was dissolved in milliQ water to obtain the solution with pH 7.4. BSA stock solution was prepared with a concentration of 1 mg/ml. The dilutions of BSA solution were prepared from the stock solution. The EDC and sulfo-NHS crosslinkers were purchased from Sigma-Aldrich (UK). Ethanolamine was used as a blocking buffer purchased from Sigma-Aldrich (UK). Bovine calf serum was

purchased from Sigma-Aldrich (UK). The production of NC3 receptor was previously described by Fresquet *et al.* [145]. The codon-optimized clone of human extracellular PLA2R was modified to generate the smaller PLA2R NC3 (~90 kDa) fragment. NC3 stock solution was prepared with a concentration of 2.5 mg/ml in PBS. The stock solution was diluted in PBS to 25 µg/ml for using in all experiments. More details about the process of production are in ESI 2.1. Murine anti-PLA2R monoclonal antibodies (Ab12) were generated previously for a binding study and determination of detection limit made in-house based on the protocol from Mauchauffé *et al.*[259]. The patient sera samples were from patients across Northwest region of the UK who involved in the PRISM trial [206] carried out at Manchester Institute of Nephrology and Transplantation, Manchester Royal Infirmary.

## 2. Customised openQCM construction

The C-QCM system consists of an Arduino *Micro* microcontroller board and an electronic shield that holds the excitation circuit for the crystal (Pierce oscillator) and a digital temperature sensor (MCP9808) placed in close proximity to the quartz crystal. The crystal is supported by a HC-48U type quartz holder. An enclosure for the C-QCM device and a fluidic cell were custom designed and fabricated using a Formlabs Form 2 3-D printer with clear resin (RS-F2-GPCL-04). The fluidic cell was designed to be suitable for pipetting liquid into the cell, see **Fig. 6.1(a)**. The volume of the fluidic cell is approximately 35 µL. The gold-coated quartz crystals with a fundamental frequency of 10 MHz (AT10-CUT) were purchased from Quartz Pro (Sweden). A custom graphic user interface (GUI) for data visualization and recording was developed in Matlab R2018a. A figure of the complete set-up of this device is included in ESI 2.2.

## 3. QCM chip surface coating and characterization

The stock dispersion of GO was diluted to a concentration of 0.8 mg/ml. QCM chips with gold surface electrode for both QSense (QSX-301, Biolin Scientific) and the C-QCM (QCM10140CrAu051-051-C1, Quartz Pro) were used in this study. The chips were cleaned following the protocol provided in Melendrez *et al.* [6], then coated with GO via spin coating (speed: 3000 rpm, acceleration: 350 s<sup>-1</sup>, 2 mins) to form a GO film on the entire surface of the chip. A controlled thermal treatment of the GO-coated chips was performed in a vacuum oven (Townson+Mercer EV018) with a temperature of 180°C for

6 hours to reduce the GO and obtain a highly hydrophobic rGO coating as described in our previous study [200].

The degree of reduction was characterized by means of their wetting contact angle (WCA) using sessile drops of DI water (Kruss DSA100) in combination with X-ray photoelectron spectroscopy (XPS) using a SPECS custom built system composed of a Phoibos150 hemispherical electron analyser with 1-D detector. The XPS data was analyzed using CasaXPS software (version 2.3.18). Scanning electron microscopy (SEM) was performed on a Zeiss Ultra using an accelerating voltage of 5 kV and 5 mm working distance with secondary electron imaging to characterize the morphology of graphene coatings on Au surfaces.

#### 4. Receptor immobilization and antibody binding studies using QCM-D

The NC3 receptor was immobilized on different functional surfaces followed by antibody-receptor binding studies, under QCM-D monitoring using the QSense Pro system. The temperature of the system was stabilized at 25 °C to avoid the effects of thermal drift. The basic sequential injection steps for QCM-D monitoring of the antibody binding include: (1) a baseline stabilization regime in which PBS is flowed until stability is reached, (2) immobilization of the NC3 receptor, (3) blocking non-specific adsorption and (4) detection of the antibody followed by rinsing. The complete procedure is described in ESI 2.3.3. The concentration of NC3 and the antibody in PBS were fixed at 25 µg/ml and 1 µg/ml, respectively. In this work, the odd harmonics from the 3<sup>rd</sup> to the 11<sup>th</sup> were recorded. Our discussion of results is based on the 3<sup>rd</sup> harmonic. The measurement of the frequency shift after the adsorption of the antibody was used to investigate the capability of each sensing surface to detect the antibody. From these observations the highest shift was selected for further studies.

#### 5. Concentration sequence and specificity studies

Using the QCM-D system, the binding of various concentrations of Ab12 was first studied. NC3 receptor at a concentration of 25 µg/ml in PBS was injected on the selected functional surfaces of the sensing chip following the receptor immobilization protocol (ESI 2.3.3), followed by the injection of PBS to rinse the surface. Ethanolamine was used as a blocking agent to prevent non-specific adsorption on the amine functional groups.

Before binding with the antibody, the sensing surface was rinsed with PBS until baseline stability was reached and the acquisition was restarted. This procedure was repeated twice to ensure adequate cleanse of unbound molecules. Then, the diluted antibody was injected for approximately 20 minutes and finally rinsed with PBS for 20 minutes. The flow rate for this experiment was kept at 10  $\mu\text{l}/\text{min}$ . Various concentrations of the antibody – 0.5  $\mu\text{g}/\text{ml}$ , 1  $\mu\text{g}/\text{ml}$ , 20  $\mu\text{g}/\text{ml}$ , 50  $\mu\text{g}/\text{ml}$  and 100  $\mu\text{g}/\text{ml}$  were monitored in this study where each sensing chip measured one concentration. A group of frequency shifts was recorded as a quantitative measure for each concentration of the antibody. The measurement for each concentration was repeated 3 times.

To evaluate the selectivity of the sensor in complex fluids such as serum, calf serum was used as a sample media. Three different samples were used in this experiment. First, plain calf serum diluted with PBS 1:1 was used as a negative control. The second sample is Ab12 mixed in diluted calf serum (1:1 serum: PBS) to obtain an antibody concentration of 50  $\mu\text{g}/\text{ml}$ . The third sample is Ab12 in PBS with a concentration of 50  $\mu\text{g}/\text{ml}$ . QCM-D monitoring of adsorption of the samples on NC3-functionalised sensing chips were run at the same time to reduce variability due to environmental effects.

In addition, a QCM-D measurement was conducted in order to contrast the results of diluting various concentrations of the antibody in the diluted calf serum with those obtained from the series of the antibody concentration in PBS. The concentrations used for this experiment include: 0.5  $\mu\text{g}/\text{ml}$ , 1  $\mu\text{g}/\text{ml}$ , 20  $\mu\text{g}/\text{ml}$ , 50  $\mu\text{g}/\text{ml}$  and 100  $\mu\text{g}/\text{ml}$ .

#### 6. Ab12 detection using the C-QCM

The C-QCM system was then used to evaluate the detection of Ab12. The G-QCM sensing chips were functionalized with NC3 receptor using the same steps as for the QCM-D system, **Fig. 6.2(b)**. In each step, 40  $\mu\text{L}$  of sample were pipetted into the fluidic cell and allowed to stabilize until the frequency signal was stable. This process was then followed by the injection of the next reagent. A peak in the frequency response occurs during the liquid injection due to the abrupt change of pressure on top of the sensing chip, however, the signal stabilizes within a few minutes. Due to the fact that QCM sensors with higher frequencies are prone to be affected by hydrodynamic pressure, a poor signal to noise ratio (SNR) is presented under flowing fluids, resulting in less sensitivity of the measurements [260], [261]. Therefore, our measurements were performed under



static fluid pressure in order to prevent any effects from eventual pump noise and to improve the sensitivity.

After functionalizing the receptor on the QCM chip and blocking the non-specific adsorption with the ethanolamine blocking buffer, the samples with different concentrations of the antibody in PBS buffer ranging from 0.1  $\mu\text{g/ml}$  to 100  $\mu\text{g/ml}$  were assessed. For each measurement, the specimen was injected into the fluidic cell and allowed to bind for 10 minutes followed by the injection of PBS to rinse the surface until a flat signal was achieved indicating that no further adsorption occurs. The final frequency shift was recorded as a value that corresponds to the antibody binding. This experimental procedure was repeated at least twice for each specimen.

#### 7. Patient serum evaluation using the QSense and the C-QCM

To investigate the feasibility of the C-QCM immunoassay for practical diagnostic applications, we analyzed eight human serum samples. Each serum sample was diluted with PBS to a ratio of 1:3. The QSense and the C-QCM systems were used to perform comparative analysis. The aforementioned procedures for the immobilization of the receptor and the measurement of antibody binding were applied. The testing protocol for the QSense system starts by flowing PBS over the functionalized chip for five minutes to obtain a baseline, then the sample is injected with a flow rate of 10  $\mu\text{L/min}$  for 20 minutes (total sample volume of 200  $\mu\text{L}$ ) and finally rinsing with PBS for at least 10 minutes. For the C-QCM system, the PBS solution was kept static over the functionalized QCM chip reading the settling frequency as a baseline then 40  $\mu\text{L}$  of the specimen was injected and let to be adsorbed for 10 minutes. After this, sequential injections of PBS were performed to rinse the surface of chip until the observed signal was flat. Each test was repeated at least three times. The results from the two systems were compared to each other and with those obtained by the ELISA test performed in-house.

#### 8. ELISA Assay

The ELISA tests were performed using serum samples from the patients across the Northwest region of the UK involved in the PRISM trial [206]. Samples were analyzed using our in-house ELISA using previously published protocol [262]. The enzyme substrate is TMB. The purified extracellular recombinant PLA2R protein was used to coat ELISA microplates at a concentration of 0.125  $\text{mg/ml}$  in sodium bicarbonate buffer of pH

9.6 for 18 hours as a receptor for anti-PLA2R antibody. Patient serum diluted 1:100 in superblock (0.1% Tween 20) was added in duplicate 100-ml aliquots to the ELISA plate, then the plate was left two hours for incubation at room temperature on a plate shaker. After that, the plates were washed thoroughly (8 times) with PBS plus 0.1% Tween 20. Anti-human IgG-HRP conjugate (Jackson Immuno Research, Newmarket, UK) diluted 1:25,000 in Superblock was added (100 ml per well) and incubated for two hours then washing and adding enzyme substrate TMB (Sigma Aldrich). After leaving it for 10 mins, 0.5 mol/l H<sub>2</sub>SO<sub>4</sub> was added to stop the reaction. The plates were read at 450 nm and standard curves were plotted using the Softmax software Molecular Devices (Sunnyvale, CA). A dilution series covering the range of 3000–12.3 U/ml was applied for each ELISA plate. The samples with ELISA results less than 40 U/ml were considered normal or negative. Upper limit is 3000 U/ml.

## Results and discussion

### 1. Binding studies

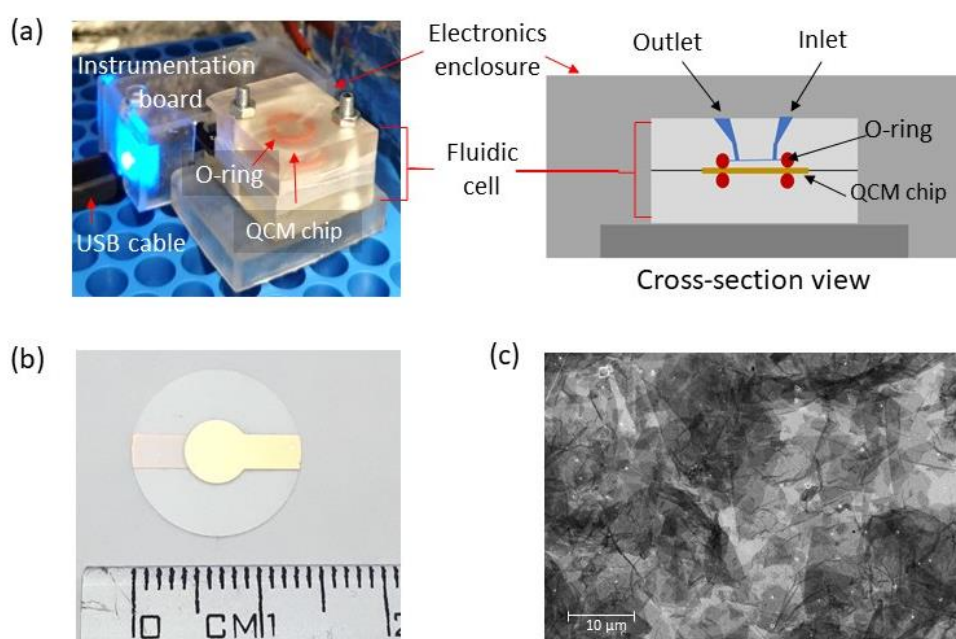
#### Dot blot

The binding between the NC3 and the Ab12 was tested using the dot blot technique. A varied concentration set of NC3 and the denatured NC3 were used. The results and discussion from this evaluation are detailed in ESI 2.4. In brief, it was confirmed that the Ab12 specifically binds with the non-denatured NC3.

#### Characterization of graphene coating and functionalization

We have explored different methods to functionalize the protein receptor including both physical adsorption and covalent immobilization. Eight different functional surfaces were used in this comparative study including: 1) Au, 2) GO, 3) rGO, 4) Au with denatured BSA coating (Au-BSA), 5) rGO with BSA coating (rGO-BSA), 6) rGO with non-denatured BSA coating (rGO-BSA), 7) Au with self-assembled monolayer (SAM) with COOH terminal groups (Au-SAM), and 8) rGO-BSA activated with EDC/NHS for amine coupling (rGO-BSA+EDC/NHS). Based on our previous paper, a denatured layer of BSA is formed when BSA is adsorbed on Au or highly hydrophobic rGO surface from a low concentration solution [200]. SEM imaging reveals that the spun-on graphene coatings

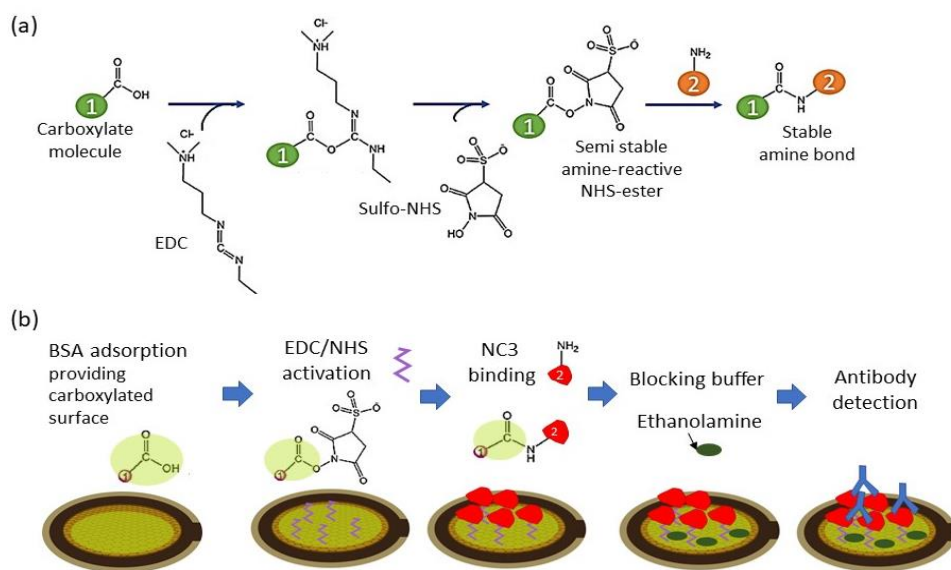
on the Au surface of QCM-D chips comprises of a continuous film of overlapping flakes covering the entire surface, with film thickness varying from one to few monolayers **Fig. 6.1(c)**. The individual graphene flakes are comprised of 100% of monolayers (ESI 2.6). The graphene coverage is uniform over large areas on all samples studied (ESI 2.6). The surface functionalization of the different stages of rGO functionalization was characterized using XPS and Raman. XPS spectra of rGO, rGO-BSA and rGO-BSA-EDC/NHS were measured, see **Fig. S2.5** in ESI 2.7.



**Fig. 6.1** Photographs and layout of the sensor chip. **(a)** C-QCM instrument setup and cross section schematic of the C-QCM device with a custom-designed microfluidic channel. **(b)** Photograph of a rGO coated QCM sensing chip **(c)** Scanning electron microscope (SEM) image of the rGO coating on a QCM chip.

The C1s spectrum obtained from rGO displays low intensity of oxygen functional groups but high intensity of carbon peak. Adsorbing BSA on rGO adds to the carboxylate groups. After activating rGO-BSA with EDC/NHS, the deconvoluted peaks of C-N and CO-NH were enhanced while C-O decreases. The sample with EDC/NHS activation clearly shows the C-N peak observed from both C1s and N1s profiles. The spectrum for rGO-BSA with EDC/NHS shows the emergence of the C-N peak at 399.7 eV corresponding to the presence of the secondary amine and imine of EDC while the peak at 402.1 eV could be the characteristic of the nitrogen of the NHS ester [263]. The presence of carbon and nitrogen bonds confirms the activation of carboxylic acid functional group of the BSA on

rGO, see the deconvoluted peaks in **Fig. S2.6**. Further details about the XPS results are discussed in ESI 2.7.



**Fig. 6.2** Schematic for surface functionalisation using EDC/NHS crosslink (a) mechanism of carbodiimide crosslinker using EDC/NHS activation, (b) functionalization of rGO surface to detect the antibodies starting with BSA adsorption, activation with EDC/NHS, immobilization of the receptor NC3 (in red) via amine covalent cross-link and blocking with ethanolamine.

Raman spectra of rGO, rGO-BSA and rGO-BSA+EDC/NHS were measured to obtain information about lattice defects, see ESI 2.8. Two main peaks including graphitic (G) and defect (D) occur at  $\sim 1580\text{ cm}^{-1}$  and  $\sim 1350\text{ cm}^{-1}$ , respectively. The relative intensity of D to G ( $I_D/I_G$ ) indicates the in-plane crystallite size or the disorder in the sample. The  $I_D/I_G$  value of rGO is 0.89 which is lower than that of rGO-BSA and rGO-BSA+EDC/NHS samples, which exhibit similar  $I_D/I_G$  value 0.97 and 0.95 respectively. The higher  $I_D/I_G$  values obtained from functionalized rGO samples could originate from defects and effects of doping functional groups through BSA adsorption. Two other bands were observed at  $2700$  and  $2900\text{ cm}^{-1}$ , known as 2D and D+G peaks, respectively. The 2D band is an indicator of the number of graphene layers if it is a sharp peak. Another band is a second-order peak derived from the D–G peak combination. All samples present broadened band, attributed to the fact that the graphene coating contains few layers with some defects from oxygen functional groups in rGO and protein doping.

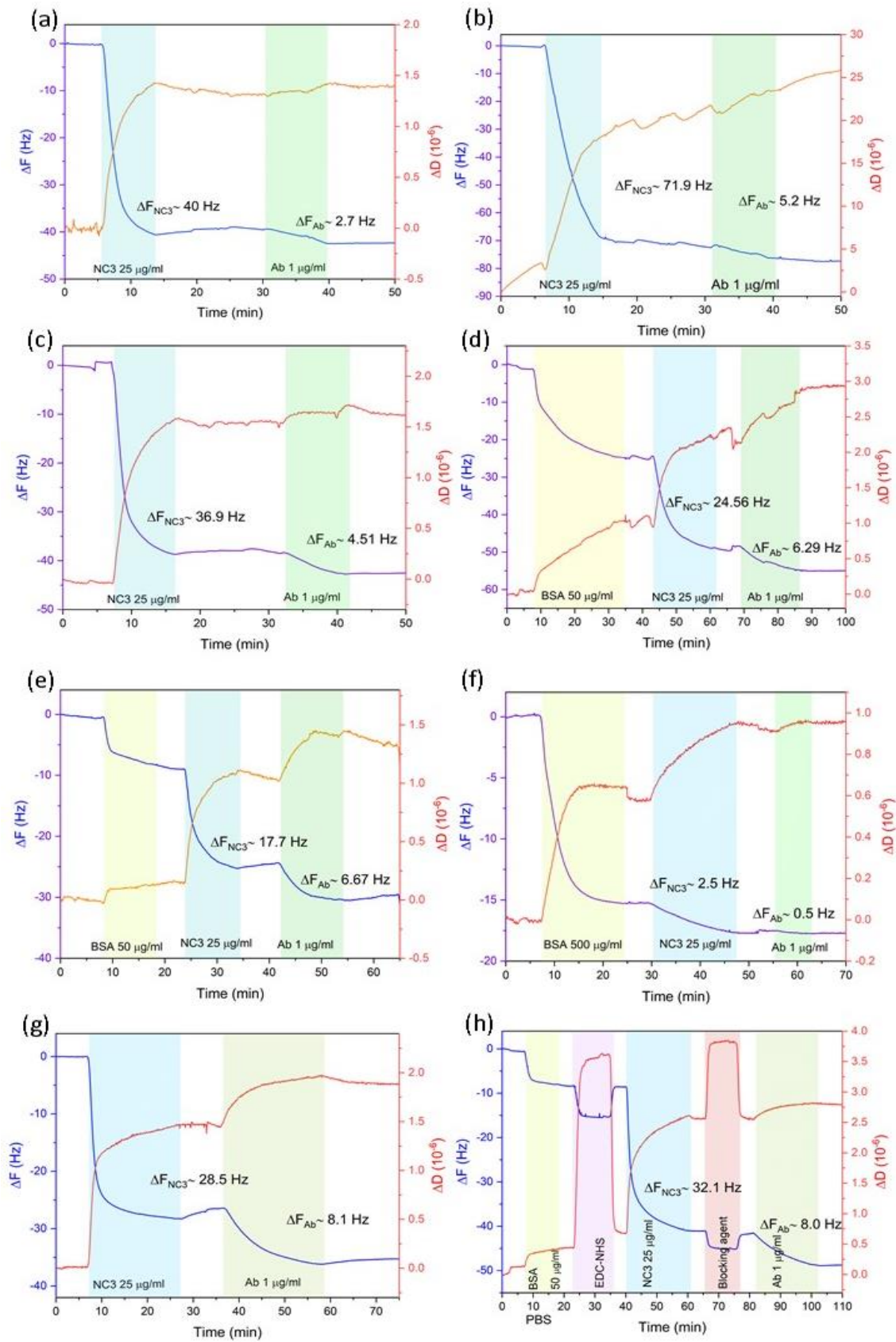
### Exploration of sensing surfaces using QCM-D

The results from the QCM-D monitoring of receptor protein (NC3) immobilization on different sensing surfaces and the detection of Ab12 are presented in **Fig. 6.3**. The resultant frequency shifts from the adsorption of NC3 (receptor) and Ab12 (analyte) are given in **Table 6.1**.

**Table 6.1** The QCM-D results of the adsorption of NC3 (receptor) and Ab12(analyte) on all sensing surfaces for comparison of sensing performance

Sample NO.	Surfaces	NC3 (receptor)		Ab12 (analyte)	
		$\Delta F$ (Hz)	$\Delta D$ ( $\times 10^{-6}$ )	$\Delta F$ (Hz)	$\Delta D$ ( $\times 10^{-6}$ )
1	Au	40.0 $\pm$ 0.8	1.39 $\pm$ 0.05	2.7 $\pm$ 0.8	0.08 $\pm$ 0.2
2	GO	70.0 $\pm$ 11.3	16.1 $\pm$ 4.5	5.4 $\pm$ 1.2	5.03 $\pm$ 2.3
3	rGO	36.0 $\pm$ 0.7	1.53 $\pm$ 0.02	4.5 $\pm$ 0.8	0.14 $\pm$ 0.05
4	Au-BSA	24.6 $\pm$ 3.2	1.21 $\pm$ 0.08	6.5 $\pm$ 2.1	0.56 $\pm$ 0.08
5	rGO-BSA	17.7 $\pm$ 1.1	0.89 $\pm$ 0.06	6.5 $\pm$ 1.3	0.33 $\pm$ 0.05
6	rGO-BSA	2.4 $\pm$ 0.8	0.37 $\pm$ 0.03	0.2 $\pm$ 0.1	0.03 $\pm$ 0.01
7	Au-SAM	27.0 $\pm$ 1.2	1.47 $\pm$ 0.04	8.0 $\pm$ 1.2	0.50 $\pm$ 0.2
8	rGO-BSA+EDC/NHS	32.5 $\pm$ 4.3	1.89 $\pm$ 0.07	8.1 $\pm$ 2.2	0.40 $\pm$ 0.04

The adsorption of NC3 on Au and rGO surfaces display lower dissipation values compared to GO possibly due to the different orientation of the molecules on the surfaces [200]. When high dissipation values were obtained higher errors on the frequency shifts occurred as it can be observed in Table 1. Thus, we propose that the GO surface is not suitable to be used as a sensing platform for a traditional QCM immunoassay as it could result in high detection errors. Direct immobilization of NC3 on Au and rGO detected less antibody compared to those surfaces with an adlayer of BSA (samples 4, 5) as the thin layer of BSA could prevent the denaturation of the NC3 during the adsorption process [200]. However, the rGO with non-denatured BSA sensor (sample 6) presents relatively less adsorption of NC3 and no binding of the Ab12 was detected. This is due to the fact that BSA acts as a blocking agent preventing other molecules to adsorb onto the surface.



**Fig. 6.3** QCM-D monitoring of receptor protein (NC3) immobilisation and anti-PLA2R antibody (Ab12) detection using different sensing surfaces (a) Au, (b) GO, (c) rGO, (d) Au-BSA, (e) rGO-BSA, (f) rGO-BSA, (g) Au-SAM, and (h) rGO-BSA+EDC/NHS.

Quantitatively, the detection of antibody was higher on the platform using the covalent binding methods (samples 7, 8) as specific-binding sites can be promoted through the crosslink of functional groups. Both the rGO-BSA+ EDC/NHS and the Au-SAM samples present the highest antibody binding responses, in terms of the frequency shifts, with similar values of approximately 8.0 Hz. We reason that the covalent binding due to amine coupling on the carboxylate surface can promote the specific-site binding of NC3 on the surface and reduce its denaturation allowing the antibody binding sites remain actively functional. The mechanism of EDC/NHS activation is presented in **Fig. 6.2(a)**.

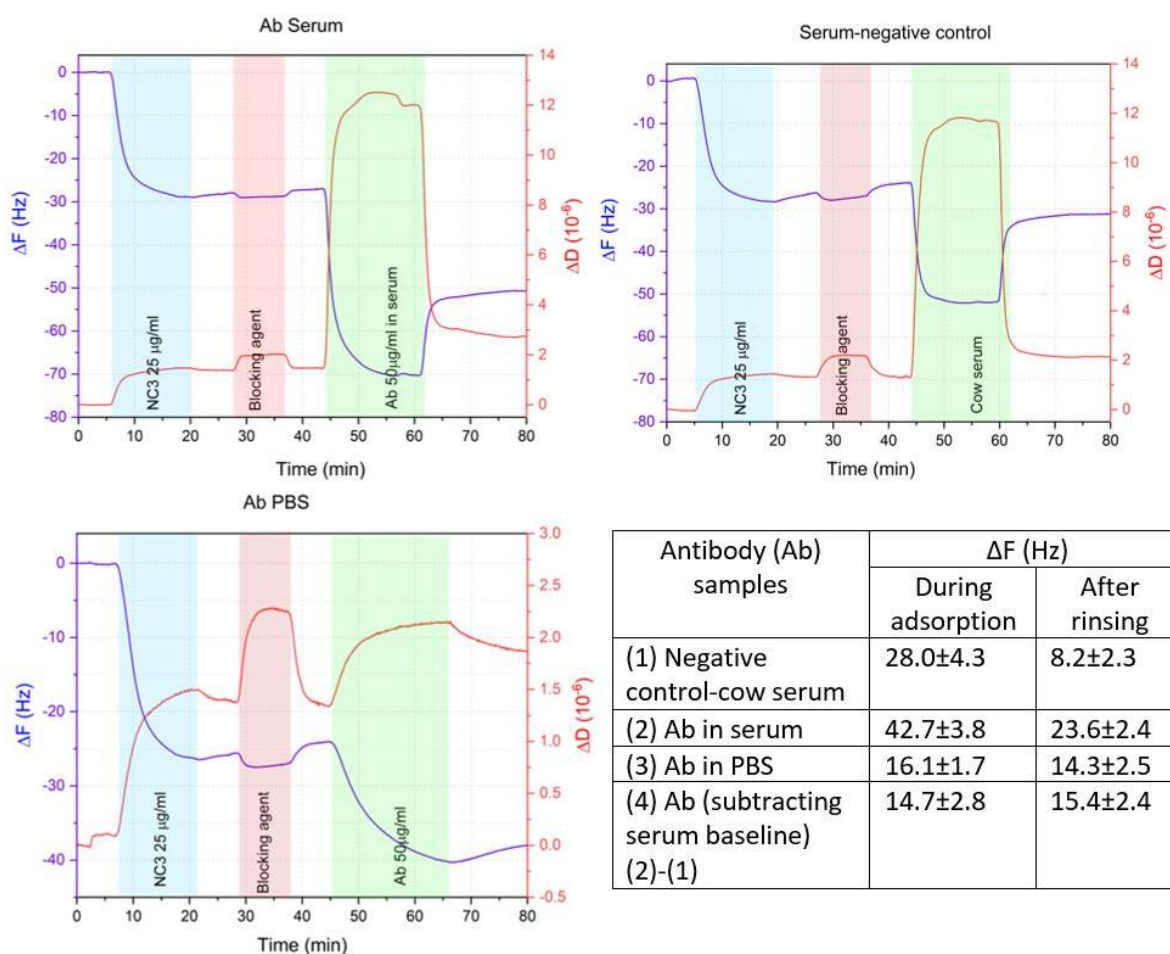
Although both surfaces present comparable results for antibody detection, the preparation for rGO-BSA + EDC/NHS surface requires simple adsorption of the protein and activating agent on rGO at room temperature; process that is much simpler and less time-consuming compared to Au-SAM preparation requiring more chemicals and overnight preparation (see ESI 2.5 for details of Au-SAM preparation). Therefore, the rGO-BSA + EDC/NHS platform was selected for further studies.

## **2. Ab12 detection and specificity analysis using QCM-D**

The rGO-BSA+EDC/NHS surface was used as a sensing platform for this study. The schematic for QCM surface functionalization using EDC/NHS crosslink is presented in **Fig. 6.3** with the following injection sequence: BSA 50  $\mu\text{g}/\text{ml}$   $\rightarrow$  EDC/NHS  $\rightarrow$  NC3  $\rightarrow$  blocking buffer  $\rightarrow$  antibody sample. We observe that both the frequency and dissipation increase as a function of the antibody concentration. The adsorption rate increases with respect to the concentrations. After the rinsing step, some loosely bound molecules lifted off from the surface as observed from the decrease of the frequency shift.

The results for the selectivity test with calf serum are presented in **Fig. 6.4**. The adsorption of three different samples, (1) the negative control calf serum, (2) 50  $\mu\text{g}/\text{mL}$  Ab12 in the diluted calf serum and (3) 50  $\mu\text{g}/\text{mL}$  Ab12 in PBS, on NC3-functionalised sensing chips were obtained at the same time and under the same environmental conditions. The sample (1) exhibits a final frequency shift of  $\sim 8$  Hz which corresponds to the serum background, while sample (2) presents a final shift of  $\sim 24$  Hz. By subtracting the frequency shift in sample (1) from (2), the result is similar in value to that from sample (3). These results confirm that the binding of the antibody can be selectively detected directly in concentrated animal serum. The concentration of

antibody in serum can be quantified by subtracting the final frequency shift from the background value obtained from the plain serum.



**Fig. 6.4** QCM-D study for selectivity test against calf serum of the sensing platform rGO-BSA with EDC/NHS activation. **a)** the detection of the antibody diluted in serum **b)** bare serum (negative control) **c)** the antibody diluted in PBS and a table for frequency shifts resulting from the detection of the antibody measured during adsorption and after rinsing process

The detection of Ab12 with the NC3, at various concentrations ranging from 0.5 μg/ml to 100 μg/ml in PBS, was monitored in real-time using the QCM-D technique (**Fig. 6.5(a)**). The frequency shift ( $\Delta F$ ) obtained from the QCM-D measurement relates to the mass adsorbed on the sensing surface, while the dissipation change ( $\Delta D$ ) is related to the viscosity of adsorbed material. Further details on the QCM-D operation principle are discussed in ESI 2.3. From the  $\Delta D$ - $\Delta F$  plot of the QCM-D results (**Fig. 6.5(b)**), the slope increases with respect to the concentration of the antibody.

The binding of various concentrations of the Ab12 in calf serum (ranging from 0.5 μg/ml to 100 μg/ml) was measured, shown as **Fig. 6.5(c)**. During the adsorption process (green



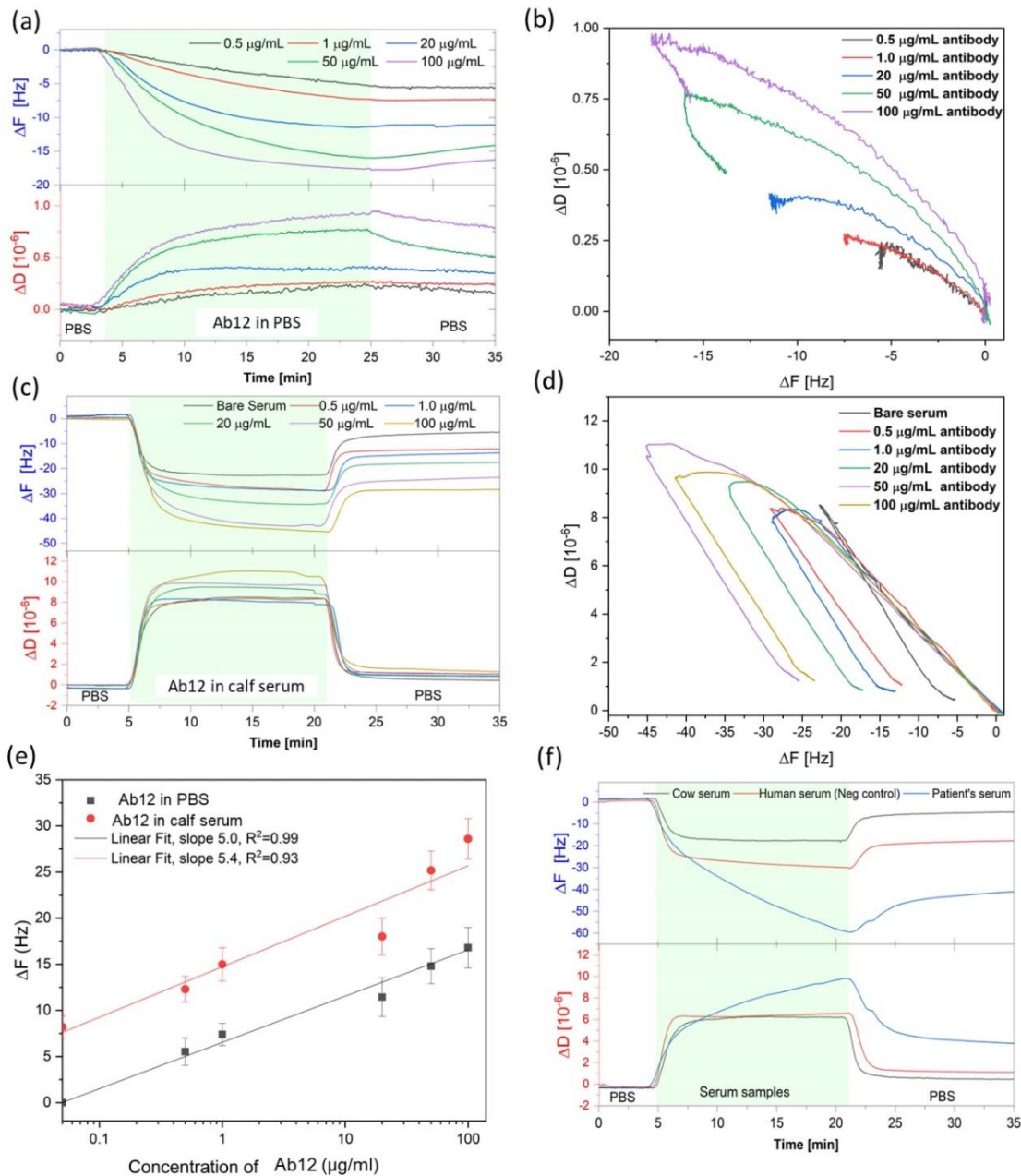
band), all samples exhibited the same high adsorption rate at the initial stage. In addition, the  $\Delta D-\Delta F$  plot (**Fig. 6.5(d)**) shows that the initial slopes are of the same value implying that the same adsorption event occurs. Thus, we reason that this adsorption behavior could result from loading the serum on the chips.

Then, the adsorption rate for each sample slows down or flattens due to a possible saturation of the surface. After the rinsing step, the final frequency for each sample shifted back by approximately 25 Hz as non-specific and unbound molecules in the serum were rinsed off. However, the final energy dissipation values observed from all concentrations are similar, between 0.5 to  $1.3 \times 10^{-6}$ . Interestingly, in the case of blank serum, the  $\Delta D-\Delta F$  graph shifts back immediately after reaching the highest point while the other cases exhibit association curves at the highest region (**Fig. 6.5(d)**). We assume that the association curves could originate from the antibody binding.

**Fig. 6.5(e)** shows the comparison between the detection of the antibody in PBS and in calf serum by plotting the Ab12 concentration against frequency shift. A series of frequency shifts obtained from the antibody in calf serum are higher than those in PBS around 8 Hz due to the serum background. However, the plots from both series show similar trends with slopes of 5.0 and 5.4 for the antibody in PBS and in calf serum, respectively. Therefore, the frequency shift can be used as a comparative value to indicate the antibody concentration.

**Fig. 6.5(f)** presents the comparison of the antibody detection in three different media including plain calf serum, human serum from a healthy person (blank) and MN-patient serum (serum with high anti-PLA2R). The final frequency shifts obtained from these three samples are 8.5 Hz, 20 Hz and 44 Hz, respectively. Serum are aqueous solutions with high protein contents including mainly albumins and globulins. It also contains a variety of other substances such as lipoproteins, enzymes and hormones, carbohydrates, lipids and amino acids as well as electrolytes, organic wastes and organic molecules [264]. For identifying serum components, the remaining serum on the chip can be transferred to be characterized using mass spectrometry. These components could contribute to the background signal from the blank samples due to non-specific substance adsorption on the unblocked gaps on sensing surface or even on the receptor protein.

Additionally, the adsorption results from blank human serum are higher than that from calf serum. This suggests that non-specific binding in the assay is higher in human serum than in calf serum. It is possibly because the components of human serum can bind to the protein receptor NC3 more than those from animal serum as NC3 was cloned from human extracellular PLA2R.



**Fig. 6.5** QCM-D results for binding studies (a) frequency and dissipation profiles upon detection of varied concentrations of the Ab12 in PBS buffer and (b) their  $\Delta D$  -  $\Delta F$  plots of the antibody detection. (c) QCM-D monitoring of varied concentrations of the Ab12 in calf serum and (d) their  $\Delta D$  -  $\Delta F$  plots (e) comparison of the detection results obtained from varied concentration of the antibody in PBS and calf serum (f) QCM-D monitoring of three serum samples including plain calf serum, human sera from a healthy person and a MN patient.

### 3. Detection of Ab12 using the C-QCM system

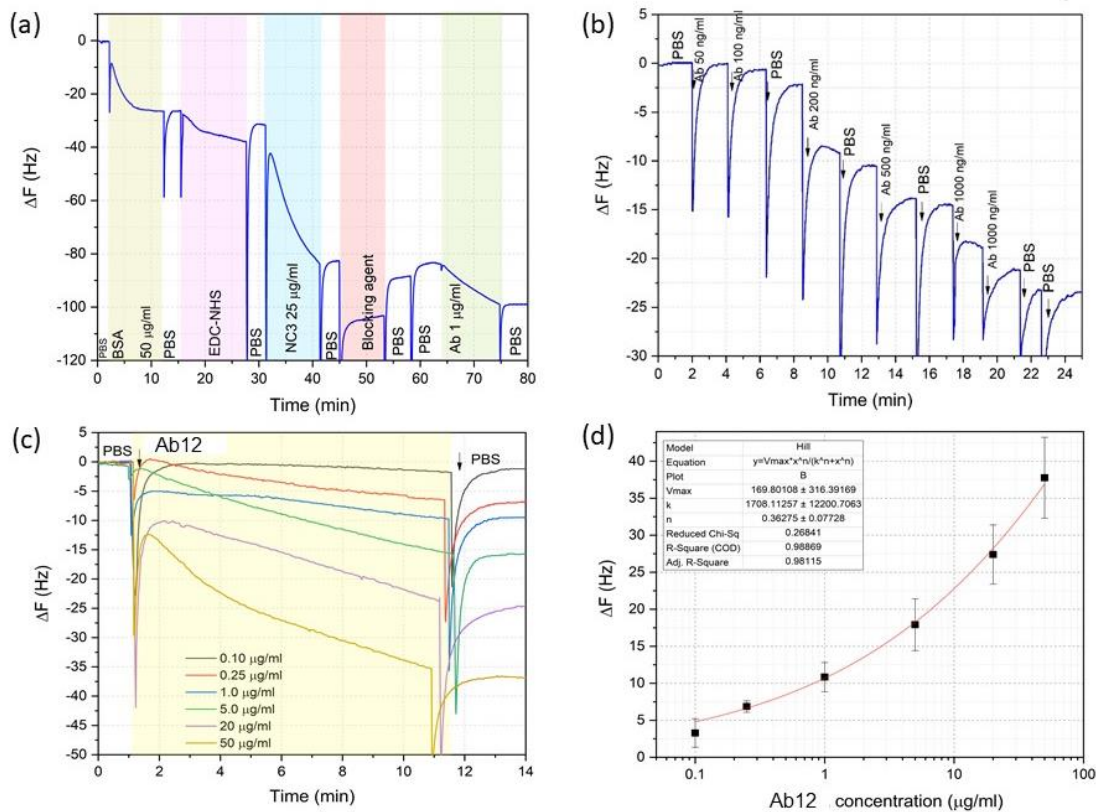
Before the immunoassay studies, our C-QCM system set-up and rGO-coated chips were tested for reproducibility when liquid samples were sequentially injected via pipetting. DI water and PBS buffer were used as liquid samples. The results are presented in ESI 2.10. The resultant frequency shifts due to the weight of DI and PBS buffer are 2107 Hz and 2361 Hz with standard deviation of 18 Hz and 19 Hz, respectively. The observed values are in line with the results presented by Kanazawa and Gordon for the air-water loading of QCM sensors [265], [266]. We conclude that the measurements using this C-QCM system could display an error of up to 1%, reflecting good reproducibility of the proposed technique.

To detect the Ab12 using the C-QCM, we replicated the same analytical steps from the QCM-D experiments including the doping BSA on rGO, the activation using EDC/NHS, receptor immobilisation and blocking, as shown in **Fig. 6.6(a)**. The overall frequency monitoring from both QSense and C-QCM systems present similar responses.

We further investigated the quantitative analysis capabilities of this immunoassay system with a series of antibody concentrations in PBS samples. We initially explored the detection in one QCM chip, see **Fig. 6.6(b)**. The starting chip is rGO-BSA+EDC/NHS functionalised with NC3 as a receptor. The antibody concentrations, ranging from 0.05  $\mu\text{g/ml}$  to 50  $\mu\text{g/ml}$ , were injected on to the functionalized chip. An observable frequency change occurs when the antibody concentration is equal or higher than 0.1  $\mu\text{g/ml}$ . After the initial exploration, we detected the level of antibody binding from individual concentrations. The final  $\Delta F$  value was recorded after 10 minutes from the initial injection of the sample followed by rinsing with PBS. The measurements were repeated at least three times. **Fig. 6.6(c)** and **(d)** present the QCM profiles for the different antibody concentrations and the plot of the final  $\Delta F$  value for each concentration. It is clear that the  $\Delta F$  value linearly increases with respect to the antibody concentration. In these two experiments, the detection limit was estimated to be 100 ng/ml. The obtained mean  $\Delta F$  for 0.10  $\mu\text{g/ml}$  is  $4.1 \pm 1.7$  Hz.

Previous reports have suggested that the cut-off point for an abnormal anti-PLA2R-IgG concentration can be defined as  $> 0.9 \mu\text{g/ml}$  [144], [267]. Huang *et al.* quantified anti-PLA2R-IgG antibody concentration in 45 healthy volunteers, 31 IgA nephropathy, 9 lupus

nephropathy, and 52 idiopathic membranous nephropathy patients using fluorescent-based immunoassay [144]. They reported that serum anti-PLA2R-IgG levels in healthy volunteers ranged from 0.09–0.91  $\mu\text{g}/\text{ml}$  [267]. Based on this cut off concentration, the developed QCM immunoassay can detect the concentration of anti-PLA2R antibody at about one magnitude lower than the cut-off value.



**Fig. 6.6** Results from Ab12 antibody detection using C-QCM system. **(a)** The whole injection sequence on rGO coated on Au QCM chip **(b)** QCM results for sequential injection of varied concentrations of the Ab12 samples. **(c)** QCM profile for varied concentrations. The starting chip for **(b)** and **(c)** is rGO-BSA+EDC/NHS functionalised with NC3 as a receptor. **(d)** calibration curve obtained from the final frequency shifts against concentration of the antibody.

#### 4. Comparison between QCM-D and the C-QCM

Comparing the results obtained using the QSense and the C-QCM, certain similarities and differences were observed. Considering all the steps involved in performing an immunoassay using the QCM-D and the C-QCM instruments, as seen in in **Fig. 6.3(h)** and **Fig. 6.6(a)**, the sequential frequency shifts and recoveries recorded by both systems look similar. However, there are specific differences between the results from the two systems due to the use of different crystals and measuring protocols.

Firstly, frequency spikes occurred at the injection points in the result from the C-QCM, due to the change of hydrodynamic pressure during pipetting. However, it does not affect the overall measurement if the signal is allowed to stabilize.

Secondly, the frequency shift values for each injection step monitored by the C-QCM are higher than the values from the QSense, because higher fundamental frequency crystals (10 MHz) were used in a static fluid configuration in the C-QCM while 5 MHz crystals were used in the QSense under fluid flow. With the same amount of adsorption, in theory, the frequency shift value obtained from the 10 MHz crystal should be four times higher than the 5 MHz one. However, the main problem of using high fundamental frequency crystal is a low signal to noise ratio [260], especially in liquid phase adsorption as the signal can be really fluctuated due to unstable liquid flow, and the full 4x gain is not achieved. Thirdly, the total assay time spent on the C-QCM is less than the total time for the QCM-D measurement. As 10 MHz crystals were used, higher  $\Delta F$  results are presented in a shorter time. The  $\Delta F$  result for the detection of 1  $\mu\text{g}/\text{ml}$  Ab12 in PBS obtained from the QSense and the C-QCM are  $\sim 7$  Hz and  $\sim 18$  Hz respectively. The clear change of  $\Delta F$  for antibody detection can be seen in 10 minutes when using the C-QCM.

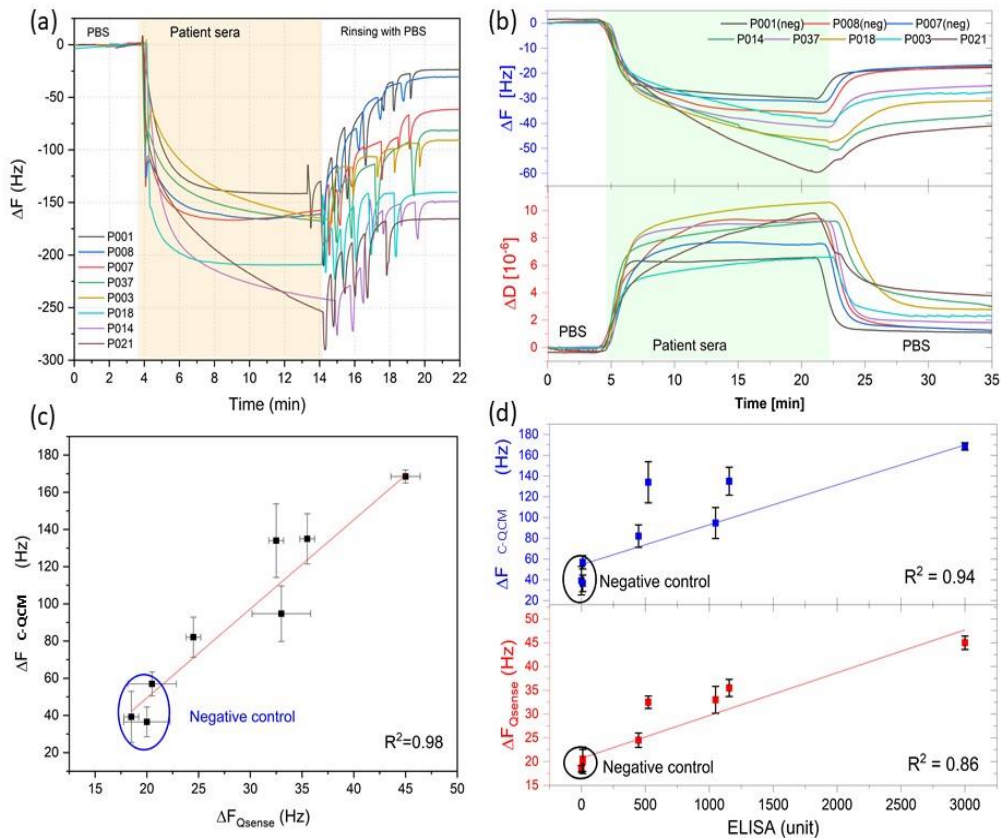
## 5. Testing with patient serum samples

To validate the feasibility of developing the QCM immunoassay for clinical applications, we analysed 8 human serum samples obtained from patients living in the UK using the commercial QCM-D from QSense and our C-QCM system and compared our results with those obtained by ELISA.

**Fig. 6.7(a)** presents the QCM profiles measured by the C-QCM system. Samples P001, P007 and P008 are negative controls. The final  $\Delta F$  values range from 30 Hz to 170 Hz.

**Fig. 6.7(b)** displays the frequency and dissipation changes after testing with patient sera obtained from the QCM-D measurement. The final  $\Delta F$  values are in the range of 20 Hz to 50 Hz, and  $\Delta D$  values after rinsing are between  $1.7 \times 10^{-6}$  and  $4.5 \times 10^{-6}$ . The final  $\Delta D$  value linearly corresponds to the final  $\Delta F$  for each specimen, shown in **ESI 2.11**. Yet,  $\Delta D$  profiles during serum adsorption present a different trend to the final values resulting from the differences in viscosity of patient sera. By comparing the  $\Delta F$  results obtained from the QSense and the C-QCM, we obtained the regression equation  $y = 4.8(\pm 0.2)x - 46(\pm 9)$ , where  $x$  represents the frequencies for the QSense system while

y corresponds to the frequencies for our C-QCM. A correlation coefficient ( $R^2$ ) of 0.98 was obtained, shown as **Fig. 6.7(c)**. This indicates that the results from both systems are comparable in terms of quantitative analysis and specificity.



**Fig. 6.7** Detection results for the anti-PLA2R antibody in 8 patients' sera using (a) the C-QCM system and (b) QCM-D system. (c) Correlation plot of the final frequency shifts obtained from the C-QCM and the QCM-D (d) Comparison of the results obtained from C-QCM measurements and ELISA.

We compared QCM results obtained from both systems to those obtained from ELISA which is a standard immunoassay method to screen patients. As can be seen in **Fig. 6.7(d)**,  $\Delta F$  results from both QCM systems show correlated results to those from ELISA titration with  $R^2$  of 0.94 for the C-QCM and 0.86 for the QSense. Moreover, specimens with very low or zero anti-PLA2R (negative control) can be identified using the C-QCM and present consistency to the ELISA results. These results indicate that the C-QCM immunoassay could be comparable to ELISA in terms of analytical sensitivity, thus, providing an alternative tool for rapid clinical diagnosis, particularly for the screening of membranous nephropathy.

**Table 6.2** Comparison of existing technique for the anti-PLA2R detection

Technique	Label	Detection limit		Sample	Assay time (hr)	Cost (per instrument or test kit)	Ref.
		Lower (ng/ml)	Upper (ng/ml)				
Commercial ELISA	Yes	0.6	10	Buffer or diluted serum 1:100	3.5	Inst.: £50k Test kit: £300	[268]
Fluoroimmuno assay	Yes	30	3400	Buffer or diluted serum 1:100	3.5	Inst.: £50k Test Kit: £300	[144]
SPR	No	100	>3000	Buffer	1	Inst.: £200k Test Kit: £400	[36]
QCM-D (QSense, 5 MHz crystal)	No	500	10 <sup>5</sup> (100 µg/ml)	Buffer or Concentrated serum	1	Inst.: £100k Test Kit: £200 - £400	This work, [43]
C-QCM (10 MHz crystal)	No	100	10 <sup>5</sup> (100 µg/ml)	Buffer or Concentrated serum	0.5	Inst.: £1000 Test Kit: £20	This work

## 6. Comparison with other techniques

In the C-QCM, higher fundamental frequency QCM chips (10 MHz) were used to achieve higher sensitivity compared to QSense. As can be seen in Table 2, the C-QCM offers lower detection limit to the antibody binding compared to the QSense system. This also results in less amount of serum sample (40 µL for the C-QCM and 200 µL for the QSense) required for the test.

Comparing with SPR which is a commonly used label-free technique, the QCM system presents similar detection limit of the anti-PLA2R to the SPR [145], [146]. Fresquet *et al.* used the SPR to study the binding of the anti-PLA2R antibody on immobilised NC3 and other PLA2R domains. The detection limit of the antibody concentration was shown to be 1nM (~100 ng/ml) [145].

Another advantage of the QCM over the SPR is that the QCM can be used with concentrated to whole serum or viscous specimens while the sample for SPR needed to be highly diluted or in the buffer. Thus, a specialised laboratory with professional technicians is required to perform the test. These drawbacks also apply to ELISA and other optical sensing techniques although the sensitivity obtained from those techniques could be higher. Additionally, the C-QCM is a rapid assay that can be completed within 30 minutes, whereas ELISA requires a few hours to complete plus the additional control sample. Testing time is important for disease screening as it can speed up clinical diagnosis. Another significant advantage of the C-QCM assay over other techniques is the low cost of testing kits and the instrument. As the C-QCM is an electronic-based and label-free sensor, expensive elements like optical systems and label chemicals or antibodies are not required. For these reasons, the C-QCM system can potentially be developed as a point-of-care clinical diagnosis tool.

## Conclusions

We have shown that rGO coating on QCM chips helps improve surface functionality as it allows hydrophobic interactions and  $\pi$ - $\pi$  stacking to bind with biomolecules, however, it could denature the protein due to the strong hydrophobic nature of the interaction. We proposed to use a BSA layer formed on the graphene surface of G-QCM chips to serve as an inert layer and a bio-functional cross-linker to conjugate the protein receptor NC3 to detect the anti-PLA2R antibody, the biomarker for diagnosis of membranous nephropathy (MN). QCM-D results verified that the BSA layer acted both as a blocking layer against non-specific interactions from complex fluids whilst also maintaining the NC3 protein in a suitable conformation for ligand binding. We have shown that functionalizing hydrophobic 2-dimensional (2-D) materials using BSA could offer controllable functionalization methods for various bio-interfaces for immunosensors, nanomedicine and drug delivery.

As the QCM-D system from QSense exhibits inadequate sensitivity for antibody detection, as well as possessing other disadvantages such as high cost and complexity of the operation, we have developed our C-QCM system to overcome these limitations. The proposed assay enables quantitative detection of the anti-PLA2R concentrations as



low as 0.1  $\mu\text{g/ml}$  which is a magnitude lower than the cut-off concentration for patients with MN. Our results for human serum specimens from healthy people and patients demonstrate that the detection sensitivity and specificity of the QCM immunoassay are comparable to those of ELISA. Moreover, the C-QCM offers advantages over the conventional methods in that the analytical operations are more rapid, easier to perform, no sample pre-treatment required and less expensive. Our C-QCM method with G-QCM chips can be tailored as an on-field applicable tool for rapid clinical diagnosis and screening of in remote areas or epidemic situations. More importantly, this technology could be extended to other autoimmune tests for wider diagnostic applications.

## **Acknowledgements**

P.H. acknowledges the financial support of the Development and Promotion of Science and Technology Talents Project (DPST), Thailand. D.M. acknowledges The National Council for Science and Technology (CONACyT), Mexico for the financial support. A.V. acknowledges the Engineering and Physical Sciences Research Council (EPSRC) grant EP/L01548X/1. We acknowledge the support of the Biomolecular analysis facilities, Faculty of Biology Medicine and Health, The University of Manchester. This work was supported by a Wellcome Trust Senior Fellowship award (202860/Z/16/Z) to R.L. The authors also acknowledge core funding from the Wellcome Trust (203128/Z/16/Z) to the Wellcome Centre for Cell-Matrix Research at the University of Manchester.

## **Declaration**

This study has full ethical approval by the NHS Health Research Authority Research Ethics Committee (REC reference 16/NW/0560). All study sites also have local Research and Development approval. All samples obtained under the auspices of the Manchester Renal Biobank 2016-2021 and the PRISM trial [49]. All patients provided written informed consent and the studies had full ethical approval from the NHS Health Research Authority Research Ethics Committee (PRISM - REC reference 16/NW/0560; Manchester Renal Biobank 2016-2012 - REC reference 16/NW/0119), along with local Research and Development approval.

## CHAPTER 7. Publication 3 (In the process of publication)

### Binding kinetics and biological recognition of nanobodies functionalised on graphene derivatives for immunosensing applications

Piramon Hampitak<sup>1</sup>, Daniel Melendrez<sup>1</sup>, Maria Iliut<sup>1</sup>, Ben Spencer<sup>1</sup>, Thomas Jowitt<sup>2</sup>, and Aravind Vijayaraghavan<sup>1,\*</sup>

*This draft is in the process of submission for publishing.*

#### **Authors contributions:**

**Piramon Hampitak** prepared the QCM sensors and carried out all the QCM-D experiments. She prepared all samples for material characterization including samples for SEM, Raman and XPS. She analysed and interpreted SEM, Raman and XPS results. She carried out a dot blot and performed the analysis.

D. Melendrez and T. Jowitt supervised on QCM analysis and interpretation.

D. Melendrez acquired Raman spectroscopy data.

M. Iliut prepared and purified GO dispersions.

B. Spencer performed all XPS measurements.

T. Jowitt, and A. Vijayaraghavan supervised P. Hampitak on conceptualization and experimental design. T. Jowitt, A. Vijayaraghavan, D. Melendrez and M. Iliut helped P. Hampitak in the writing of the manuscript.

## Binding kinetics and biological recognition of nanobodies functionalised on graphene derivatives for immunosensing applications

Piramon Hampitak<sup>1</sup>, Daniel Melendrez<sup>1</sup>, Maria Iliut<sup>1</sup>, Ben Spencer<sup>1</sup>, Thomas Jowitt<sup>2</sup>, and Aravind Vijayaraghavan<sup>1,\*</sup>

<sup>1</sup>*Department of Materials and National Graphene Institute, Faculty of Science and Engineering, The University of Manchester, Oxford Road, Manchester M13 9PL, UK.*

<sup>2</sup>*School of Biological Sciences, Faculty of Biology Medicine and Health, The University of Manchester, Oxford Road, Manchester M13 9PL, UK.*

### Abstract

The development of nanobodies for therapeutic and diagnostic applications has attracted significant attention from a number of biomedical research groups due to their smaller size and ease of production on a large scale. Nanobodies are considered effective protein receptors because of their single antigen-binding site and fewer possible orientations than conventional antibodies. However, their bio-interface functionalization on solid platforms is still challenging. This study explores methods to functionalize nanobodies and graphene derivatives based on physical adsorption, amine crosslinking, and streptavidin (SA)-biotin interaction. The nanobody against lysozyme was used as a model protein pair. The QCM-D technique was used to monitor the adsorption of the nanobody on different surfaces and to describe its biomolecular recognition and selectivity against other proteins and animal serum. The kinetics dissociation constant at equilibrium ( $K_D$ ) was determined from the QCM-D results and compared with those from Surface Plasmon Resonance (SPR) for validation. We demonstrated that the sensing chip coated with rGO-biotinylated BSA+ SA functionalized with biotinylated nanobody provides the highest selectivity against serum proteins, including BSA and IgG, with less standard error compared to other tested functional surfaces. This sensing surface exhibited good specificity and high sensitivity toward the target, with a detection limit of 0.5  $\mu\text{g/ml}$ , and capable of detecting an analyte in serum media. The concentration of lysozyme in animal serum can be quantified after the deduction of the serum baseline. The  $K_D$  value obtained from this sensing platform is 545 nM which is comparable to the standard value from the SPR technique, validating its capability to be used as the basis of a highly selective and reliable immunosensing device. The same functionalisation method was tested with the other five lysozyme-specific nanobodies with different binding strengths varying from

low to high. The binding behaviours observed from the QCM-D results correspond to the  $K_D$  of each nanobody, proving the possibility to use our proposed method as a universal nanobody functionalisation technique.

**Keyword** graphene, graphene oxide, protein, QCM-D, nanobody

## Introduction

A nanobody is a small antigen-binding fragment of an antibody containing a single monomeric antibody domain derived from heavy-chain antibodies (hcAB). It can selectively bind to a specific antigen like the conventional antibody, but the size of the nanobody molecule is much smaller, only at about 12–15 kDa, while that of a common antibody is approximately 150–160 kDa. Besides keeping a high binding affinity to antigens, the long and flexible binding region of the nanobody can penetrate into cavities on antigens, thus, recognizing hidden epitopes that are difficult for antibodies to recognize [269]. Accordingly, nanobody technology has become the next generation of tools for antigen-recognition applications in which conventional antibodies are incapable of reaching their specific binding sites. As the generation, production, functionalization, and intracellular application of full-length antibodies can be challenging due to their structural and chemical complexities, novel classes of recombinant antigen-binding proteins, providing high binding efficiency and with easy large-scale production, like nanobodies, are on the rise. The development of nanobodies for therapeutic and diagnostic applications has gained significant attention in recent years [158]–[160]. For example, several publications reported promising clinical data of nanobody-based molecular imaging in cancer diagnoses such as ovarian cancer [161] and breast cancer [162], [163]. Very recently, Xiang et al. (2020) developed nanobodies that can bind to the receptor-binding domain (RBD) of SARS-CoV-2 spike protein, obtaining affinities from the picomolar to the femtomolar range [164].

Although nanobodies are considered effective protein receptors due to their single antigen-binding site and fewer possible orientations than conventional antibodies, selective functionalization of nanobodies on solid platforms is still challenging as unselective functionalisation can potentially lead to a significant reduction in epitope recognition and stability of the nanobodies [157]. Several protein attachment methods

have been applied to functionalize nanobodies including thiol-based methods [270], non-natural amino acids incorporation [271], and crosslinking using N-hydroxysuccinimide (NHS) activation [272], [273]. Thiol based method can be achieved by incorporating a single cysteine residue that has the free thiol group into a nanobody to make it cysteine-selective. However, introducing additional cysteines into a nanobody could damage its binding site located close to the disulfide bridge [270]. The incorporation of non-natural amino acids is becoming a more widespread technique for protein engineering as new and beneficial properties can be added into a protein through the selection of non-intuitive mutations [274], [275]. In the case of nanobodies, a non-natural amino acid is incorporated into a random site within the sequence of the target protein using engineered expression machinery. Yet, it could be technically demanding and it can result in a significantly lower expression yield compared to the wild-type nanobody [276]. N-hydroxysuccinimide (NHS)-functionalized methods have been widely used to covalently attach and immobilize nanobodies based on lysine-selective functionalisation [272], [273]. This method can benefit sample loading, due to a high number of lysine residues, and limit disturbance of the binding site as free lysines locate far from the active site. This lysine-selective functionalisation has been proven to be effective for functionalising nanobodies with peptide [277] and biotin [278].

Graphene-based materials are potential candidates for the future of drug delivery and diagnostic biosensors [65], [72], [113], [208], [209] due to their biocompatibility [210], high specific surface area [2], and ease of functionalization [211]. The graphene-based solid supports require functionalisation with molecular receptors to promote specific binding to the target molecules. We have previously reported an effective method to obtain a film of denatured BSA (BSA) on reduced graphene oxide (rGO) and its application in immunosensing [200], [279]. We have also demonstrated the development and use of graphene-coated (G-) quartz crystal microbalance (QCM) sensor chips to study interactions between biomolecules and graphene surfaces [6], [200], [280] and the application of G-QCM in clinical diagnostics [279]. An important number of publications have reported the use of carbon-based materials functionalized with nanobodies for biosensing applications [281]–[283]. Filipiak et al. reported using carbon nanotube transistors with nanobody receptors to detect proteins in buffer using

polyethylene glycol as a surface modifier [281]. Zhou et al. proposed and developed a simple nanobodies-graphene oxide electrochemical immunosensor for highly selective and sensitive detection of Cry1C, a toxin protein [282]. Chen et al. used NHS-lysine and maleimide-cysteine coupling to functionalize graphene oxide nanosheets with single-domain antibodies, *ergo* nanobodies, for rapid and efficient capture of cells [283]. However, to date, there is no report regarding the use of graphene-nanobody interface for probing analytes in complex fluids like serum that will potentially lead to real-world critical applications.

In this work, we investigate the utilization of graphene-QCM sensors with novel protein nanobodies probes aiming to be used as a universal platform for detecting an analyte in both buffer and serum solutions. We first explored different methods to functionalise the protein receptor, including physical adsorption, covalent immobilisation, and the biotin-streptavidin system. The specific nanobody against lysozyme was used as a model protein pair. The QCM with dissipation monitoring (QCM-D) technique was used to capture the adsorption of the nanobody and thus study the binding and dissociation of the analyte in real-time. From the QCM-D measurements, the interaction dynamics between the receptor and the analyte can be systematically investigated. The frequency shift ( $\Delta F$ ) parameter provides information from both the adsorbed mass and the film's thickness while the dissipation parameter ( $D$ ) can provide mechanical details such as viscoelasticity of the adsorbed film on underlying surfaces [256], [257]. The binding kinetics and selectivity against serum proteins were also investigated. The equilibrium kinetic dissociation ( $K_D$ ) values of nanobodies functionalised on different surfaces were interpreted from the QCM results and validated using the standard result from the Surface Plasmon Resonance (SPR) technique. Moreover, the sensing platform with the best performance was used to test with other five lysozyme-specific nanobodies with different binding strengths to prove the feasibility to use it as a universal technique for nanobody functionalisation. It has been shown that novel nanobodies with distinctive binding strengths against a single target are ideal molecules for standardization protocols [284].

Lysozyme is known as an enzyme with antibiotic properties abundantly found in secretions like saliva, tears, mucus and also in egg white [114]. It acts synergistically with

other antimicrobial polypeptides against most bacteria. Lysozyme is a monomeric globular protein conformed of 129 amino acid residues with a molecular weight of 14.3 kDa [116]. Under physiological conditions, the molecule is always positively charged [285], [286]. Due to its small size and simple molecular structure, lysozyme has been commonly chosen as a model protein for protein interaction studies [118]. Since human lysozyme is regarded as 'body's own antibiotic', it plays a key role as a biomarker for various medical diagnostics such as bacterial infections, coronary artery diseases, sarcoidosis and breast cancer [120], [126], [127]. Arterial plasma lysozyme levels are measured to identify patients with varying degrees of coronary artery disease, observed in separate cohorts of patients using a cut-off value of 1.5  $\mu\text{g}/\text{mL}$  [126]. By using this lysozyme-nanobodies protein pair as a model protein, not only molecular functionalisation routes and interaction mechanisms can be elucidated, but their study can also help to define a pathway for developing biosensors for diagnostic tools for many diseases where lysozyme quantification is required.

## Materials and Methods

### 1. Materials and reagents

GO dispersion was prepared by a modified Hummers' method [202], followed by exfoliation and purification. The complete protocol can be found in our previous publication [200]. The GO dispersion with a concentration of 0.8 mg/ml was used for coating the QCM chips.

The production of nanobodies specific for lysozyme with different binding strengths, namely FO7, FO8, FO9, Cablys and TS, was previously described by Birchenough *et al.* [284]. Briefly, the nanobody VHH sequence was engineered into an expression vector with a C-terminal 6-His tag. Then, the vector was transformed into competent T7-Express E. coli cells and selected for an amplification process and finally purification. The stock solution for each type of nanobody was prepared with a concentration of 1 mg/mL in PBS. The stock solution was diluted in PBS to 50  $\mu\text{g}/\text{mL}$  for use in all experiments. More details about the production process are described in ESI 3.1.

Lysozyme powder (protein  $\geq 90\%$ ) (L6876), streptavidin (85878), albumin monomer bovine (A1900), and phosphate buffered saline or PBS (P4417), pH 7.4, were purchased



from Sigma-Aldrich, UK. BSA stock solution was prepared with a concentration of 1 mg/ml. The dilutions of the BSA solution were prepared from the stock solution. The EDC and sulfo-NHS crosslinkers were purchased from Sigma-Aldrich (UK). 11-Mercaptoundecanoic acid or MAU (450561 from Sigma) and 11-Mercapto-1-undecanol or MUD (447528 from Sigma Aldrich) were used as a self-assembly monolayer for gold surface for the reference experiment was purchased from Sigma-Aldrich (UK). Ethanolamine was used as a blocking buffer and purchased from Sigma-Aldrich (UK). Bovine calf serum was purchased from Sigma-Aldrich (UK).

BSA and nanobodies were conjugated with biotin for the experiments involving biotin-SA platforms. NHS-PEG4-Biotin (21330) was purchased from Thermo Scientific. The NHS group reacts specifically with lysine and N-terminal amino groups to form stable amide bonds between the proteins and biotin molecules. The hydrophilic polyethylene glycol (PEG) spacer arm helps reduce aggregation of labelled proteins stored in solution by improving solubility and also provides the reagent with a long and flexible connection to minimize steric hindrance for binding to avidin molecules. The protocol for biotin-protein conjugation from ForteBIO [287] was followed to achieve the biotinylated BSA and nanobodies. Briefly, it started with preparing the protein and NHS-PEG4-Biotin reagent following the ratio below using molar coupling ratio (MCR)=2.

$$\mu\text{L 1 mM biotin reagent} = \frac{\text{Protein Conc (mg/mL)}}{\text{MW Protein (kDa)}} \times \text{MCR} \times \text{volume Protein } (\mu\text{L})$$

Then, the appropriate volume of biotin reagent, as calculated, were added into the protein sample immediately mixing them. The mix was incubated for 30 mins at room temperature. Finally, the reaction was stopped by removing the excess biotin reagent using a desalting column.

## 2. QCM chip surface coating and characterization

QCM chips with gold surface and SiO<sub>2</sub> from QSense (QSX-301, Biolin Scientific) were used in this study. The chips were cleaned following the protocol provided in Melendrez *et al.* [6]. The main coating surfaces include a self-assembly monolayer (SAM) on gold and graphene-based coating. Gold precoated QCM chips were functionalized with SAM following the protocol described in ESI 3.3.1 For the coating of graphene oxide on QCM-D sensors, the GO dispersion was spin-coated on the entire surface of the chip (speed:

3000 rpm, acceleration:  $350\text{ s}^{-1}$ , 2 mins). A controlled thermal treatment of the GO-coated chips was performed in a vacuum oven (Townson+ Mercer EV018) with a reduction temperature of  $80\text{ }^{\circ}\text{C}$  for 15 mins and 1 hour to obtain two surfaces of partially reduced GO 1 (PrGO1) and PrGO2. To obtain a fully-reduced GO surface (rGO), the reduction conditions were changed to a temperature of  $180\text{ }^{\circ}\text{C}$  for 6 hours as described in our previous study [200].

The degree of reduction was characterized by the average wetting contact angle (WCA) of DI water sessile drops. All values were obtained using a Kruss DSA100 system and computed using the ImageJ software. . WCA values were combined with X-ray photoelectron spectroscopy (XPS) using a SPECS custom-built system composed of a Phobios150 hemispherical electron analyser with 1D detector. The XPS data were analysed using CasaXPS software (version 2.3.18).

### 3. Functionalization of nanobodies on different sensing surfaces investigated by QCM-D

The FO7 nanobody was selected to be a controlled receptor in this research due to its moderate binding strength to the lysozyme molecules so that both binding and dissociation events can be distinguished. The FO7 molecules were immobilised on different functional surfaces following the injection protocol described in ESI 3.2.2. The lysozyme binding and dissociation are monitored by the QCM-D technique using the QSense Pro (Biolin Scientific) system. Twelve sensing surfaces were studied, including six bare surfaces, three amine coupling surfaces and three biotin-SA surfaces, as presented in **Table 7.1**. The temperature of the system was stabilised at  $20\text{ }^{\circ}\text{C}$  to avoid the effects of thermal drift. The basic sequential injection steps for QCM-D monitoring of the antibody binding include: (1) a baseline stabilisation regime in which PBS WAS injected until stability was reached, (2) immobilisation of the nanobody, (3) detection of the lysozyme followed by (4) rinsing (or also referred to as *lysozyme dissociation*) and finally (5) reabsorption of the nanobody to observe the non-specific binding of lysozyme. The complete procedure for each QCM surface is also described in the injection sequence in **Table 7.1**. The concentration of the nanobody and the lysozyme in PBS were fixed at  $50\text{ }\mu\text{g/mL}$  and  $100\text{ }\mu\text{g/mL}$ , respectively. For the QCM-D monitoring, the odd harmonics from the 3<sup>rd</sup> to the 11<sup>th</sup> were recorded. Our discussion of results is based on

the 3<sup>rd</sup> harmonic. The measured frequency shifts of the adsorption of the FO7 ( $\Delta F_{FO7}$ ), the lysozyme binding ( $\Delta F_{Lys}$ ), the dissociation ( $\Delta F_{Dis}$ ) and the reabsorbed nanobody ( $\Delta F_{non-specific}$ ) were used to investigate the capability of each sensing surface to detect the lysozyme specifically. More details and exemplification regarding the measurement of frequency shifts can be found in ESI 3.2.

#### 4. The varied concentration of lysozyme and binding kinetic studies

The binding of various concentrations of lysozyme was studied using the QCM-D system. The FO7 nanobody at a concentration of 50  $\mu\text{g}/\text{mL}$  in PBS was immobilised on the selected functional surfaces of the sensing chip following a receptor immobilisation protocol (ESI 3.3.2), then injecting PBS to rinse the surface. For the amine coupling surfaces, the ethanolamine was used as a blocking agent to prevent non-specific adsorption. Before the binding of lysozyme, the sensing surface was rinsed with PBS until baseline stability was reached, and then the acquisition was restarted. Then, the lysozyme was injected for 10 minutes and finally rinsed with PBS for 15 minutes. The flow rate was kept at 10  $\mu\text{l}/\text{min}$ . Various concentrations of diluted lysozyme from the stock solution of 500  $\mu\text{g}/\text{mL}$  or 35  $\mu\text{M}$  were used, including 100% undiluted stock, 50% (250  $\mu\text{g}/\text{mL}$ ), 25% (125  $\mu\text{g}/\text{mL}$ ), 12.5% (62.5  $\mu\text{g}/\text{mL}$ ), 6.25% (31.2  $\mu\text{g}/\text{mL}$ ), 3.1% (15.6  $\mu\text{g}/\text{mL}$ ), 1.6% (7.8  $\mu\text{g}/\text{mL}$ ), 0.8% (3.9  $\mu\text{g}/\text{mL}$ ), and 0.1% (0.5  $\mu\text{g}/\text{mL}$ ). Each sensing chip measured an individual concentration from the latter list. For lysozyme adsorption, the frequency shifts ( $\Delta F_{Lys}$ ) were recorded and averaged at the steady-state region or when the signal reached a plateau. These signals represent the quantitative amount of lysozyme binding. The measurement for each concentration was repeated at least twice.

#### 5. Specificity studies

To evaluate the selectivity of the selected sensing surfaces, other proteins, including BSA and IgG, which are abundant proteins in serum, were introduced to bind to the functionalised nanobody. BSA 200  $\mu\text{g}/\text{mL}$  and IgG 50  $\mu\text{g}/\text{mL}$  were sequentially injected over the pre-functionalised QCM surface with the FO7 nanobody. The sensing surface was rinsed with PBS after the injection of each protein. The frequency shifts upon protein binding were recorded to be compared with those obtained from lysozyme. No binding from neither BSA nor IgG should be expected if the sensing surface offers good

selectivity. The sensing platform that provides the best selectivity was further used for testing with calf serum as a sample media.

**Table 7.1** Sensing surfaces tested in this study including their complete injection sequences for constructing the functional surfaces and investigating the binding and dissociation.

Surfaces	Surface type	Injection sequence
S.1 - SiO <sub>2</sub>	Bare	
S.2 - Au		
S.3 - rGO		
S.4 - GO		
S.5 - PrGO1		
S.6 - PrGO2		
S.7 - Au-SAMs-COOH	Amine coupling	
S.8 - PrGO2 +EDC/NHS		
S.9 - rGO-BSA +EDC/NHS	SA- Biotin Nanobody	
S.10 - Au- SA		
S.11 - PrGO2-SA		
S.12 - rGO-BiotBSA+ SA		

## 6. Detection of lysozyme in calf serum

A QCM-D measurement for detecting lysozyme in calf serum was conducted to contrast the results of diluting various concentrations of the lysozyme in the diluted calf serum and those in PBS buffer. The adsorption of plain calf serum diluted with PBS 1:50 was

measured as a negative control or blank sample. The concentrations used for this experiment were 0.5  $\mu\text{g}/\text{mL}$ , 3.9  $\mu\text{g}/\text{mL}$ , 15.6  $\mu\text{g}/\text{mL}$ , 62.5  $\mu\text{g}/\text{mL}$ , 125  $\mu\text{g}/\text{mL}$  and 500  $\mu\text{g}/\text{mL}$  which correspond to the same concentrations tested with PBS media. If the sensing platform provided specificity against calf serum, the final frequency shift of each concentration in the serum after deduction of blank frequency should be close to the result obtained from PBS media.

#### 7. Testing with different nanobodies

To prove the feasibility of the method to be universal for nanobody functionalisation, the selected sensing platform was tested with five other nanobodies that are specific to lysozyme with different binding strengths from low to high. The use of multiple binding strength molecules against a single target can be an ideal route to determine molecules for standards [284]. In this experiment, the nanobodies were functionalised onto the QCM chips following the method for S.12 described in ESI 3.3.2. Each sensing chip was functionalised with one nanobody receptor. Then, lysozyme (10  $\mu\text{g}/\text{mL}$ ) was injected to bind with the nanobody for 10 mins then rinsed with PBS for 15 mins. The frequency shift due to the immobilisation of nanobodies onto the surface ( $\Delta F_{\text{xx}}$ ), the binding for lysozyme ( $\Delta F_{\text{Lys}}$ ) and the dissociation ( $\Delta F_{\text{Dis}}$ ) were recorded.

### Results and discussion

We first discuss the properties of the different graphene surfaces, as revealed through SEM, XPS, Raman Spectroscopy and contact angle measurements. We have then explored different methods to functionalise the protein receptor, including physical adsorption, covalent immobilisation, and the biotin-streptavidin system. In this comparative study, twelve different functional surfaces were used, as presented in **Table 7.1**. We report on the ability to detect the analyte of interest for each sensing surface specifically. The five sensing surfaces that showed outstanding results, including three amine coupling surfaces and 2 biotin-SA surfaces, were selected to investigate binding kinetics and selectivity against other proteins. The best-performing platform corresponding to rGO-biotBSA-SA was selected to test with calf serum media. Finally, the same functionalisation method was used with five lysozyme-specific nanobodies with gradual binding strengths. The binding mechanisms and kinetics dissociation of each nanobody were analysed and are discussed here.

## 1. Characterization of graphene coating and functionalization

Graphene derivatives, like GO and rGO, help in forming surfaces with tuneable hydrophobicity achieved through a controlled thermal reduction of GO, as described in [200]. In the present study, the samples for graphene characterisation include plain GO, PrGO1,2 and rGO bare surfaces and their EDC/NHS activation of carboxylic acids as they were used for developing the sensing platforms. We hypothesized that since both GO and PrGO 1,2 surfaces contain -OH and -COOH functional groups, these can contribute to amine crosslinking through EDC/NHS activation. On the other hand, the rGO surface having much lower oxygen functional group contents requires the BSA layer which provides abundant -COOH groups serving then as a linker [279]. **Table 7.2** presents data obtained from the characterisations of the graphene surfaces and their carboxylic acid activation. Water contact angle measurements reveal hydrophilic predominance GO (WCA  $\approx 34^\circ$ ) while the hydrophobicity increases on the PrGO1,2 samples reaching the highest on rGO-coated sensors (WCA =  $99^\circ$ ). The contact angles of graphene surfaces with EDC/NHS activation were also measured to compare the changes in hydrophobicity due to the carboxylic acid contents. Sensors coated with GO, PrGO2 with direct EDC/NHS activation and rGO-BSA activated by EDC/NHS were tested for comparison. The activation generally reduces the hydrophobicity of the surfaces, as observed from the decrease in the WCA. Especially in the case of rGO, the WCA was decreased by  $\sim 50\%$ .

The surface chemistry of the sample surfaces was characterised using Raman and XPS. Raman spectra were captured to obtain information about lattice defects (see ESI 3.5). Two main peaks, including both graphitic (G) and defect (D) peaks, occur at  $1580\text{ cm}^{-1}$  and  $1350\text{ cm}^{-1}$ , respectively. The relative intensity of D to G ( $I_D/I_G$ ) indicates the in-plane crystallite size or the disorder in the sample. There is no critical difference in the value of  $I_D/I_G$  for the cases of GO, PrGO and their activation. The obtained  $I_D/I_G$  value for rGO is 0.84, which is fairly lower than that of GO, PrGO and also rGO-BSA+EDC/NHS samples. The higher  $I_D/I_G$  values obtained from functionalised rGO samples could originate from defects and effects of doping functional groups through BSA adsorption, as we have explained in our previous paper [279].

XPS spectra of the samples were obtained to investigate the carboxylic acid activation on graphene derivatives. From **Table 7.2**, the C/O ratio of bare samples increases

according to the WCAs due to the removal of the oxygen groups as seen from the higher intensity of the C1s peak [200]. After activation with EDC/NHS, the samples present similar C/O ratios ranging between 0.90 and 1.05 while their atomic percentual contents of nitrogen logically increase compared to the results from bare samples. The direct activation of GO and PrGO2 surfaces with EDC/NHS displays ~5% of nitrogen contents. In contrast, the sample of rGO-BSA+EDC/NHS presents the highest percentage of nitrogen from the enhanced deconvoluted peaks (ESI 3.6) of C-N and CO-NH corresponding to the presence of the secondary amine and imine of EDC and the characteristic of the nitrogen of the NHS ester [263]. It is suggested that the carboxylic activation on this surface as discussed in our previous publication [279]. Complete XPS spectra and further details are presented in ESI 3.6.

**Table 7.2** Surface characterisations of the graphene surfaces and their carboxylic acid activation obtained from contact angle, Raman and XPS techniques

Surface	Contact angle	Raman $I_D/I_G$	XPS	
			C/O	Atomic% of N
GO	$34^\circ \pm 3^\circ$	1.01	0.93	1.17
PrGO1	$46^\circ \pm 3^\circ$	1.01	0.93	1.17
PrGO2	$56^\circ \pm 2^\circ$	1.02	0.94	1.28
rGO	$99^\circ \pm 2^\circ$	0.84	4.98	1.24
GO+EDC/NHS	$32^\circ \pm 5^\circ$	1.05	0.95	4.85
PrGO2+EDC/NHS	$51^\circ \pm 3^\circ$	1.05	1.05	4.71
rGO-BSA-EDC/NHS	$55^\circ \pm 4^\circ$	0.95	0.90	14.2

SEM imaging shows the topography of the GO films obtained through spin coating on the Au surface of QCM-D chips. A continuous film formed of overlapping flakes varying from one to a few layers of GO covering the whole sensor's surface. The graphene coverage is uniform over large areas on all samples studied (see ESI 3.7). The thickness, roughness and other surface imaging results were previously characterised and discussed in our previous papers [200], [279].

## 2. Exploration of sensing surfaces using QCM-D and selection criteria

The set of QCM-D measurements for the nanobody immobilisation on different sensing surfaces and the detection of lysozyme are presented in **Fig. 7.1(a-h)**. The values of

$\Delta F_{FO7}$ ,  $\Delta F_{Lys}$ ,  $\Delta F_{Dis}$  and  $\Delta F_{non-specific}$  describe the amount of protein binding occurring on each surface. **Fig. 7.1(h)** presents a comparative performance from the sensors' ability to detect lysozyme of the nanobody after functionalisation. From these observations, the criteria for selecting sensing surfaces for further studies include:

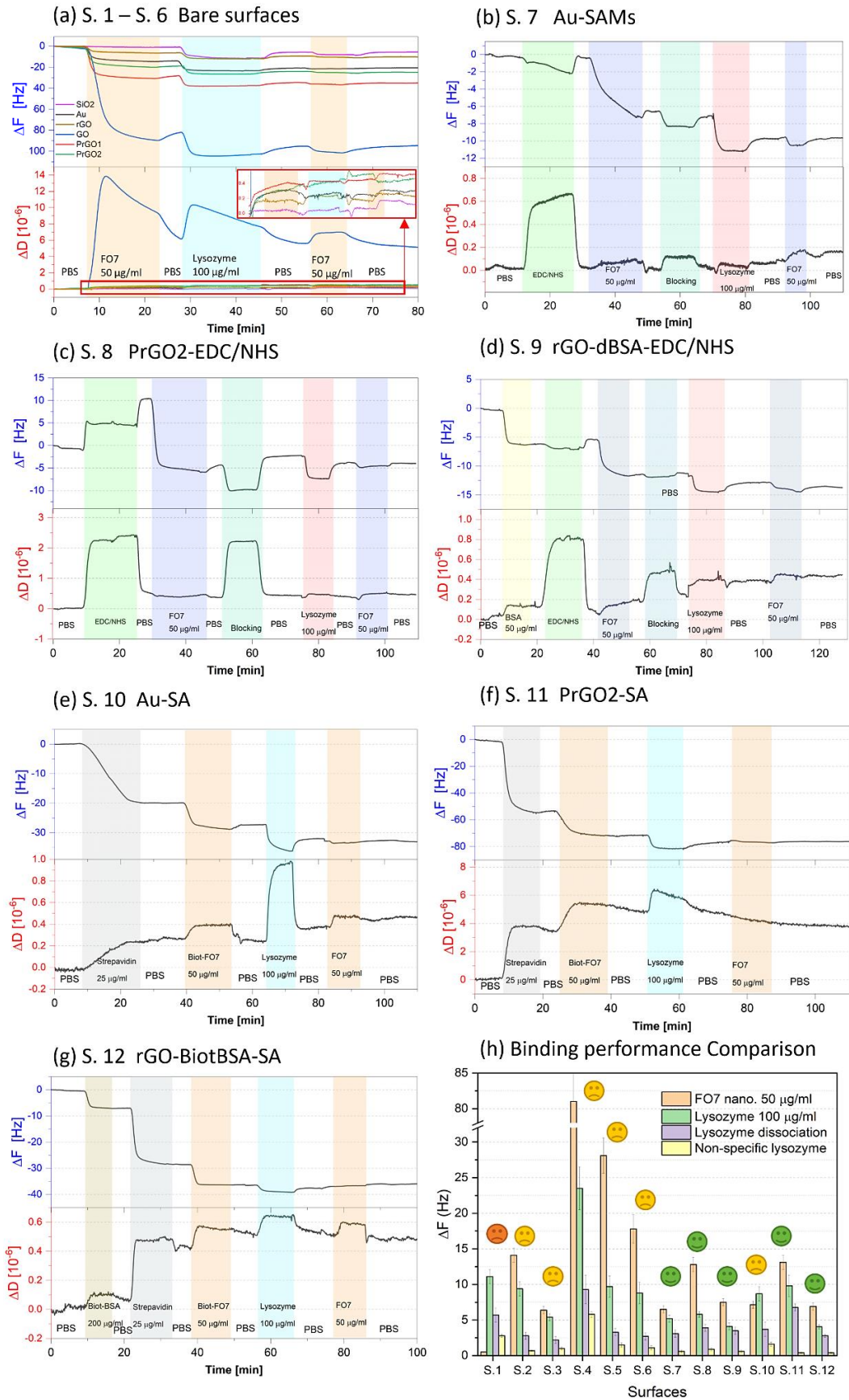
1.  $\Delta F_{FO7} \geq \Delta F_{Lys}$  since the specific binding of lysozyme cannot exceed the amount of FO7 due to its single binding site.
2.  $\Delta F_{Lys}$  should be approximately equal to  $\Delta F_{Dis}$  since in this step lysozyme molecules are assumed to be mostly or completely rinsed off due to the low binding strength of the FO7. The QCM-D signal should show a partial to complete recovery of  $\Delta F_{Lys}$ . To meet this criterion, the  $\Delta F_{Lys}$  value must be higher than that from  $\Delta F_{Dis}$  by no more than 3 Hz.
3.  $\Delta F_{non-specific}$  should be close to zero or less than 1 Hz, since the nanobody should not be bound to the sensing surface again if lysozyme molecules that bounded to the first immobilised nanobody were completely rinsed off.

From the adsorption results in **Fig. 7.1(h)**, the justification of each testing system based on the selection criteria above is summarized in **Table 7.3**. Only five surfaces met the established criteria and were selected for further studies, including S.7 (reference), S.8, S.9, S.11 and S.12.

**Table 7.3** Summary and justification of the sensing feasibility for the 12 testing platforms based on the selection criteria discussed in the main text.

Surfaces	Surfaces type	Criteria			Feasibility for sensing platform
		1. $\Delta F_{FO7} \geq \Delta F_{Lys}$	2. $\Delta F_{Lys} \approx \Delta F_{Dis}$	3. $\Delta F_{non-specific} \approx \text{Zero}$	
1. SiO <sub>2</sub>	Bare	×	×	×	No
2. Au		✓	×	✓	No
3. rGO		✓	×	×	No
4. GO		✓	×	×	No
5. PrGO1		✓	×	×	No
6. PrGO2		✓	×	×	No
7. Au-SAM-COOH	Amine coupling	✓	✓	✓	Yes
8. PrGO2+EDC/NHS*		✓	✓	✓	Yes
9. rGO-BSA +EDC/NHS		✓	✓	✓	Yes
10. Au- SA	SA- Biotin Nanobody	×	×	×	No
11. PrGO2- SA		✓	✓	✓	Yes
12. rGO-BiotBSA+ SA		✓	✓	✓	Yes





**Fig. 7.1** The QCM-D measurement for the monitoring of the nanobody immobilisation on different sensing surfaces and the detection of lysozyme

On bare surfaces (**Fig. 7.1(a)**), the nanobodies were directly adsorbed on the surfaces through physical adsorption that results in random orientation or denaturation of the protein as reflected by the ineffective detection of lysozyme. The SiO<sub>2</sub> surface, in particular, shows almost zero adsorption of the nanobody while it adsorbed much more lysozyme. The higher level of lysozyme adsorption suggests that the lysozyme molecules randomly adsorbed on SiO<sub>2</sub> without binding with the nanobody receptor. On graphene derivative surfaces, the dissociation of lysozyme is relatively low ( $\Delta F_{\text{Dis}} \ll \Delta F_{\text{Lys}}$ ), suggesting that some immobilised nanobodies might be inactive or denatured after adsorption the graphene surfaces, and thus it is unable to detect lysozyme effectively. The lysozyme might adsorb non-specifically over the denatured nanobody or on the empty graphene surface areas. Moreover, the dissipation values during adsorption increase with respect to the degree of reduction due to the different orientations of the molecules on the surfaces, as already reported in our previous publication [200]. We reason that the high dissipation value could result in a higher measurement error due to the adsorbed layers' viscosity [279].

All amine crosslinking surfaces- S.7, S.8 and S.9 meet the above criteria. The S.7 (**Fig. 7.1 (b)**) Au-SAMs-COOH is a reference surface, commonly used as a crosslinking of protein on gold. For the S.8 case, the PrGO2 surface was selected to be directly activated with EDC/NHS instead of GO and PrGO1 as it shows better surface stability, i.e., lower dissipation and less reduction of mass on sensor surface during the activation process. As it can be seen in **Fig. 7.1 (c)**, the QCM-D signal shifts up during the injection of EDC/NHS. This is theoretically caused by a reduction of mass on the surface. We infer that this effect is due to the detachment of graphene flakes from the surface. We tested the injection of EDC/NHS on GO and PrGO1. A considerable increase of  $\Delta F$  and  $\Delta D$  implies a significant loss of graphene coating on the sensor (see ESI 3.8.1). After the carboxylic acid activation, the assay for detecting lysozyme was constructed, and the QCM-D monitoring displays the lysozyme binding and dissociation that meet the selection criteria. The S.9-rGO-BSA+ EDC/NHS (**Fig. 7.1 (d)**) was investigated and used in our previous study [279], where the functionality and mechanism of the system were discussed in depth. The denatured BSA on rGO serves as the cross-linker to immobilize the protein receptor and prevents the denaturation of the protein. As a result, the

nanobody can be covalently bound to the sensor surface and is capable of detecting lysozyme in PBS.

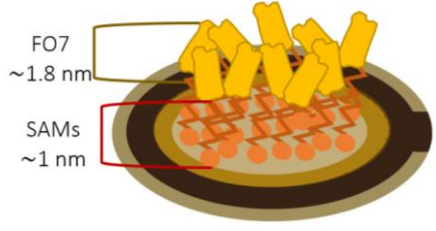
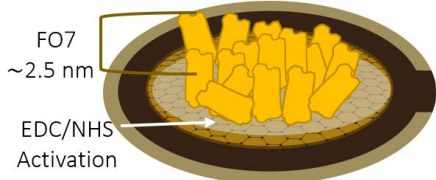
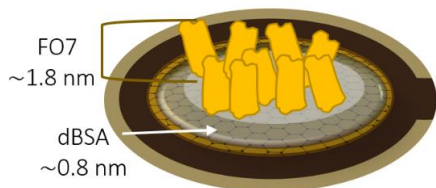
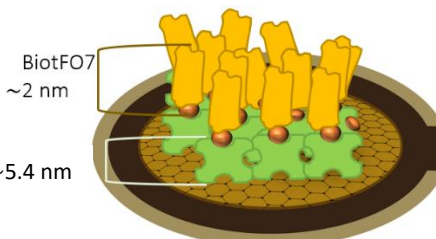
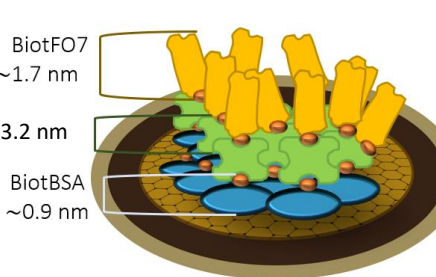
For the functionalisation method using SA- Biotin, the QCM-D results obtained from S.10 (**Fig. 7.1 (e)**) shows that the SA molecules were slowly adsorbed on Au which could, in turn, cause the protein denaturation. Therefore, we pose that this surface cannot serve for binding of Biot-nanobody. For S.11 (**Fig. 7.1 (f)**), SA directly adsorbed on PrGO2 serves as a platform to functionalise with biot-nanobody, while on the S.12 (**Fig. 7.1 (g)**) biot-BSA was injected on the rGO surface before the binding of SA and the biot-nanobody. It is hypothesized that biot-BSA can reduce the non-specific adsorption that could occur during the analyte detection measurement as BSA can form a thin film layer uniformly on the rGO surface and prevent the denaturation of SA, thus promoting selectivity. The results from both S.11 and S.12 meet the established criteria and were selected for further tests to prove both their sensitivity and selectivity in later sections.

### 3. Functional surface model and thickness

The thickness of a blocking protein layer plays a crucial role in preventing non-specific adsorptions due to the effects of the solid surface, such as charges, hydrophobic and hydrophilic forces and other types of bonding [288]. **Table 7.4** presents the cartoon models of five selected sensing surfaces and the thickness of the sensing layer of each functional surface. The thicknesses were determined from the QCM-D results using the Sauerbrey equation. The total thickness of the sensing layer is calculated from the sum of each protein layer over the solid surface. Further details are included in ESI 3.9.

The total thicknesses obtained from amine-crosslinked surfaces (S.7, S.8 and S.9) are approximately 2.5 nm, while those of S.11 and S.12 range from 5 nm to 10 nm. The thicknesses of BSA film on the S.9 and S.12 are similar, at about 0.8 nm. This thickness value is believed to be a layer of denatured BSA based on our previous study [200].

**Table 7.4** The models of five selected sensing surfaces and the thickness of the sensing layer of each functional surface

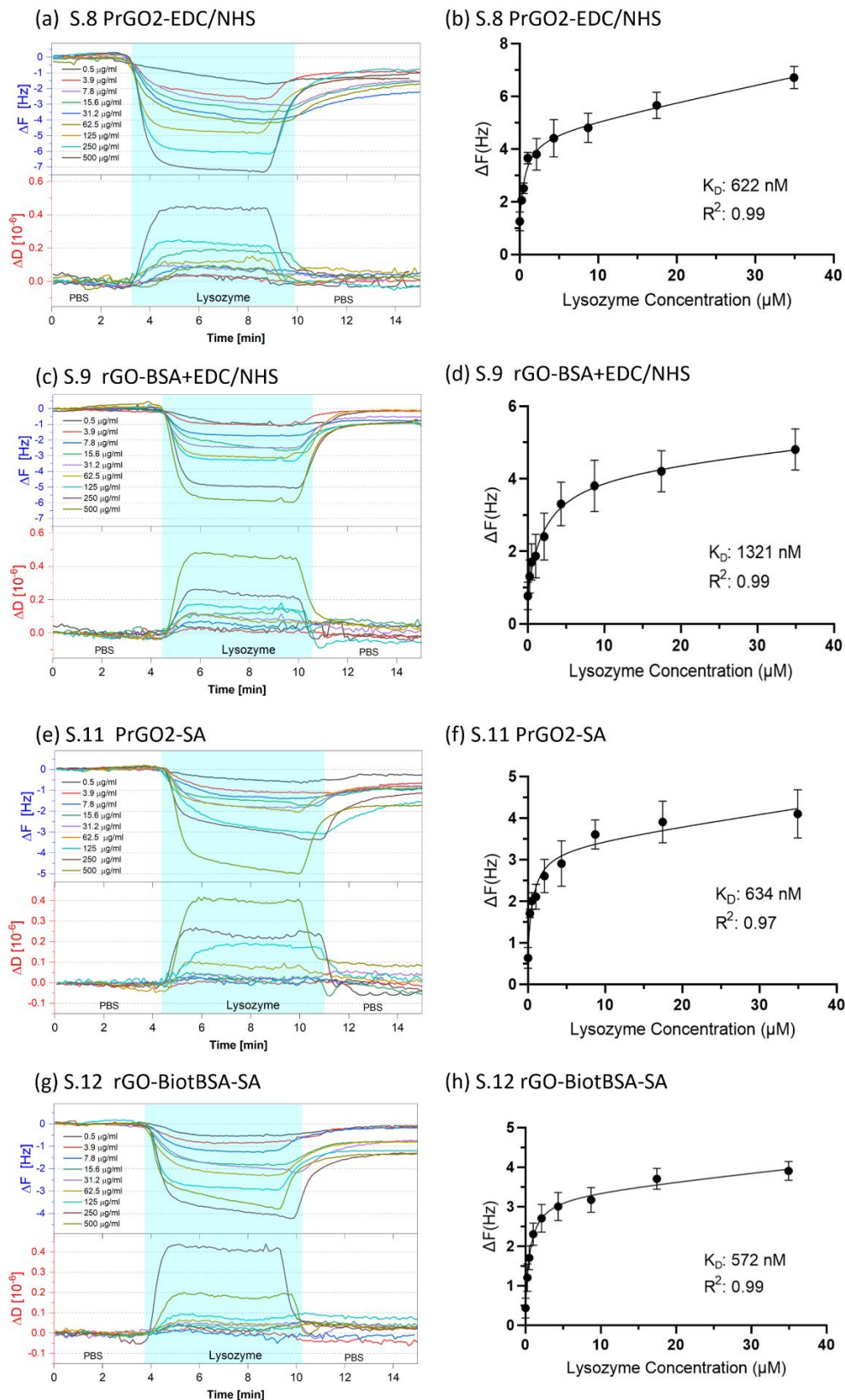
Functional surface	Model & Thickness	Ref.
(7) Au-SAMs +EDC/NHS +FO7	 <p>FO7 ~1.8 nm</p> <p>SAMs ~1 nm</p> <p>Total thickness: ~2.8 nm</p>	SAMs thickness [106], This work (ESI 3.9)
(8) PrGO2+ EDC/NHS +FO7	 <p>FO7 ~2.5 nm</p> <p>EDC/NHS Activation</p> <p>Total thickness: ~2.5 nm</p>	This work (ESI 3.9)
(9) rGO-BSA +EDC/NHS +FO7	 <p>FO7 ~1.8 nm</p> <p>dBSA ~0.8 nm</p> <p>Total thickness: ~2.6 nm</p>	This work (ESI 3.9)
(11) PrGO2- SA +BiotFO7	 <p>BiotFO7 ~2 nm</p> <p>SA: ~5.4 nm</p> <p>Total thickness: ~7.4 nm</p>	This work (ESI 3.9)
(12) rGO-BiotBSA+ SA +BiotFO7	 <p>BiotFO7 ~1.7 nm</p> <p>SA: ~3.2 nm</p> <p>BiotBSA ~0.9 nm</p> <p>Total thickness: ~5.8 nm</p>	This work (ESI 3.9)

The height of the SA layers on S.11 and S12 is approximately 5 nm and 3 nm, respectively. The SA layer contributes to higher total thicknesses compared to other surfaces and also prevents non-specific adsorptions on the platform [288]. The dimension of the SA is about 4x4x4 nm. The thickness reduction of SA in S.12 could be due to a lower population density of adsorbed SA. The number of SA molecules bound to S.12 is limited by the number of biotin molecules, which is functionalised with BSA. In contrast, on S.11, SA is directly adsorbed on PrGO2 resulting in random orientation of SA. Nevertheless, some binding sites might be hidden and the protein layer could lack uniformity resulting in both poor detection limit and reproducibility, as described in **Table 7.5**. In ESI 3.8, we have shown that the direct adsorption of the SA on other reduction degrees of GO, including GO, PrGO1 and rGO, present a reduced binding affinity for the biotin-nanobody pair. This deficiency could be a result of the molecular arrangement and conformation of the adsorbed proteins.

The thickness of the nanobody layer on all surfaces is about 2 nm, which corresponds to the approximate size of a nanobody molecule, indicating a single layer binding.

#### 4. Lysozyme detection and binding analysis using QCM-D

This study aims to construct a standard curve for each sensing surface and determine the  $K_D$  value, which is an important characteristic of the nanobody representing its binding strength. **Fig. 7.2 (a,c,e,g)** presents the QCM-D results from the five sensing surfaces used as a sensing platform for the detection of varied concentrations of lysozyme. The frequency shift ( $\Delta F$ ) obtained from the QCM-D measurement is proportional to the mass adsorbed on the sensing surface, while the dissipation change ( $\Delta D$ ) is related to the viscosity of adsorbed material. We observe that both the frequency and dissipation increase as a function of the concentration of lysozyme, thus, the adsorption rate increases with respect to the enzyme concentrations. After the rinsing step, most molecules were rinsed off from the surface, as observed from the decrease of both the frequency and dissipation shift; however, the signals might not be fully recovered due to the presence of impurities and non-specific binding molecules.



**Fig. 7.2** QCM-D results from the five sensing surfaces used as a sensing platform for detecting varied concentrations of lysozyme (a) S.8 PrGO2-EDC/NHS (c) S.9 rGO-BSA-EDC/NHS (e) S.11 PrGO2-SA (g) S.12 rGO- BiotBSA-SA and the standard curve with the computed  $K_D$  values of the nanobody on different sensing platforms.

Based on the standard plot of all surfaces (**Fig. 7.2 (b,d,f,h)**), the value of  $\Delta F$  starts reaching a plateau at a concentration of approximately 125  $\mu\text{g/ml}$ . The “one site—total binding” function was used as a data fitting model. This model is based on the law of mass action mode representing the equilibrium binding that takes non-specific binding (NB) into account [289]. The model equation is the following:

$$Y = \frac{(B_{\text{max}})X}{K_d + X} + (NS)X + \text{Background}$$

With this model, maximum specific binding ( $B_{\text{max}}$ ) and  $K_D$  can be determined by fitting only the total binding parameter, assuming that the amount of nonspecific binding is proportional to the concentration of lysozyme. The plots were fitted using the Prism software (Version 9.3. 1). The data shows a good fit using this model with  $R^2 > 0.97$ . The same nanobody should result in the same  $K_D$  value if the binding process occurs with high specificity. A comparison of the obtained  $K_D$  values is presented in **Table 7.5**. Section 7 includes a discussion in this regard.

The  $K_D$  values for all samples were determined from the value of the concentration at half-maximum binding at equilibrium. This method for determining  $K_D$  is selected since the adsorption profile from the QCM-D measurements cannot fit well with the binding kinetics function including the association for on-rate and dissociation for off-rate. We believe that this could be caused by the non-specific adsorption on the sensing surface and the impact of turbulence from the sample injection procedure. The QCM-D cell volume is 40  $\mu\text{l}$  which is almost 650 times larger than the volume from the SPR instrument which is only 0.06  $\mu\text{l}$ . This high volume could cause significant disturbances to the signal. Thus, the on-rates for the instrument cannot be applied. Similarly, off-rates will be significantly inaccurate due to the time it takes to fill the chamber with buffer. Increasing the flow rate can help tackle this limitation, however, using QCM-D data for on and off rate analysis is not a general practice and therefore it is not recommended.

#### 5. Specificity studies with other proteins

The five selected surfaces were functionalised with the nanobody and tested against BSA and IgG proteins. **Fig. 7.3 (a)** shows a graphic depiction that represents the ability to detect a specific analyte (lysozyme) of the functional surfaces compared to other proteins, measured by the QCM-D technique. The complete QCM-D profiles can be

found in ESI 3.10. All surfaces display specificity against BSA; however, a high amount of IgG non-specifically adsorbed on the amine-crosslink surfaces S.7, S.8, S.9. Interestingly, only S.11 and S.12 present selectivity against both proteins. S.8 does not have an adlayer that prevents non-specific binding whereas S.7 and S.9 have both SAMs and BSA layers contributing to the observed 1 nm thickness. However, this thickness might be too thin to block the non-specific adsorption caused by electrostatic forces between solid surface charges and the proteins. Still, non-specific molecules can be adsorbed on the sensing surface. It has been reported that the thickness and density of the interfacial regions affect the proteins diffusing through it due to ionic strength and surface charge [290]. The higher thickness of the S.11 and S.12 sensing layers, arising mainly from a SA layer (3-8 nm, see **Table 7.4**), acts as an interfacial barrier to prevent electrostatic and other possible interactions between the solid surface and the proteins.

**Fig. 7.3(b)** presents the adsorption of diluted calf serum in PBS (1:50) on the five functional surfaces. The S.11 and S.12 surfaces adsorb the lowest amounts of calf serum (17 Hz) compared to other surfaces. These results clearly show that the SA-biotin surfaces functionalised with the nanobody provide better detection selectivity compared to the amine-crosslinking system.

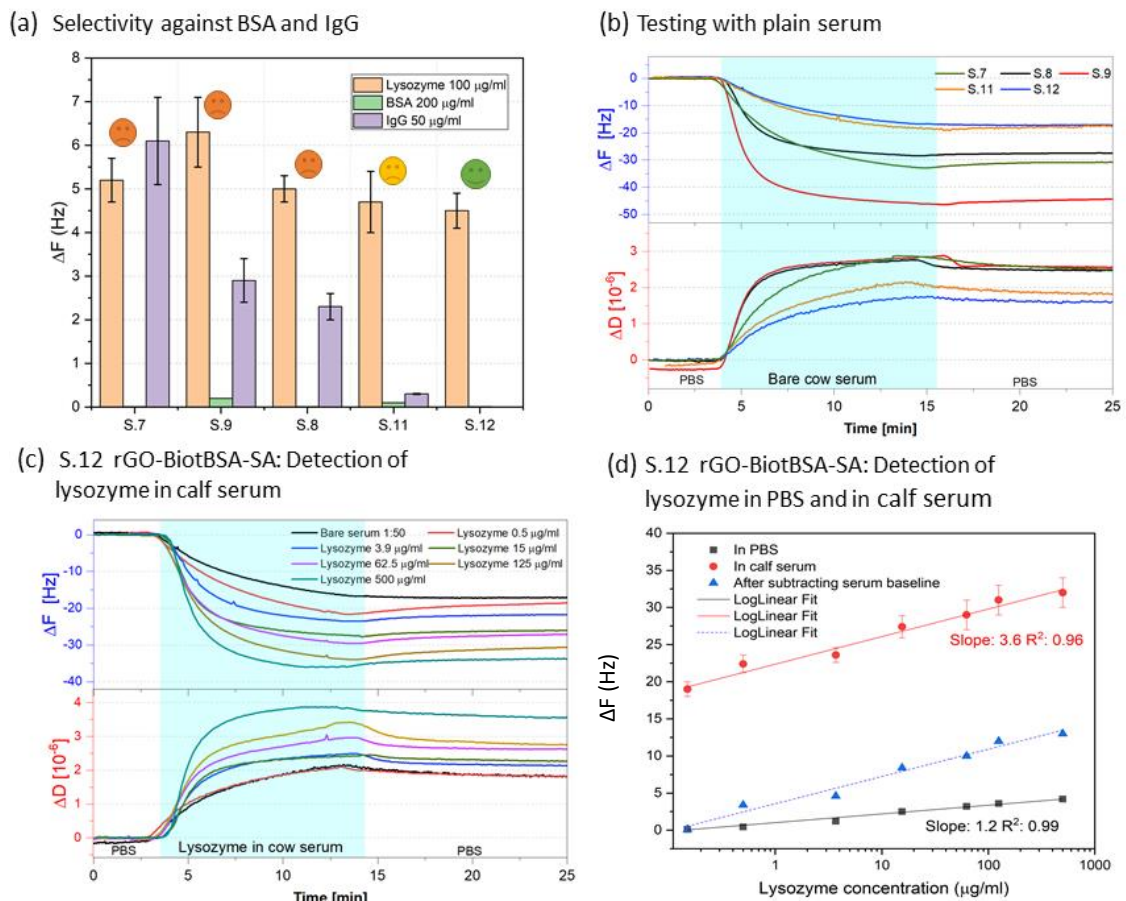
## 6. Quantification of lysozyme in calf serum

Only the S.12 surface, which corresponds to rGO-biotBSA-SA functionalised with the FO7 nanobody was chosen for quantifying lysozyme in cow serum functional as it provides the best selective performance with zero adsorption of BSA and IgG. Another reason for selecting this surface is because the highly hydrophobic rGO coating can be repeatedly produced to get the same observed properties and it is easier than the PrGO2, in which the reduction level is harder to achieve with enough precision to preserve its final properties.

The binding of various concentrations of the lysozyme in calf serum (ranging from 0.5  $\mu\text{g/mL}$  to 500  $\mu\text{g/mL}$ ) was measured (**Fig. 7.3(c)**). The  $\Delta F_{\text{Lys binding}}$  and  $\Delta D_{\text{Lys binding}}$ , measured at the highest region of the graph (the highest adsorption) increases with the concentration. The bare-serum, which is a control sample, displays a frequency shift of 17 Hz, representing the background value. It clearly shows higher frequency shifts in the



sample with lysozyme added into the diluted serum compared to the control, indicating specificity against animal serum. During the adsorption process (blue band), the binding rate increases with respect to the concentration of lysozyme. The frequencies from serum with lysozyme samples shift up after rinsing, demonstrating the binding characteristic of the FO7 nanobody.



**Fig. 7.3** Results for selectivity tests of the functional surfaces **(a)** Selectivity comparison chart of sensing surfaces to different proteins. The S.12- rGO-BiotBSA-SA presents the highest specific detection of lysozyme with zero detection of other proteins. **(b)** QCM-D profiles obtained from the adsorption of plain serum on sensing surfaces. The SA-biotin surfaces (S.11, S.12) functionalised with the nanobody provide much less adsorption from plain calf serum compared to the amine crosslinking system. **(c)** QCM-D profiles for detection of varied concentrations of lysozyme diluted in serum media operated on S.12. The  $\Delta F$  and  $\Delta D$  increase as the concentration increases. **(d)** The plot of  $\Delta F_{Lys}$  binding in both PBS and calf serum against lysozyme concentration. The lysozyme in serum media shows higher frequency shifts compared to the sample in PBS due to the serum background. The triangular markers are the frequency shifts of lysozyme in serum after subtracting the serum background.

The plot of the  $\Delta F_{\text{Lys binding}}$  in both media, PBS and calf serum, against lysozyme concentration, are presented in **Fig. 7.3(d)**. The plots from both series in PBS and serum show linear trends with slopes of value 1.2 and 3.6, respectively. The slope obtained from the lysozyme in the serum is higher than that in PBS. Such value could result from the binding of lysozyme compounding with other impurities such as albumin protein and carbohydrate ligands [291], [292]. RÖch et al. reported that lysozyme could slightly bind with serum protein, like albumin, which is negatively charged at neutral pH, whereas lysozyme carries a positive net charge [291]. Based on the linear correlation between lysozyme concentration and frequency shift, the latter can be used as a comparative value to indicate the concentration of lysozyme.

## 7. Sensing surface comparison

**Table 7.5** presents a comparison of the sensing characteristics obtained from 5 sensing platforms used in this research, namely S.7, S.8, S.9, S.11, S.12 and the results from the SPR technique with Au-SAM sensing surface with the activation of EDC/NHS reported by Birchenough et al. as a reference [284]. SPR is a commonly used label-free biosensing technique. The Biocore T200 SPR was used, and the profiles were fitted with a global 1:1 non-linear model and the affinity constant or  $K_D$  for each as determined by the model [284].  $K_D$  is the constant characteristic value of the specific ligand-binding pair representing its binding strength. The same nanobody- FO7 was used on all surfaces. The  $K_D$  value of each surface in this work was determined, as explained in Section 4.

In contrast to the  $K_D$  obtained from the SPR technique (400 nM), the  $K_D$  values obtained from the QCM system are relatively higher than that from SPR. This could be due to either the errors from non-specific binding, the presence of impurities, differences in the computation methods or a mix of them. The calculated  $K_D$  obtained from S.9 rGO-BSA+EDC/NHS is 1321 nM which is three times higher than the reference value. Since a higher  $K_D$  value represents a lower binding strength, it is assumed that the binding strength of FO7 is reduced after binding on this surface. We believe that there might be repulsive forces that slightly push lysozyme molecules from binding with nanobodies as the binding affinity could be influenced by non-covalent intermolecular interactions. These forces could be a mix of electrostatic, hydrophobic and Van der Waals forces between the lysozyme and the nanobodies cross-linking on BSA.

The  $K_D$  values for S.8, S.10 and S.11 are within the range of 600 to 700 nM which is about 200 nM higher than the reference value. In this case, the higher  $K_D$  could be the result of non-specific adsorption occurring on the surfaces as the nanobodies might not be arranged closely packed leaving some gaps on the surfaces. However, the S.12 with rGO-BiotBSA + SA system shows the closest  $K_D$  (~572 nM) to that from SPR, corresponding to lower non-specific binding compared to other surfaces as evidenced in **Fig. 7.3(a)** validating its feasibility to be used as a highly selective and reliable sensing platform.

The limit of detection (LOD) is estimated from the standard deviation of the blank samples. The standard error (SE) is a statistical term representing the possible error of the measurement. The LOD and SE for each QCM sensing surface were calculated using the formulas at the bottom of **Table 7.5**. The S.12 presents the lowest detection limit, down to 0.5  $\mu\text{g/ml}$ , followed by platform S.7 (reference surface for QCM) with 1.2  $\mu\text{g/ml}$  and S.9 with 1.9  $\mu\text{g/ml}$ . We pose that the detection limit can be significantly improved by using QCM chips with a higher fundamental frequency, like 10 MHz crystals [279] or higher. For the SE, the smaller value shows the lower error. S.12 also presents the lowest SE of ~0.9, followed by S.7 and S.11.

It is clear that the functionalisation method using rGO-biotBSA+SA with biot-nanobody provides a lower detection limit and less measurement error compared to other functional surfaces presented in this work. The use of biotinylated BSA adsorption on graphene to surfaces functionalised with SA was also demonstrated on DNA detection by Guangyu et al. [293]. The biotBSA acts as a link for SA to bind, preventing the denaturation of the nanobody and blocking non-specific bindings [200], [279], showing an increase in sensitivity and selectivity [293]. Moreover, the biotinBSA-SA layer helps block the negative surface of rGO [294] from random interactions with non-specific substances and positively charged nanobody molecules [157].

More importantly, the S.12 is the only surface that can detect analytes in serum media, confirming its potential to be practically used in clinical applications. This also represents an advantage of the QCM over the SPR as the QCM can be used with whole concentrated serum or viscous specimens, making it suitable for developing a point-of-care (POC) clinical diagnostic tools while the sample for SPR needs to be highly diluted or in the buffer where a specialised laboratory with technicians is required to perform the test.

**Table 7.5** Comparison of sensing characteristics obtained from 5 sensing platforms used in this research

Transducer	Surface	K <sub>D</sub> (nM)	LOD* (µg/ml)	SE**	Selectivity		Sample		ref
					BSA	IgG	PBS	serum	
QCM	(7) Au-SAM	616	1.2	1.1	✓	✗	✓	✗	This work
QCM	(8) PrGO2+ EDC/NHS	662	2.4	1.7	✓	✗	✓	✗	This work
QCM	(9) rGO-BSA +EDC/NHS	1321	1.9	1.7	✓	✗	✓	✗	This work
QCM	(11) PrGO2-SA	634	4.0	1.3	✓	✓	✓	✗	This work
QCM	(12) rGO-BiotBSA + SA	572	0.5	0.9	✓	✓	✓	✓	This work
SPR	Au-SAM	405	N/A	N/A	N/A	N/A	✓	✗	[284]

\*Limit of detection (LOD) = 3 x σ (5 blanks); 3-Sigma method

\*\*Standard Error (SE) =  $\frac{\sum \sigma}{\sqrt{n}}$  ; n refers to the number of samples

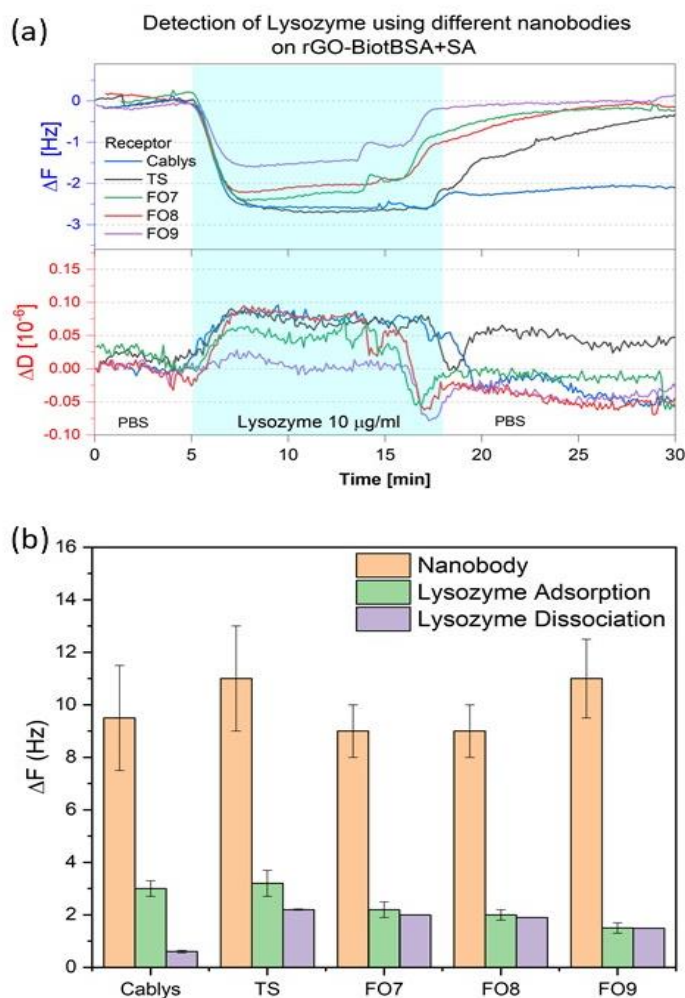
#### 8. Binding of different nanobodies and comparison with other techniques

The sensor S.12 (rGO-biotBSA-SA) was used as a sensing platform in this study. Five different nanobodies Cablys, TS, FO7, FO8 and FO9 were biotinylated and allowed to bind to the sensing surface to act as receptors. These nanobodies possess high to low binding consecutive strengths with K<sub>D</sub> ranging from 5 to 1300 nM, specifying in **Table 7.6** (reference values). The smaller the K<sub>D</sub> value, the greater the binding strength of the ligand for its target. The concentration of lysozyme was fixed at 10 µg/ml (700 nM) as a control as it is approximately the mid-range of the standard curve (**Fig. 7.2 (h)**). With this concentration, the binding and dissociation of lysozyme on different nanobodies can be clearly distinguished as presented in **Fig. 7.4 (a)**.

**Table 7.6**  $K_D$  values of five nanobodies against lysozyme with different binding strength determined from QCM adsorption profiles compared to reference values from SPR characterisation

Nanobody	$K_D$ (nM)	
	SPR (ref)	QCM ( $K_D=K_{off}/K_{on}$ )
1. Cablys	5±4	8±3
2. TS	105±58	203±62
3. FO7	401±56	375±68
4. FO8	410±55	393±59
5. FO9	1300±82	1365±76

**Fig. 7.4(a)** presents the QCM-D results from lysozyme detection using five different nanobodies as receptors. The Cablys and TS nanobodies show the highest detection of lysozyme with a frequency shift of  $\sim 2.8$  Hz, while the FO9 presents the lowest binding of lysozyme in terms of the observed frequency shift. During the rinsing process with PBS, the lysozyme adsorption on TS, FO7, FO8 and FO9 the QCM signal shows a positive shift due to a critical detachment of lysozyme molecules from the surface. However, the wash-off rate on the TS sample is slower than that from others, and the binding on FO9 decays with the fastest rate. With Cablys, the signal slightly shifts up at the start of the rinsing process and remains mostly flat. The comparative numbers of lysozyme binding and dissociation measured from  $\Delta F_{Lys}$  binding and  $\Delta F_{Dis}$  were plotted in a bar chart for easy visual comparison **Fig. 7.4(b)**. These results elucidate the effects of the binding strength of the nanobodies on lysozyme binding and dissociation. The nanobody with a high binding strength like Cablys can bind tighter to the analyte resulting in a stable QCM signal after rinsing. As observed, when lysozyme binds on FO7 and FO8, which have intermediate binding strength, it can be completely rinsed off within 10 min, while the lysozyme is presented to the TS nanobody with higher binding strength takes longer to be rinsed off. Finally, nanobody FO9, with the weakest binding strength, promoted the lowest lysozyme binding and the fastest rinse-off rate.

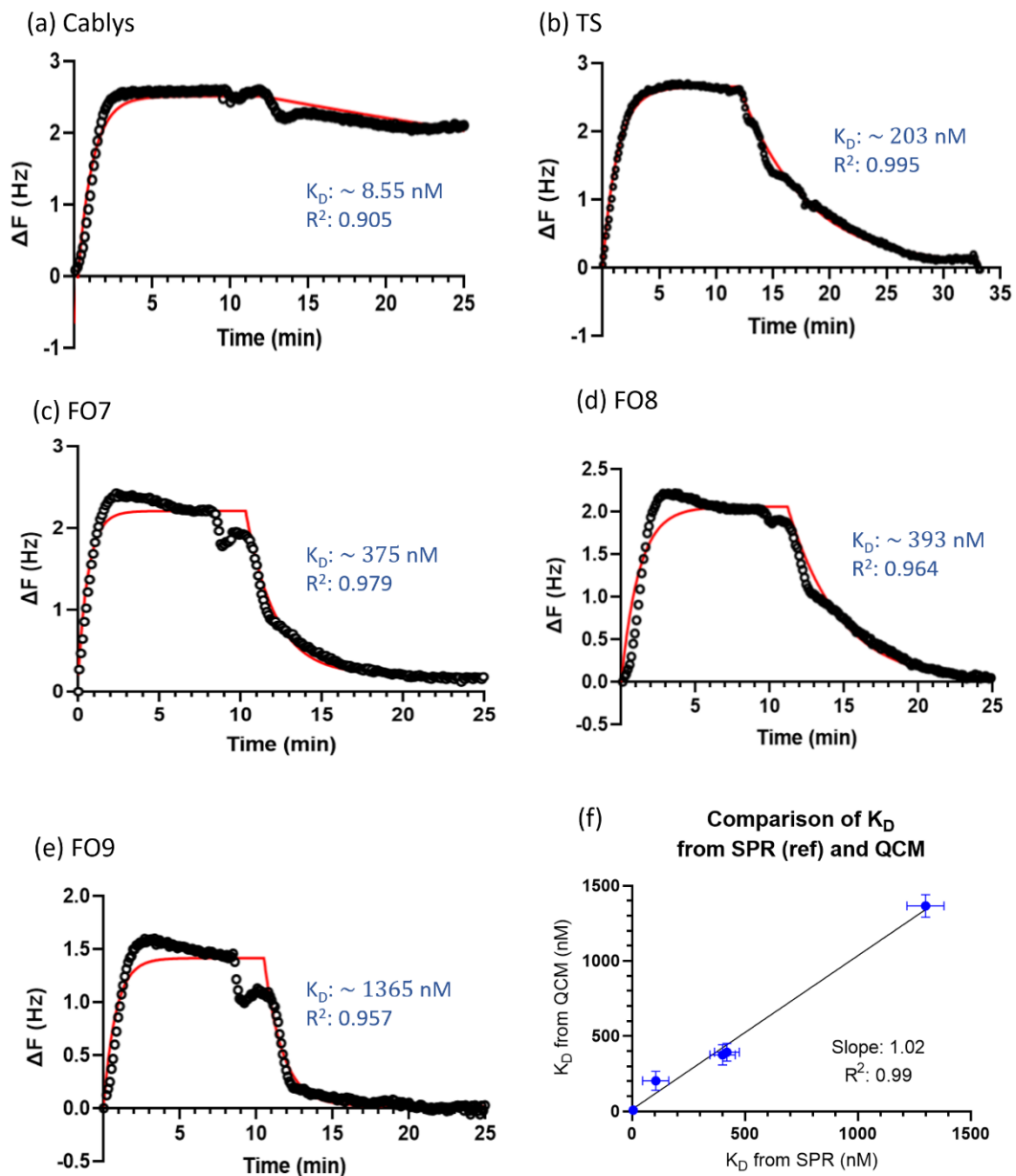


**Fig. 7.4 (a)** QCM-D results of lysozyme detection using five different nanobodies as receptors, **(b)** the comparative numbers of lysozyme binding and dissociation measured from  $\Delta F_{binding}$  and  $\Delta F_{Dis}$ .

The data from the QCM adsorption profile in **Fig. 7.4(a)** were used for the determination of  $K_D$ . The profiles were converted into a positive scale in the y-axis and fitted with the binding kinetic function—“association and dissociation” using Prism GraphPad. According to this function, the  $K_D$  can be calculated from the simple ratio  $K_{off\ rate}/K_{on\ rate}$ . The fitting and the computed  $K_D$  values are presented in **Fig. 7.5 (a-e)**. The fitting quality ( $R^2$ ) of the data is more than 0.90 indicating a good fit of the data to the kinetic function although the on rate function is slightly unfitted, as seen in **Fig. 7.5 (a, c, d, and e)**. This could be due to the effects of the turbulence that occurs in the QCM-D fluidic cell, as previously discussed in Section 4.

**Fig. 7.5 (f)** presents a comparison plot between  $K_D$  obtained from QCM and the known values determined through the SPR technique from previous work by Birchenough et al.

[284]. A resultant  $R^2$  value of 0.99 from the data fitting for both techniques validates the binding affinity of nanobodies functionalized on this sensing surface. Thanks to highly studied standard samples of nanobodies, the  $K_D$  values measured by QCM-D and standard SPR techniques are remarkably close giving a high degree of confidence in the analysis. The results also demonstrate that the proposed sensing platform – rGO-BiotBSA-SA, can be effectively used for functionalising universal nanobodies.



**Fig. 7.5 (a-e)** Kinetic fitting results of lysozyme detection using five different nanobodies as receptors, **(f)** the comparison of  $K_D$  determined by SPR and QCM-D systems

## Conclusion

We have developed a graphene-biointerface platform for functionalising with nanobodies as bioreceptors. We initially explored different methods to functionalise the protein receptor. We found that amine crosslinking and biotin-streptavidin systems can be used for functionalising nanobodies on graphene surfaces to detect an analyte in buffer. However, the graphene functionalisation with biotin-streptavidin provides better selectivity against serum proteins, like BSA and IgG, with almost zero detection, while the IgG protein can still be non-specifically adsorbed on amine-crosslinked surfaces. It is reasoned that the thicker thickness arising from the SA layer prevents electrostatic interactions between the solid surface and the proteins. The sensing surface of rGO-biotBSA-SA functionalised with nanobodies shows the best selective detection of the lysozyme with the lowest standard error compared to other surfaces studied in the present work. Based on the QCM-D results, the biotinylated BSA film formed on the rGO-coated sensing chips showed a denatured protein layer due to its strong hydrophobic interaction with the rGO surface, matching our previously reported results [200], [279]. This layer serves two main purposes: as a linker for SA binding and as a blocking agent non-specific interaction from complex fluids. Interestingly, the nanobodies can be biotinylated and effectively functionalised on this rGO-BiotBSA-SA platform. We have shown that the nanobodies against lysozyme functionalised on this platform are capable of detecting lysozyme in both PBS buffer and animal serum. The same functionalisation method was also tested with five nanobodies possessing distinctive binding strengths to lysozyme. The  $K_D$  values of the nanobodies measured on this sensing surface using the QCM technique are acceptably close to the reference values obtained from the standard SPR technique, validating the feasibility of our technique to be a selective and reliable sensing platform. This graphene-nanobody sensor offers a controllable and straightforward functionalization method with highly specific detection of biomolecules. Moreover, we claim/pose that this platform could be extended to develop other chip-based immunosensors and drug delivery systems where nanobody functionalisation is applied.



## CHAPTER 8. Publication as the second author

Development of an open-source thermally stabilized quartz crystal microbalance instrument for biomolecule-substrate binding assays on gold and graphene

Meléndrez, D., Hampitak, P., Jowitt, T., Iliut, M., & Vijayaraghavan, A. (2021). Development of an open-source thermally stabilized quartz crystal microbalance instrument for biomolecule-substrate binding assays on gold and graphene. *Analytica Chimica Acta*, 338329.

Available at <https://doi.org/10.1016/j.aca.2021.338329>

### **Authors contributions:**

**Daniel Melendrez** designed the experiment and conceptualization. He also developed the thermal chamber and QCM data acquisition software. He tested and validated the in-house QCM system. He wrote the original draft, reviewed and edited.

**Piramon Hampitak** prepared the QCM sensors and carried out all the QCM-D experiments. She prepared samples for XPS measurement and analysed the results. She wrote e-original draft including the section of 'Protein adsorption on Au and rGO, Mass adsorption and comparison with QSense, and discussion', Writing e-review & editing.

M. Iliut prepared and purified GO dispersions. She also carried out AFM imaging.

T. Jowitt, and A. Vijayaraghavan supervised P. Hampitak on conceptualization and experimental design. All authors read and approved the final manuscript.

## **Development of an open-source thermally stabilized quartz crystal microbalance instrument for biomolecule-substrate binding assays on gold and graphene**

Daniel Meléndrez<sup>§</sup>, Piramon Hampitak<sup>a</sup>, Thomas Jowitt<sup>b</sup>, Maria Iliut<sup>a</sup> and Aravind Vijayaraghavan<sup>a,\*</sup>

<sup>a</sup>*Department of Materials and National Graphene Institute, The University of Manchester, Oxford Road, Manchester M13 9PL, UK.*

<sup>b</sup>*School of Biological Sciences, Faculty of Biology Medicine and Health, The University of Manchester, Oxford Road, Manchester M13 9PL, UK.*

*\*Corresponding Author: aravind@manchester.ac.uk; +441612750136*

### **Abstract**

The interaction of biomolecules, such as proteins, with biomaterial surfaces, is key to disease diagnostic and therapeutic development applications. There is a significant need for rapid, low-cost, field-serviceable instruments to monitor such interactions, where open-source tools can help to improve the accessibility to disease screening instruments, especially in low- and middle-income countries. We have developed and evaluated a low-cost integrated quartz crystal microbalance (QCM) instrument for biomolecular analysis based on an open-source QCM device. The custom QCM instrument was equipped with a custom-made electronically controlled isothermal chamber with a closed-loop control routine. A thermal coefficient of 5.6 ppm/°C was obtained from a series of evaluations of the implemented control. Additionally, a custom-designed data acquisition system and a mathematical processing and analysis tool is implemented. The quartz crystal detection chips used here incorporate gold and reduced graphene oxide (rGO) coated surfaces. We demonstrate the system capability to monitor and record the biomolecular interaction between a typical protein bovine serum albumin (BSA) and these two substrates. The Sauerbrey mass adsorption modelling on rGO-coated crystals shows that a detection limit down to ~7 µg/mL is possible, with significant room for improvement. This instrument was compared to a commercial QCM, demonstrating good correspondence between the computed mass adsorption density responses using the Sauerbrey model. The instrument presented here has the potential to serve as a ubiquitous bioelectronic tool for point-of-care disease screening and rapid therapeutics development.

## Keywords

Quartz crystal microbalance, Bovine serum albumin, Reduced graphene oxide, Biosensor, Open-source

## Introduction

Standard biomedical instrumentation equipment and immunological research tools present limitations such as high cost, complexity of use and related steep learning curves that require highly skilled operators, and large size that makes point-of-care installation challenging, all of which hinders their use for early disease detection and delays medical interventions [295]–[297]. Their cost, complexity and use of proprietary technologies that limit field-serviceability also hinders their accessibility for low- and middle-income (LMI) countries. However, one route to develop easy-to-use, low-cost, adaptable and field-serviceable disease screening tools is to use affordable yet powerful embedded systems under open-source licensed ecosystems [295], [298]. Modern embedded systems are not only capable of reading and converting the signals produced by different types of biosensors, but some platforms also offer internet connectivity that makes possible sharing data with practitioners in remote locations for real-time diagnosis under the Internet of Things (IoT) scheme of intelligent devices [299].

A biosensor is an analytical sensing device in which specific physiochemical changes that occur during the interaction between recognition bioelements such as proteins, enzymes or antibodies and an analyte are quantitatively converted into an electronic signal by a transducer [300], [301]. Depending on the mechanism of transduction, a biosensor can be identified as optical, thermal, ion-sensitive, electrochemical or mass-sensitive, amongst others.

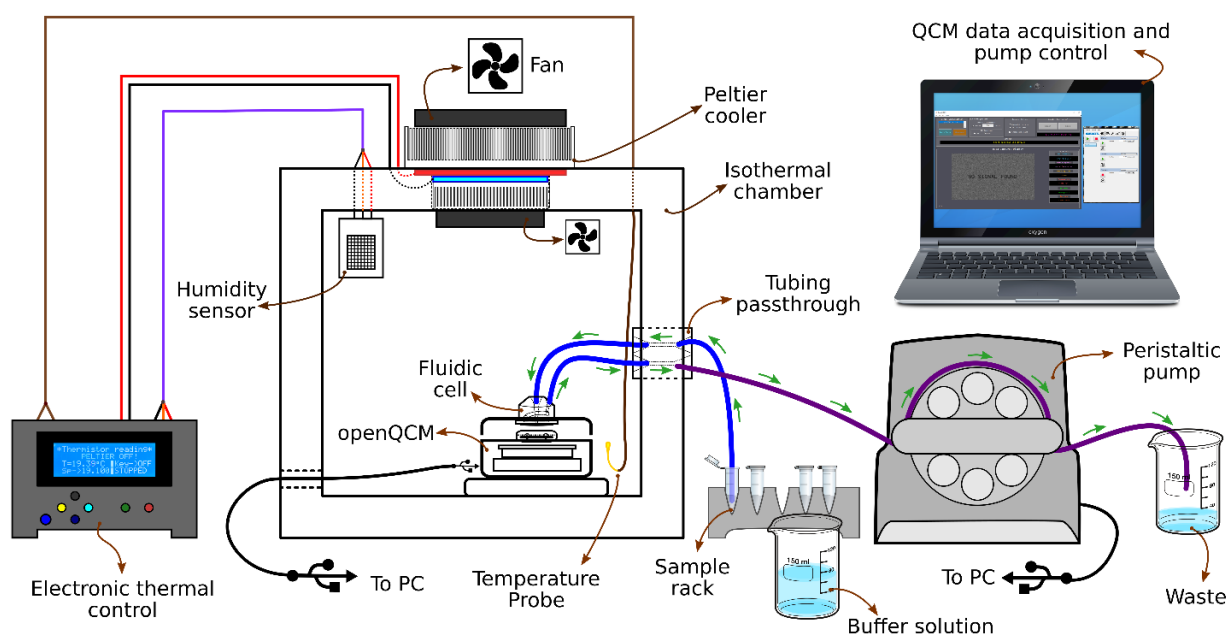
In this paper, we report on the development and evaluation of an inexpensive quartz-crystal microbalance (QCM) instrument to study the biochemical binding interactions occurring at the sensor's surface. A QCM is a mass-sensitive technique based on the piezoelectric effect. It offers real-time and label-free capabilities for monitoring interfacial interactions with high sensitivity, quantifying mass adsorption events at the  $\text{ng}\cdot\text{cm}^2$  range [302]–[304]. Our instrument is based on the *openQCM* device (Novaetech, S.r.l, Italy), the first open-source QCM released under the Creative Commons license.

The QCM technique enables the modulation of the biomolecular adsorptions through the modification of the sensor's working electrode, which typically is made of a chromium-supported gold layer. Gold is a widely used material for biotechnological applications thanks to its inert chemical nature [305], [306]. Invariably, gold substrates are coated with self-assembled monolayers (SAMs) to enable the biochemical functionalisation by tailoring the hydrophilic or hydrophobic nature of the substrates [306]–[308]. For instance, SAMs of thiol chains can render the surface hydrophobic [309], [310].

Graphene has recently attracted attention as a promising biosensor surface material is due to its unique physical, chemical and electronic properties [311]–[315]. Graphene has been shown to improve the sensitivity of a biosensor thanks to its high specific surface area and electrical conductivity [208], [311], [316], [317]. Reduced graphene oxide (rGO) is commonly obtained through chemical, photochemical or thermal deoxygenation of graphene oxide (GO) to obtain a material that resembles, to an extent, the properties of pristine graphene, including increased electrical conductivity and a highly hydrophobic surface. It has been shown that the performance of a biosensor can be tuned by modifying its surface with thin GO or rGO films where hydrophilic or hydrophobic interactions and  $\pi$ - $\pi$  stacking are dominant forces at the interface [86], [200], [312], [318]. We have previously reported on the formation of supported phospholipid monolayers and multilayers [6] as well the adsorption dynamics of bovine serum albumin (BSA) on rGO platforms [200] using the QCM with Dissipation monitoring (QCM-D) technique, where we revealed the pivotal role that the hydrophobicity and surface chemistries of the supporting substrates play during the adsorption events.

Despite the analytical advantages offered by monitoring the energy dissipation occurring at the QCM's interface during a mass adsorption event, the adsorption of small, rigid proteins may be effectively measured and quantified by exclusively monitoring frequency changes. For instance, serum albumins are small model proteins that are extensively used to prevent non-specific adsorption by blocking nonconjugated surfaces during a biosensing event [319]. Therefore, BSA was selected as the protein for the evaluation of the QCM instrument reported here.

We have developed an affordable custom QCM (cQCM) instrument based on the openQCM device. It is aimed at point-of-care operation for rapid detection and diagnosis based on protein-binding methodologies. Additionally, we equipped the cQCM with a custom-made electronic closed-loop control for temperature stabilisation (**Fig. 8.1**). We assessed the stability of the instrument's response under controlled thermal conditions. Additionally, we evaluated our system through biomolecular adsorptions occurring at bare gold and graphene modified substrates. The sensors were conditioned and coated with GO and rGO films by following our procedure reported previously [6]. Finally, the results obtained with the cQCM were contrasted with a commercial QCM system with dissipation monitoring capabilities in order to validate the performance of our system. The resultant mass adsorption densities are comparable for both gold and graphene sensors, at a small fraction of the cost.



**Fig. 8.1** Thermally stabilized cQCM laboratory instrument setup showing the openQCM device inside an isothermal chamber, Peltier cooler, temperature and humidity sensors and front panel of the custom-made electronic temperature control. A portable computer captures the QCM data through a custom GUI and controls the 3-channel peristaltic pump for sample flowing.

## Materials and methods

### 1. Chemicals and materials

GO dispersion was prepared by a modified Hummers' method [202] followed by exfoliation and purification (see ESI 4.1). The stock dispersion of GO was diluted to a concentration of 0.8 mg/mL. Albumin, monomer bovine (A1900), and phosphate buffered saline (PBS), pH 7.4 (P4417) (Sigma-Aldrich UK) were used as received. Buffer solution was prepared dissolving 1 PBS tablet in 200 mL of ultrapure water. This solution was stirred for at least 30 minutes and filtered using sterile syringe filter units with a pore size of 0.22  $\mu\text{m}$  (Millex-GP, PES membrane). This buffer solution was degassed using pulsed bath ultrasonication under vacuum for at least one hour. BSA stock solution was prepared with a concentration of 5 mg/mL. Serial dilutions of BSA were prepared from the stock solution. A mild solution for initial cleaning of the QCM and QCM-D systems and quartz crystals was prepared with 2% SDS and Hellmanex II solution in MilliQ water. A stronger cleaning solution was prepared using the following reagents ratios:  $\text{H}_2\text{O}_2:\text{NH}_3:\text{DI water} = 1:1:5$ .

### 2. Equipment

#### 2.1 QCM chips

All adsorptions measured using our cQCM instrument, driven by the openQCM device, were performed on Gold QCM sensors from Quartz Pro (Stockholm, Sweden) with a fundamental frequency of 10 MHz. For the QSense Pro (Biolin Scientific, Gothenburg, Sweden) system, QCM-D sensors with gold surface electrode (QSX-301, Biolin Scientific) and a fundamental frequency of 5 MHz were used. The value for the 3<sup>rd</sup> harmonic for both frequency ( $\Delta f_{n=3}$ ) and energy dissipation ( $\Delta D_{n=3}$ ) components were captured for comparative analysis.

To form GO thin films, a spin-coater (Laurell Tech., WS-650MZ) was used. Both QCM and QCM-D sensors were thoroughly cleaned according to the following procedure: QCM sensors were first soaked for at least 20 minutes in the 2% SDS/Hellmanex solution to remove oil-based contaminants. This initial step is followed ultrasonication for 10 minutes in acetone, then isopropanol; intercalating DI water rinsing steps between each solution. Then, the crystals were treated under oxygen plasma at 80% power for 2

minutes (a 100W reference system is used). Using the strong cleaning solution, the crystals were soaked at 75 °C for 5 minutes. Finally, the sensors were rinsed with copious amounts of ultrapure water and dried with a mild stream of Nitrogen gas before storing them in a dust-free and humidity-controlled environment before coating.

After the cleaning process, the crystals were coated with GO via spin coating (speed: 3000 rpm, acceleration: 350, 2 min) to form thin GO films on the chips. To obtain rGO-coated sensors, GO-pre-coated crystals were annealed at 180 °C under vacuum (~1 mBar) for 24 hours (Townson + Mercer EV018 vacuum oven).

The degree of reduction was characterised via wetting contact angle (WCA) measurement (Kruss DSA100) of sessile drops (~5 $\mu$ L) of DI water and X-ray photoelectron spectroscopy (XPS) using SPECS custom built system composed of a Phobios150 hemispherical electron analyser with 1D detector. The XPS data was analysed using CasaXPS software (version 2.3.18). The rGO sample for XPS was prepared using the same conditions used for the reduction of GO on QCM crystals. The GO was first casted and dried on the Si/SiO<sub>2</sub> (290 nm) substrate, followed by the reduction in vacuum at 180 °C for 20-25 hours.

Scanning electron microscopy (SEM) was performed on a SEM Zeiss Ultra setup, using an acceleration voltage of 5 kV and a working distance of 5 mm. AFM topography images were acquired using a Bruker Alpha system in tapping mode with FastScan-A probes with a cantilever spring constant of 18 N/m.

## 2.2 cQCM system construction

The core monitoring device from our custom QCM instrument is the openQCM device. A detailed description of the principle of operation of this device is included in ESI 4.2.

A thermistor with a Negative Temperature Coefficient (NTC), (Vishay PN: NTCLE201E3103SB) with a room temperature resistance ( $R_0$ ) of 10.00 k $\Omega$  and  $\beta_{25/85}$  of 3977 was used as the temperature sensor for the isothermal chamber. It was configured in a voltage divider circuit (ESI 4.2 **Fig. S4.2**) with a reference resistor with a value of 10.00 k $\Omega$   $\pm$ 0.1%. A detailed description of the implemented instrumentation for temperature reading and digitization are included in ESI 4.3.1 and ESI 4.3.2, respectively. The humidity of the system was monitored during temperature stabilization. This

humidity sensor (DHT22, Aosong Electronics) is an embedded digital device that uses a polymer capacitor as the sensing element and outputs the value of the sensor as a digital signal. A 20W thermoelectric Peltier cooling assembly (AR-AR-019-12, Adaptive Thermal Management) was attached to a fully-insulated polystyrene (PS) box with the cold side facing inwards the box. A peristaltic pump (Ismatec Reglo ICC, 3 Ch) was placed after the QCM sensor to draw the liquid from the sample vials (**Fig. 8.1**) in order to minimise the formation of microbubbles.

A custom-made graphic user interface (GUI) was developed in Matlab R2018a to perform data acquisition, baseline calibration and data post-processing. ESI 4.4 describes the general functionalities and implementation of this software.

### 2.3 Development of a thermally stabilized QCM system

In order to accurately control the temperature of the inner atmosphere of the chamber, a Proportional Integral Derivative (PID) closed-loop control was implemented. Please refer to ESI 5 for a complete description of the PID control technique. The temperature control is driven by an Arduino Pro *Micro* microcontroller (**ESI Fig. S4.3**) board mounted on a custom-designed PCB. It captures and converts the readings from the thermistor, reads the user input for control parameters, processes the PID control algorithm and accordingly activates an electromechanical relay that powers a Peltier cooler. The temperature reported by the digital temperature sensor from the openQCM shield board showed an offset of 4.9 °C with respect to temperature registered by an NTC installed inside the chamber. This value was used as a correction factor in the firmware from the electronic control. ESI 4.6 provides a detailed description of the digital implementation of the temperature control algorithm.

### 2.4 Validation of the closed-loop thermal control

One of the few disadvantages of the openQCM device is that it presents an intrinsic self-heating effect that can be attributed to the simplicity of its construction. The processing unit, an Arduino *Micro* development board, which is in direct spatial contact with the printed circuit board that drives the QCM sensor, warms up after power-up affecting the frequency of oscillation over a defined stabilisation period (< 1 hour). Therefore, the

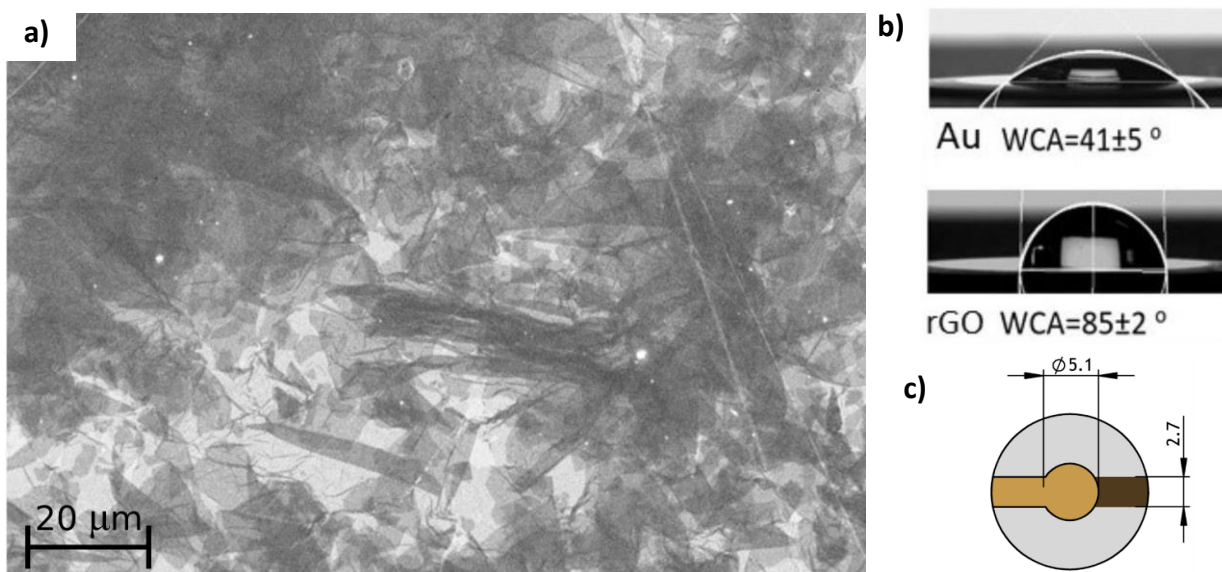


system was enclosed in an electronically-controlled thermal chamber in order to reduce any thermal effects on the oscillations.

The first description of how capable the isothermal chamber is for keeping a stable temperature was done in terms of the frequency shift reported by the crystal during a low-to-high temperatures excursion on air. To do this, a clean crystal was mounted in the openQCM enclosure and a temperature of 13°C was manually set on the controller and left overnight in order to ensure complete stability. Raw frequency values were captured and no liquid was flowed during this evaluation. Once the frequency and the temperature were stable, the QCM was let to warm up via its self-heating effect and the isothermal chamber was left to stabilize. When a frequency plateau was reached a new temperature was selected and the system left to stabilize again until a new stable frequency was reached. Five temperatures were conFig.d during this evaluation: 13 °C, 15 °C, 20 °C, 24 °C and 30 °C.

A second analysis was performed during constant forced cooling to determine the thermal performance of the chamber. This evaluation would shed light on the change rate of the frequency with respect to the temperature until the QCM sensor reported a stable oscillating frequency once it reached a target temperature. From this result, a two-variable function,  $F(t,T)$  expresses the evolution of the resonant frequency in terms of the temperature decay during the period that the cQCM system usually takes to reach complete frequency stability (< 2 hours).

This examination was started by loading a clean Quartz Pro sensor in the cQCM enclosure, then the system was placed inside the isothermal chamber which had been left at room temperature. The board was powered on through the USB port of the acquisition computer and the crystal was left overnight to unperturbedly oscillate on air without thermal control so that the board could gradually self-heat. After ~12 hours of stable oscillation, the board reported a maximum temperature of 34.1°C. The acquisition was then restarted and after 10 minutes of capturing raw frequencies the thermal control was activated with a setpoint of 20 °C.



**Fig. 8.2 a)** SEM micrograph from rGO coated on Au QCM sensor. The working surface is fully covered with a varied number of graphene layers from one to few monolayers, **b)** Wetting contact angle (WCA) of bare Au and rGO-coated QCM sensors, **c)** Quartz Pro QCM sensors working electrode dimensions.

### 3. BSA protein adsorption study

Prior to every experiment a clean sensor was left inside the isothermal chamber for at least 1 hour with the electronic control enabled in order to guarantee absolute stability. The overall resultant frequency dependence on the temperature was lower than 5 Hz/°C. Sample injection was kept at a continuous flow rate of 50  $\mu\text{L}/\text{min}$  during 18 mins, therefore approximately 850  $\mu\text{L}$  were flowed over the crystal. Then, the buffer solution was flowed until the frequency reached good equilibrium ( $\text{SD} < 0.2$ ). At the completion of the experimental routine, SDS 2% solution was flowed at 100  $\mu\text{L}/\text{min}$  followed by ultrapure water at the same rate for at least 2 hours to ensure complete cleanse of the fluidic circuit.

In order to provide contrasting evidence of the functionality of the system, the same concentrations and experimental conditions were used on the QSense Omega Pro system from Biolin Scientific using bare Au

and rGO-coated crystals. The Sauerbrey equation was used to model the aerial mass adsorption for the range of BSA concentrations used.

## Results and discussion

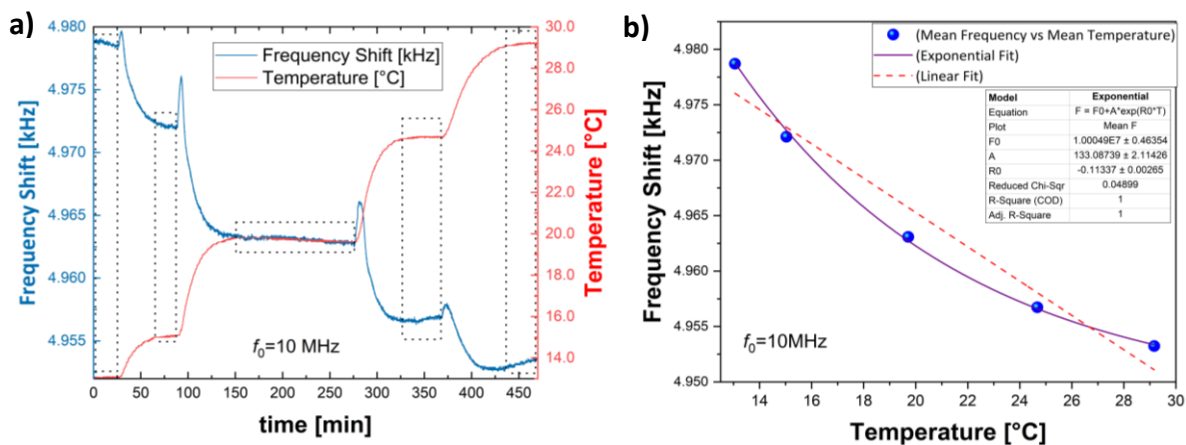
### 1. Characterisation of rGO-coated QCM sensors

SEM imaging reveals the topography of the GO film on the surface of the Au working electrode of QCM chips obtained by spin-coating. It is formed by a continuous film of overlapping flakes covering the entire surface (**Fig. 8.2a**), with film thicknesses varying from one to few monolayers. **Fig. 8.2b** shows sessile drops of DI water on the surface of the bare Au and rGO-coated QCM chips (**Fig. 8.2c**). The Au surface exhibits a hydrophilic property with a WCA of  $41^{\circ}\pm 5^{\circ}$  while the rGO surface is hydrophobic with a WCA of  $85^{\circ}\pm 2^{\circ}$ . XPS images for rGO coatings are presented in ESI 4.7. Refer to ESI 4.8 for AFM topography images from bare and coated sensors.

### 2. Thermal chamber evaluation

During this temperature dependence analysis, the onboard digital temperature sensor from the openQCM device showed a slight readout variation with respect to the selected values, as reported by the thermistor from the chamber, however the differences are mostly negligible as confirmed by their respective standard deviation (SD). **Table 8.1** summarizes the results for the differences in temperature and the statistical evaluation of the results. **Fig. 8.3** illustrates the results of this evaluation process. The sections highlighted with dotted squares on **Fig. 8.3a** are considered as regions of acceptable stability based on their flatness and the SD of the responses for both variables  $f$  and  $T$ . The observed overshoot in the frequencies may be attributable to a thermal inertial effect resulting from the specific thermal gradient of the whole system. **Fig. 8.3b** includes two different fitting curves for the points obtained from the stability regions. The best-fitting curve is an exponential function that adjusts the obtained values for  $F$  and  $T$ . The linear fit was selected to represent the overall change rate of the frequency with respect to the total temperature change during the evaluation process. From this result it becomes evident that maintaining a constant temperature to reduce the observed self-heating effect throughout a whole experimental routine is crucial to preserve a flat frequency response. Moreover, this result justifies the necessity of thermally stabilizing the chamber before starting and during the whole duration of an experiment as well as maintaining a thermally unperturbed system.

The result for the continuous thermal evaluation over a period of 100 minutes is presented in **Fig. 8.4**. A manifest thermal drift is observed as a result of the temperature dependence of quartz resonators. The progress curves for frequency dependence on temperature change showed an initial rate period with linear trend (**Fig. 8.4a**), then both curves bend before reaching a stability region. The individual responses for frequency and temperature,  $F(t)$  and  $T(t)$  were then parametrized and plotted as  $F(T)$  in **Fig 8.4b**. This result demonstrates the impact of the temperature on the response of the QCM sensors. Interestingly, this trend is in line with the same evaluation presented in the seminal work from Sauerbrey (Sauerbrey, 1959) for the same type of QCM sensors used, AT-Cut crystal at  $35^\circ 15'$  (please refer to **Fig. 8.10** from (Sauerbrey, 1959)). When the temperature increases within the temperature range of  $30^\circ\text{C}$  to  $40^\circ\text{C}$ , the frequency shows a semi-linear region with a negative change rate, equivalent to the trend discussed here.



**Fig. 8.3** Results for long thermal evaluation of the isothermal chamber. Vertical axis expressed the frequency shifts in kHz **a)** Thermal evaluation of the system's self-heating effect under controlled cooling. Temperature reported by the openQCM onboard sensor when controlling the temperature of the chamber upon self-heating, **b)** Temperature dependence of the frequency response of a QCM sensor under controlled cooling. Frequency vs Temperature response curve (•) for the data regions highlighted in (a) and two curve fits, linear and exponential, are shown and discussed in the text. Crystal's fundamental frequency,  $f_0 = 10 \text{ MHz}$ .

**Table 8.1** Summary of mean temperature values and frequencies during the selected stabilization ranges

Temperatures [°C]				Frequencies [Hz]	
Target Temp.	Obtained Mean Value	Difference	SD	Mean Value	SD
13	13.05	0.05	0.02	10,004,978.7	0.155
15	15.03	0.03	0.03	10,004,972.1	0.113
20	19.71	-0.29	0.07	10,004,963.1	0.176
24	24.67	0.67	0.02	10,004,956.7	0.137
30	29.17	-0.83	0.04	10,004,953.2	0.208

The resultant slope shown in **Fig. 8.4b**, with an absolute value of 4.94 Hz/°C, can be refactored in terms of the resolution of our thermal control, equal to 0.0875°C (see ESI 4.3.2). Therefore, the change rate of the frequency per Celsius is approximately 56.45 Hz/°C. Thus, the resultant temperature coefficient of frequency for our thermal control is 5.6 ppm/°C, for QCM sensors with a fundamental frequency of 10 MHz. This value represents the frequency stabilization capabilities of the designed isothermal chamber.

### 3. Protein adsorption studies with cQCM and QCM-D systems

#### 3.1 QCM theory

In 1959, Sauerbrey demonstrated that upon adding mass to a QCM sensor surface a frequency decrease proportional to the added mass occurs and given that the mass is small compared to the total weight of the crystal the frequency change is directly proportional to the mass of the crystal (Eq. 1) [252]. therefore their use as microbalances is based on the linear relationship between changes in the resonator mass and in the resonance frequency [252], [320].

$$\frac{\Delta m}{A} = -\frac{\sqrt{\rho_Q \mu_Q}}{2f_0^2} \Delta f \quad [g/cm^2] \quad (\text{Eq. 1})$$

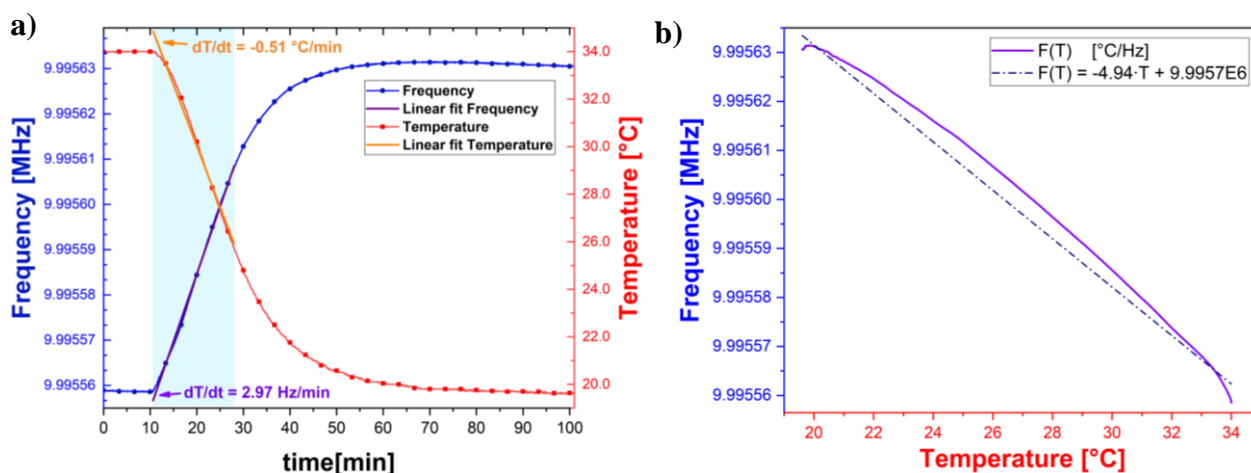
A detailed mathematical development of Eq. 1 is included in ESI 4.9).

Several reports have demonstrated the possibility to study the adsorptions of small proteins using conventional QCM surfaces due to the rigid coupling of some proteins to the substrate obtaining negligible or low viscoelastic characteristics, therefore allowing

the use of the Sauerbrey model [321]–[323]. However, it is important to acknowledge that no absolute standard exist to establish dissipation as negligible. An often-used rule of thumb is that the Sauerbrey equation gives a correct value for mass added if the associated dissipation value with the adlayer is less than  $2 \times 10^{-6}$  [324], [325]. The dissipation values reported in the literature for the adsorption of BSA onto QCM-D substrates meet this criterion [326]–[328].

### 3.2 Protein adsorption on Au and rGO

Once the cQCM instrument was thermally stable, it was used to measure the adsorption of different BSA protein concentrations, ranging from  $10 \mu\text{g/mL}$  to  $1000 \mu\text{g/mL}$  on QCM surfaces. Two substrates with different surface chemistries, Au and rGO were used for these adsorption studies. The humidity of the chamber throughout these experiments was registered in the project workbook with an average value below 65%. The overall temperature for the QCM experiments described here was  $20.3 \text{ }^\circ\text{C} \pm 0.0014^\circ\text{C}$ . **Fig. 8.5a** and **5b** present the results from the adsorptions of BSA on bare Au and rGO-coated QCM sensors, respectively. Similarly, **Fig. 8.5c** and **8.5d** present the same pair for the QSense system.



**Fig. 8.4** Results for the continuous cooling of the openQCM system **a)** QCM frequency response at continuous temperature decrease. Frequency response and temperature evolution over time. Both frequency and temperature present a linear region (in light blue) with change rates of  $2.97 \text{ Hz/min}$  and  $-0.51 \text{ }^\circ\text{C/min}$ , respectively, **b)** Frequency vs temperature ( $F(T)$ ) characteristic.

On bare Au, during BSA adsorption the frequency increasingly shifts with respect to the degree of protein concentration. **Fig. 8.5a** shows QCM measurement for BSA adsorption on Au using our cQCM instrument. The total frequency shifts for all concentration of BSA are from about 10 Hz to 500 Hz. Similarly, the results from the QSense system show an increase on the frequency shift and adsorption rate as the concentration of protein is increased, (**Fig. 8.5c**). However, the range of the total frequency shifts for all concentrations lies between 4 to 35 Hz, which are considerably lower than those obtained with our cQCM.

**Fig. 8.5b** corresponds to the adsorption of BSA onto an rGO-coated sensor using our cQCM. For a BSA concentration of 10  $\mu\text{g/mL}$ , the adsorption shows a fast adsorption rate at the initial stage followed by a notably slow adsorption, as the change of frequency is almost flat. The total frequency shift after the rinsing process is approximately 20 Hz. For BSA concentrations of 20  $\mu\text{g/mL}$  and 50  $\mu\text{g/mL}$ , a fast adsorption rate at the initial stage followed by no further adsorption after a few minutes, as evidenced by the flat frequency shift. The total frequency shift in both cases are similar at approximately 32 Hz. With a BSA concentration of 100  $\mu\text{g/mL}$ , the adsorption rate is initially high then slows down after a few minutes, resulting in a total frequency shift of about 40 Hz. For the highest used BSA concentration of 1000  $\mu\text{g/mL}$ , the protein was rapidly adsorbed onto the surface with a frequency shift of approximately 140 Hz, then no more adsorption was observed, as noted by the flat frequency response.

Similar to the results obtained with our cQCM system, the adsorption of BSA on rGO-coated sensors measured with the QSense system shows different adsorption characteristics depending on the concentration of the protein. For low concentrations of BSA (10, 20, 50  $\mu\text{g/mL}$ ), the adsorption shows a comparable trend: fast adsorption rate at the initial stage followed by a slower adsorption after a few minutes, as the frequency responses are almost flat. The total frequency shifts for those three cases are about 5 Hz. In contrast, for a BSA concentration of 100  $\mu\text{g/mL}$ , the graphs show a 2-stage adsorption with different adsorption rates. The initial stage presents a fast adsorption rate with an intermediate frequency shift of about 5 Hz, then the adsorption rate decreases and the frequency changes homogeneously reaching a plateau at 11 Hz. For a

BSA concentration of 1000  $\mu\text{g}/\text{mL}$ , the protein was rapidly adsorbed onto the surface, then slowed down reaching a total frequency shifts of approximately 17 Hz.

The adsorption kinetics obtained from both systems are fairly similar, observing a 2-stage adsorption for 100  $\mu\text{g}/\text{mL}$  BSA onto rGO. We have recently evidenced this behaviour in a systematic study of the adsorption of BSA on graphene platforms [200]. At this point is important to highlight the differences on the sample injection/flowing methods as they can render specific hydrodynamic pressure profiles. While our system uses a peristaltic pump that withdraws liquid from the sample vials (**Fig. 8.1**), the QSense system uses a top-injection and lateral-withdrawal syringe pumps with precision motorized stages.

### 3.3 Mass adsorption and comparison with QSense

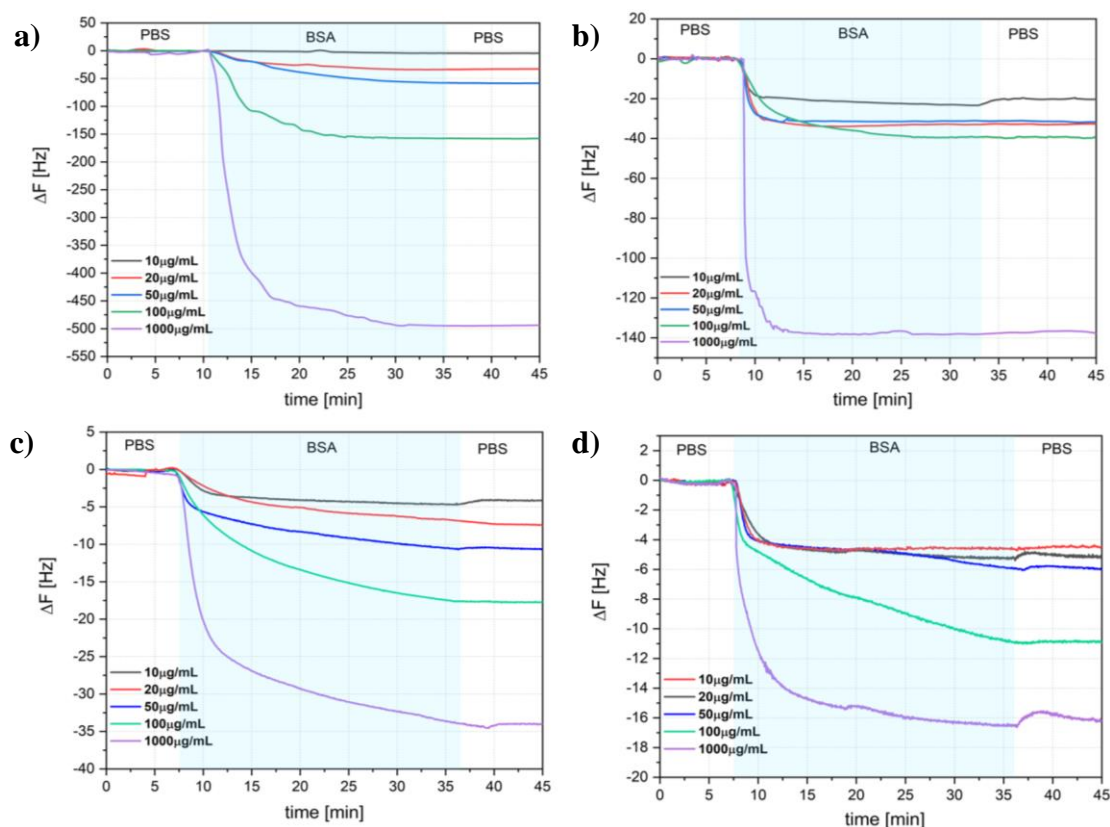
A comparative evaluation of the adsorption of BSA with the same five concentrations using the QSense system is presented. The total aerial mass density adsorption was obtained from the Sauerbrey equation (Eq. 1) for both frequency responses and are shown in **Fig. 8.6**. Quantitatively, the mass densities obtained using both systems show similar trends and their magnitudes are comparable within the margins of error for both gold and rGO surfaces. For the adsorption on rGO surface, the adsorption mass of all concentrations, calculated from QSense results, are slightly higher than those measured from our in-house system probably due to the topographical differences between the two types of crystals, QSense vs. Quartz Pro.

## 4. Discussion

BSA can be modelled as an oblate ellipsoid with approximate dimensions 4 nm x 4nm x 14 nm in an aqueous solution with a molecular weight of 66 kDa [101]–[103],[106]. BSA adsorbs with specific orientations lead to specific adsorption kinetics when in contact with substrates with different chemistries [107]. The BSA protein adsorption at the solid and liquid interface can occur due to electrostatic interactions, hydrogen-bonding and hydrophobic interactions [15], [106], [329]. The hydrodynamic adsorption of BSA molecules onto a surface may align in two orthogonal extreme orientations: side-on and end-on; this model has been used in several reports [106]–[109]. If a side-on orientation is considered, one BSA molecule will occupy an approximate area of 56  $\text{nm}^2$ , resultant from a projection on the X-Y plane of the ellipsoidal shape of the protein [106], [327].



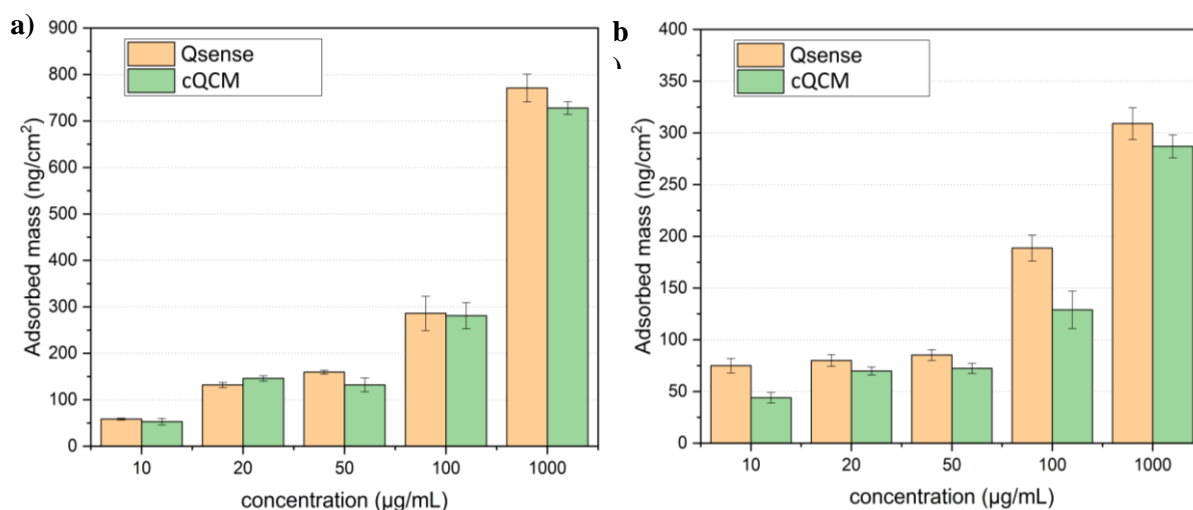
This results in a maximal density of  $1.78 \times 10^{12}$  BSA molecules per  $\text{cm}^2$  or  $194 \text{ ng/cm}^2$  for the monolayer side-on arrangement. For the end-on scenario, a BSA molecule occupies an approximate area of  $16 \text{ nm}^2$  corresponding to  $9.63 \times 10^{12}$  BSA molecules per  $\text{cm}^2$  or  $685 \text{ ng/cm}^2$  for the monolayer end-on adsorption.



**Fig. 8.5** QCM results for the adsorptions of BSA on **a)** bare Au and **b)** rGO-coated using the cQCM, **c)** and **d)** present the same pair for the QSense system.

On a gold sensing surface, the mass adsorption for the BSA concentration  $10 \mu\text{g/mL}$  to  $1000 \mu\text{g/mL}$  ranges from  $40 \text{ ng/cm}^2$  to  $800 \text{ ng/cm}^2$ . For the case of BSA concentrations lower than  $100 \mu\text{g/mL}$ , a side-on deposition on gold of the protein can be assumed due to low adsorption density. Also, the adsorbed layer might be denatured as lower concentrations the protein has a longer time to spread on the surface leading to structural changes [228]. In this regard, McArdle et al. studied the effect of concentration of MvBOx to bare and SAM-modified surfaces using QCM and DPI, claiming that low concentrations protein has time to relax on the surface and form a more rigid layer due to the lack of electrostatic repulsion from the presence of neighbouring proteins and extensive denaturation of the protein occur the case of low concentration ( $100 \mu\text{g/mL}$ ) [228].

For BSA at a high concentration environment, the observed high amounts of adsorbed mass could be due to more adsorbed molecules and water entrapment into the protein layers [112], [327]. The interaction between BSA and gold could be driven by hydrophobic interaction via hydrophobic residues, electrostatic interaction via the positively charged lysine residues and bonding between the single free thiol on BSA (associated with a cysteine residue) and Au surface [330], [331]. Moreover, several reports on the interaction of BSA with Au have stressed the importance of the maximization of hydrophobic interactions as a crucial factor in the irreversible adsorption of proteins with denaturation [106], [326].



**Fig. 8.6** BSA mass adsorption densities comparison on **a)** bare Au and **b)** rGO-coated sensors. Results for the cQCM instrument are shown in green bars while QSense results correspond to the orange bars. See online version for colour.

In contrast, on rGO surfaces, the mass adsorption ranges from 30 ng/cm<sup>2</sup> to 300 ng/cm<sup>2</sup> for the concentration range used in this study. The adsorption mass on rGO surface is relatively lower than that on gold surface. It is assumed that deposited BSA molecules flattened and denatured on rGO surfaces due to the strong hydrophobic interaction with rGO resulting in lower adsorbed mass [200]. A two-stage adsorption process in the case of BSA concentration higher than 100 µg/mL could have begun with the formation of a rigid layer, where the spreading of molecules is higher, followed then by the formation of an additional layer of BSA molecules [200], [228]. Interestingly, an initial fast adsorption rate of low BSA concentrations (< 50 µg/mL) on rGO surfaces is observed. It is believed that this effect is due to predominant hydrophobic interactions between rGO

and the hydrophobic functional groups of BSA in addition to  $\pi$ - $\pi$  stacking processes, which in turn flatten the protein molecules, saturating the surface of the working electrode [200], [332], [333].

**Table 8.2** summarises the evaluation results from our system, including: limit of detection, sensitivity and linear ranges for the concentrations studied. The complete set of calibration curves is included in ESI 4.10.

The limit of detection (LOD) was computed using the 3-sigma method, according to **Eq. 2**.

$$LOD = \frac{3\sigma}{S_{LR}} \quad [\mu g/mL] \quad (\text{Eq. 2})$$

Where:

$\sigma$  is the standard deviation (SD) of the response from blank sensors

$S_{LR}$  is the slope from the Linear Range (LR) of the respective calibration curves

In general, the cQCM system offers higher sensitivity and lower detection limits compared to the QSense system due to the higher fundamental frequency from the cQCM sensor (10 MHz vs 5 MHz).

The highest sensitivity was observed on the bare Au substrate with the cQCM system. The resultant  $\Delta F$  vs concentration pairs for both cQCM and QSense systems were plotted and fitted using Hill curve fitting, a widely used model to describe occupancy of biomolecules on surfaces, like BSA-Au [334]. The linear regions from bare Au substrates lie within the concentration range of 10  $\mu g/mL$  to 100  $\mu g/mL$ , obtained from the fitted sigmoidal curves for both systems.

Interestingly, rGO-coated substrates present a relatively wider range of linearity compared to bare-Au. It is reasoned that a thin film of squashed BSA molecules forms on the rGO surface followed by the stacking of an additional layer of BSA, exposing more hydrophilic regions where more molecules can be adsorbed [200]. This results in the increase of the molecular saturation point of the crystal. On bare-Au, in contrast, the crystal reaches a faster BSA saturation without molecular flattening as the concentration increases, matching the Hill model.

In terms of the LOD, values of  $\sim 6.8 \mu\text{g/mL}$  and  $\sim 9.8 \mu\text{g/mL}$  were obtained for the cQCM and QSense systems, respectively. The rGO surface in the cQCM system linearly responded within the concentration range of  $20 \mu\text{g/mL}$  to  $1000 \mu\text{g/mL}$  while the QSense system reported a lower linear range from  $50 \mu\text{g/mL}$  to  $1000 \mu\text{g/mL}$ , for the rGO surface. This difference could be due to intrinsic properties of the QSense and cQCM systems i.e. hydrodynamic pressure, noise floor and sensor instrumentation principle.

**Table 8.2** Summary of sensitivity, limits of detection and linear ranges for the cQCM and QSense systems

System	Surface	LOD ( $\mu\text{g/mL}$ )	Sensitivity ( $\text{Hz}/\mu\text{g mL}^{-1}$ )	Linear Range ( $\mu\text{g/mL}$ )
cQCM	Bare Au	$\sim 2.6$	1.63	10-100
	rGO	$\sim 6.8$	0.10	20-1000
QSense	Bare Au	$\sim 4.4$	0.14	10-100
	rGO	$\sim 9.8$	0.01	50-1000

## Conclusions

We have evaluated the performance of a thermally stabilised open source-based QCM instrument through protein adsorptions. The designed instrument is targeted at biomolecular interactions studies with field-operability capacity at an affordable total cost of  $\sim \text{£}2000$ . It was observed that a continuous cooling process has a stronger effect on the frequency stabilization rate compared to that for forced cooling upon self-heating. In the linear fittings for the two responses of  $F(T)$  (**Fig. 8.3b** and **8.4b**), the discrete evaluation showed a slope of  $-1.5477 \pm 0.1988 \text{ Hz}/^\circ\text{C}$  while the continuous cooling showed a change ratio of  $-4.94 \pm 0.01082 \text{ Hz}/^\circ\text{C}$ , which represents an increase in the cooling capability by a factor of  $\sim 3$ . The overall humidity of the chamber throughout these experiments was below 65%. In spite of the low SD for the temperatures obtained for the BSA adsorption studies and the good temperature stability during the lifetime of each experimental session, there is a possibility of increasing the accuracy of the target

temperature by interfacing the readout value from the openQCM board to the PID control via the GUI for data acquisition. In this way, the chamber sensor would be bypassed as the QCM temperature monitoring device and the control could be driven by the temperature reported by the openQCM's on-board digital sensor. This new approach would eliminate the resultant offset from the temperatures reported by the two sensors and, in consequence, the efficacy of the thermal control would significantly improve. Additionally, it is possible to increase the granularity of the temperature reading by changing to an external 12-bit or higher resolution ADC module.

In spite of the fact that the cQCM system presented here inherently lacks dissipation monitoring capabilities, it showed higher sensitivity and lower detection limits compared to the commercial system and at a much lower cost. It was observed that the adsorption dynamics strongly depends on the protein concentrations and surface chemistries. Particularly, rGO-coated QCM sensors present relatively wider range of linearity for BSA adsorption compared to bare-Au as an additional protein layer is formed promoting hydrophilic regions where more molecules can be adsorbed. This can be useful to tailor QCM-based biomolecular assays, as we have recently demonstrated on the development of a Point-of-Care immunosensor for membranous nephropathy [279].

The functionalization of QCM substrates with biochemical species, including the formation of rGO-supported biotinylated lipid monolayers or the use of "reporter" molecules, can be explored. This integrated system presents an opportunity for materials scientists, biomedical engineers or practitioners for studying chemical and biomolecular interactions with surfaces. Moreover, it can help develop label-free, fast and low-cost immunoassays readily available for homecare use without extensive training. It has the potential to become a rapid and highly sensitive point-of-care diagnostic instrument especially well-suited for low- and middle-income countries. Future upgrades will endow the instrument with a multi-channel reading of bio-functionalised sensors, reversible chamber cooling and heating, machine learning and mobile access with both clouds- and host-based computing capabilities.

## **CRedit authorship contribution statement**

**Daniel Melendrez:** conceptualization, investigation, software, validation, data curation, formal analysis, writing - original draft, writing – review & editing, funding acquisition.

**Piramon Hampitak:** investigation, methodology, data curation, formal analysis, writing – original draft, writing – review & editing, funding acquisition. **Thomas Jowitt:**

supervision, methodology, resources. **Maria Iliut:** investigation, resources, writing – review & editing. **Aravind Vijayaraghavan:** conceptualization, methodology,

supervision, writing - original draft, writing – review & editing, project administration, funding acquisition.

## **Acknowledgments**

D. M. acknowledges The National Council for Science and Technology (CONACyT), Mexico for the financial support. D.M. thanks Marco Mauro from Novaetech (*openQCM* team) for the technical support and feedback provided during the course of this research. P.H. acknowledges the financial support of the Development and Promotion of Science and Technology Talents Project (DPST), Thailand. We acknowledge the support of the Biomolecular Analysis Core Facility, Faculty of Biology Medicine and Health, The University of Manchester. AV acknowledges funding from the Engineering & Physical Sciences Research Council (EP/K016946/1).

## CHAPTER 9. Conclusions

In this thesis, graphene derivatives were used as a coating material for QCM sensing chips to improve their surface functionalities. Three main pieces of research were presented. First, a fundamental study of graphene and biomolecule interaction was described. Then, the development of a real-world application, a biosensor-based tool for disease screening, where the development of a sensor prototype and its testing and validation was discussed. Finally, the utility of the graphene-QCM immunosensor was further explored by functionalising with nanobodies as protein receptors for lysozyme detection.

Graphene derivative surfaces were intensively characterised using various techniques, including SEM, AFM, contact angle, XPS, and Raman, to understand the materials' physical and chemical properties. A fundamental understanding of graphene-proteins interaction was achieved by systematically investigating the interaction between graphene derivatives and the serum protein BSA through the QCM-D technique. It was observed that the adsorption and orientation of the protein on graphene significantly depend on the hydrophilic and hydrophobic domains of the graphene surface, acting as a platform with tuneable hydrophobicity. The molecular conformations of BSA upon adsorption on graphene with varying degrees of hydrophobicity were mapped and presented in publication 1. Based on these results, different routes to functionalise different kinds of protein receptors, including fragments of antigen and nanobodies, were explored, as presented in publications 2 and 3. Furthermore, a real-world application of the graphene bio-interface sensor was exemplified.

In publication 2, a novel graphene-protein bio-interface was constructed by adsorbing a low concentration of denatured bovine serum albumin (BSA) on the reduced graphene oxide (rGO) sensor surface. The BSA film prevented the denaturation of the protein receptor on the rGO surface and served as the cross-linker for immobilisation of the receptor for anti-PLA2R antibodies on the surface. As a result, the detection limit and selectivity of our in-house G-QCM biosensor are comparable to a commercial QCM system. Furthermore, the results obtained from patient sera compared favourably with

those from enzyme-linked immunosorbent assay (ELISA), validating its feasibility for clinical applications.

In publication 3, a to be published work, we have explored using the graphene-QCM sensing tool with single-domain antibodies or nanobodies as receptors for antigen protein. The nanobody against lysozyme was used as a model protein pair. We found that graphene with amine crosslinking and biotin-streptavidin systems can be used for functionalising nanobodies to detect an analyte in the buffer. However, only the interface corresponding to graphene functionalised with biotin-streptavidin proved to have selectivity against serum proteins, including BSA and IgG. The sensing surface rGO-biotBSA-SA functionalised with nanobodies showed a highly selective detection of the lysozyme in both buffer and calf serum media with a lower standard error of the measurement compared to other tested surfaces. The same functionalisation method was tested with the other five nanobodies specific to lysozyme. The observed binding trends from the QCM-D results align with the kinetics dissociation values from each nanobody, demonstrating the feasibility of the method to be universally adopted for nanobody functionalisation.

In the collaborative publication, we have evaluated the performance of a thermally stabilised open source-based QCM instrument through BSA protein adsorptions. The instrument was designed to be a low-cost and field-serviceable system that can potentially benefit the development of point-of-care medical devices. The BSA adsorption on Au and rGO were tested on the in-house-QCM and the commercial QCM instrument. Our QCM system presented higher sensitivity and lower detection limits compared to the commercial system.

From a general perspective, this Doctoral research work has traversed the field of 2D materials, especially graphene, passing through the fundamentals of the core sensing technique applied in the present thesis, the QCM technique, pinpointing its applicability in biotechnology. From a professional standpoint, the accumulated knowledge set solid theoretical and experimental grounds that led me to perform a series of systematic studies on the biomolecular interactions of a serum protein, BSA, with graphene. A comprehensive understanding of bio-interface interactions and the vast experience



gained from working with the primary sensing technique led to the development of immunosensing platforms using antigens and nanobodies as protein receptors. The prototype of a point-of-care immunosensor based on the QCM technique was developed and validated with patient serum samples emphasising its potential to be a real-world disease screening tool. Further clinical trials will be conducted to transfer the scientific findings and technological aspects from this research to commercial medical instruments of high impact. Moreover, the graphene-protein platform proposed and described here could help to diversify the detection capabilities and performance of immunosensing instruments.

## APPENDICES

Electronic Supporting Information 1 for publication 1

Electronic Supporting Information 2 for publication 2

Electronic Supporting Information 3 for publication 3

Electronic Supporting Information 4 for the publication as a second author

## Electronic Supporting Information 1.

This supporting information is for publication 1.

### **Protein interactions and conformations on graphene-based materials mapped using quartz-crystal microbalance with dissipation monitoring (QCM-D)**

Piramon Hampitak<sup>1</sup>, Daniel Melendrez<sup>1</sup>, Maria Iliut<sup>1</sup>, Maryline Fresquet<sup>2</sup>, Natalie Parsons<sup>1</sup>, Ben Spencer<sup>1</sup>, Thomas Jowitt<sup>2</sup>, and Aravind Vijayaraghavan<sup>1,\*</sup>

<sup>1</sup>*Department of Materials and National Graphene Institute, Faculty of Science and Engineering, The University of Manchester, Oxford Road, Manchester M13 9PL, UK.*

<sup>2</sup>*School of Biological Sciences, Faculty of Biology Medicine and Health, The University of Manchester, Oxford Road, Manchester M13 9PL, UK.*

Here, we provide the protocol for QCM-D measurement and present the computational methods for calculating mass adsorption as well as supplementary results and analysis. More information about experimental protocols related to graphene coating and the QCM-D measurement are described in the supplementary information of Melendrez et al.[6].

#### **1.1 Protocol for QCM-D measurement of protein adsorption study**

##### **1.1.1 Initial preparation of Quartz Crystals**

The quartz crystal sensors with a gold surface with fundamental frequency of 5 MHz (QSX-301) were purchased from Biolin Scientific. To prepare the sensors for studying the adsorption of biomolecules on graphene derivatives surfaces, the QCM chips were cleaned following a modification of the protocol provided by QSense, then coated with GO using a spin coater to get the GO chips. To get rGO chips, the GO pre-coated chips were thermally reduced to rGO at controllable conditions following **Fig. S1.5** in ESI 1.5.

##### **Cleaning protocol for Au QCM chips**

This cleaning process is required to be carried out under a fumes hood, wearing adequate PPE.

1. Wash the crystals by soaking them for at least 20 minutes in a cleaning solution containing any of the following surfactants: 10% Decon-90 or 2% SDS and/or 2% Hellmanex in water to remove any oil-based contaminants. This process is followed by ultrasonication of the crystals for 10 mins in acetone, then in isopropanol, intercalating DI water rinsing steps between each solution. This process ensures that the surfaces are free of any organic and/or polymeric residue.
2. Treat the crystals with oxygen plasma treater at 80% power (100 W reference system) for 2 mins.
3. Wash with cleaning solution for gold crystals ( $\text{H}_2\text{O}_2$ :  $\text{NH}_3$ : DI water= 1:1:5) at 75 °C for 5 mins
4. Rinse with MilliQ water, keeping the sensor surface wet while rinsing. 5. Dry the crystals with a mild stream of nitrogen gas and store them in a dust-free and humidity-controlled environment before using the bare sensors or during the coating procedure.

### **Coating the sensors with GO**

After the thorough cleaning procedure, the QCM crystals were coated with an in-house prepared GO dispersion via spin coating (Laurell Technologies Corp, WS-650MZ-23NPPB). The following parameters were set: speed: 3500 rpm, acceleration: 350 rpm/sec, time: 2 mins. With these parameters, thin and uniform GO films were achieved on QCM-D Au substrates. A GO dispersion with a concentration of 0.8 mg/mL was drop-casted on the QCM chip fully covering the area of its working electrode. The solution was left to settle for 30 seconds before spin coating.

#### **1.1.2 BSA solution preparation**

Albumin, monomer bovine (A1900) and phosphate-buffered saline (PBS, P4417 - pH 7.4) were purchased from Sigma–Aldrich. Ultrapure water was obtained from a Milli-Q Integral Water Purification System. BSA stock solution was prepared with a concentration of 5 mg/mL. Different concentrations of BSA solution including 10 $\mu\text{g}/\text{mL}$ , 50  $\mu\text{g}/\text{mL}$ , 100  $\mu\text{g}/\text{mL}$  500  $\mu\text{g}/\text{mL}$  and 1 mg/mL were prepared from the stock solution.

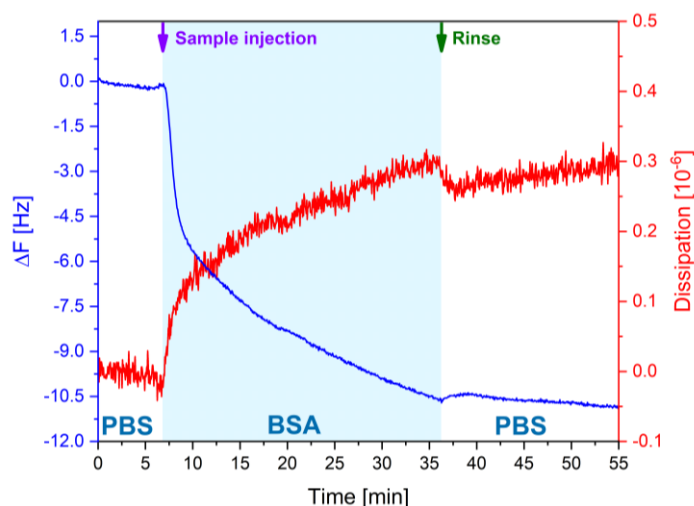
### 1.1.3 QCM-D measurement procedure

The QCM-D measurements for BSA adsorption on both Au and GO- and rGO-coated Au chips were carried out using the Q-Sense Omega Auto system (Biolin Scientific). The system consists of eight sensing ports that can be automatically fed through customized scripts. As each fluidic cell has an O-ring the same size as the sensing area of the QCM-D chip, the fluid flow is isolated over the sample area. Before every experimental session, the ports and sensors holder were cleaned using clean maintenance chips following the protocol described below. The temperature of the system was set at 20°C to avoid the effects of possible thermal drift on the response signals. Once the system was primed, the sensors for experimentation were loaded on the sensors holder.

At the beginning of each measurement, the sensors were primed by continuously flowing PBS until a stable baseline was obtained. This process is crucial for the removal of trapped bubbles, to verify the quality of the sensors and thus to obtain reliable measurements. Once a stable baseline was observed, the corresponding measurement script was started.

In the present report, the standard steps for measuring the adsorption of BSA onto different substrates are continuous injection of PBS to obtain a flat baseline, then BSA sample injection followed by a stabilization period, then a final PBS rinse stage, as shown in **Fig. S1.1**. A flow rate of 10  $\mu\text{L}/\text{min}$  was selected for all measurements.

Once the measuring script is completed, to avoid contamination it is recommended to run a washing routine to clean the sensors, syringes and tubing using surfactant solutions such as Hellmanex and/or SDS to be then finally rinsed with MilliQ water and left to dry overnight. This process ensures that the system is left clean and dry for subsequent experiments.



**Fig. S1.1** Injection sequence for measuring protein adsorption with QCM-D. During the initial stage, a stable baseline must be reached. After stabilizing the QCM chip with PBS, the sample is injected then flowed through the sensor continuously for ~30 mins, then rinsed with PBS to remove loosely bound molecules.

## 1.2 Theory of QCM-D

QCM-D monitors molecular adsorption on surfaces through real-time measurement of changes in frequency ( $\Delta f$ ) and dissipation ( $\Delta D$ ) with high temporal resolution. Higher mass adsorption will result in large frequency down-shift. The amount of adsorbed mass can be determined by using the Sauerbrey equation [167], (equation 1), and viscoelastic modelling [169].

$$\Delta m = -\frac{A\sqrt{\rho_q\mu_q}}{2f_0^2}\Delta f \quad (1)$$

where

$f_0$  is the resonant frequency (Hz)

$\Delta f$  is frequency the change (Hz)

$\Delta m$  is adsorption mass change (g)

$A$  is the Piezoelectrically active crystal area (area of working electrode,  $\text{cm}^2$ )

$\rho_q$  is the density of quartz (typically  $2.648 \text{ g/cm}^3$ )

$\mu_q$  is the shear modulus of quartz for AT-cut crystal (typically  $2.947 \times 10^{11} \text{ g}\cdot\text{cm}^{-1}\cdot\text{s}^{-2}$ )

The dissipation or damping is the sum of total energy losses in the system in an oscillation cycle defined as the lost energy divided by the total energy stored in the

system,  $E_{\text{loss}}/E_{\text{total}}$ . High dissipation will be the result of viscoelastic adsorption of molecules creating a soft film on the surface. In contrast, a rigid film adsorbed on the crystal usually gives low dissipation values. The slope of the plot of  $\Delta D$  vs  $\Delta f$ , also known as dissipation density, reveals regions of different adsorption behaviour in terms of the viscoelastic structure of the adsorbed material.

### **QCM-D modelling**

Computational mathematical modelling of the acquired QCM-D data was carried out to determine the mass, thickness and viscoelasticity of the adsorbed films using QSense Dfind software provided by Biolin Scientific. QSense Dfind supports QCM-D profile data obtained from QSense and is employed to visualise and model the physical properties of the molecular layers under analysis. The software provides computational methods to determine the mass adsorbed onto a QCM sensor surface including Sauerbrey and viscoelastic modelling based on Voigt-Voinova model[169]. The general procedure for extracting information from QCM-D profiles is shown in **Fig. S1.2**.

Briefly, for processing the '.QSOD' files that contain the acquired QCM-D data, the following procedure was performed. First, after importing the files using Dfind, a series of parameters including the density of adsorbed materials, buffer and periods of each adsorption process must be set before starting the computational processes. To accurately determine the adsorbed mass, thickness and viscoelastic properties, it is crucial to choose the right model according to the observed adsorption kinetics. If there is no considerable separation in the frequency shifts between the harmonics and no significant shifts on the dissipation curves, it is recommended to use Sauerbrey's model. On the other hand, the viscoelastic modelling with Smart Fit or Broad Fit should be performed if the measurement contains great dissipation shifts and/or well-spread frequencies for the different harmonics. The fitting process works by first calculating the output values for a model with a certain set of input parameters and then adjusted until the output values are close as much as possible to the original values. To achieve a good fit for the viscoelastic modelling, Chi-square and fit quality are the statistical parameters considered to determine the goodness of the fit. Chi-square is the most common criterion for minimizing  $\chi^2$  defined as:

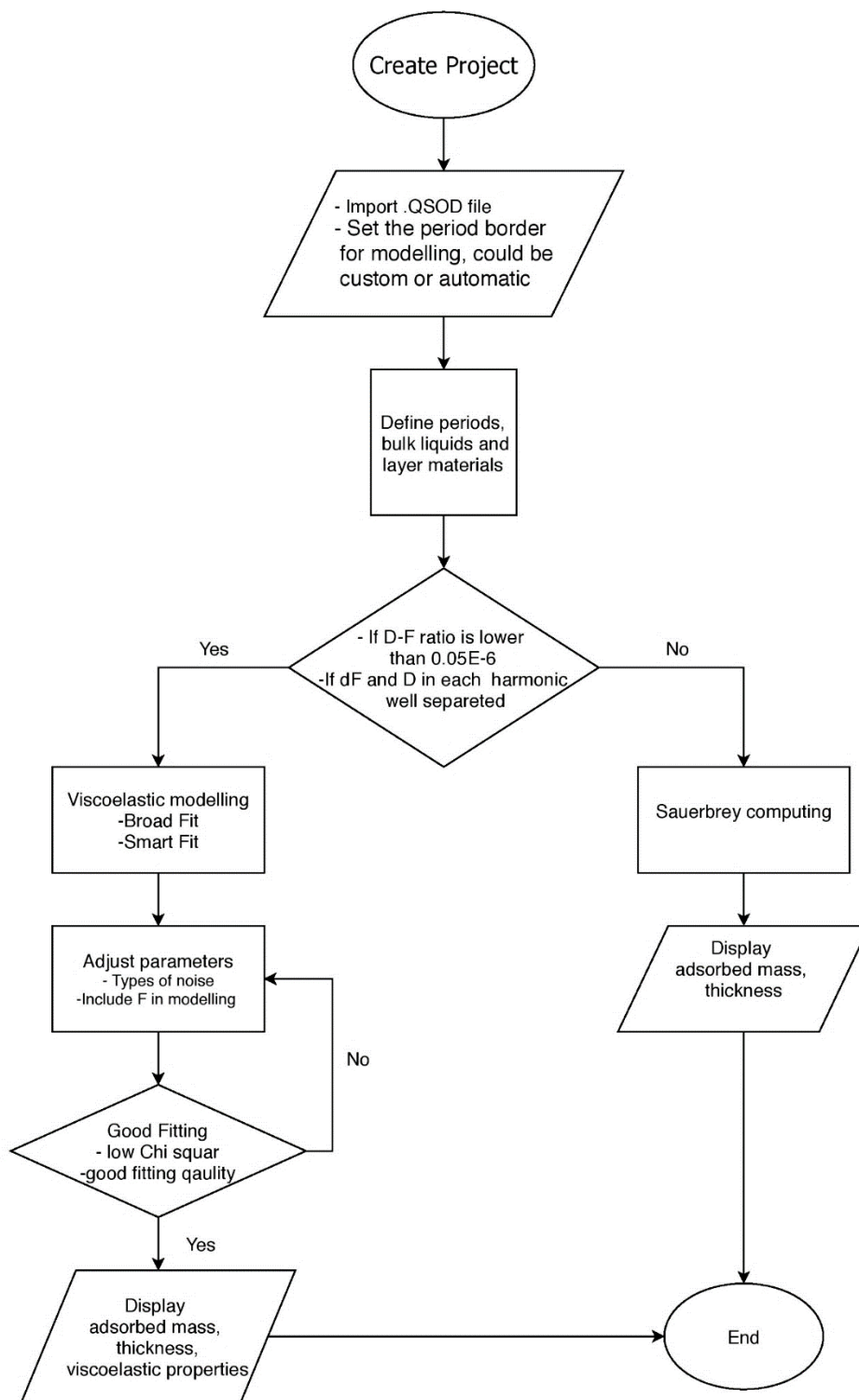
$$\chi^2 = \sum_i \left[ \frac{Y_{theory,i} - Y_{exp,i}}{\sigma_i} \right]^2$$

where  $\sigma_i$  is the measurement error, or standard deviation of the  $i$ -th data point,  $Y_{theory,i}$  and  $Y_{exp,i}$  are the calculated and experimental  $Y$ -values, respectively.  $1/\sigma_i$  is the weight of each measured point. Chi-square should be as low as possible. Fit quality is the sum of chi-square over the span of the data. It is shown for every modelling result of the dataset. Fit quality is displayed with a coloured circle above the modelling **Fig. S1.2** colour scale gradually ranging from red, to yellow then green, indicates the quality of the fit, where green represents a good data fit.

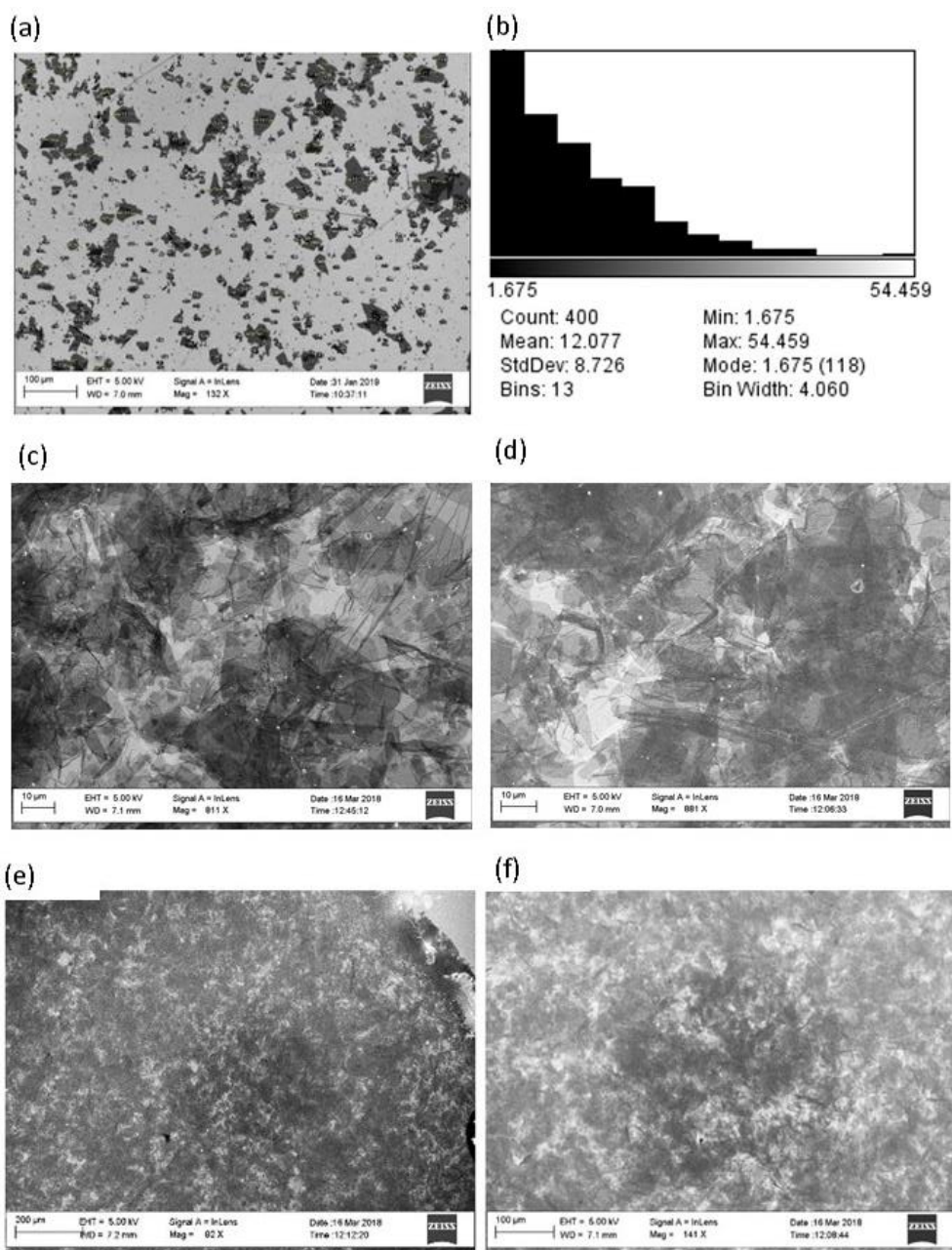
### 1.3 Scanning electron microscopy (SEM) results

The SEM imaging of graphene oxide flakes and crystal coatings was performed on a SEM Zeiss Ultra setup, using an accelerating voltage of 5 kV. First, on **Fig. S1.3(a,b)** the size distribution analysis of GO flakes on a  $\text{SiO}_2$  wafer substrate is shown. This flake size distribution was computed with the aid of ImageJ software. A predominant lateral flake size of 1.6 nm can be observed while an average flake size is  $\sim 12$  nm. The before and after reduction of GO-coated on QCM chip shows the same surface morphology, see **Fig. S1.3(c,d)**. Both GO and rGO surfaces show full coverage of the gold substrate. **Fig. S1.3c** and **d** show SEM images of spin-coated GO on Au QCM chips with a magnification of 92x and 141x, respectively. Graphene-coated sensor surfaces with uniform coverage and the presence of flake overlaps can be observed.





**Fig. S1.2** Data modelling flowchart showing the conditions for determining mass, thickness and viscoelastic properties of adsorbed films on surfaces



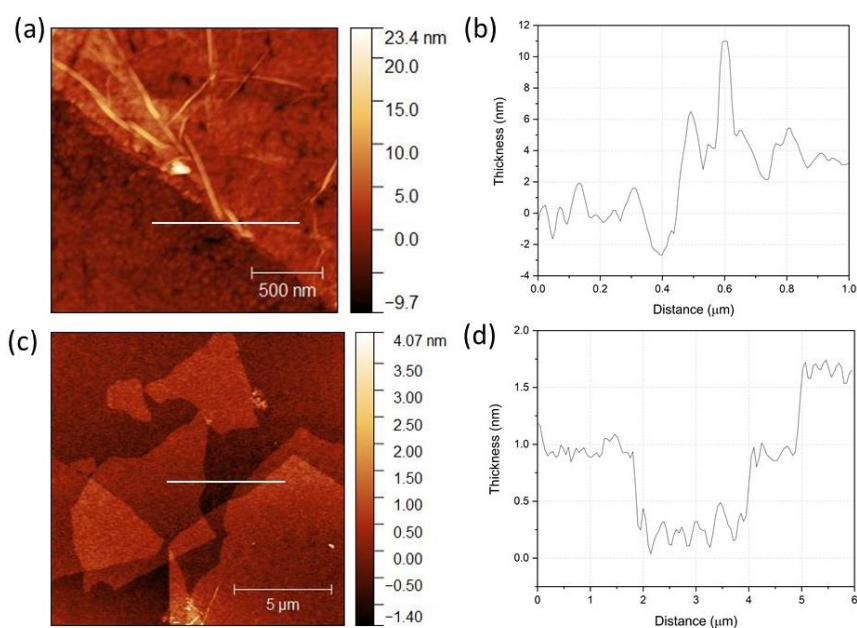
**Fig. S1.3** Scanning Electron Microscopy images, showing (a) flake size distribution of GO on SiO<sub>2</sub>, as described in (b), (c) GO, (d) rGO coated on QCM chip (e) and (f) show scans of GO on gold substrates with a magnification of 92x and 141x respectively. In all cases, the accelerating voltage was 5 kV. All measurements are in μm.

#### 1.4 AFM surface characterization

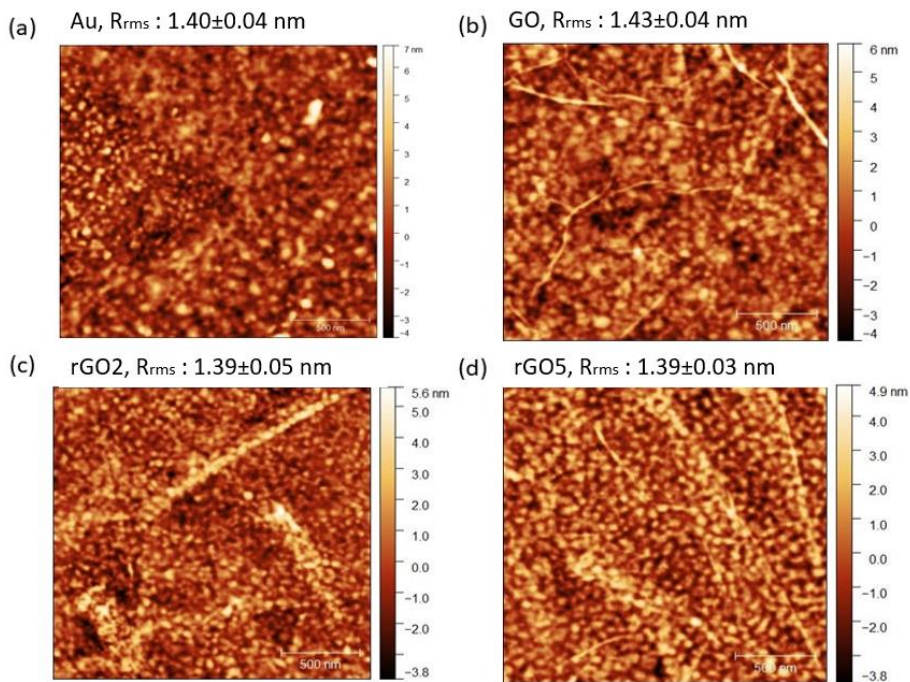
The topography of the GO coating was characterized using the AFM imaging technique, as shown in Fig. S1.4.1. The images were processed using Gwyddion 2.53 software. After spin-coating and drying, the sample reveals the presence of flakes due to their characteristic creases, folds and crumbles resulting in a deposition ranging from single

to few-layer overlaps, as observed from the height profile on **Fig. S1.4.1(b)** corresponding to the highlighted white line from **Fig. S1.4.1(a)**. The thickness of the coating layer is approximately  $4 \pm 2$  nm pointing at a stacking of 2 to 6 layers, respective to the typical thickness of a single GO sheet of  $\sim 1$  nm.

By following the same coating procedure described in the main paper, the topography of bare, GO, rGO2 and rGO5 coatings on Au QCM chips are presented in **Fig. S1.4.2**. Surface roughness for each sample was measured to assess its impact on protein adsorption. As it can be seen on **Fig. S1.4.2**, the  $R_{rms}$  values for all samples are lie within the same range of 1.4 nm, therefore, in this case, surface roughness should not have a major effect on the protein adsorption. However, the  $R_{rms}$  value of the GO surface is slightly higher than the rGO ones. This can be attributed to the water molecules trapped between the substrate and GO in addition to the wrinkles, folds and overlaps of GO flakes due to the hydrophilic nature of GO. In the case of rGO2 and rGO5 coating on Au, the roughness seems very similar to the bare Au one. This could be due to the flattening of the GO flakes upon the thermal reduction process accompanied by dehydration.



**Fig. S1.4.1** Atomic Force Microscopy images of **a)** GO spin coating on Au, **b)** its corresponding height profile **c)** GO flakes on SiO<sub>2</sub> and **d)** its corresponding height profile



**Fig. S1.4.2** AFM mappings and Root-mean-square roughness ( $R_{rms}$ ) in nm scale are shown for (a) bare Au (b) GO-Au, (c) rGO2-Au, (d) rGO5-Au. Scan area in all images is  $2 \mu\text{m}^2$ .

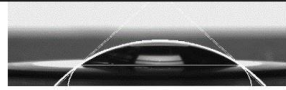
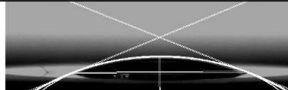
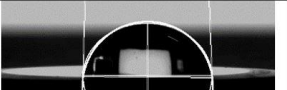
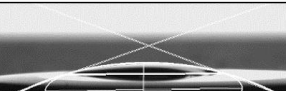
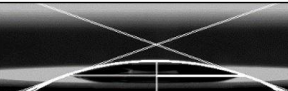
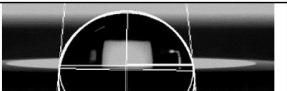
### 1.5 Contact angle analysis

For the wetting properties study, a Kruss DSA100 (Hamburg) system was used to measure the wetting contact angles (WCA) for all substrates. Sessile drops ( $\sim 5 \mu\text{L}$ ) of DI water were cast on top of the substrates. The computation of the WCAs from the captured images was carried out using a plugin for ImageJ developed by Marco Brugnara [335].

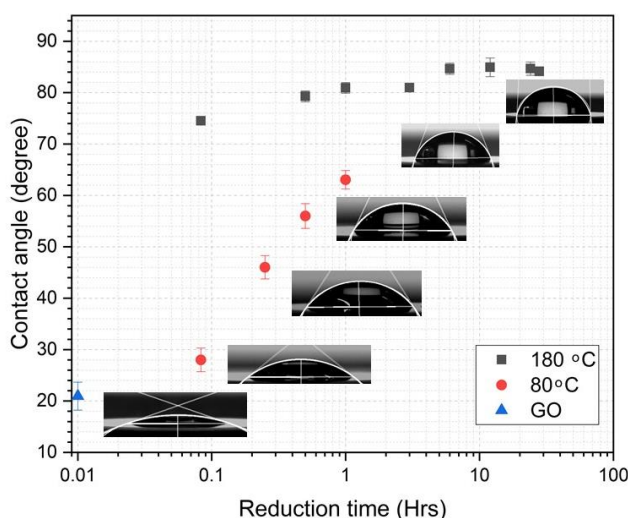
Table 1 presents the wetting contact angles (WCAs) of Au and  $\text{SiO}_2$  QCM-D chips and GO and rGO coating on both substrates. Both Au and  $\text{SiO}_2$  are hydrophilic with a WCA of  $41.3 \pm 5.1^\circ$  and  $17.3 \pm 2.2^\circ$ , respectively, however, after coating with graphene, the WCA of GO and rGO on both substrates are similar.

The relation between contact angle and thermal reduction time at two different temperatures is presented in **Fig. S1.5**.

**Table S1.1** Wetting contact angle (WCA) of DI water droplet of GO and rGO5 coating on Au and SiO<sub>2</sub> substrates

Substrate	Bare	GO	rGO5
Au	 WCA=41±5 °	 WCA=21±3 °	 WCA=85±2 °
SiO <sub>2</sub>	 WCA=17±2°	 WCA=20±4 °	 WCA=83±5 °

The red circles correspond to the reductions performed at 80 °C while the dark squares indicate the contact angles obtained at 180 °C. The maximum reduction period was 28 hours while the blue triangle corresponds to no reduction time namely, the contact angle of a GO-coated QCM surface. The contact angle of GO is about 21° which indicates its hydrophilic characteristic. The thermal reduction process occurred very fast even at a relatively low temperature possibly because the surface is a thin film containing a few layers of GO. By using a reduction temperature of 180°C, the contact angle rapidly increased to approximately 75°. From a 1-hour reduction until 28 hours of thermal treatment, the value of the WCA does not present a significant change. The highest achieved WCA is about 85°. It can be assumed that oxygen functional groups were mostly removed from the first hour of the reduction at 180°C.

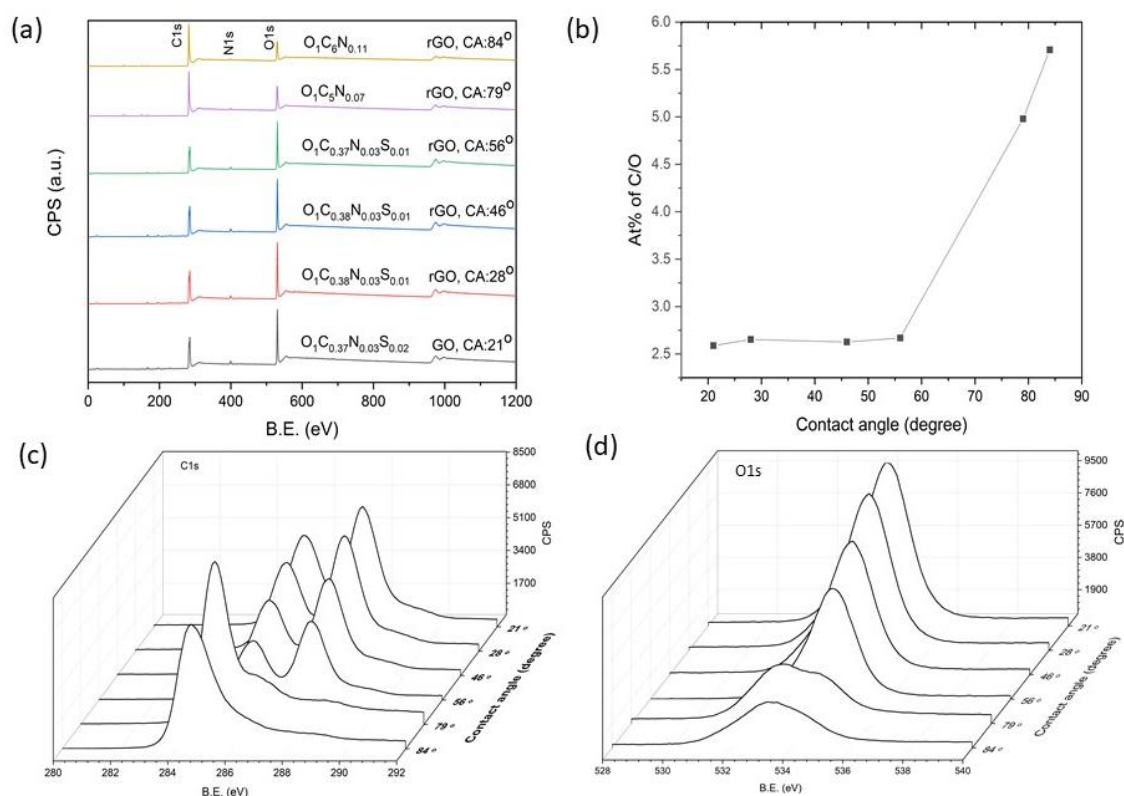


**Fig. S1.5** Wetting contact angles for GO and reduced GO with different reduction conditions including reduction temperature and time.

## 1.6 XPS analysis

The samples for X-ray photoelectron spectroscopy (XPS) analysis were prepared by drop-casting the dispersion of GO on a clean Si/SiO<sub>2</sub> substrate and drying at room temperature in a vacuum oven to achieve a film with a thickness of not less than 10 nm. The GO samples were thermally reduced at controllable conditions to achieve different levels of hydrophobicity, characterized by their WCA.

The XPS data were collected on a SPECS custom-built system composed of a Phobios 150 hemispherical electron analyser with a 1D detector. The X-ray source is a microfocus monochromated Al K-alpha (1486.6 eV) source. All spectra were collected with a pass energy of 20 eV. Combined ultimate resolution as measured from Ag 3D is 0.5 eV with the X-ray source and 20 eV pass. The XPS data processing was done using CasaXPS software (version 2.3.16 PR 1.6). The calibration of the C1 spectrum was performed using the sp<sup>3</sup> carbon (C-C, C-H) as a reference at 284.8 eV peak position and the background type used was spline Tougaard. The C1s spectrum fitting was performed using 7 synthetic components ascribed to different chemical species and a satellite peak respectively. The sp<sup>2</sup> C component is represented by an asymmetric line shape of A(a,b,n)GL(p) type (CasaXPS version 2.3.16 Manual) where A(0.3,0.8,40)GL(45); the other synthetic components are represented by a symmetric line shape of GL(p) type where GL(30) (Gaussian/Lorentzian mix with 30% Lorentzian). The constraints applied where the FWHM constraint (0.9-1.1) and the position constraints (between max ±1 eV to min ±0.1 eV). XPS C 1s region was fitted with the synthetic components in the manner which minimizes the total square error fit (0.91) and corresponds to the literature reports.

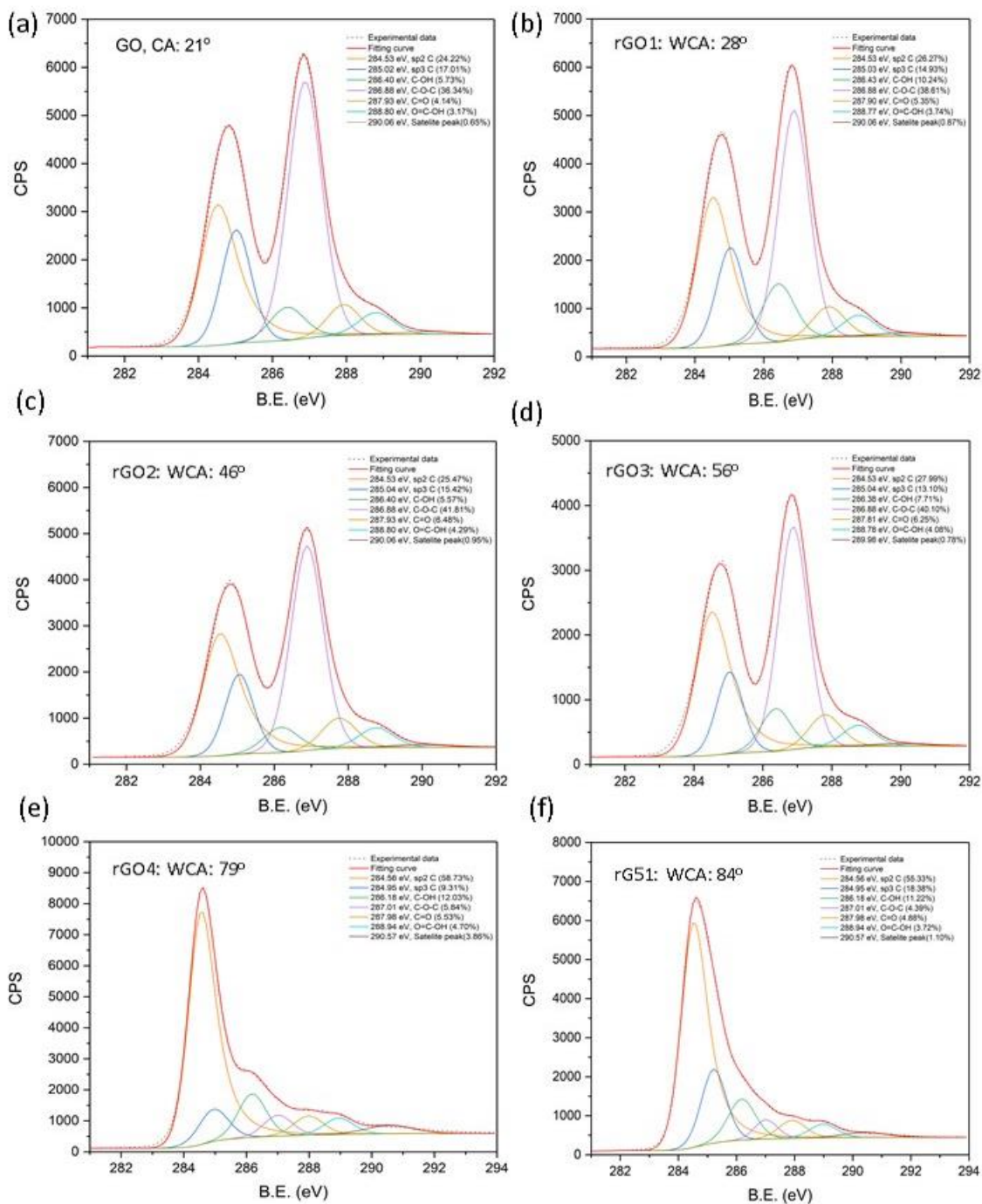


**Fig. S1.6.1 (a)** Wide scan XPS spectra **(b)** Atomic percent of C/O obtained from the wide scans and plot against the contact angle **(c)** detail spectra of C1s and **(d)** O1s for GO and reduced GO with different reduction conditions characterized by the contact angle. Oxygen content reduces with respect to the increase of contact angle.

Here we present the full set of XPS data obtained for the group of sensors used on this report. **Fig. S1.6.1(a)** shows the spectra for the thermally reduced samples in descending order, where the top graph is the highest level of reduction of GO performed with a contact angle of 84° and the bottom graph is bare GO coating. **Fig. S1.6.1(b)** shows the atomic percent of C/O obtained from the wide scans and is plotted against the WCA of the coated substrates to present an extensive evaluation of the oxygen reduction level. Oxygen functional groups reduce as a hydrophobic level of rGO increases as observed from the detailed scan profiles of O1s in **Fig. 6.1(d)**.

**Fig. S1.6.2** presents the individual curve fittings of C1s spectrum with both Gaussian and Lorentzian components, as discussed before. The C1s spectrum of GO shows the presence of different functional groups decorating the basal plane and the edges of the flakes, ranging from hydroxyl (C-OH) and epoxy (C-O-C) groups between ~286 and 287 eV, carbonyl (C=O) and carboxyl (O=C=O) groups between ~287 and 289 eV. Carbons sp<sup>2</sup> and sp<sup>3</sup> located around ~284 eV and ~285 eV, respectively, are observed. The peak for

epoxy group is also predominant in rGO1 to rGO3. With the higher level of reduction (Fig. S1.6.2 (e, f)), the rGO4 and rGO5 present fewer oxygen groups, i.e. single and double carbon–oxygen groups with a binding energy of ~286 and 287 eV respectively, and an increased intensity carbon peak. It is demonstrated that the reduction of GO to rGO provides a significant restoration of  $sp^2$  carbons.

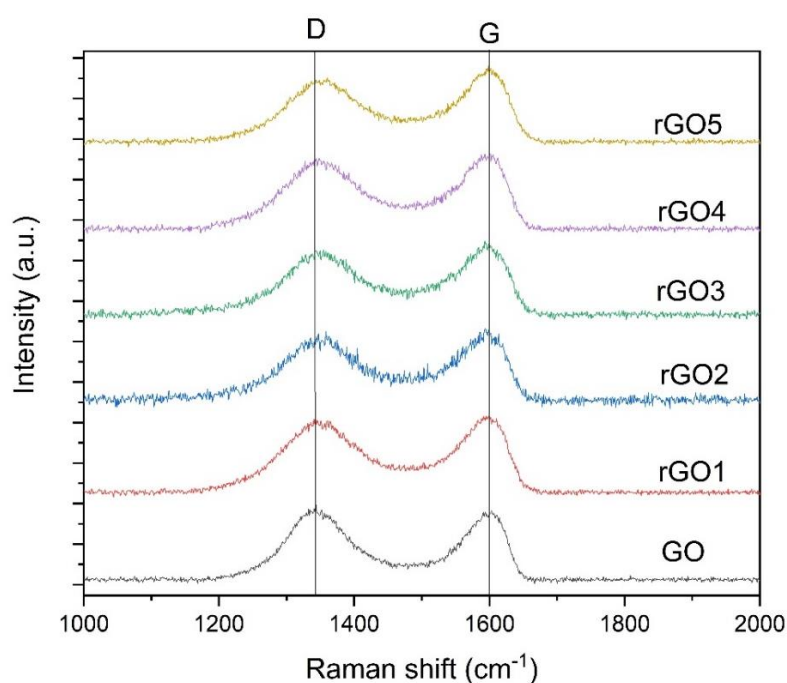


**Fig. S1.6.2** Deconvoluted details of  $C_{1s}$  spectra for GO and rGO with various reduction levels. The reduction of GO to rGO via controlled thermal reduction can significantly restore  $sp^2$  carbons



## 1.7 Raman spectroscopy

Raman spectra were taken on a Renishaw Raman system equipped with a Leica microscope and a CCD detector. Raman spectrum was recorded using 532 nm laser line (Cobolt Samba) continuous wave diode-pumped solid-state laser, 20 mW. The laser power was kept below 10  $\mu\text{W}$  to avoid thermal degradation of the samples. The relative intensity ratio ( $I_D/I_G$ ) was measured from the averaged acquired spectra, 10 spectra per sample. Two main peaks, including the graphitic (G) and defect (D), occur at  $\sim 1580\text{ cm}^{-1}$  and  $\sim 1350\text{ cm}^{-1}$ , respectively. All samples show no difference in D and G peak positions. The  $I_D/I_G$  value of GO is 1.01 which is slightly higher than that of rGO samples that are in between 0.97 to 0.98.

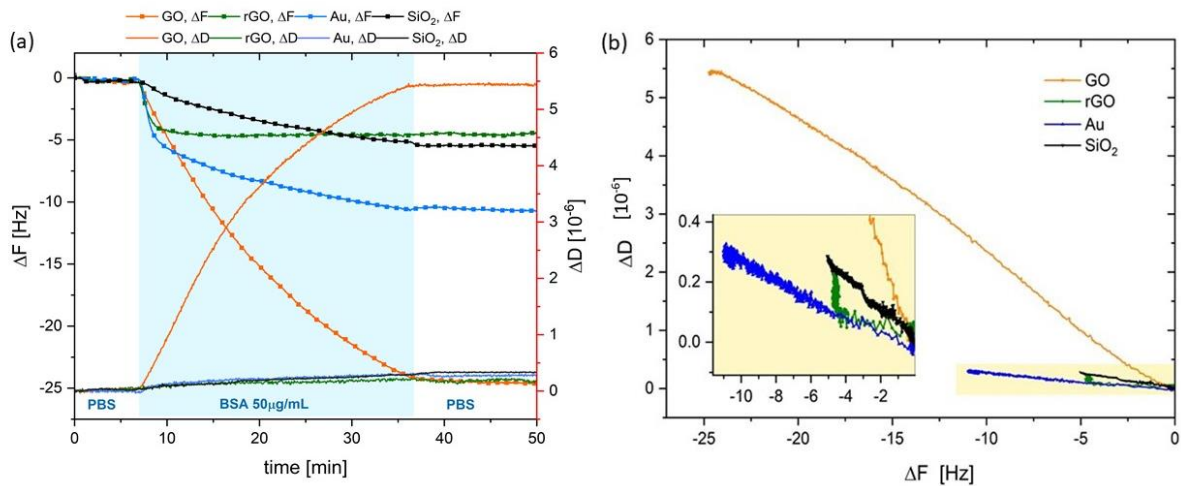


*Fig. S1.7 Raman spectra of GO and rGO with different level of reduction*

## 1.8 QCM-D analysis – the effect of different surfaces – Au, GO, rGO

The QCM-D response for the adsorption of BSA (50  $\mu\text{g}/\text{mL}$ ) onto different substrates: bare Au,  $\text{SiO}_2$ , GO and rGO are presented on **Fig. S1.8a**. On Au, a two-step continuous adsorption can be observed, an initial fast adsorption rate is followed by a sudden decrease on such rate during the continuous injection of BSA. On the  $\text{SiO}_2$  substrate, a slower monotonic adsorption rate is observed. The highest adsorption was obtained on the GO-coated sensor with a single-step response, similar to the one observed on  $\text{SiO}_2$ . We pose that this monotonic adsorption is due to a predominant hydrophilic interaction

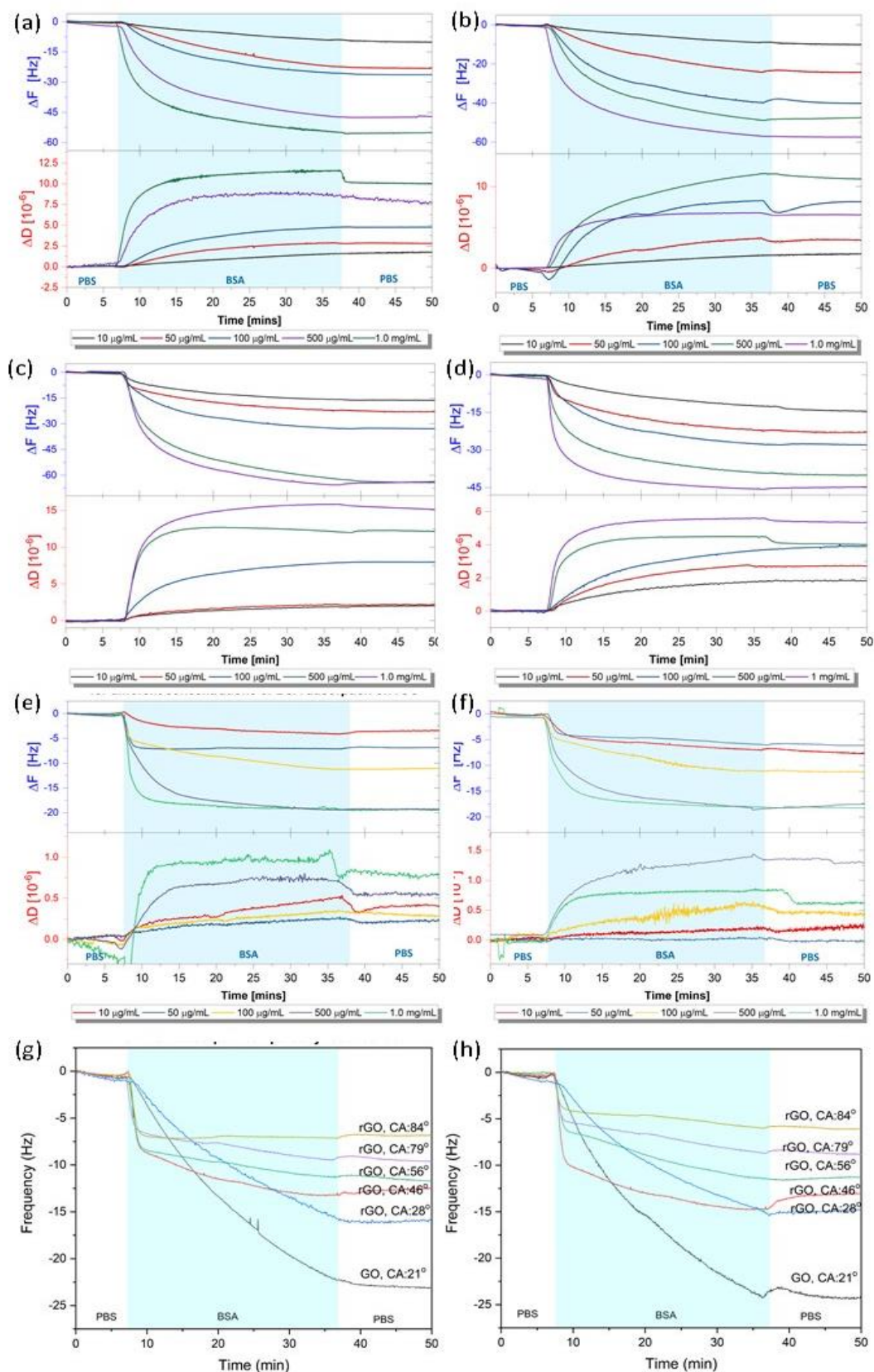
as both GO and SiO<sub>2</sub> substrates present such property. On rGO, BSA molecules rapidly organize saturating the sensor's area reaching stability where no further adsorption of material is observed. The dissipation density plot (**Fig. S1.8b**) expresses the conformational changes through the relation  $\Delta D$  vs  $\Delta F$ . The lower the slope, the more rigid the membrane formed is. On bare Au, the formation of a rigid membrane occurs with a linear trend, indicating continuous adsorption of molecules. Similarly, BSA adsorption on SiO<sub>2</sub> presents a total dissipation value of  $0.3 \times 10^{-6}$ , however, the slope of the SiO<sub>2</sub>  $\Delta D - \Delta F$  plot is relatively higher than that of the Au and rGO substrates, indicating a less rigid film. The adsorption on GO presents a one-step process with a linear trend, while the graph corresponding to the adsorption on rGO shows a two-step process, as discussed in the main text. These results indicate that the protein adsorption on each surface shows different adsorption trends and properties, including rigidity and thicknesses.



**Fig. S1.8** QCM-D data on different surfaces **a)** BSA adsorption on Au and graphene derivatives **b)** Dissipation density graph ( $\Delta D$  vs  $\Delta F$ )

### 1.9 QCM-D duplicated results

The set of QCM-D measurements for BSA adsorption on graphene derivatives surfaces was repeated twice, as shown in **Fig. S1.9**. Two repeated results for the adsorption of different concentrations of BSA on GO, rGO2 and rGO5 are shown in **Fig. S1.9(a,b)**, **(c,d)** and **(e,f)** respectively. **Fig. S1.9(g,h)** presents repeated results for the effects of hydrophobicity. Overall, these results show similar trends and the reproducibility of the observed responses, supporting the reliability of the present study.

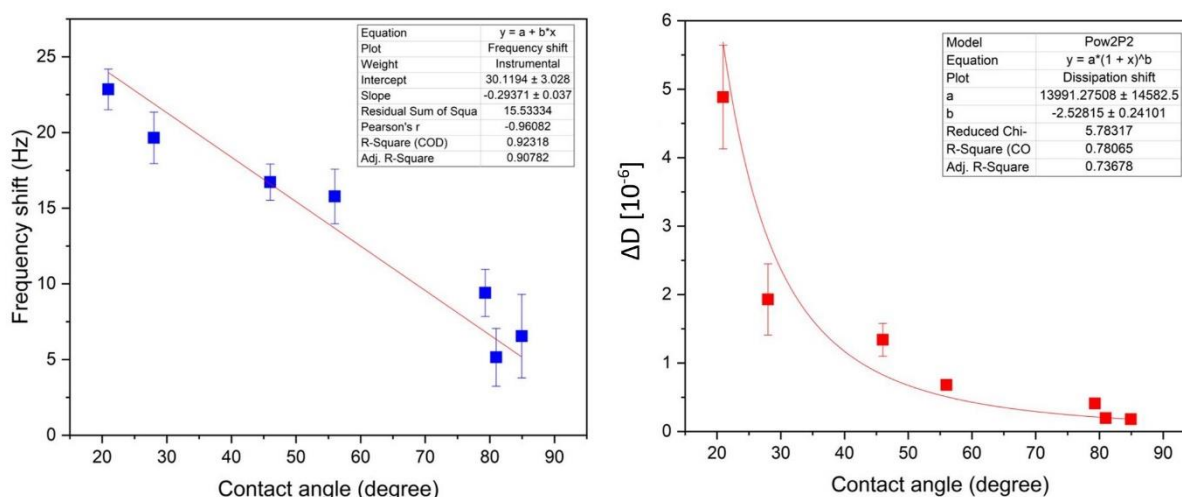


**Fig. S1.9** Repeated results for QCM-D study of BSA adsorption on (a,b) GO and (c,d) rGO (e,f) partially reduced GO. The repeated results show reproducible and similar trends to the main results.

### 1.10 $\Delta F$ and $\Delta D$ vs contact angle

The effects of substrate hydrophobicity were systematically studied through QCM-D measurements of BSA adsorbed onto rGO-coated sensor surfaces with distinctive hydrophobic degrees as a result of controlled thermal reduction conditions.

rGO-coated surfaces with higher WCA show less mass adsorption, as observed from the shift of frequency after the adsorption process (see **Fig. S1.10(a)**). The relation between the frequency shift and contact angle seems to be inversely linear. It is believed that the amount of BSA adsorbed onto the experimental surfaces inversely increases with respect to the hydrophobicity of graphene derivatives. However, the energy dissipation parameter exponentially decreases as the hydrophobic level increases (see **Fig. S1.10(b)**). This could be due to a change on the arrangement of BSA molecules on the surface, resulting in a more rigid film on rGO-coated substrates.



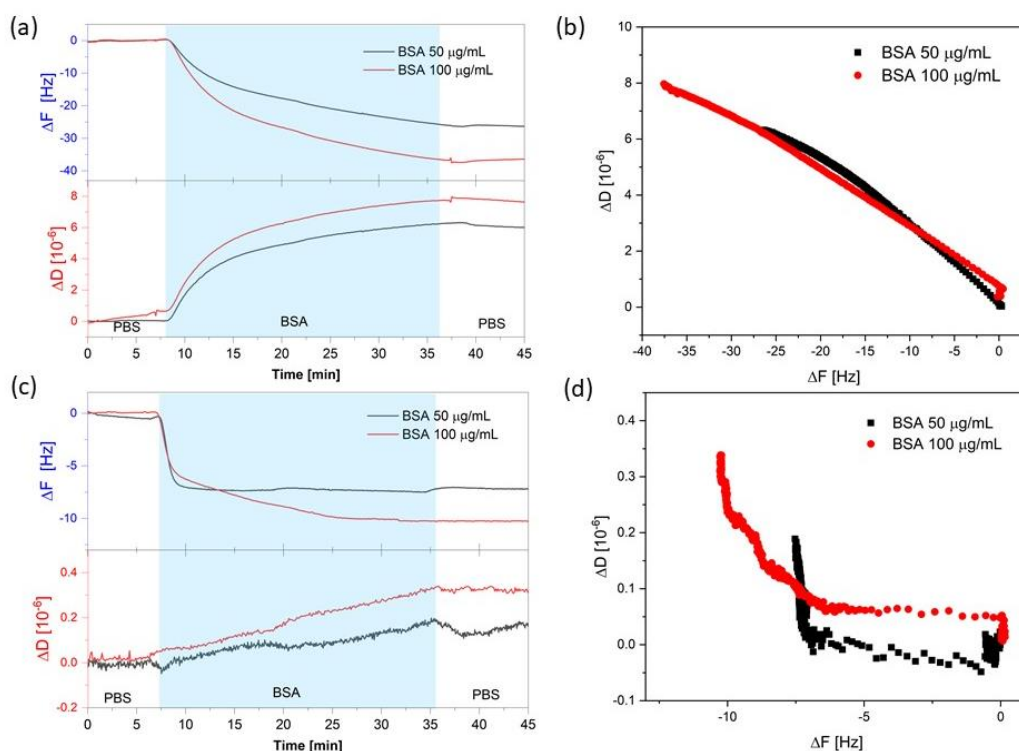
**Fig. S1.10 (a)** frequency and **(b)** dissipation shift due to BSA adsorption on GO and partially reduced GO with respect to the contact angle of rGO.

### 1.11 Protein adsorption on graphene derivatives coating on $\text{SiO}_2$ sensing chip

In the main paper, we discussed the adsorption of BSA protein on graphene derivatives on gold QCM-D sensors. To confirm that the adsorption processes originate exclusively from the effect of the graphene coating and not from the underlying substrate, like bare gold, we have investigated the adsorption of protein on GO and rGO5 coating onto a  $\text{SiO}_2$  sensing chip. Our analysis of the WCA (ESI 5) shows that both the Au and  $\text{SiO}_2$  chips are hydrophilic with WCA of  $16^\circ \pm 3^\circ$  and  $43^\circ \pm 2^\circ$ , respectively; however, the  $\text{SiO}_2$

substrate is considerably more hydrophilic. The result of the graphene coating layer presented a thickness of approximately 5 nm, ESI 1.4. The comparison of QCM-D results for the adsorption of BSA on bare gold and SiO<sub>2</sub> substrates can be seen in ESI 8. The results for GO and rGO5 on SiO<sub>2</sub> display similar adsorption mass and kinetics to those on gold as observed from the shift frequency and dissipation as well as the  $\Delta D$ - $\Delta F$  plot, as shown in **Fig. S1.11**. Like gold substrate, SiO<sub>2</sub> substrate with GO coating shows the relatively constant rate of change of frequency, whereas the rGO5 present short, fast adsorption for 50  $\mu\text{g/mL}$  BSA and 2-stage adsorption, a short, fast step then a slower adsorption rate for 100  $\mu\text{g/mL}$  BSA. The latter results suggest that both substrates, gold and SiO<sub>2</sub>, do not influence the protein adsorption process on graphene layers.

The majority of this study has been conducted on Au chips rather than the SiO<sub>2</sub> ones because Au QCM chip is the most commonly used for study biological interaction due to its biocompatibility and ease of functionalisation and also more commercially available compared to SiO<sub>2</sub> one. As we have seen no different on adsorption results from graphene coating on Au and SiO<sub>2</sub>, therefore, Au sensing chip has been selected to be the substrate for the coating for all experiments.



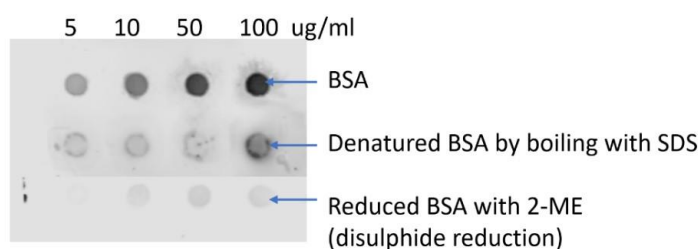
**Fig. S1.11.** The QCM-D real-time adsorption monitoring and  $\Delta D$ - $\Delta F$  plots of different concentration BSA on (a,b) GO coated on SiO<sub>2</sub>, (c,d) rGO5 coated on SiO<sub>2</sub>.

### 1.12 Dot blot for the antibody test

In this study, dot blot test for the binding function of anti-BSA toward BSA was carried on by blotting varied concentration of BSA and denatured BSA by adding 2-mercaptoethanol (2-ME) reducing agent and by boiling protein with SDS. The reducing agent can denature BSA by breaking disulphide bond while the process of boiling with SDS makes protein to lose its secondary and tertiary structure. If BSA is denatured, the antibody will not bind correctly with BSA resulting in no fluorescent signal.

The protocol started with spotting 50  $\mu$ L of BSA samples onto a nitrocellulose membrane and letting it dry in air. The membrane, then, was incubated in Odyssey blocking buffer to prevent non-specific binding for one hour. Then, it is incubated with a dilution of anti-BSA (primary antibody) in PBS with tween 0.05% (PBS-T), ratio 1:2000, for one hour followed by rinsing with PBS-T three times. After finishing rinsing, the membrane was incubated for one hour with detection molecules with a chemiluminescent, anti-rabbit, diluted with PBS-T, ratio 1:10000. Finally, the membrane was rinsed with MilliQ water and then was imaged with Fluorescent scanner with wavelength 700 nm (Odyssey<sup>®</sup> CLx Imaging System from LI-COR Biosciences).

**Fig. S1.12** shows that only non-denatured BSA can present the strong fluorescent signal of antibody adsorption. The strength of the signal increases with the concentration of the protein. The anti-BSA antibody is specific to the endogenous levels of total BSA protein.



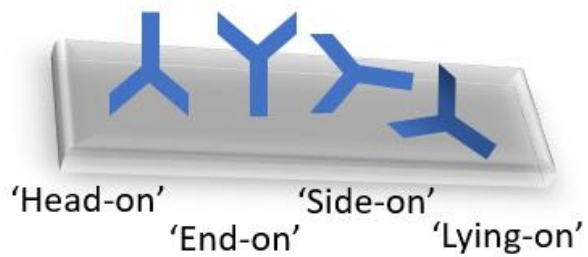
**Fig. S1.12** Dot blot results of different concentration BSA adsorbing anti-BSA antibody in comparison to the denature BSA. Only non-denatured BSA can present the signal of antibody adsorption.

### 1.13 IgG injection for investigating non-specific binding

IgG antibody (50  $\mu$ g/mL) was injected over BSA previously adsorbed onto graphene surfaces in order to investigate the specificity of the adsorption and denaturation of BSA.

IgG and anti-BSA possess the same molecular structure and molecular weight where anti-BSA specifically binds to BSA.

**Fig. S1.13.1** presents possible orientations of IgG antibody including “head-on” in which both Fab sites bind with antigen on a substrate, “side-on”, in which the antibody orients a Fab and Fc sites toward, “lying-on”- the antibody is flattened on the surface and lastly “end-on” in which the Fc stands on the substrate.



**Fig. S1.13.1** Possible orientation of IgG antibody

## Electronic Supporting Information 2.

This supporting information is for publication 2.

### **A point-of-care immunosensor based on quartz crystal microbalance with graphene biointerface for antibody assay**

Piramon Hampitak<sup>1</sup>, Thomas A Jowitt<sup>2</sup>, Daniel Melendrez<sup>1</sup>, Maryline Fresquet<sup>2</sup>, Patrick Hamilton<sup>3,4</sup>, Maria Iliut<sup>1</sup>, Kaiwen Nie<sup>1</sup>, Ben Spencer<sup>1</sup>, Rachel Lennon<sup>3,5</sup>, and Aravind Vijayaraghavan<sup>1,\*</sup>

<sup>1</sup> *Department of Materials and National Graphene Institute, Faculty of Science and Engineering, The University of Manchester, Oxford Road, Manchester, UK.*

<sup>2</sup> *School of Biological Sciences, Faculty of Biology Medicine and Health, The University of Manchester, Oxford Road, Manchester, UK.*

<sup>3</sup> *Wellcome Centre for Cell-Matrix Research, Division of Cell-Matrix Biology and Regenerative Medicine, School of Biological Sciences, Faculty of Biology Medicine and Health, The University of Manchester, Manchester Academic Health Science Centre, Manchester, UK.*

<sup>4</sup> *Manchester Academic Health Science Centre (MAHSC), The University of Manchester, Manchester, UK*

<sup>5</sup> *Department of Paediatric Nephrology, Royal Manchester Children's Hospital, Manchester University Hospitals NHS Foundation Trust, Manchester Academic Health Science Centre, Manchester, UK.*

\*Corresponding author: [aravind@manchester.ac.uk](mailto:aravind@manchester.ac.uk)

Here, we provide supporting information including the production of the receptor NC3, the protocol for QCM measurement using the QSense and our customised OpenQCM systems as well as supplementary results and analysis.

#### **2.1. Production of NC3**

PLA2R NC3 was produced by the modification of human extracellular PLA2R (NC8) previously described by Kanigicherla *et al.*[262]. To clone PLA2R NC3, the following primers were first used to amplify an N-terminal portion of the NC8 by PCR using the following oligonucleotides:





## 2.2. The customized OpenQCM instrument development

The customised OpenQCM (C-QCM) instrument was developed based on an open-source QCM (OpenQCM, Novaetech Srl). To set up the QCM system, the temp-control chamber will be powered on and the QCM device will be connected to the laptop via USB (**Fig. S2.2(a)**). A custom-made graphic user interface (GUI) was developed in Matlab R2018a (**Fig. S2.2(b)**). It is used to perform QCM data acquisition, temperature, baseline calibration, the change of frequency and data post-processing.

## 2.3. QCM-D principle and procedure

### 2.3.1 Principle of QCM-D

In 1959, Günter Sauerbrey [252] demonstrated that upon adding mass to a QCM sensor surface a frequency decrease proportional to the added mass occurs and given that the mass is small compared to the total weight of the crystal the frequency change is directly proportional to the mass of the crystal [252], therefore their use as microbalances is based on the linear relationship between changes in the resonator mass and in the resonance frequency [252]. Under vacuum, the rigid attachment of a film of mass  $\Delta m$  to the crystal surface causes a decrease  $\Delta f$  in the resonant frequency  $f_0$ . Sauerbrey was the first who derived that the relationship between  $\Delta f$  and  $\Delta m$  is linear in the limit of small  $\Delta m$  and is expressed by a simple relationship:

$$\frac{\Delta f}{f_0} = -\frac{\Delta m}{m_Q} \quad (\text{Eq. S1})$$

where  $m_Q$  is the mass of the unloaded resonator

From **Eq. S1** one can introduce the mass sensitivity factor  $C_r$ , and depends only on the fundamental resonant frequency  $f_0$  and the material properties of the crystal used [336].

Hence:

$$C_r = \frac{m_Q}{f_0} \quad (\text{Eq. S2})$$

where the mass of the resonator can be expressed as the product of the average density of quartz crystal,  $\rho_Q$  and its thickness  $h_Q$ . Thus,  $C_r$  can be expressed in terms of an appropriate dimensional analysis:

$$C_r = \frac{m_Q}{f_0} = \frac{\rho_Q h_Q}{f_0} = \frac{\left[ \frac{ng}{cm^3} \cdot cm \right]}{[Hz]} = [ngcm^{-2}Hz^{-1}] \quad (\text{Eq. S3})$$

For 10 MHz quartz crystals,  $C_r$  equals  $4.5 ngcm^{-2}Hz^{-1}$  if only one side is covered [303]. For crystals with  $f_0 = 5$  MHz, the density is  $\rho_Q = 2.648 g/cm^3$  and the average thickness is  $h_Q \approx 300 \mu m$ , thus  $C_r \approx 18 ngcm^{-2}Hz^{-1}$ .

Assuming rigid adsorption to the substrate enables the use of Sauerbrey modelling to approximate the mass adsorbed on Au electrodes. To obtain the aerial mass density, the values captured for  $\Delta f$  can be plugged in the Sauerbrey equation (Eq. S1). Rearranging terms, we obtain.

$$\frac{\Delta m}{A} = -\frac{\sqrt{\rho_Q \mu_Q}}{2f_0^2} \Delta f \quad [g/cm^2] \quad (\text{Eq. S4})$$

where A is the area of the working electrode ( $0.2043 cm^2$ ),  $\mu_Q$  is the shear modulus of AT-cut quartz crystals ( $2.947 \times 10^{11} gcm^{-1}s^{-2}$ ) and  $f_0 = 10 MHz$  for the crystals used in all C-QCM instrument experiments.

Therefore, the amount of adsorbed mass can be determined by using Equation S1, and combined with viscoelastic modelling [169] one can obtain a physical description of the adlayers. Higher mass adsorption will respond in large frequency down-shifts. Results obtained from Sauerbrey computation will be more accurate if the adsorbed film is rigid, otherwise, dissipation parameter could play a key role for the viscous adsorbed film.

The QCM-D monitoring technique provides a real-time measurement of changes in both frequency ( $\Delta f$ ) and dissipation ( $\Delta D$ ) as molecular adsorption on surfaces. The dissipation value is the sum of total energy losses in the system in an oscillation cycle defined as the lost energy divided by the total energy stored in the system,  $E_{loss}/E_{total}$  [303], [320]. High dissipation values will result from viscoelastic adsorption of molecules generating a soft film on the surface. On the other hand, a rigid film usually gives low dissipation values.

The slope of the plot of  $\Delta D$  vs  $\Delta f$  could reveal regions of different adsorption behaviour in terms of the viscoelastic structure of the adsorbed material.

### 2.3.2 Initial preparation of quartz crystals

QCM chips with gold surface electrode for both QSense (QSX-301, Biolin Scientific) and our C-QCM system (QCM10140CrAu051-051-C1, Quartz Pro) were used in this study. We used the same protocol for cleaning and surface coating.

To prepare the sensors for studying the adsorption of biomolecules on graphene derivatives surfaces, the QCM chips were cleaned following a modification of the protocol that in Ref 6, then coated with GO using a spin coater to get the GO chips. To get rGO chips, the GO pre-coated chips were thermally reduced to rGO at 180 °C for 6 hours.

### 2.3.3 QCM-D monitoring procedure for binding studies

The QCM-D measurements were carried out using the QSense Omega Auto system (Biolin Scientific). The system consists of eight sensing ports that can be controlled to be fed through customized scripts. Before every experimental session, the ports, tubing and sensors holders were cleaned using clean maintenance chips following the protocol described below. The temperature of the system was set at room temperature (25 °C). Once the system was cleaned and primed, the sensors for experimentation were loaded on the sensors holder.

At the beginning of each measurement, the sensors were primed by continuously flowing PBS until a stable baseline was obtained. Once a stable baseline was observed, the corresponding measurement script was started. In the present report, the steps for monitoring the functionalisation of the assay and the binding of Ab12 were presented in **Fig. S2.3** in the main paper. The injection sequence for each sample shows as follows:

Sample (1) Au: PBS → NC3 → PBS → antibody sample → PBS

Sample (2) GO: PBS → NC3 → PBS → antibody sample → PBS

Sample (3) rGO: PBS → NC3 → PBS → antibody sample → PBS

Sample (4) Au-BSA: PBS → BSA 50 µg/mL → PBS → NC3 → PBS → antibody sample → PBS

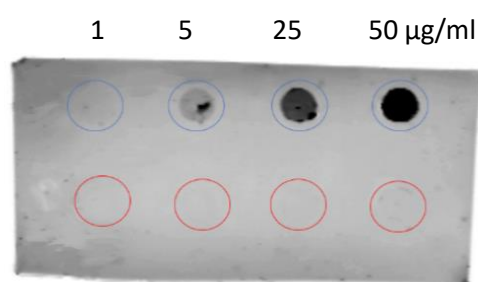
Sample (5) rGO-BSA: PBS → BSA 50 µg/mL → PBS → NC3 → PBS → antibody sample → PBS

Sample (6) rGO-BSA: PBS → BSA 500 µg/mL → PBS → NC3 → PBS → antibody sample → PBS

Sample (7) Au-SAM: PBS → BSA 50 µg/mL → PBS → NC3 → PBS → antibody sample → PBS

Sample (8) rGO-BSA+NHS: PBS → BSA 50 µg/mL → PBS → EDC/NHS → PBS → NC3 → PBS → blocking buffer → antibody sample → PBS

Once the measuring script is completed, to avoid contamination it is recommended to run a washing routine to clean the sensors, syringes and tubing using sodium dodecyl sulphate (SDS) surfactant solution to be then finally rinsed with MilliQ water and left to dry overnight. This process ensures that the system is left clean and dry for subsequent experiments.



**Fig. S2.3** Dot blot results of different concentration of NC3 binding with murine anti-PLA2R antibody (Ab12) in comparison to the denature NC3. Only non-denatured NC3 can present the response of antibody binding.

#### 2.4. Dot blot

The murine anti-PLA2R antibody (Ab12) was tested for binding affinity with NC3 using dot blotting, the measurement shown in **Fig. S2.3**. Varied concentrations of NC3 (blue circle) and denatured NC3 (red circle) were blotted against the Ab12 antibody. The NC3 can be denatured by boiling it with SDS making the protein lose its secondary and tertiary structure. If the NC3 is denatured, the antibody will not bind to the NC3 resulting in no fluorescent signal. **Fig. S2.3** shows that only non-denatured BSA can present the strong fluorescent signal of antibody adsorption. The strength of the signal increases with the concentration of the protein. Thus, we confirm that the Ab12 antibody can specifically bind with the NC3.

## 2.5. Preparation of sensing surfaces for binding study

The sensing surfaces used in this study include Au, graphene oxide (GO) and reduced GO (rGO). Both physical adsorption and covalent crosslinking methods were used for functionalising the protein receptor, NC3. Therefore, eight different functional surfaces were tested as shown in the main paper. Samples 1 to 6 use the physical adsorption method for the receptor immobilisation while covalent crosslink functionalisation was used in samples 7 and 8.

GO surface coating was prepared using spin coating (speed: 3000 rpm, acceleration: 350 s<sup>-1</sup>, 2 mins) to form a GO film on the entire surface of the gold surface QCM-D chip. A rGO-coated chip was performed in a vacuum oven (Townson+Mercer EV018) with temperature of 180 °C for 6 hours to reduce the GO. The full protocols were described in our previous study [200].

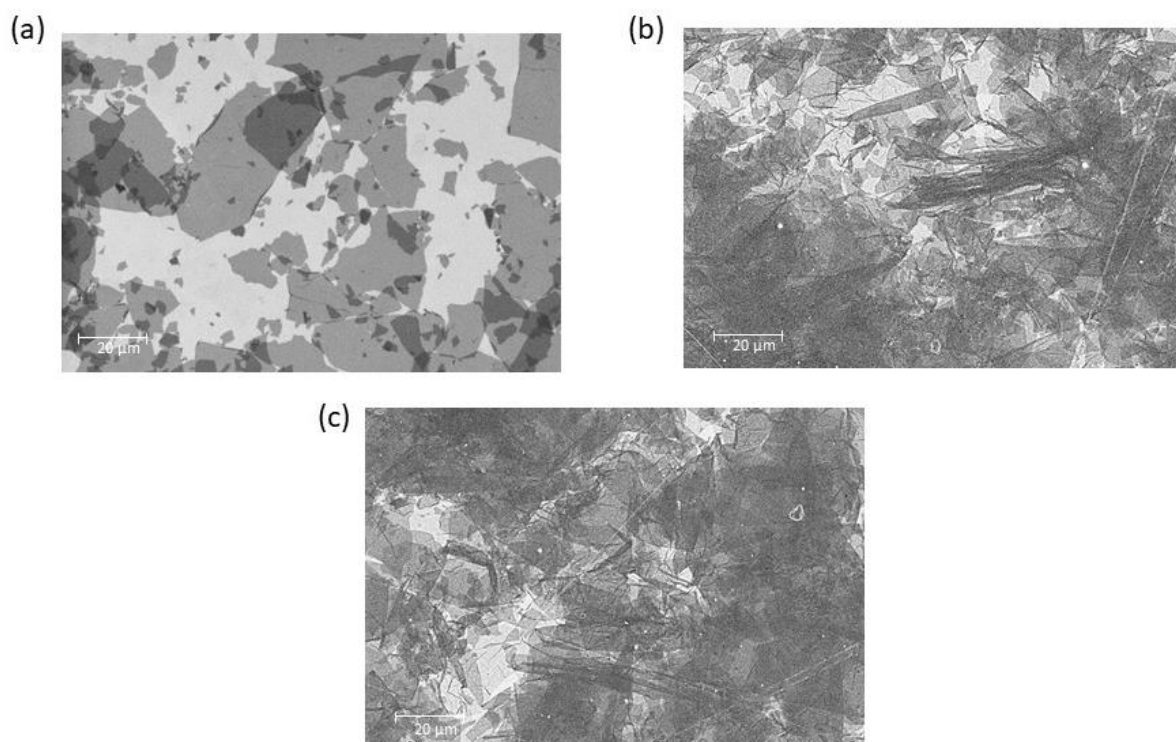
Au-SAM was prepared using general protocol from Sigma Aldrich following these steps 1) add 1 ml ethanol to a tube, and pipette to prepare 1 mmol/l Carboxylic acid-SAM solution, then, dilute the solution 10-fold with ethanol for Step 2) then immerse a gold substrate in the reagent solution prepared at step 1) at room temperature and leave it overnight and finally 3) wash the substrate several times with ethanol and purified water sequentially.

## 2.6. SEM imaging

The SEM imaging of GO flakes and rGO coatings was performed on a SEM Zeiss Ultra setup, using an acceleration voltage of 5 kV and 5 mm working distance. We previously reported the size distribution of GO and surface properties of GO before and after reduction [200].

**Fig. S2.4 (a)** presents SEM image of GO flakes indicating that the GO is 100% monolayer. More detailed characterisation of the GO material including atomic force microscopy confirmation of layer thickness can be found in the paper in Ref. 6. As QCM crystal from QSense and Quartz Pro were used, rGO coating on crystals from both companies are presented in **Fig. S2.4 (b)** and **(c)**, respectively. There was no significant difference in

the coating. Fully-coverage and uniform coating with the presence of flake overlaps display in both crystals.



**Fig. S2.4** Scanning Electron Microscopy images, showing **(a)** monolayer GO flake on SiO<sub>2</sub> **(b)** rGO coating on QCM-D chip from QSense and **(c)** rGO coating on QCM chip. In all cases, the accelerating voltage was 5 kV. All measurements are in  $\mu\text{m}$ .

## 2.7. XPS Results

The surface chemistry of three different samples including bare rGO, rGO-BSA and rGO-BSA+EDC/NHS were investigated using X-ray photoelectron spectroscopy (XPS) analysis to understand functionalisation mechanism of the EDC/NHS coupling on rGO-BSA. The rGO samples were prepared by drop-casting the dispersion of GO on a clean Si/SiO<sub>2</sub> substrate and drying at room temperature in a vacuum oven to achieve a film with a thickness of not less than 10 nm. The GO samples were thermally reduced at 180 °C for 6 hours to obtain rGO samples. The sample of rGO-BSA was prepared by drop-casting BSA 50  $\mu\text{g}/\text{mL}$  on rGO surface and leaving on for 10 minutes then rinsing with PBS and DI water and drying at room temperature in a vacuum oven. The rGO-BSA+EDC/NHS samples were obtained from drop-casting EDC/NHS solution on rGO-BSA, let it activated for 15 minutes and then rinsing and drying with the aforementioned conditions.

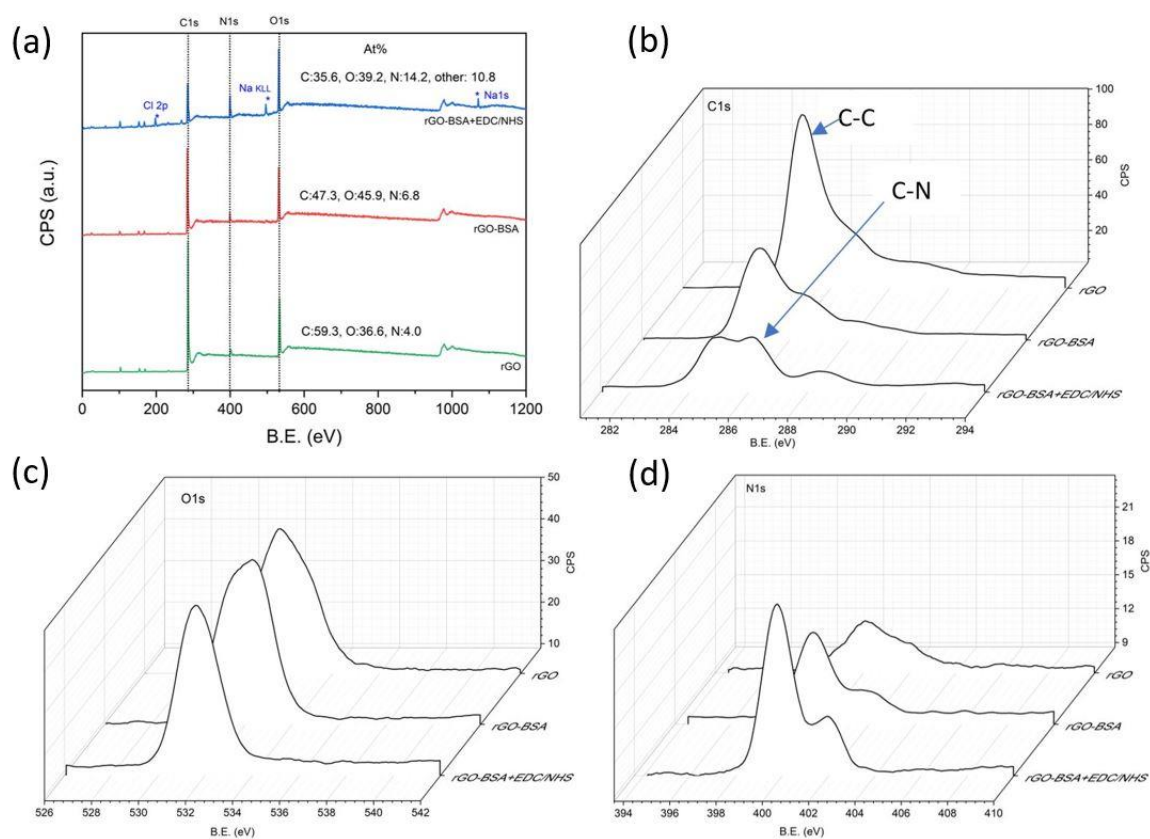
The XPS data were collected on a SPECS custom-built system composed of a Phobios 150 hemispherical electron analyser with a 1D detector. The X-ray source is a microfocus monochromated Al K-alpha (1486.6 eV) source. All spectra were collected with a pass energy of 20 eV. Combined ultimate resolution as measured from Ag 3D is 0.5 eV with the X-ray source and 20 eV pass. The XPS data processing was done using CasaXPS software (version 2.3.16 PR 1.6).

The calibration of the C1s spectrum was performed using the sp<sup>3</sup> carbon (C-C, C-H) as a reference at 284.8 eV peak position and the background type used was Shirley. The C1s spectrum fitting was performed using synthetic components ascribed to different chemical species including hydroxyl (C-OH) and epoxy (C-O-C) groups between ~286 and 287 eV, carbonyl (C=O) and carboxyl (O-C=O) groups between ~287, 289 eV and a satellite peak, respectively. The spectrum of N1s was assigned as graphitic nitrogen at a peak of 400.5 eV. The background type Shirley was subtracted. The synthetic components including C-N and N-Ester were used for spectrum fitting [263]. The O1s spectrum is in the region of 525–580eV. The background type used was spline Tougard. Three synthetic components including quinone, C=O and C-OH were assigned at 530.1 eV, 532.0 eV and 533.5 eV for spectrum fitting [205]. The constraints applied where the FWHM constraint (0.9-1.1) and the position constraints (between max ±1 eV to min ±0.1 eV). XPS region was fitted with the synthetic components in the manner which minimizes the total square error fit (0.91) and corresponds to the literature reports.

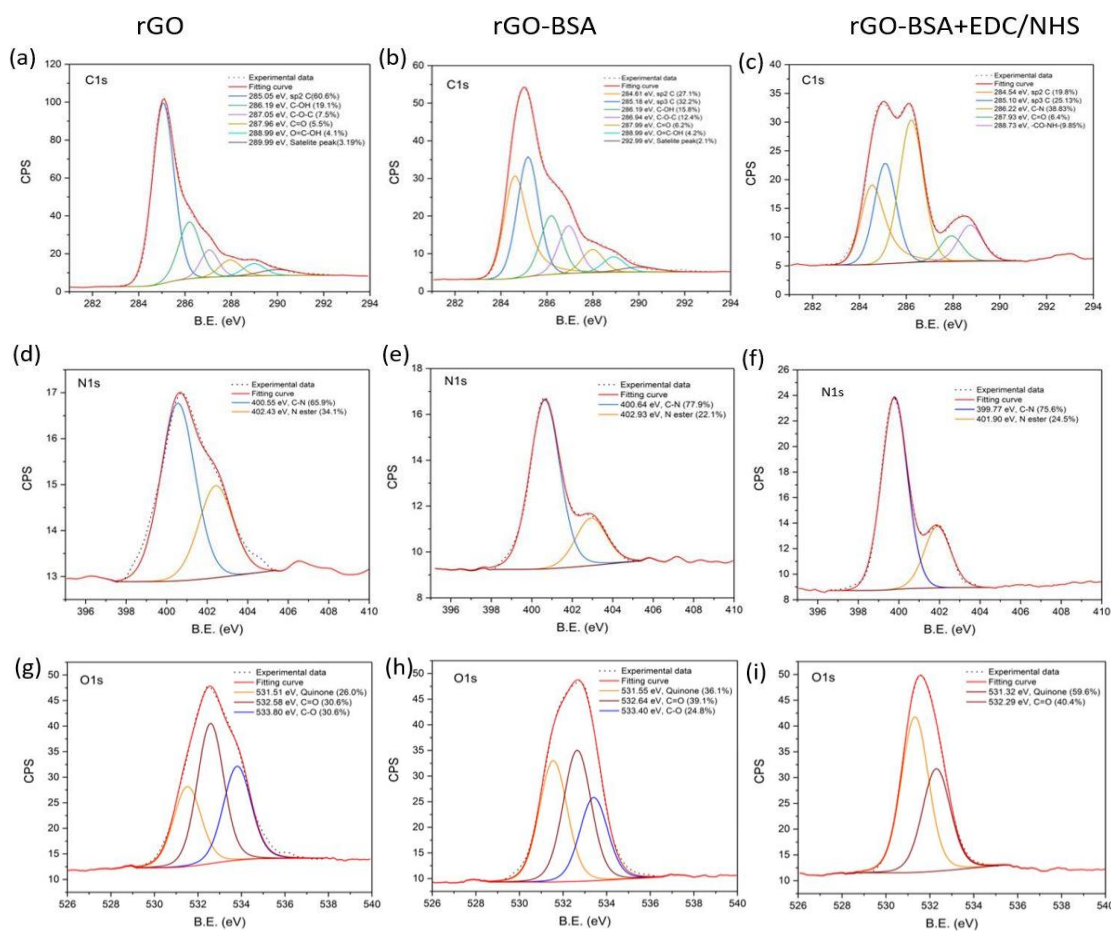
**Fig. S2.5(a)** shows the wide scan spectra for the three samples including rGO, rGO-BSA and rGO-BSA+EDC/NHS. The atomic percentage of carbon, nitrogen and oxygen were presented. The percentages of oxygen and nitrogen increase after the adsorption of BSA on rGO. The presence of sodium and chlorine peaks on the spectrum of rGO-BSA+EDC/NHS could due to the salt ion in buffer solution. **Fig. S2.5(b), (c) and (d)** present the XPS spectra of C1s, O1s and N1s, respectively. The sample with EDC/NHS activation clearly shows the C-N peak observed from C1s and N1s profiles. This confirms the covalent functionalisation of nitrogen functional groups on the rGO-BSA surface. The individual curve fittings of C1s, N1s and O1s spectra of all samples were presented in **Fig. S2.6**. The C1s spectrum obtained from rGO displays the low intensity of oxygen functional groups but the high intensity of carbon peak. The intensity of C-C peak



decreases after the adsorption of BSA, while the presence of oxygen functional groups like ether increases. After activating the surface with EDC/NHS, the graphitic nitrogen peaks (C-N and CO-NH) are obviously shown, while the carbon-carbon bond is lower than that from another two samples. The evidence from the detail scan peak of N1s in **Fig. S2.6(f)** confirms the presence of covalent bonding of carbon and nitrogen in the sample of rGO-BSA with EDC/NHS. The binding energy peak at 399.7 eV could indicate the presence of the secondary amine and imine of EDC. The peak at 402.1 eV could be the characteristic of the nitrogen of the NHS ester, shifted to higher energy due to the electronegative oxygen bonded to the nitrogen [263]. Regarding the curve fittings of O1s spectra, the oxygen peak is sharper in the case of EDC/NHS activation as the C-O peak disappears.



**Fig. S2.5** XPS results obtained from bare rGO, rGO-BSA and rGO-BSA+ NHS samples **(a)** Wide scan spectra with atomic percent. **(b)** detail spectra of C1s **(c)** O1s and **(d)** N1s for all samples. The sample with EDC/NHS activation clearly shows functionalisation of carbon and nitrogen on the surface.



**Fig. S2.6** Deconvoluted details of C1s spectra for C1s, N1s and O1s spectra of three functional graphene samples (a, d, g) rGO (b, e, h) rGO-BSA and (c, f, i) rGO-BSA with EDC/NHS activation.

Based on these XPS results, it could be implied that certain oxygen functional groups, like carboxyl and ester, on the rGO-BSA surface were activated by EDC/NHS allowing covalent crosslink between the activated surface and amine groups from binding molecules.

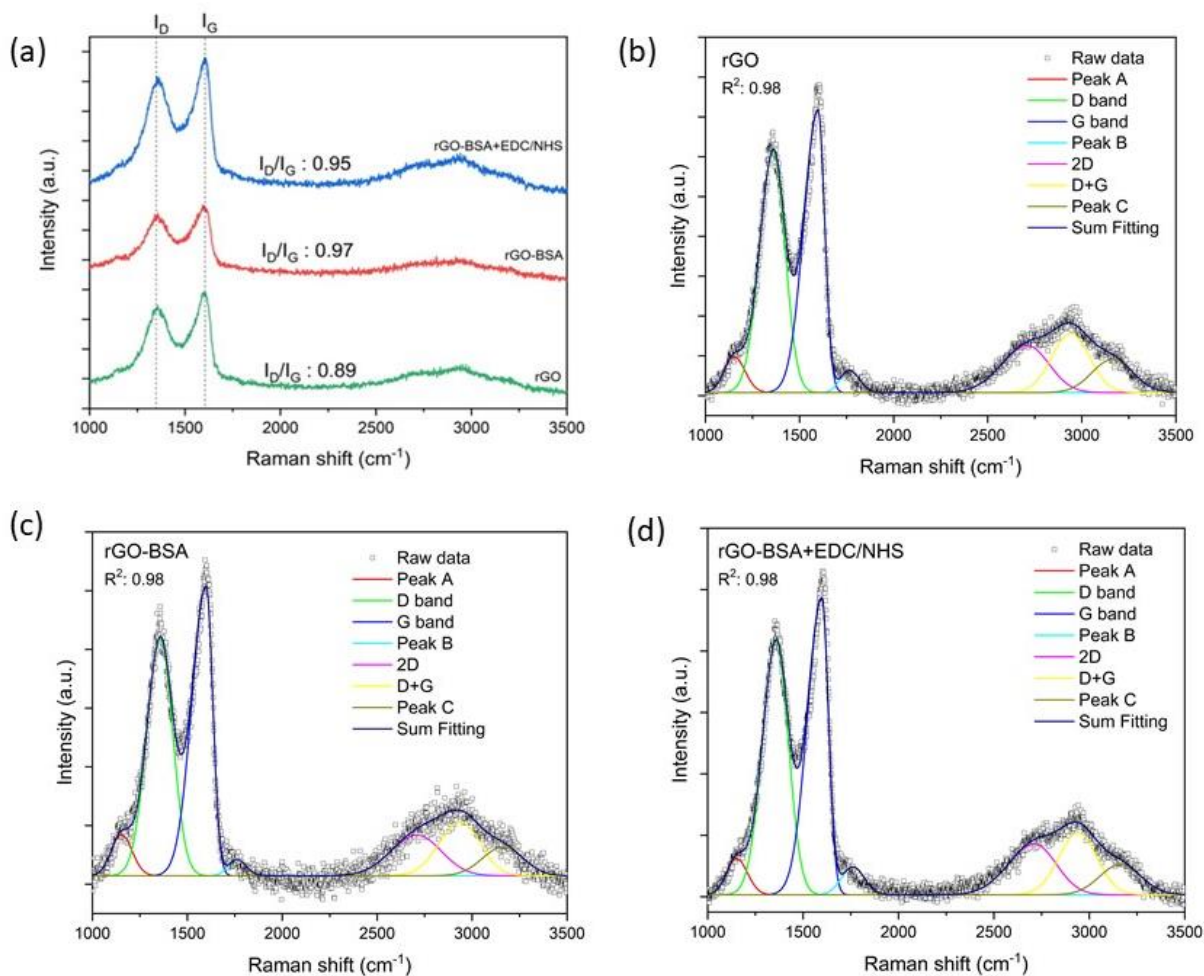
## 2.8. Raman spectroscopy

Samples for Raman spectroscopy including rGO, rGO-BSA and rGO-BSA+EDC/NHS were prepared on rGO coating on QCM chips. After monitoring the adsorption of BSA on rGO and the EDC/NHS activation using QCM technique, the QCM chips were taken out from QCM equipment, rinsed with milliQ water and dried with nitrogen gas to be samples for Raman measurements. Raman spectra were taken on a Renishaw Raman system equipped with a Leica microscope and a CCD detector. Raman spectrum was recorded using 532 nm laser line (Cobolt Samba) continuous wave diode-pumped solid-state

laser, 20 mW. The laser power was kept below 10  $\mu$ W to avoid thermal degradation of the samples. The relative intensity ratio ( $I_D/I_G$ ) was measured from the averaged acquired spectra, 10 spectra per sample. Gaussian and Lorentzian curves were used for Raman spectra fitting using Origin Pro 8.

Raman region (1000 to 1900  $\text{cm}^{-1}$ ) was fitted well to 4 peaks of Gaussian and Lorentzian curves. Two main peaks, including the graphitic (G) and defect (D), occur at  $\sim 1580 \text{ cm}^{-1}$  and  $\sim 1350 \text{ cm}^{-1}$ , respectively. All samples show no difference in D and G peak positions. The  $I_D/I_G$  values obtained from the sample of rGO-BSA and rGO-BSA+EDC/NHS show slightly higher than that of rGO samples. This indicates that more defects are presented after the physical adsorption of protein on graphene surface. The defects could originate from oxygen and nitrogen functional groups from BSA protein and the carboxylic acid activation from EDC/NHS. The weak peaks labelled A and B at around 1130 and 1700  $\text{cm}^{-1}$  are the well-known peaks of defective graphite [337]. These two peaks seem to be signatures of GO thin films as well as in highly reduced GO [337]. The peak A, in this case, could be original from the edges and overlapping of the GO flakes whereas the peak B could be due to the effect of highly reduction corresponding to previous studies [337], [338].

In the Raman region between 2300 to 3500  $\text{cm}^{-1}$ , three bands were observed at around 2700, 2900 and 3200  $\text{cm}^{-1}$ , known as 2D, D+G and 2D' or C, respectively. The 2D peak is the overtone of the D band activated by a double-resonance process while the D–G peak is combination of overtone of the D and G bands [337], [338]. Díez-Betriu (2013), studied reduction mechanisms of GO using Raman, proposed that the C peak corresponds to the C–H stretching mode of aromatic C [337]. In this study, the shape and intensity ratio of these three bands looks similar in all samples, thus, no clear effect of protein doping on these bands.



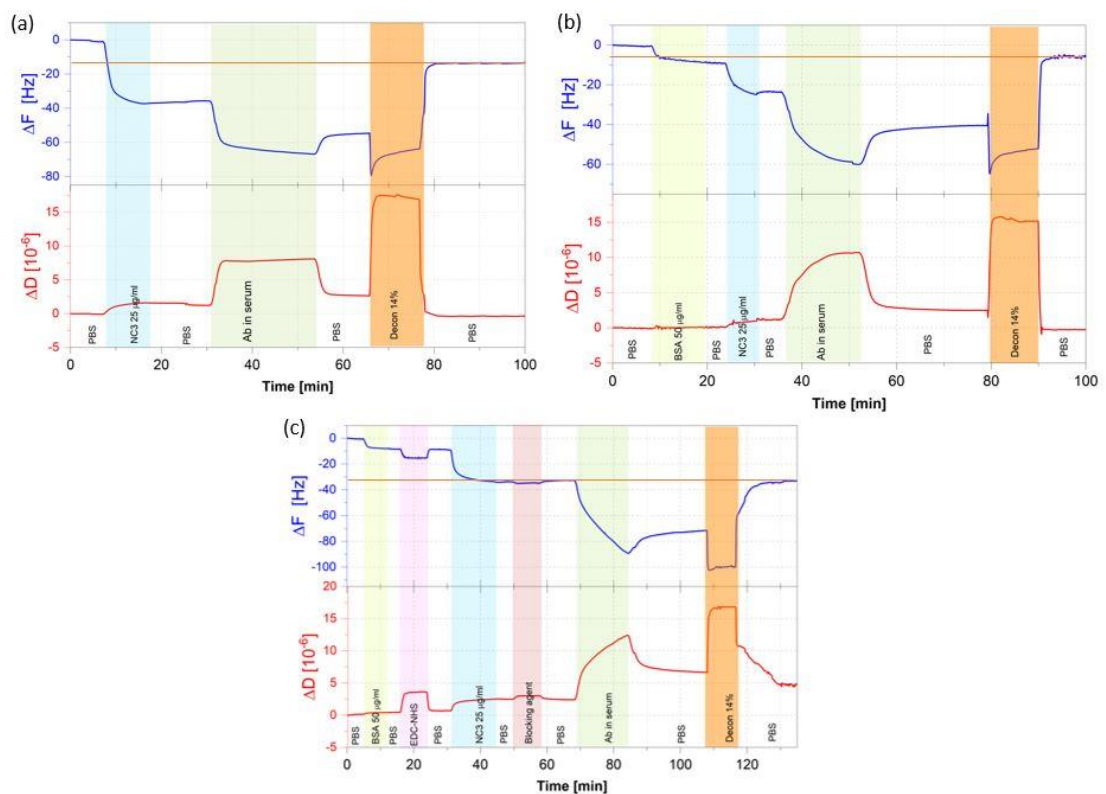
**Fig. S2.7** Raman spectra of (a) three different functional surfaces including bare-rGO, BSA-rGO and rGO-BSA+EDC/NHS. Deconvoluted details of the spectra of (b) bare-rGO (c) BSA-rGO (d) rGO-BSA+EDC/NHS

## 2.9. QCM-D Desorption

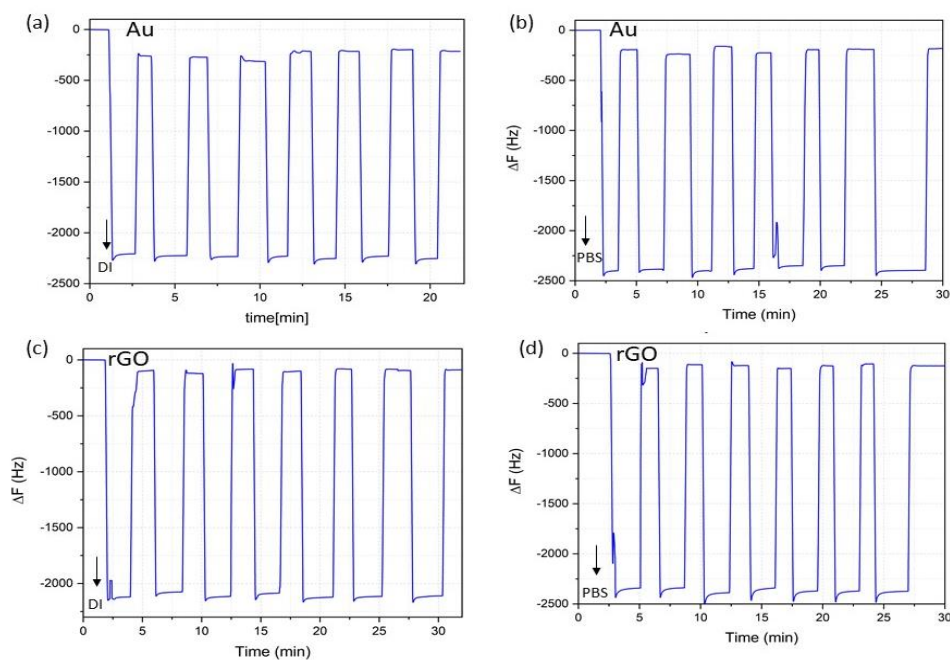
A series of desorption studies were conducted to confirm the covalent functionalisation of the NC3 on the functionalised-rGO surfaces. The NC3 immobilisation on rGO, rGO-BSA and rGO-BSA+EDC/NHS surfaces coupled with the binding with the Ab12 in serum were monitored using QCM-D, then the desorption was studied by injecting a surface-active cleaning agent (Decon 14%) which was flowed over the surface for five minutes before rinsing with PBS to recover the baseline. **Fig. S2.8(a)** presents baseline recovery occurring on rGO sample after rinsing the functionalisation with Decon 14%. The baseline shifts back from 53 Hz after antibody adsorption to 17 Hz after the rinsing. This means the antibody and partial amounts of NC3 were washed off. **Fig. S2.8(b)** presents

the desorption occurring on the rGO-BSA surface. After the final rinsing, the signal recovers from 40 Hz to 6 Hz which is the same level as BSA adsorption. It could be inferred that any layers above the BSA were removed, with only the BSA layer remaining. We suggested that the BSA molecules denatured and squeezed on the rGO surface through strong hydrophobic interaction [200]. The shift of baseline observed from the rGO-BSA activated with EDC-NHS (**Fig. S2.8(c)**) recovers to the level of NC3 confirming the covalent functionalisation of NC3 on the surface. This is the only case where the NC3 cannot be washed off.

In other cases, the NC3 was mostly washed off. As the Decon 14% can remove physically adsorbed molecules but not the covalently attached ones, the shift of the baseline observed from the rGO-BSA activated with EDC-NHS confirms the covalent functionalisation of NC3 on the surface.



**Fig. S2.8** Desorption study presenting QCM-D monitoring of the protein receptor NC3 adsorption and detection of antibody in human serum and washing-off process on 3 sensing platforms **(a)** immobilisation of NC3 on rGO **(b)** rGO-BSA **(c)** rGO-BSA with EDC/NHS activation surfaces.



**Fig. S2.9** QCM results for sequential injection of liquid samples by pipetting DI water and PBS buffer on (a), (b) Au and (c), (d) rGO surfaces, respectively.

## 2.10. The C-QCM testing for stability

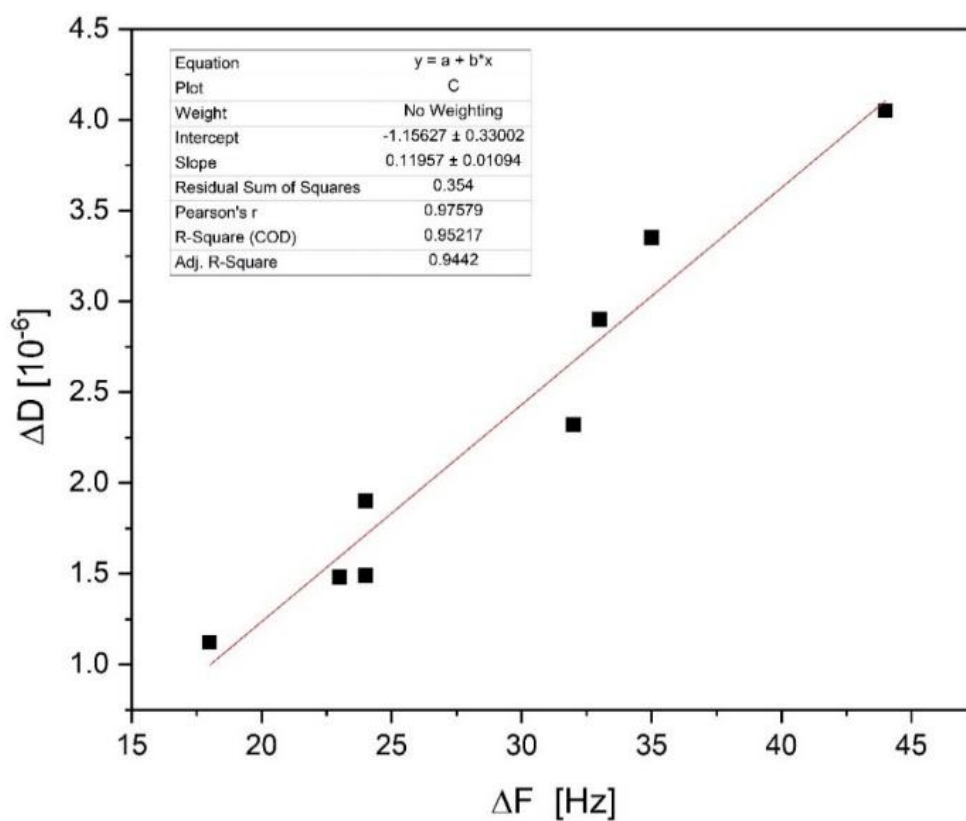
Our C-QCM system and rGO-coated chips were tested for reproducibility when cycling injection of DI water and PBS buffer on Au and rGO coated QCM chips (**Fig. S2.9**). The frequency shift results for seven cycles were collected presented in **Table S2.1**.

**Table S2.1** Comparison of frequency shift results between Au and rGO QCM chip

Cycle	Au		rGO	
	DI	PBS	DI	PBS
1	2209	2343	2120	2342
2	2222	2339	2076	2340
3	2232	2389	2114	2387
4	2230	2342	2088	2343
5	2253	2370	2124	2371
6	2231	2373	2114	2372
7	2252	2374	2110	2373
<b>Avg</b>	2233	2361	2107	2361
<b>S.D.</b>	16	20	18	19

### 2.11. QCM-D patient results

Regarding QCM-D measurement for the detection of the anti-PLA2R antibody in patient sera, the collinear plot of the final  $\Delta F$  the final and  $\Delta D$  value for each specimen is presented with a correlation coefficient ( $R^2$ ) is 0.98. Thus, the  $\Delta D$  increases linearly with respect to the  $\Delta F$ .



**Fig. S2.10** Correlation plot of the final  $\Delta F$  the final and  $\Delta D$  value obtained from the test with 8 patients' sera.

## Electronic Supporting Information 3.

This supporting information is for publication 3.

### Binding kinetics and biological recognition of nanobodies functionalised on graphene derivatives for immunosensing applications

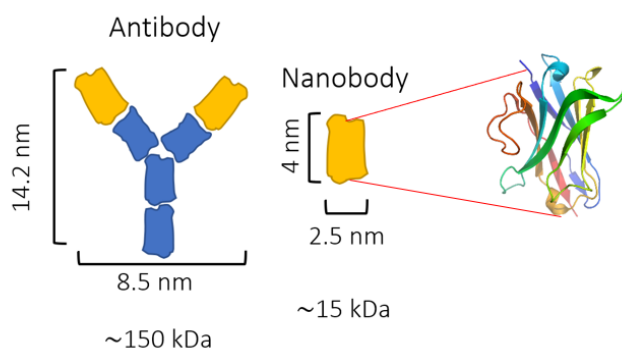
Piramon Hampitak<sup>1</sup>, Daniel Melendrez<sup>1</sup>, Maria Iliut<sup>1</sup>, Ben Spencer<sup>1</sup>, Thomas Jowitt<sup>2</sup>, and Aravind Vijayaraghavan<sup>1,\*</sup>

<sup>1</sup>Department of Materials and National Graphene Institute, Faculty of Science and Engineering, The University of Manchester, Oxford Road, Manchester M13 9PL, UK.

<sup>2</sup>School of Biological Sciences, Faculty of Biology Medicine and Health, The University of Manchester, Oxford Road, Manchester M13 9PL, UK.

#### 3.1 Production of Nanobodies

Nanobody is a binding domain of heavy-chain antibodies (HCAbs) found abundantly in camelid sera. The structure of HCAbs is noticeably different from conventional mammalian IgG structure due to the lack of L-chain polypeptides and the first constant domain (C<sub>H1</sub>). Its H chain contains only a variable domain-VHH (nanobody) served as an antigen binding site at the N-terminal region. The molecular weight of a nanobody is only 12–15 kDa. The comparison of the size of antibody and nanobody is presented in Fig. S3.1. Nanobodies or immunoglobulin-based recombinant antigen-binding proteins can be generated by immunising the particular animal with the target antigen or evolving existing Naïve libraries [155].



**Fig. S3.1.** The dimension and molecular weight of antibody and nanobody with tertiary structure of a nanobody



The protocol for nanobody production in this project was described by Birchenough 2021 as follows [284]:

1. Engineer the VHH sequence into pET-22B expression vector with a C-terminal 6-His tag.
2. Transform the vector into competent T7-Express E. coli cells (New England Biolabs)
3. Select one colony for overnight growth in 5 ml LB broth supplemented with 100 µg/ml ampicillin and shaking at 37 °C.
4. Pelleted the cells by centrifugation at 2000 rpm for 5 min and resuspended in 5 ml of sterile LB. This suspension was used to inoculate 1 litre of Magic Media™ (Thermofisher)
5. Divide the suspension to two baffled flasks and incubate for 24 h at 28 °C on a rotary shaker set to 180 rpm.
6. Extract the cells by centrifugation at 4500 rpm for 20 min at 4 °C with 250 ml cell suspension per 500 ml centrifuge tube and resuspended in 50 ml 50 mM phosphate-buffered saline (10 mM phosphate buffer with 138 mM NaCl, 2.7 mM KCl) with 1% glycerol pH 7.0. Cells were then frozen at -80 °C until needed.
7. Extract protein by thawing the cells quickly then left on ice for 20 min before sonication in a Soniprep 150 tissue homogenizer kept on ice. Cell debris was centrifuged at 14,000 rpm at 4 °C for 10 min and the supernatant collected.
8. Dilute the supernatant into 1:2 in 10 mM PBS pH 7.4 and injected onto a 5 ml Profinity IMAC column (BioRad) at 4 ml/min using a BioRad NGC FPLC. Protein was eluted in PBS supplemented with 0.5 M ultrapure imidazole (Sigma) without a gradient and collected in deep-well 96-well plates.
9. Further purified on a 10/300 Superdex-75 column in PBS plus 0.005% P20 with a flowrate of 0.75 ml/min.

## **3.2 QCM-D principal and procedure**

### **3.2.1 QCM-D principle**

The QCM-D technique is used to monitor molecular adsorption on surfaces and the binding event between molecule through real-time measurement of changes in

frequency ( $\Delta F$ ) and dissipation ( $\Delta D$ ). Higher frequency down-shift reflects in higher mass adsorption as the amount of rigid mass adsorption can be determined by using the Sauerbrey equation [167], (equation 1).

$$\Delta m = -\frac{A\sqrt{\rho_q\mu_q}}{2f_0^2}\Delta f \quad (1)$$

where

$f_0$  is the resonant frequency (Hz)

$\Delta f$  is the frequency the change (Hz)

$\Delta m$  is adsorption mass change (g)

$A$  is the Piezoelectrically active crystal area (area of a working electrode,  $\text{cm}^2$ )

$\rho_q$  is the density of quartz (typically  $2.648 \text{ g/cm}^3$ )

$\mu_q$  is the shear modulus of quartz for AT-cut crystal ( typically  $2.947 \times 10^{11} \text{ g}\cdot\text{cm}^{-1}\cdot\text{s}^{-2}$ )

### 3.2.2 The procedure of QCM-D measurement for binding studies

The QSense Omega Auto system (Biolin Scientific) was used for QCM-D measurements. The injection sequence of biosamples can be controlled through customized scripts. Before using the system, the ports, tubing and sensors holders were cleaned following the protocol from our previous publication [200]. The temperature of the system was set at  $20^\circ\text{C}$ .

Once the QCM-D system was cleaned, the experimental sensors were loaded on the sensors holder and primed by continuously flowing PBS until a stable baseline was obtained. Then, the corresponding measurement script was started. In this study, the steps for monitoring the functionalisation of the assay. The binding and dissociation of lysozyme were presented in table 1 in the main paper. The injection sequence for each sample shows as follows:

Surface (1)  $\text{SiO}_2$ : PBS  $\rightarrow$  FO7  $\rightarrow$  PBS  $\rightarrow$  lysozyme  $100 \mu\text{g/ml}$   $\rightarrow$  PBS  $\rightarrow$  FO7  $\rightarrow$  PBS

Surface (2) Au: PBS  $\rightarrow$  FO7  $\rightarrow$  PBS  $\rightarrow$  lysozyme  $100 \mu\text{g/ml}$   $\rightarrow$  PBS  $\rightarrow$  FO7  $\rightarrow$  PBS

Surface (3) rGO: PBS  $\rightarrow$  FO7  $\rightarrow$  PBS  $\rightarrow$  lysozyme  $100 \mu\text{g/ml}$   $\rightarrow$  PBS  $\rightarrow$  FO7  $\rightarrow$  PBS

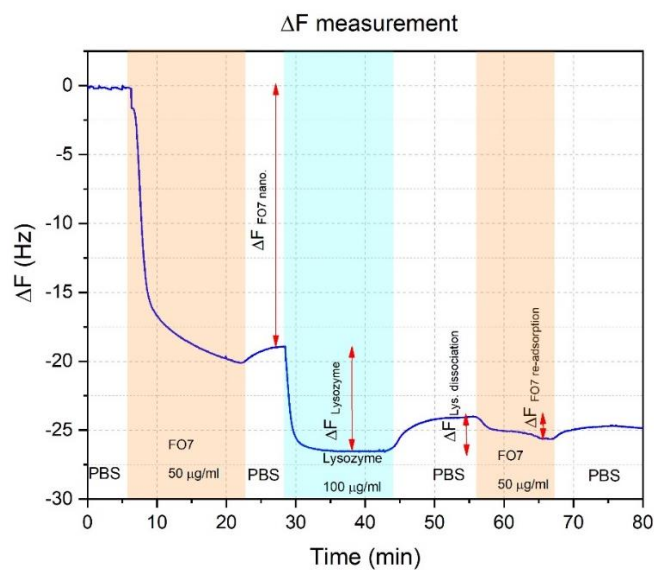
Surface (4) GO: PBS  $\rightarrow$  FO7  $\rightarrow$  PBS  $\rightarrow$  lysozyme  $100 \mu\text{g/ml}$   $\rightarrow$  PBS  $\rightarrow$  FO7  $\rightarrow$  PBS

Surface (5) PrGO1: PBS  $\rightarrow$  FO7  $\rightarrow$  PBS  $\rightarrow$  lysozyme  $100 \mu\text{g/ml}$   $\rightarrow$  PBS  $\rightarrow$  FO7  $\rightarrow$  PBS

Surface (6) PrGO2: PBS → FO7 → PBS → lysozyme 100 µg/ml → PBS → FO7 → PBS  
 Surface (7) Au-SAMs-COOH: PBS → EDC/NHS → PBS → FO7 → PBS → blocking buffer → lysozyme 100 µg/ml → PBS → FO7 → PBS  
 Sample (8) PrGO2-EDC/NHS: PBS → EDC/NHS → PBS → FO7 → PBS → blocking buffer → lysozyme 100 µg/ml → PBS → FO7 → PBS  
 Sample (9) rGO-BSA+ EDC/NHS: PBS → BSA 50 µg/mL → EDC/NHS → PBS → FO7 → PBS → blocking buffer → lysozyme 100 µg/ml → PBS → FO7 → PBS  
 Surface (10) Au-SA: PBS → SA → BiotFO7 → PBS → lysozyme 100 µg/ml → PBS → FO7 → PBS  
 Surface (11) PrGO2-SA: PBS → SA → BiotFO7 → PBS → lysozyme 100 µg/ml → PBS → FO7 → PBS  
 Surface (12) rGO-BiotBSA-SA: PBS → BiotBSA → SA → BiotFO7 → PBS → lysozyme 100 µg/ml → PBS → FO7 → PBS

The frequency shifts due to different binding events, including the FO7 ( $\Delta F_{FO7}$ ) immobilisation, the lysozyme binding ( $\Delta F_{Lys}$ ), the dissociation ( $\Delta F_{Dis}$ ) and the reabsorbed nanobody ( $\Delta F_{non-specific Lys}$ ) were recorded for analysing the functionalisation of the nanobody and its ability to recognise the analyte. The measurements of frequency shifts are exemplified in **Fig. S3.2**.

Once the measuring script is completed, it is recommended to run a washing routine using sodium dodecyl sulphate (SDS) surfactant solution and rinsed with MilliQ water.



**Fig. S3.2** The measurements of frequency shifts obtained from different adsorption events including the FO7 ( $\Delta F_{FO7}$ ) immobilisation, the lysozyme binding ( $\Delta F_{Lys}$ ), the dissociation ( $\Delta F_{Dis}$ ) and the reabsorbed nanobody ( $\Delta F_{non-specific Lys}$ )

### 3.3 Sensing surface preparation

#### 3.3.1 Preparation of Au-SAMs surface

Au-SAMs was prepared using general protocol from Sigma Aldrich following these steps 1) add 1 ml ethanol to a tube, and pipette to prepare 1 mM thiol solution (OH:COOH, 1:1), then dilute the solution 10-fold with ethanol for Step 2) then immerse a gold substrate in the reagent solution prepared at step 1) at room temperature and leave it overnight and finally 3) wash the substrate several times with ethanol and purified water sequentially.

#### 3.3.2 Receptor immobilisation protocol

The standard injection sequence can be expressed as follows:

S<sub>x</sub>: Surface → Buffer → Linker → PBS → FO7 → PBS → Blocking agent (in some cases)  
→ PBS → sample → PBS

Thus:

S.7 Au-SAMs-COOH: PBS → EDC/NHS → PBS → FO7 → PBS → blocking buffer → sample

S.8 PrGO<sub>2</sub>-EDC/NHS: PBS → EDC/NHS → PBS → FO7 → PBS → blocking buffer →

sample → PBS S.9 rGO-BSA+ EDC/NHS: PBS → BSA 50 µg/mL → EDC/NHS → PBS → FO7  
→ PBS → blocking buffer → sample

S.11 PrGO<sub>2</sub>-SA: PBS → SA → BiotFO7 → PBS → sample

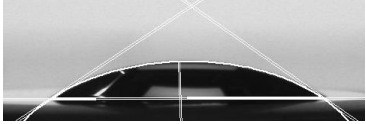

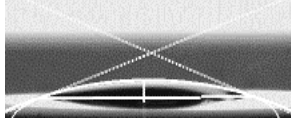


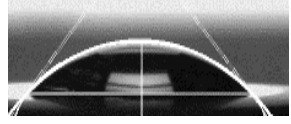
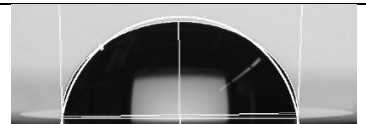
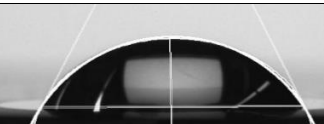
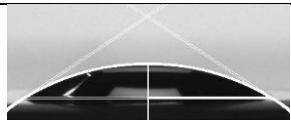
S.12 rGO-BiotBSA-SA: PBS → BiotBSA → SA → BiotFO7 → PBS → sample

### 3.4 Contact angle

A Kruss DSA100 (Hamburg) system was used to measure the wetting contact angles (WCA) for all graphene substrates. Sessile drops (5 µL) of DI water were cast on top of the substrates. The computation of the WCAs from the captured images was carried out using a plugin for ImageJ developed by Marco Brugnara [335].

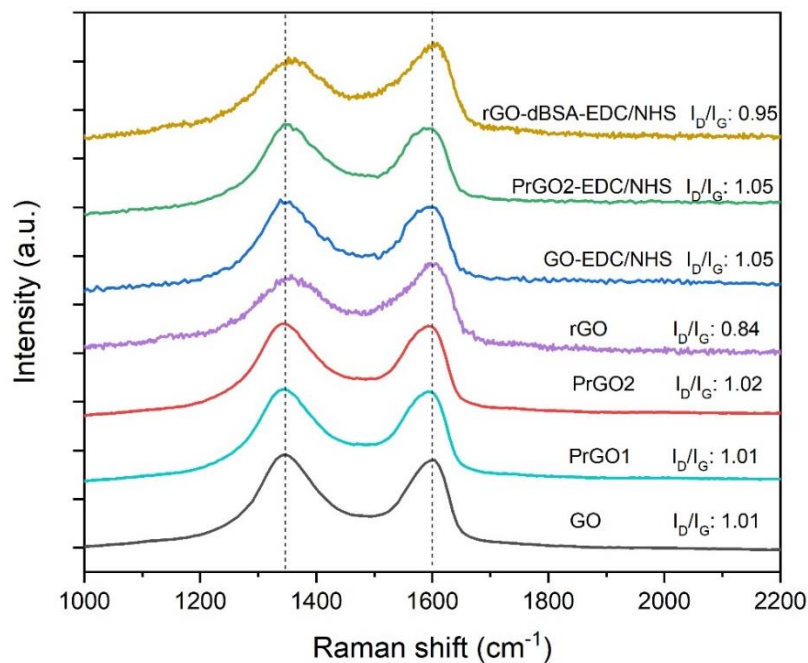
**Table S3.1** presents the wetting contact angles (WCAs) of Au, SiO<sub>2</sub> and graphene coating QCM-D chips. Both Au and SiO<sub>2</sub> are hydrophilic with a WCA of 34° ± 2° and 14° ± 2°, respectively. The results from graphene coating chips were discussed in the main paper.

**Table S3.1** The wetting contact angles (WCAs) of Au, SiO<sub>2</sub> and graphene coating QCM-D chips

Graphene surface	EDC/NHS activation	Other bare surfaces
 <p>GO CA: 34° ±3°</p>	 <p>GO+EDC/NHS CA: 32° ±5°</p>	 <p>SiO<sub>2</sub> CA: 14° ±2°</p>
 <p>PrGO2 CA:56° ±2°</p>	 <p>PrGO2+EDC/NHS CA: 51° ±3°</p>	 <p>Au CA: 34° ±2°</p>
 <p>rGO CA:99° ±2°</p>	 <p>rGO-BSA-EDC/NHS CA:55° ±4°</p>	 <p>PrGO1 CA: 46° ±3°</p>

### 3.5 Raman

Raman spectrum was recorded using 532 nm laser line (Cobolt Samba) continuous-wave diode-pumped solid-state laser, 20 mW using a Renishaw Raman system equipped with a Leica microscope and a CCD detector. The laser power was kept below 10 μW to avoid thermal damage of the graphene samples. The relative intensity ratio ( $I_D/I_G$ ) was measured from the averaged acquired spectra, 5 spectra per sample. In all samples, two main peaks, including the graphitic (G) and defect (D), appear at ~1580 cm<sup>-1</sup> and ~1350 cm<sup>-1</sup>, respectively. The  $I_D/I_G$  value of GO and PrGO is around 1, which is higher than that of the rGO sample.



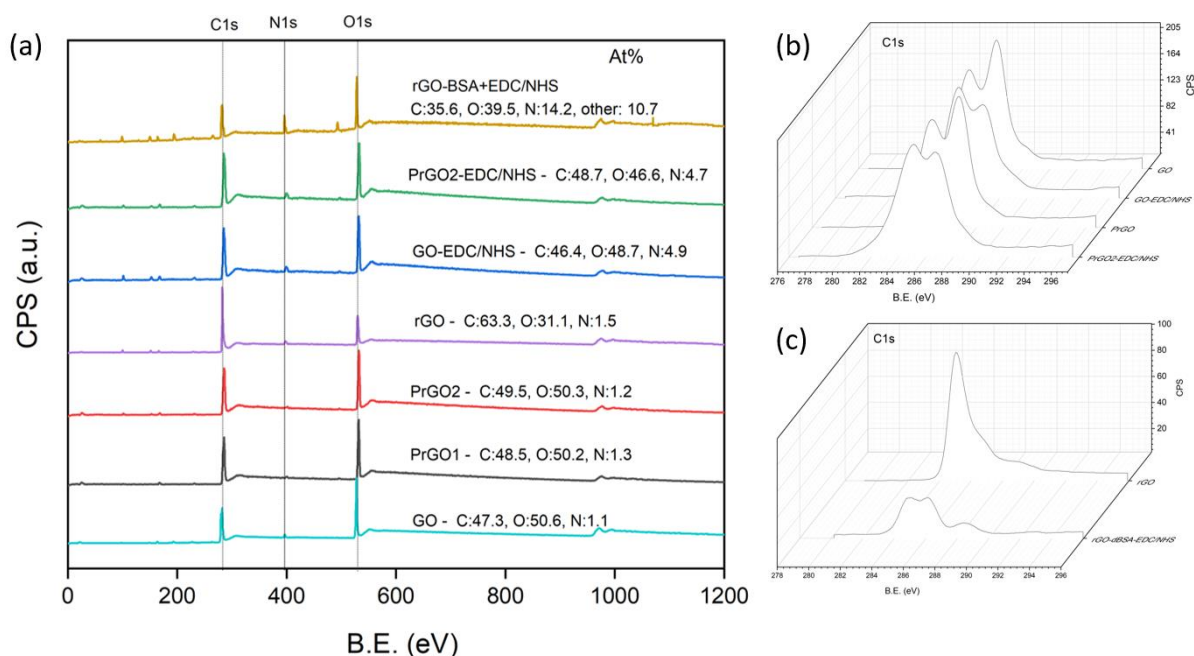
**Fig. S3.3** Raman spectra of plain GO and different levels of reduction of rGO and the graphene sample with EDC/NHS activation

### 3.6 XPS

The XPS spectra were measured using a SPECS custom-built system composed of a Phobios 150 hemispherical electron analyser with a 1D detector. The X-ray source is a microfocus monochromated Al K-alpha (1486.6 eV) source. All spectra were collected with a pass energy of 20 eV combined ultimate resolution measured from Ag 3D 0.5 eV with the X-ray source and 20 eV pass. The XPS data were processed using CasaXPS software (version 2.3.16 PR 1.6).

The C1s spectrum was calibrated using the sp<sup>3</sup> carbon peak as a reference at 284.8 eV. The N1s for graphitic nitrogen was located at the peak of 400.5 eV. The O1s spectrum is in the region of 525–580eV. The individual curve fittings of C1s of plain graphene derivative samples and their carboxylic acid activation were presented in **Fig. S3.6**. The used background type was Shirley. The C1s spectrum was fitted with synthetic components ascribed to different chemical species, including hydroxyl (C-OH) and epoxy (C-O-C) groups between 286 and 287 eV, carbonyl (C=O) and carboxyl (O-C=O) groups between 287, 289 eV, respectively. The nitrogen-carbon bonding, including C-N and N-Ester (CO-NH-), were assigned at ~286.5 and ~288.5, respectively [263]. The constraints applied were the FWHM constraint (0.9-1.1) and the position constraints

(between max  $\pm 1$  eV to min  $\pm 0.1$  eV). XPS region was fitted with the synthetic components to minimise the total square error fit (0.91) and correspond to the literature reports.

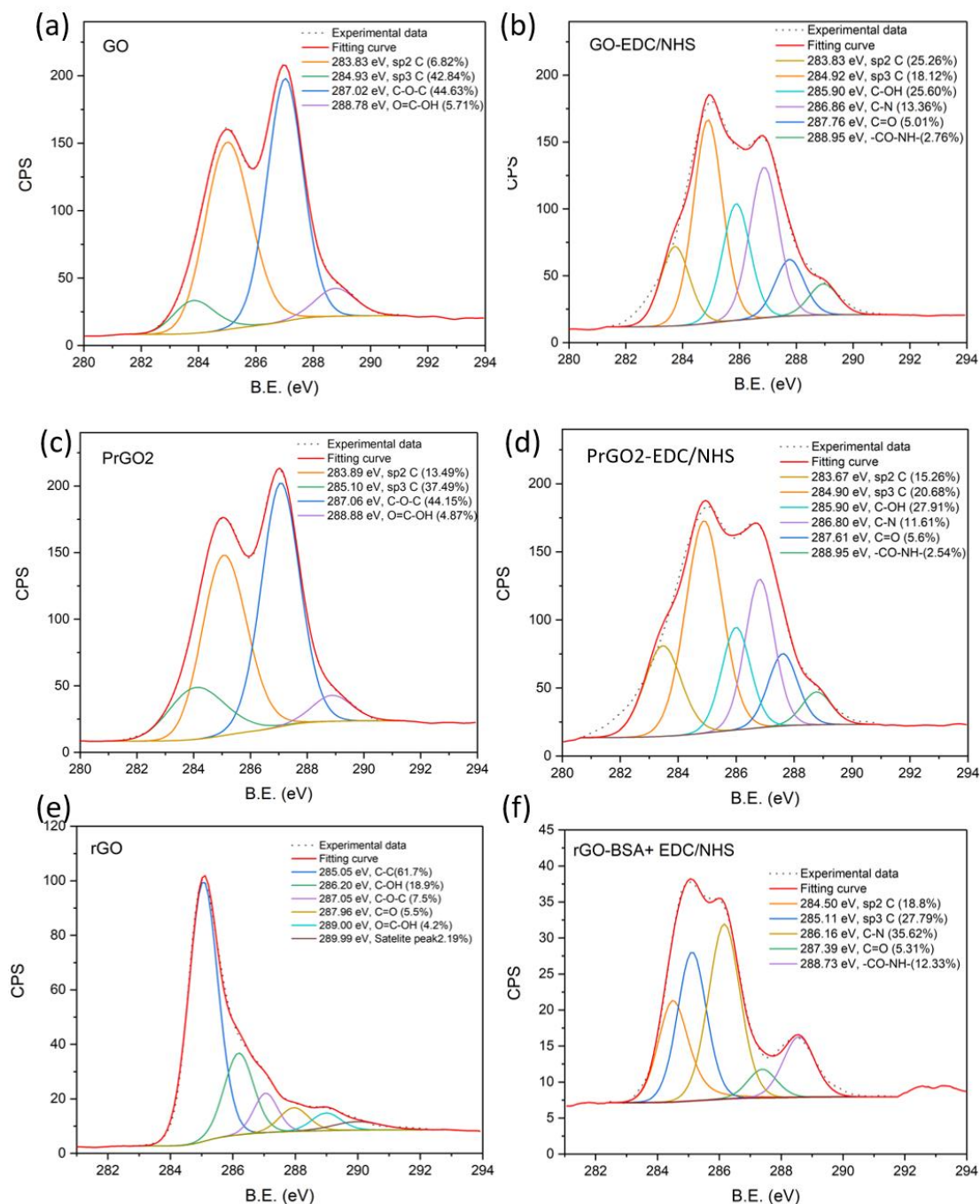


**Fig. S3.4** XPS results obtained from graphene samples. **(a)** Wide scan spectra with atomic percent. Detail spectra of C1s **(b)** GO, PrGO2 and their EDC/NHS activation **(c)** rGO and rGO-BSA-EDC/NHS

**Fig. S3.4(a)** shows the wide scan spectra for the graphene-based samples. The atomic percentage of carbon, nitrogen and oxygen were presented in the graph. The oxygen content decreases with a higher level of reduction, as explained in our previous study [200]. The percentages of nitrogen increase after the carboxylic acid activation with EDC/NHS solution, especially in the sample of rGO-BSA+EDC/NHS. The mechanism of carboxylic acid activation of rGO-BSA has already been explained in the supplementary of our previous paper [279].

**Fig. S3.4(b)** presents the comparison between XPS spectra of C1s from GO, PrGO2 and their EDC/NHS activation. The C1s spectra of GO and PrGO2 similarly show the presence of different functional groups ranging from hydroxyl (C-OH) and epoxy (C-O-C) groups between  $\sim 286$  and  $287$  eV, carbonyl (C=O) and carboxyl (O=C=O) groups between  $\sim 287$  and  $289$  eV, as presented in Fig. S6(a) and (c). The sample with EDC/NHS activation (**Fig. S3.5 (b) and (d)**) shows the second peak at  $\sim 286.7$  eV referring to C-N peak while the second peak in plain GO and PrGO2 samples are at  $\sim 287$  eV referring to C-O. The results

suggest the increase of C-N on the GO and PrGO2 surfaces as the C-O reduced could be due to the presence of the secondary amine and imine of EDC after carboxylic activation. The peak of N-Ester (CO-NH-), assigned at ~288.5, also reveal after the activation corresponding the characteristic of the nitrogen of the NHS ester [263].



**Fig. S3.5** Deconvoluted details of C1s spectra for C1s spectra of three bare surfaces (a) GO, (c) PrGO2, (e) rGO and the EDC/NHS activation samples (b) GO-EDC/NHS (d) PrGO-EDC/NHS (f) rGO-BSA with EDC/NHS activation.

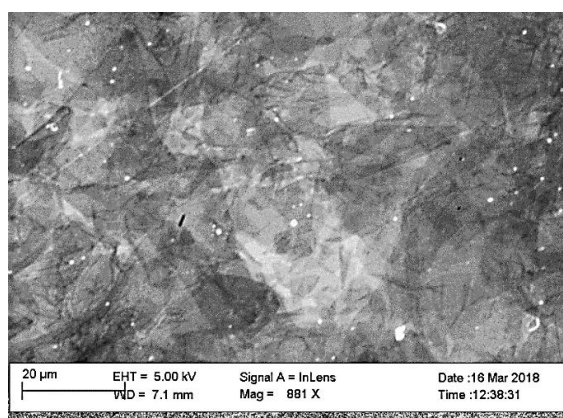


However, the spectra observed from C1s from GO, PrGO2 with EDC/NHS activation appear to be relatively broad compared to the spectra from rGO-BSA+EDC/NHS. Furthermore, it is seen from the fitting that several oxygen functional groups are remaining in GO and PrGO2 after the activation that could interfere with biomolecular binding through amine crosslinking, promoting non-specific adsorption. This evidence suggests that the direct activation of GO and PrGO2 surfaces with EDC/NHS might not be competent to the rGO-BSA+EDC/NHS system, which has been proven to be an effective route.

### 3.7 SEM

The SEM imaging of GO coatings was performed on a SEM Zeiss Ultra setup, using an acceleration voltage of 5 kV and 5 mm working distance. The size distribution of GO and surface properties of GO before and after reduction have been reported in our previous publication [200]. GO flakes indicating that the GO is 100% monolayer. There is no difference on the coating of GO or rGO with any different level of reduction.

**Fig. S3.6** presents SEM image of fully-coverage and uniform coating of GO on a QCM-D chip with the presence of flake overlaps.

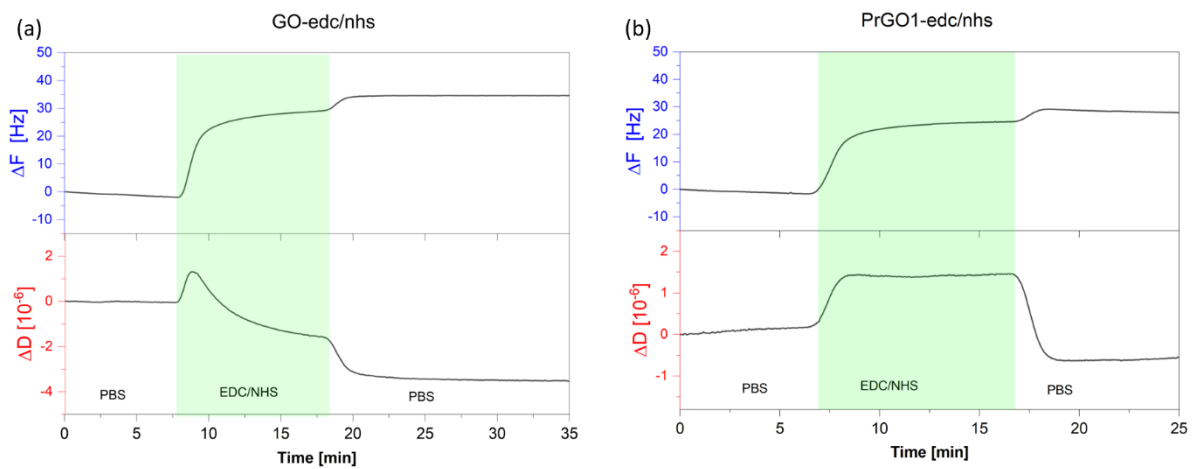


**Fig. S3.6** SEM image of fully-coverage and uniform coating of GO on a QCM-D chip

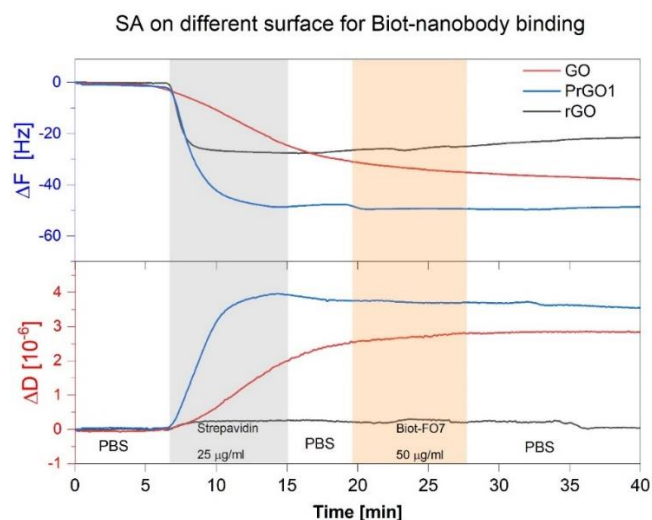
### 3.8 Exploring different surface conditions – Additional results

The direct adsorption of EDC/NHS solution on GO and PrGO1 as an carboxylic acid activation was tested. **Fig. S3.7** presents the considerable increase of  $\Delta F$  and  $\Delta D$  after the injection of EDC/NHS on GO and PrGO1 implying that there is a significant loss of mass on the sensor due to some flakes from graphene washed off.

We also tested the direct adsorption of SA on GO, PrGO1 and rGO as a platform to bind with Biot-FO7 nanobody. The QCM-D monitoring of the SA adsorption and the nanobody binding is shown as **Fig. S3.8**. On GO, the SA slowly adsorbed on the surface that could be due to protein unfolding on the surface resulting in the lack of biorecognition of Biot-FO7 as shown on the QCM-D monitoring result. On PrGO1 surface, the SA adsorbed on the surface with faster adsorption rate and the final frequency shift after the adsorption reaching 50 Hz; however, the binding of biot-FO7 shows the frequency shift of less than 2 Hz which is much less than that on the PrGO2 surface (~12 Hz, see the main paper). The lack of binding affinity on PrGO1 could be due to the random arrangement of SA on the surface, some binding sites of the SA might be hidden as too many molecules closely packed on the surface. On rGO surface, the lack of binding affinity is also presented as observed from the non-adsorption of Biot-FO7. This could be due to the denaturation of SA protein after adsorption on rGO due to strong hydrophobic interaction [200]. These results indicate that the level of GO reduction affect the arrangement and conformation of the adsorbed proteins corresponding to our previous study [200].



**Fig. S3.7** QCM-D monitoring of the direct adsorption of EDC/NHS solution on (a) GO (b) PrGO1



**Fig. S3.8** QCM-D monitoring of the direct adsorption of the SA adsorption on GO, PrGO1 and rGO and the BiotFO7 nanobody binding

### 3.9 Thickness of sensing layer

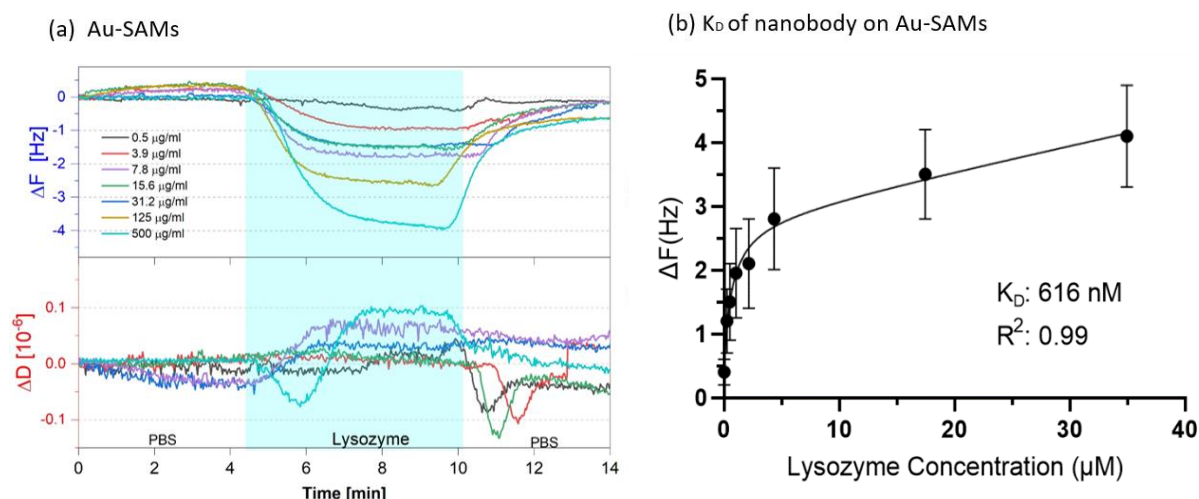
The thickness of the five selected sensing layers were determined by converting mass obtained from the Sauerbrey equation to thickness. The software Dfind from Biolin Scientific was used for the calculation. The total thickness of the sensing layer is calculated from the sum of each protein layer over the solid surface. Protein layers including BSA, SA and FO7 are assumed to be rigid observed from low dissipation shift ( $\Delta D \ll \Delta F$ ). The density of each protein for the calculation are as follows: BSA=BiotBSA: 1320 g/L, SA: 1100 g/L (hydrated protein), FO7=BiotFO7: 1330 g/L. The results of calculated thickness present in **Table S3.2**.

**Table S3.2** The results of calculated thickness of sensing layers from the Sauerbrey equation

Surface	Element	$\Delta F$ (Hz)	Average thickness (nm)	S.D.
(7) Au-SAMs +EDC/NHS +FO7	FO7	6.5	1.1	0.4
(8) PrGO2+EDC/NHS +FO7	FO7	14.8	2.5	0.5
(9) rGO-BSA +EDC/NHS +FO7	BSA	4	0.5	0.3
	FO7	8.3	1.2	0.5
(11) PrGO2- SA +BiotFO7	SA	30	5.4	1.1
	BiotFO7	9	2.0	0.2
(12) rGO-BiotBSA+ SA +BiotFO7	BiotBSA	5	0.9	0.2
	SA	20	3.2	0.5
	BiotFO7	7	1.7	0.3

### 3.10 KD from Au SAM

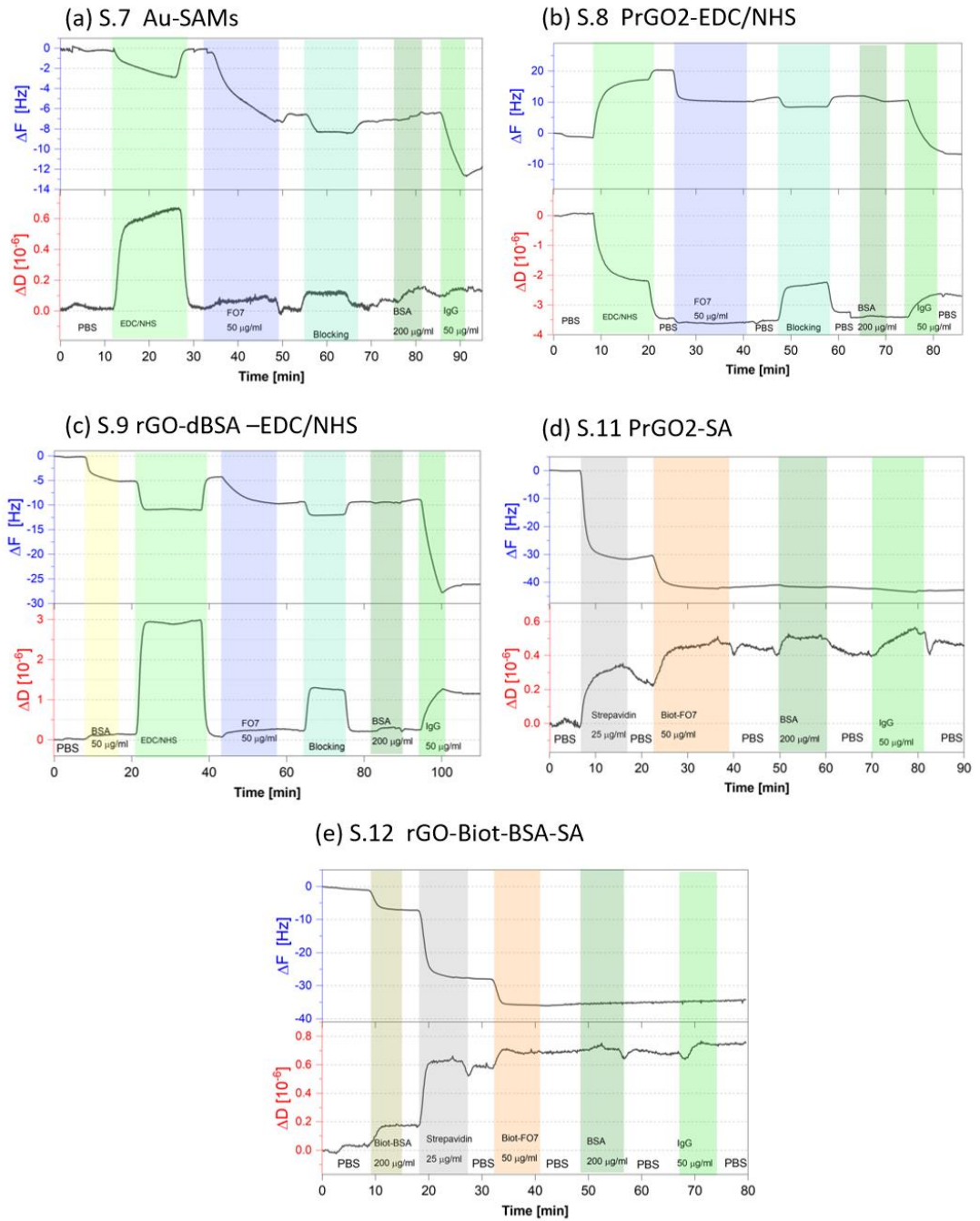
**Fig. S3.9 (a)** presents the binding of varied concentrations of lysozyme on the Au-SAMs functionalised with the FO7 nanobody (reference surface). As expected, the frequency and dissipation increase as a function of the lysozyme concentration. The plot of series of  $\Delta F_{\text{Lys}}$  values vs lysozyme concentration was generated as a standard curve. The obtained  $K_D$  is 1846 nM.



**Fig. S3.9 (a)** QCM-D result of the binding of varied concentrations of lysozyme on the Au-SAMs functionalised with the FO7 nanobody. **(b)** The standard curve with the computed  $K_D$  values of the nanobody on the Au-SAMs.

### 3.11 Selectivity tests

**Fig. S3.10.** presents the QCM-D monitoring of non-specific protein adsorption on five different functionalised surfaces. The nanobody immobilisation on different sensing surfaces and the adsorption of BSA and IgG were presented showing selectivity of the surfaces. All surfaces display specificity against BSA; however, only S.11 and S.12 present selectivity against both proteins as explained in the main paper.



**Fig. S3.10.** QCM-D monitoring of non-specific protein adsorption on five different functionalised surfaces showing selectivity against serum protein of the surfaces.

## Electronic Supporting Information 4.

This supporting information is for co-author publication.

### **Development of an open-source thermally stabilized quartz crystal microbalance instrument for biomolecule-substrate binding assays on gold and graphene**

Daniel Meléndrez<sup>s</sup>, Piramon Hampitak<sup>a</sup>, Thomas Jowitt<sup>b</sup>, Maria Iliut<sup>a</sup>, and Aravind Vijayaraghavan<sup>a,\*</sup>

<sup>a</sup>*Department of Materials and National Graphene Institute, The University of Manchester, Oxford Road, Manchester M13 9PL, UK.*

<sup>b</sup>*School of Biological Sciences, Faculty of Biology Medicine and Health, The University of Manchester, Oxford Road, Manchester M13 9PL, UK.*

\*Corresponding Author: [aravind@manchester.ac.uk](mailto:aravind@manchester.ac.uk); +441612750136

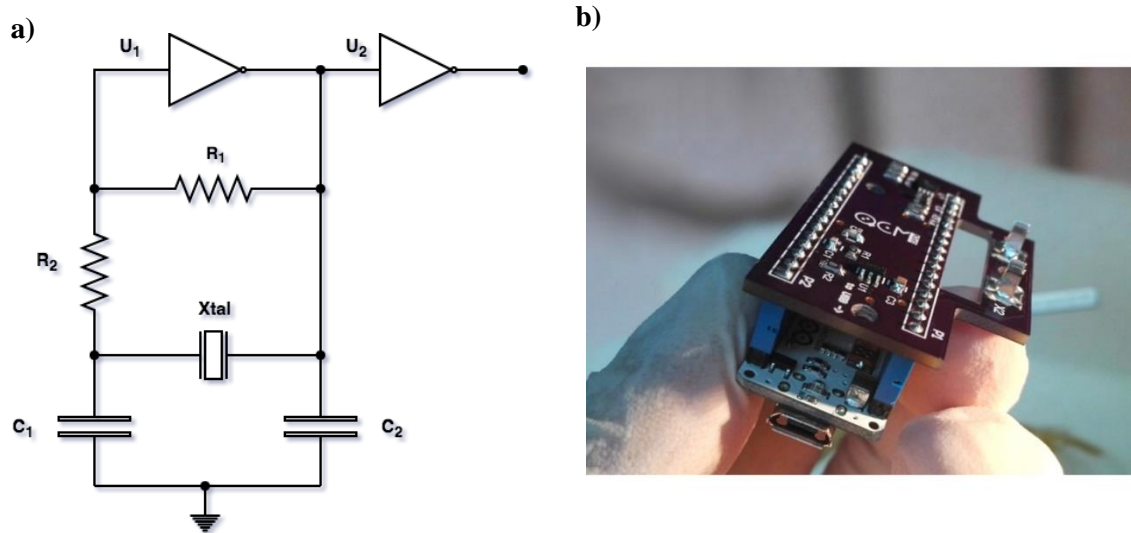
#### **4.1. Graphene Oxide Preparation**

Graphite flakes of 50 mesh (1g) and NaNO<sub>3</sub> (0.9 g) were mixed in concentrated H<sub>2</sub>SO<sub>4</sub> (35 mL) and left overnight to intercalate. The mixture was cooled down in an ice bath before slowly added with 4.5 g KMnO<sub>4</sub> during stirring. The mixture was left for 5 days at room temperature to allow graphitic oxidation. The brown slurry was diluted by slowly adding 5% H<sub>2</sub>SO<sub>4</sub> solution (100 mL), then diluted again with 100 mL mixture of 3% H<sub>2</sub>SO<sub>4</sub> and 0.5% H<sub>2</sub>O<sub>2</sub>. The homogenisation and complete exfoliation of graphite oxide was carried out using a vertical stirrer at a low speed for ~1h. The final GO dispersion was washed by repeated centrifugation and dilution with diluted H<sub>2</sub>SO<sub>4</sub>, then DI water until the pH was close to neutral.

#### **4.2. openQCM principle of operation**

The basic core of the *openQCM* (**Fig. S4.1**) device consists of an electronic board containing the excitation circuit of the crystal (**Fig. S4.1b**) that sends a digital output signal to a computer via the onboard USB port. The QCM chips are mounted on crystal holder type HC-48U. The instrumentation block is shown in **Fig. S4.3a**. This circuit is based on an electronic Pierce oscillator, a standard configuration used for clock signal generation in digital circuits. The quartz crystal (Xtal) forms a  $\pi$ -filter with the capacitors C<sub>1</sub> and C<sub>2</sub>. The filter feeds the resultant quasi-sinusoid signal through R<sub>1</sub> to the inverter U<sub>1</sub>, which initiates the oscillation. Finally, the output inverter U<sub>2</sub> creates well-defined

square-wave pulses [339]. This signal is then routed to a digital input from an Arduino *Micro* microcontroller unit (MCU) (**Fig. S4.3b**) that converts the number of pulses to frequency. Finally, the shield board also incorporates a digital temperature sensor placed in close proximity to the quartz crystal to provide a readout of the real-time thermal conditions of the resonator.



**Fig. S4.1** Instrumentation electronics for openQCM system a) Pierce oscillator where Xtal represents the QCM sensor b) Instrumentation electronics mounted on a shield for an Arduino *Micro*

### 4.3. Temperature processing

#### 4.3.1 Temperature-dependent resistors

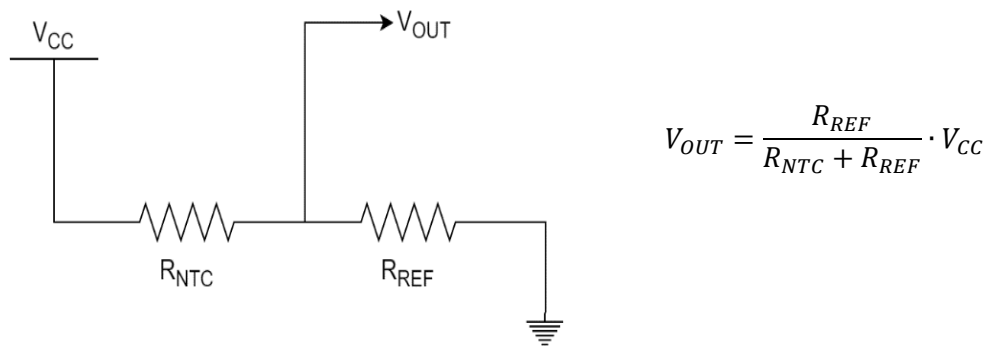
Thermistors are a special type of resistor whose resistance changes according to the temperature. Their characteristic coefficient indicates the response type of the resistance in terms of the temperature. In a negative temperature coefficient (NTC) device, when temperature increases, the resistance decreases. Such relationship is not linear, rather exponential and can be accurately approximated by computational methods through logarithmic functions which a wide range of low-cost microcontrollers are capable of computing. In practice, thermistors are configured as voltage dividers where a reference resistor ( $R_{REF}$ ) with low tolerance is required to achieve precise temperature measurements. The output voltage of this voltage divider can be easily digitized by an analog-to-digital converter (ADC) present in many microcontrollers.

Thermistors are widely used as temperature sensors in any control or instrumentation process due to its reduced size, high sensitivity, accuracy, fast response and low cost. However, these advantages come with a price because of their nonlinear relationship between the resistance of the thermistor and the temperature of its surrounding atmosphere [340]. When thermistors are used in temperature measurement, they are usually connected to an adequate circuit like voltage dividers or bridge circuits (**Fig. S4.2**).

**Since NTCs are not linear devices their temperature response must be modelled through either a first-order approximation, the Steinhart-Hart equation[341] (Eq. S1) or the beta ( $\beta$ ) formula (Eq. 2).**

$$T = \frac{1}{A + B \ln(R) + C [\ln(R)]^3} \quad (\text{Eq. S1})$$

where T is expressed in Kelvin and A, B and C are the Steinhart-Hart coefficients to be determined and depend on the model of the thermistor and the temperature range where the device will be used in.



**Fig. S4.2** Voltage divider for NTC compensation.  $R_{NTC}$  is the thermistor resistance,  $R_{REF}$  is a reference or compensation resistor.  $V_{CC}$  and  $V_{OUT}$  are the supply and output voltages, respectively. The mathematical expression represents the standard relationship for a two resistors voltage divider to determine  $V_{OUT}$ .

A faster approach is to compute the  $\beta$ -value of a thermistor which indicates the shape of the R vs T curve of the thermistor. In other words, this parameter represents the decay of the resistance relative to the temperature and it is expressed by Eq. S2.

$$\beta = \frac{\ln\left(\frac{R_{T_1}}{R_{T_2}}\right)}{\left(\frac{1}{T_1} - \frac{1}{T_2}\right)} \quad (\text{Eq. S2})$$



where  $R_{T_1}$  is the resistance at temperature  $T_1$  and  $R_{T_2}$  is the resistance at temperature  $T_2$  and are expressed in Kelvin. The material constant ( $\beta$ ) of the thermistor is determined by the activation energy  $q$  and the Boltzmann's constant  $k$  with the dependence  $\beta = q/k$ . This value is characterized and given by the manufacturer of each device.

For NTC thermistors with a known  $\beta$ -value, the temperature is expressed as:

$$\frac{1}{T} = \frac{1}{T_0} + \frac{1}{\beta} \ln\left(\frac{R}{R_0}\right) \quad (\text{Eq. S3})$$

Where  $T_0$  is the reference temperature (usually referred to room temperature),  $R$  is the sensor's resistance at any  $T$  and  $R_0$  is its resistance at  $T_0$ .

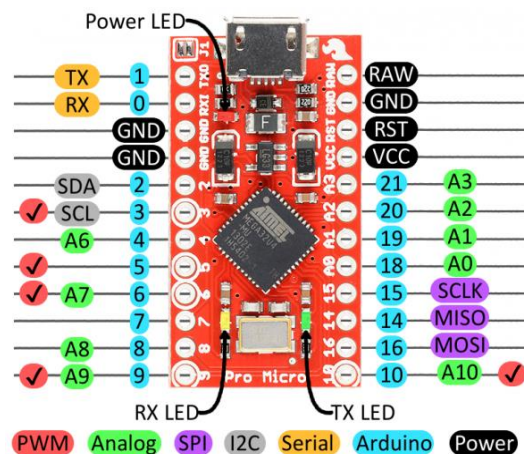
Solving Eq. S3 for  $R$ , we can obtain the exponential relationship between the resistance of the thermistor and its body temperature is expressed mathematically by Eq. S4

$$R_{NTC} = R_0 e^{\beta\left(\frac{T_0 - T}{T \cdot T_0}\right)} \quad (\text{Eq. S4})$$

### 4.3.2 Digitization of an NTC response

Solving the voltage divider equation shown in Fig. S4.2 for  $R_{NTC}$  we have

$$R_{NTC} = R_{REF} \left( \frac{V_{CC}}{V_{OUT}} - 1 \right) \quad (\text{Eq. S5})$$



**Fig. S4.3** Arduino Pro Micro pinout. Image taken from Sparkfun Electronics (Jimblom (Sparkfun Electronics), 2020) under the Creative Commons License BY-SA 4.0.

An Arduino *Pro Micro* (**Fig. S4.3**, [342]) was used as the microcontroller board to electronically control the activation of the Peltier cooler via the control algorithm described in Section 5 from this document. Since the voltage will be converted to a digital word by the internal 10-bit ADC of the microcontroller we can rename the parameters from **Eq. S6** as follows

$$R_{NTC} = R_{REF} \left( \frac{D_{MAX}}{D_{RAW}} - 1 \right) \quad (\text{Eq. S6})$$

where  $D_{MAX}$  is the maximum digital value that an ADC converter can express by means of the number of bits  $n$  and given by **Eq. S7**.  $D_{RAW}$  is the value captured by the ADC. It is important to notice the direct relationship between the supply voltage and the digital conversion value. In this case, the Arduino board utilizes 5 V as an internal power supply and reference voltage, therefore this voltage represents the full-scale conversion value.  $D_{MAX}$  also expresses the number of quantization levels that the ADC can obtain.

$$D_{MAX} = 2^n - 1 \quad (\text{Eq. S7})$$

Therefore, for  $n = 10$   $D_{MAX}$  equals 1023 with 0 (zero) as the first quantization level. The resolution of the system can be expressed as the minimum detectable voltage and is given by  $V_{CC} / D_{MAX} = 4.88$  mV/step, assuming  $V_{CC} = 5.0$  V.

$D_{RAW}$  is the digital representation of the setpoint or desired temperature. This parameter can also be described as the quantization value of the output from the voltage divider; in other words, the real-time digitization of the voltage read by the ADC.

For the sake of clarity, we can label the argument of the exponential expression from **Eq. S4** as follows

$$\alpha = \beta \left( \frac{T_0 - T}{T \cdot T_0} \right) \quad (\text{Eq. S8})$$

Merging **Eq. S4** and **Eq. S6** to solve for  $D_{RAW}$  we therefore obtain

$$R_0 e^\alpha = R_{REF} \left( \frac{D_{MAX}}{D_{RAW}} - 1 \right) \quad (\text{Eq. S9})$$

Finally,

$$D_{RAW} = \frac{D_{MAX} \cdot R_{REF}}{R_0 e^\alpha + R_{REF}} \quad (\text{Eq. S10})$$

The last equations will translate a desired temperature given in °C to an appropriate ADC value within its full scale of [0,1023].

From these results it is straightforward to convert  $D_{MAX}$  to an adequate temperature scale (e.g. Celsius) by first applying **Eq. S6** to obtain the resistance of the NTC as a resultant quantified voltage from instrumentation circuit (**Fig. S4.2**) then solving **Eq. S3** for the temperature  $T$  (in Kelvin), as follows:

$$T_{[K]} = \frac{\beta T_0}{\beta + T_0 \ln \left( R_{NTC} / R_0 \right)} \quad (\text{Eq. S11})$$

Where  $R_{NTC}$  is the value of the thermistor given by **Eq. S6**. Finally, the conversion to Celsius is done by subtracting the absolute zero from the Kelvin scale.

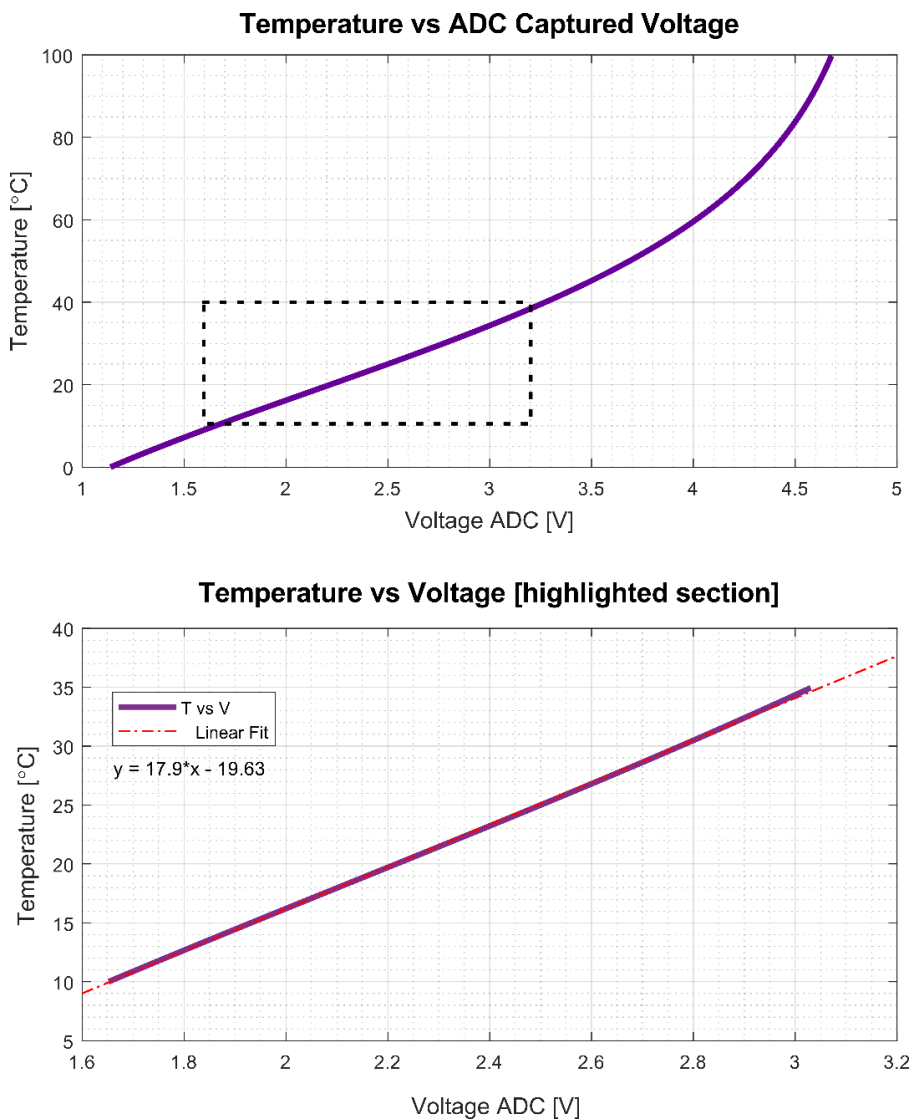
In order to obtain sensitivity from the digital instrumentation, the **Eq. S11** can be plotted as a function of the quantification value  $D_{RAW}$ . On these terms, we explicitly obtain

$$T(D_{RAW})_{[K]} = \frac{\beta T_0}{\beta + T_0 \ln \left( \frac{D_{MAX}}{D_{RAW}} - 1 \right)} \quad (\text{Eq. S12})$$

#### 4.3.3 Temperature reading resolution

From **Eq. S12**, the digital quantities can be indistinctively expressed as voltages. **Fig. S4.4** shows the graph of the respective temperatures as a function of the voltages read by the ADC. The highlighted section indicates the limits of the temperatures that were observed during the experimental sessions, i.e. [10,35] [°C]. This region presents a linear trend that was linearly fitted obtaining a slope of  $\approx 18^\circ\text{C}/\text{V}$  corresponding to the sensitivity of the system. In terms of the aforementioned resolution of the ADC

(4.88mV/step), this system is capable of measuring a temperature change as low as 87.5 m°C/step.



**Fig. S4.4** ADC readout analysis. NTC Temperature vs ADC Voltage. The top panel shows the full-scale response of the voltage divider. The lower panel covers the range of experimental temperatures and linear trend.

#### 4.4. Development of GUI for Data Acquisition

The openQCM project created by Novaetech includes a user interface for data acquisition. It was developed in Java programming language and its complete functionalities are: connecting to the communications port from the electronic (Arduino) board, reading incoming data (frequency and temperature), creating a live plot of the data and finally saving data to a text file. In spite of its simplicity, it is a robust and well written application by Marco Mauro [343] and entirely developed in NetBeans

for Java, however it is limited in options for data visualization and handling, like viewing the change of frequencies in terms of their shifts, saving data files in different formats or appending and plotting an entire acquisition upon completing an experimental session.

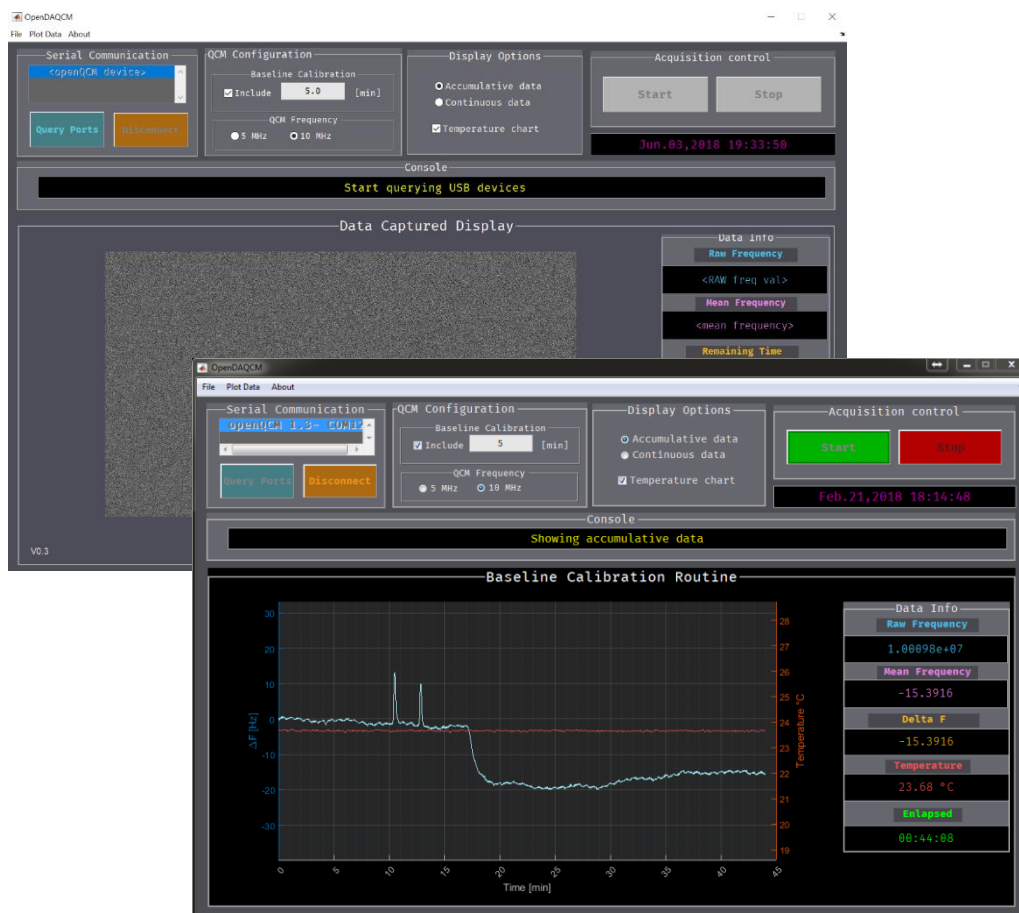
Therefore, a new GUI based on Mauro's code with extended capabilities was designed and developed

in Matlab 2018 (**Fig. S4.5**). This acquisition platform queries all the USB devices connected to the computer, identifies the unique tag of the openQCM board and starts a handshake protocol with the device in order to open a serial communication. The platform can acquire continuous data points and offers the possibility to perform a baseline calibration in order to read absolute frequency shifts, making the incoming data more readable to the user.

The front panel displays useful information from the status of the current measurement like live average and median values, time elapsed and remaining time for the baseline calibration routine to complete, finally it also provides timestamps for every registered data point and such are saved in the corresponding output Excel sheet file. Every acquired data set is continuously loaded in memory and the software was programmed so that the data is formatted and ready to be saved once the logging operation is completed. Two output file types can be selected: tab-separated text file and Excel file (.xlsx).

Finally, the user can perform a quick check of the acquired data by plotting it with or without a simple smoothing. One particular add-on is the possibility to read the raw frequencies in the output file when the baseline calibration routine is selected. This offers the possibility to process raw incoming data from the QCM sensor.

**Fig. S4.6** shows a flow chart for the complete operation of the GUI. The expanded view of the routines contained in process boxes are shown on **Fig. S4.7** and **Fig. S4.8**.



**Fig. S4.5** Graphical user interface for openQCM data acquisition, baseline calibration and logging.

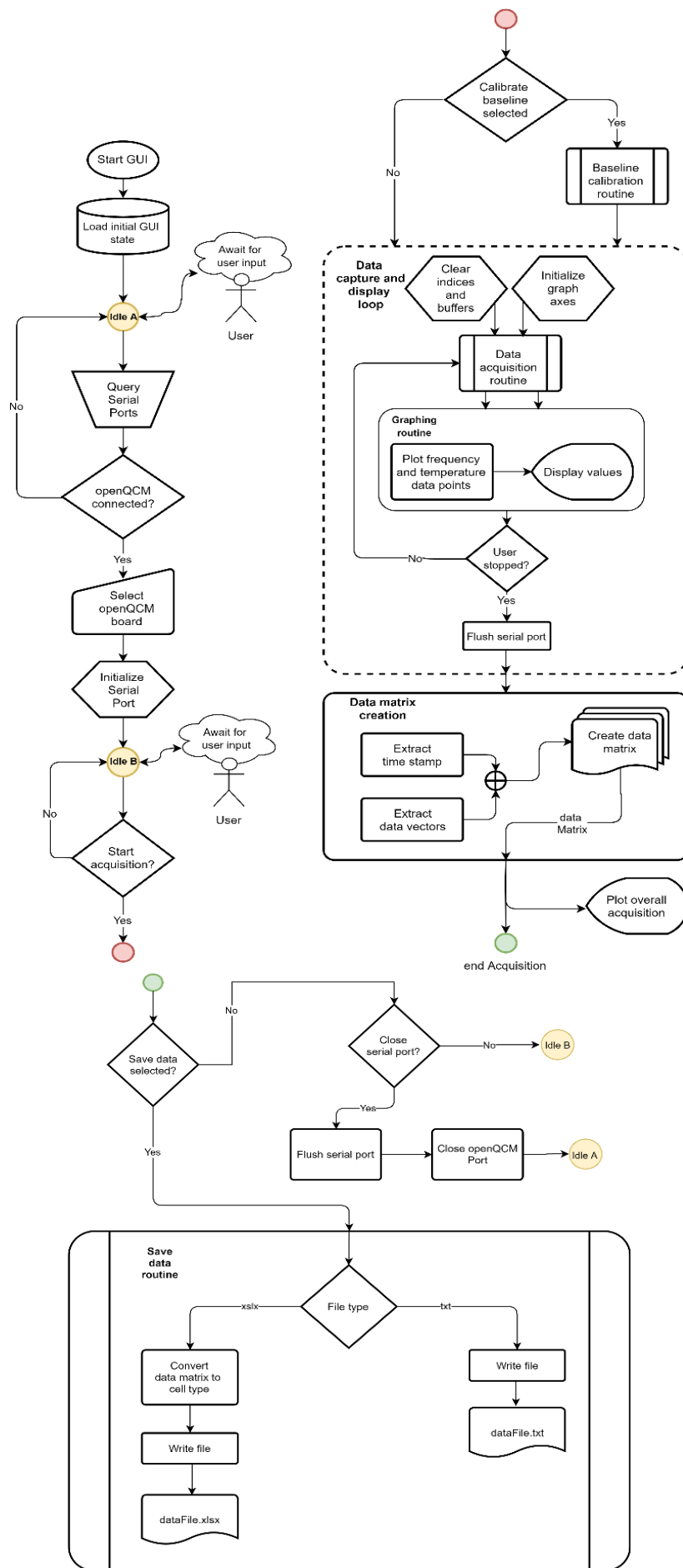
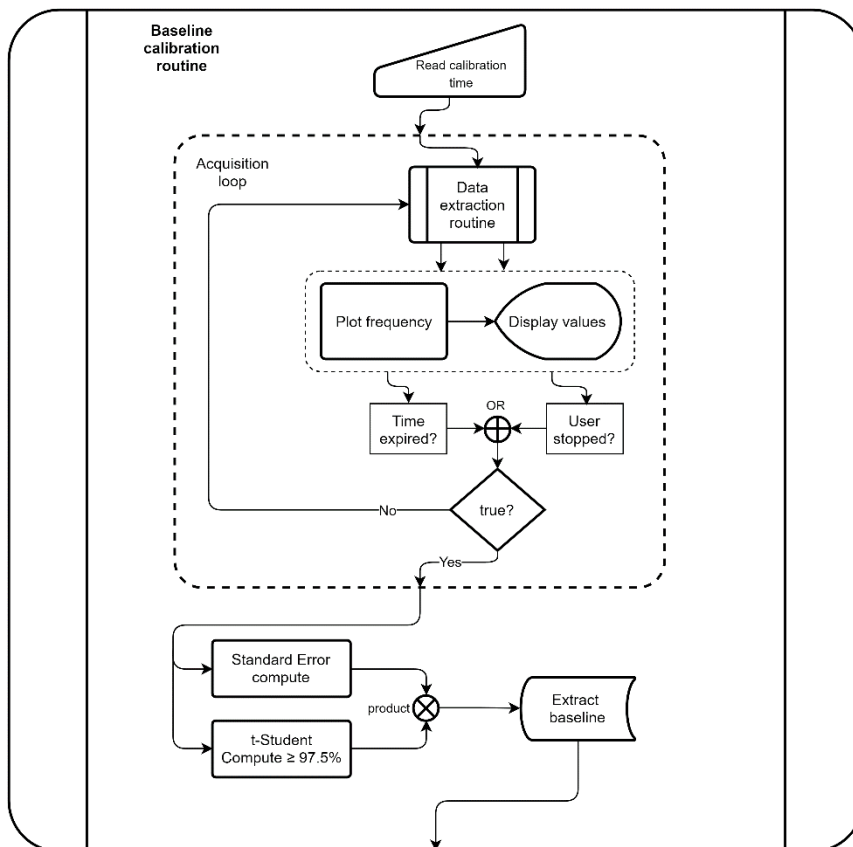
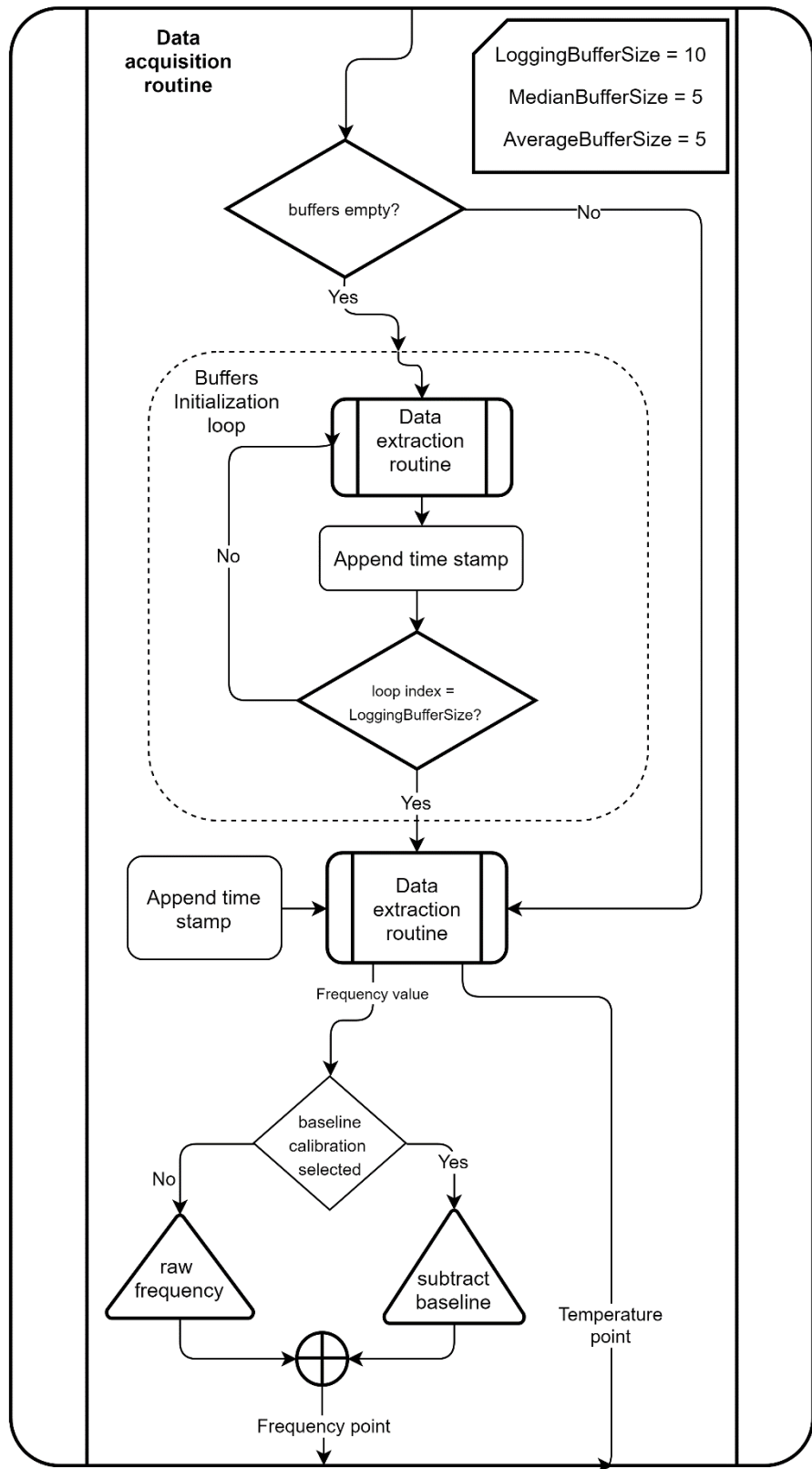


Fig. S4.6 Flow chart for the custom-made data acquisition GUI.



*Fig. S4.7 Baseline calibration routine subprocess*





**Fig. S4.8** Schematic of the data acquisition routine

#### 4.5. The PID control technique

This control technique is widely used in industrial, instrumentation and medical robotics applications due to its robust performance in a wide range of operating conditions. Its simplicity and ease of application on electronic devices ranging from high-end ASICs (e.g. FPGAs) to low-cost microcontrollers pose important advantages of this solution. A PID algorithm is based on an integrodifferential mathematical model consisting of three basic coefficients: proportional, integral and derivative which are varied to get the desired response. On a PID controller, a sensor connected to a closed loop system is read to then compute the desired actuator output by calculating the coefficients and summing them to obtain the output signal. In a closed loop system (**Fig. S4.9**) is the sensor itself the element that continuously provides the feedback signal to be compared in the input of the system with the desired setpoint obtaining then a resultant error signal. Finally, the actuator (i.e. heating element in this case) will be driven to accordingly adjust the desired response. In a PID system these parameters are directly affected by tuning the characteristic non-negative coefficients of a PID controller,  $K_p$ ,  $K_i$  and  $K_d$ , which represent the proportional, integral and derivative values, respectively (**Fig. S4.10**).

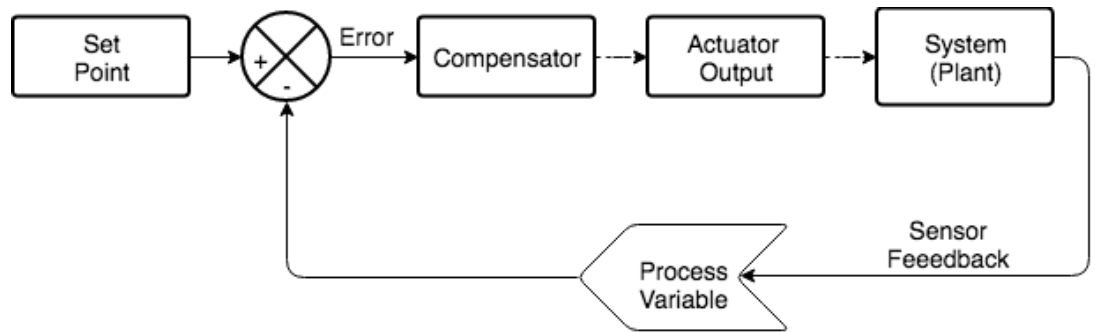
The role of each component of the output signal  $u(t)$  is briefly described as follows.

##### **Proportional Response**

This component depends only on the difference between the set point and the process variable. The proportional gain,  $K_p$ , determines the ratio of output response to the error signal  $e(t)$ . The magnitude of this value will have a strong impact on the stability of the system by making the output signal oscillate if its value is set too large. An adequate value should then increase only the speed of the control system response.

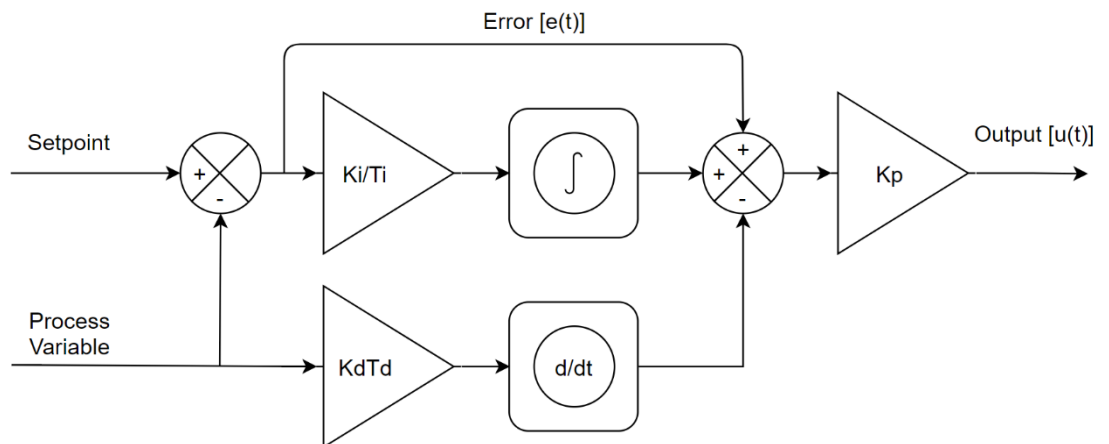
##### **Integral Response**

The integral component sums the error  $e(t)$  over the time the controller has been active. The integral value will continuously increase over time, unless the steady-state error is zero, which will produce a zero-integral response. Since component is keeps a record of past errors its main role is to minimize the steady-state error.



**Fig. S4.9** Block diagram for a closed loop system

$$u(t) = K_p e(t) + K_i \int_0^t e(t) dt + K_d \frac{de(t)}{dt}$$



**Fig. S4.10.** Mathematical expression for the PID control theory and its corresponding closed loop block diagram.  $T_i$  and  $T_d$  are the integration and derivative time, respectively.

### Derivative Response

The derivative value anticipates the future behavior of the error  $e(t)$  because the response of the derivative component is proportional to the change rate of the error. Therefore, the derivative action prevents the overshoot of the process variable and eliminates oscillations. Usually, the magnitude of  $K_d$  is low because the derivative response is highly sensitive to noise present on the signal of the process variable and in consequence the derivative component could make the control system unstable.

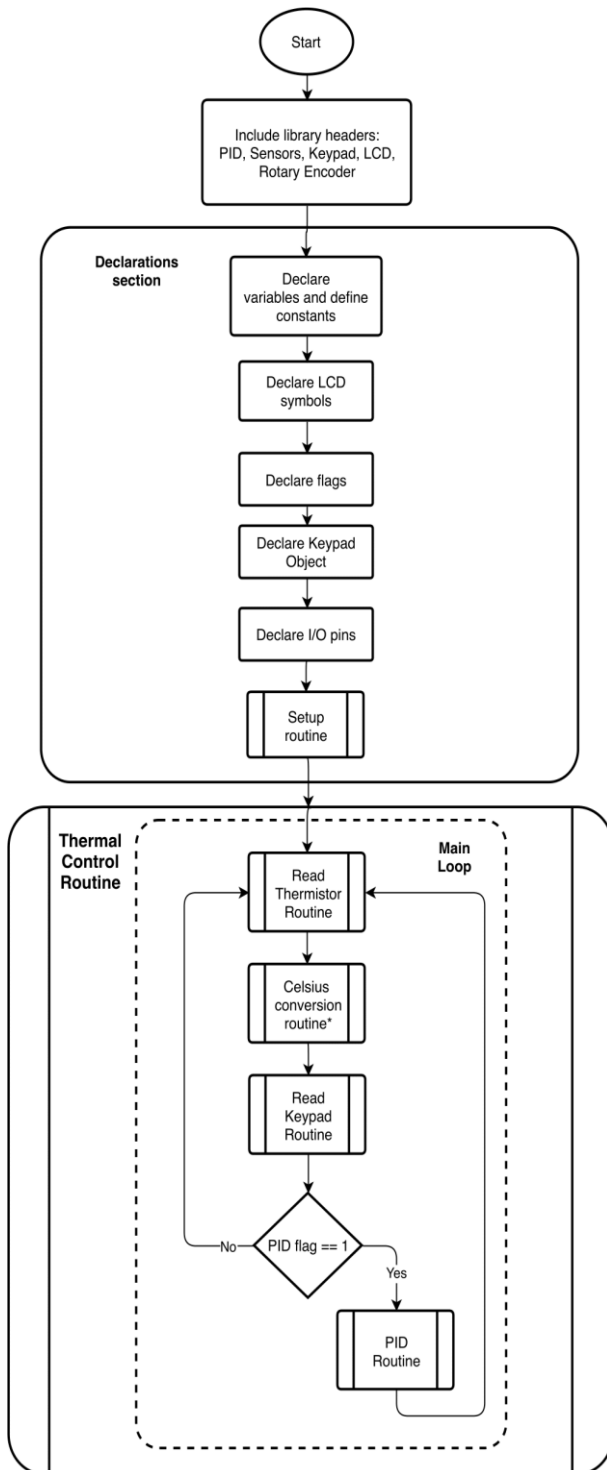
#### 4.6. Electronic PID control routines for the Peltier cell of the isothermal chamber

The core of the PID algorithm is based on a library originally developed by Brett Beauregard [344] and later ported to both the Arduino Code catalogue [345] and the library manager of the programming environment as the official PID control library for the Arduino development platform. The main body of the algorithm executed for the PID control of the Peltier cell is shown on **Fig. S4.11**. The routines marked with an (\*) are not included for the sake of simplicity.

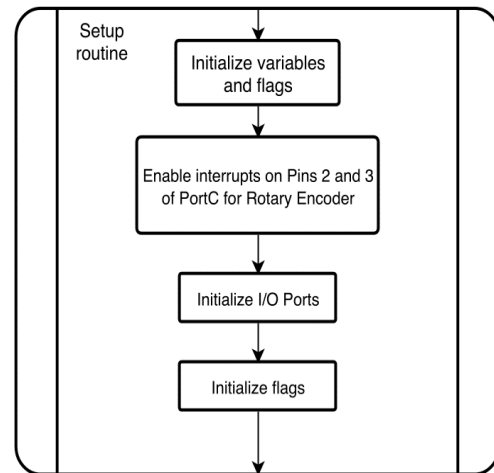
The thermal control routine was programmed in a loop that indefinitely monitors the temperature of the chamber, queries the input of the user via a frontal keypad and reads and updates the variables assigned to the routines. In this control structure the value of the thermistor is acquired in a self-contained routine (**Fig. S4.13**), then the returned value is converted to the Celsius scale and displayed on the LCD screen. The core of this algorithm is the PID routine (**Fig. S4.15**).

The range of the PID output value lies within a time window of 5 seconds (5000 ms), therefore the value of the PID output will be an activation time between 0 (lower limit) and 5000 (upper limit) and its magnitude will be a result of the computation and sum of each component of the PID expression from **Fig. S4.10**.

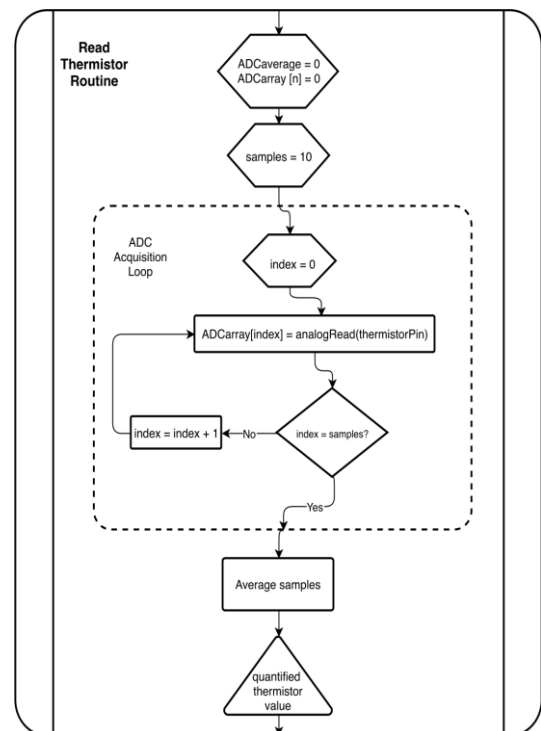
**Fig. S4.16** provides a graphical description of the activation process of the control signal from the PID controller. When the result of the PID computation is higher than the elapsed time the control signal changes from a LOW state to a HIGH state. Conversely, if the output of the PID is lower than the elapsed time, then the control signal changes to deactivate the Peltier cell. This method is analogous to the pulse width modulation (PWM) technique, in which by varying the duration of the pulses within a fixed period, the power delivered to a load can be adjusted according to the percentage of activation time of the control signal. **Fig. S4.17** shows possible activation percentages of a control signal. **Fig. S4.16b** exemplifies the timing scale for a specific activation process. After the starting point ( $t_0$ ) the signal changes from LOW to HIGH as the PID output value expressed the necessity of activation of the Peltier cell for a period of time  $t_d - t_a$ . When the length of the defined window size is reached, the algorithm adds another time period of equivalent length ( $t_0 + WS$ ) and continues the process. This timing and computing loop will run indefinitely until stopped by the user.



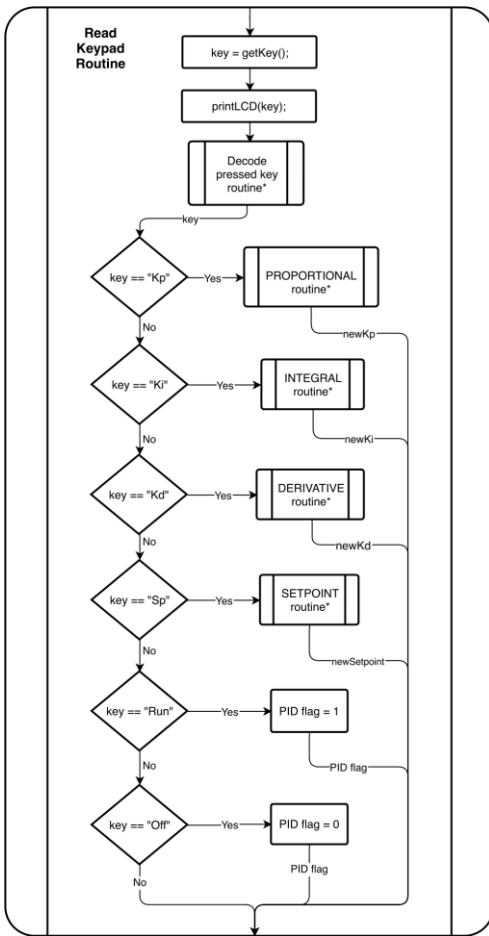
**Fig. S4.11** Complete PID algorithm implemented on the Arduino Microcontroller for controlling the temperature of the chamber.



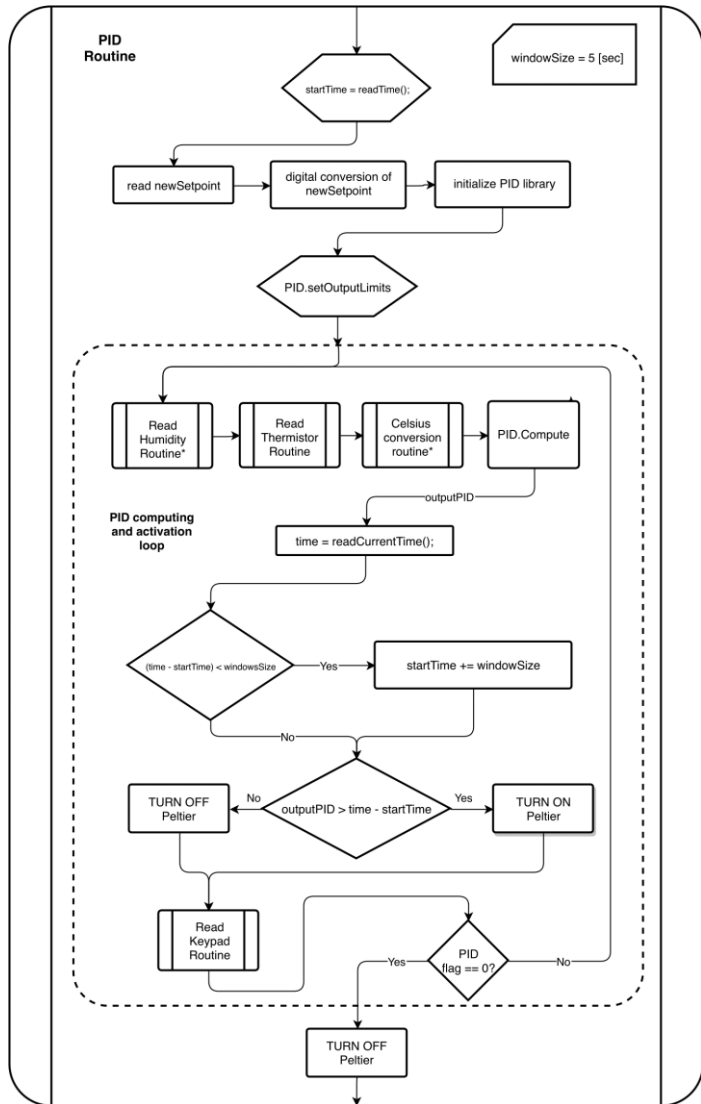
**Fig. S4.12** Setup routine for variables, flags and ports initialization. This routine runs only once.



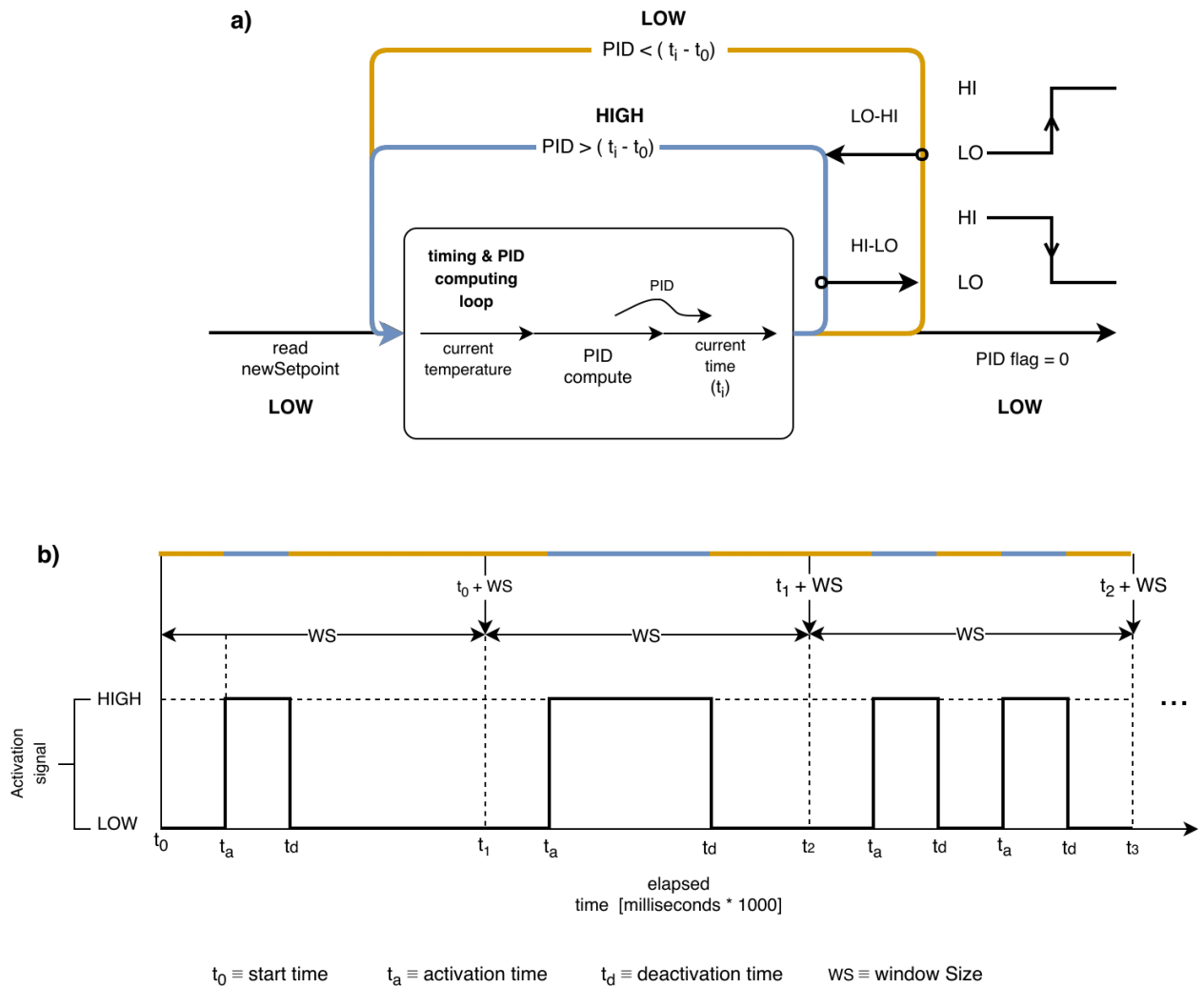
**Fig. S4.13** Routine for reading voltages from the NTC voltage divider attached to analog channel 0. Samples are averaged on each acquisition cycle.



**Fig. S4.14** Routine for reading the keyboard of the thermal control. Each subroutine returns the new value for the PID parameters. If the PID flag is active the control algorithm runs otherwise it stops.

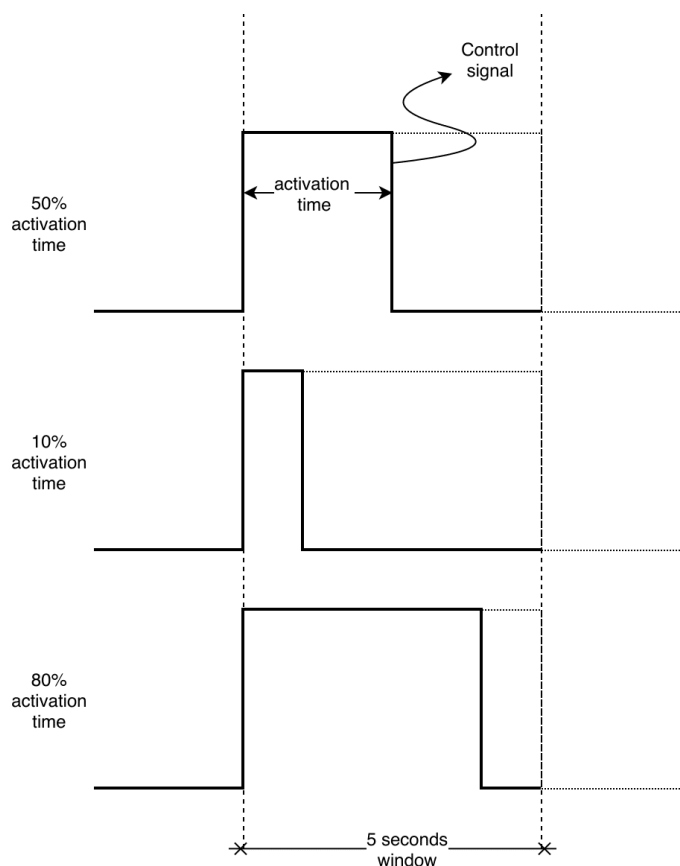


**Fig. S4.15** Full PID computing and Peltier activation routine. The output of the PID algorithm is an equivalent activation time within a window (period) of 5 seconds.



**Fig. S4.16** Schematic representation of a) continuous PID computing, signal activation conditions and edge change from LO-state to a HI-state b) Timing scheme example the activation and deactivation of the Peltier cell.

Finally, for its implementation on the selected microcontroller (**Fig. S4.3**), the room temperature ( $T_0$ ) was converted to the conventionally accepted value of 298.15 K (25 °C),  $\beta$  equals 3977 according to the value given by the manufacturer of the selected NTC with a nominal resistance value of  $10 \text{ k}\Omega \pm 0.5\%$ . The desired temperature is represented in Kelvin. The reference resistance at room temperature is expressed by a constant value. Finally, a precision reference resistor  $R_{REF}$  with a measured resistance of  $9999 \text{ }\Omega$  and a nominal tolerance of 0.1% was used.



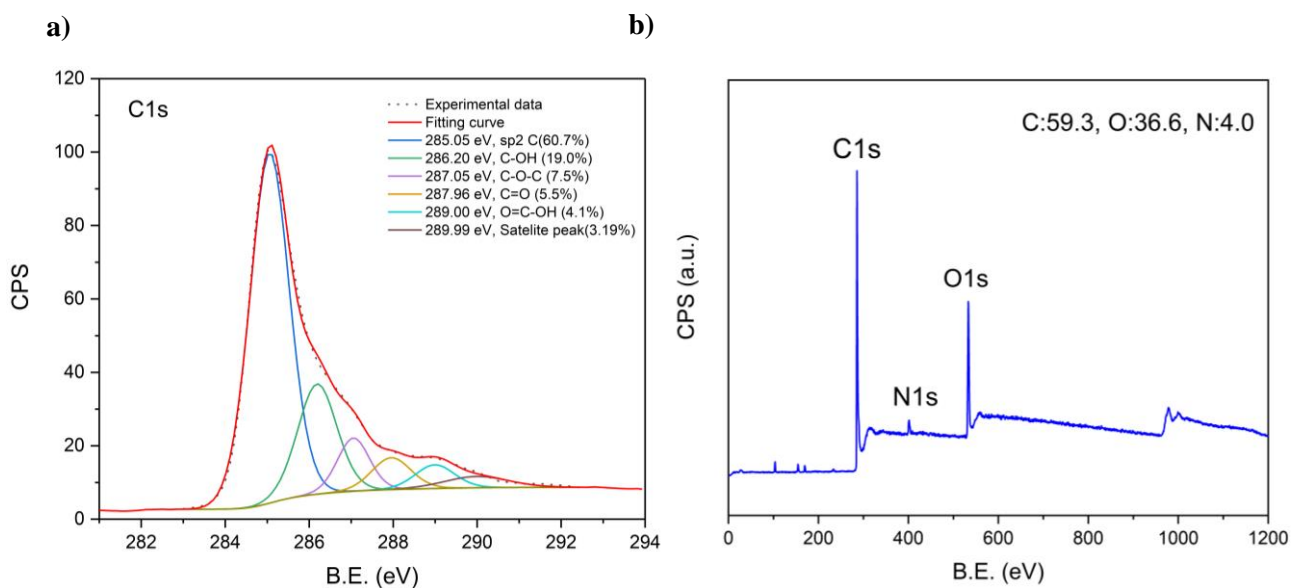
**Fig. S4.17** Possible activation states for a PWM signal of 5 seconds

#### 4.7. XPS Analysis

Combined ultimate resolution as measured from Ag 3D is 0.5eV with X-ray source and 20 eV pass. The XPS data processing was done using CasaXPS software (version 2.3.18) (**Fig. S4.12**). The calibration of C1 spectrum was performed using the sp<sup>3</sup> carbon (C-C, C-H) as reference at 284.8 eV peak position and the background type used was spline Tougaard. The C1s spectrum fitting (**Fig. S4.18a**) was performed using 7 synthetic components ascribed to different chemical species and a satellite peak, respectively. The sp<sup>2</sup> C component is represented by an asymmetric line shape of A(a,b,n) GL(p) type (CasaXPS version 2.3.18 Manual) where A(0.3,0.8,40) GL(45); the other synthetic components are represented by a symmetric line shape of GL(p) type where GL(30) (Gaussian/Lorentzian mix with 30% Lorentzian). The constrains applied where the FWHM constrain (0.9-1.1) and the position constrains (between max ±1eV to min ±0.1 eV). XPS C 1s region was fitted with the synthetic components in the manner which minimizes the total square error fit (0.91) and corresponds to the literature reports. In the case of rGO, it was impossible to distinguish between sp<sup>2</sup> and sp<sup>3</sup> carbons, therefore



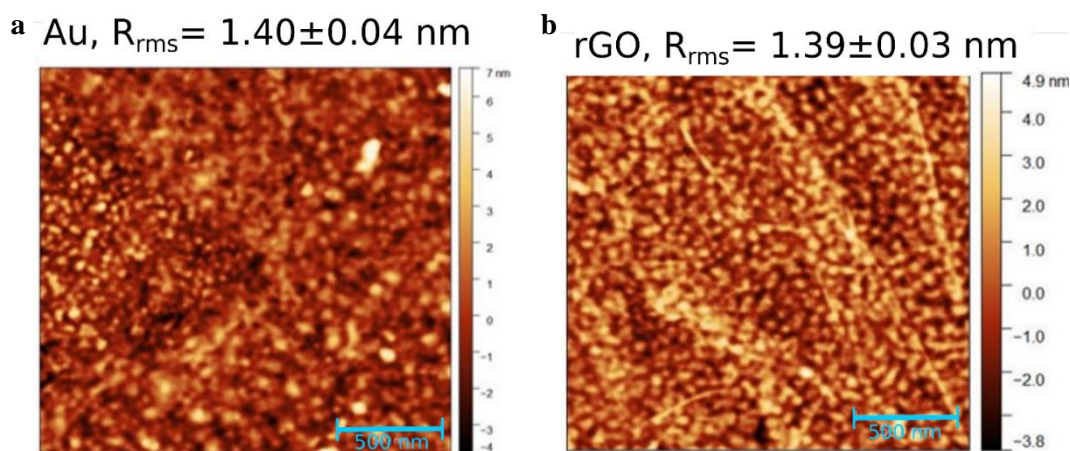
the signal was fitted with a single asymmetric component. **Fig. S4.18b** show the fitted peaks from widescan data.



**Fig. S4.18** XPS data for rGO films a) C1s peaks b) Widescan peaks fitting

#### 4.8. AFM topography

In accordance to the same coating procedure described in the main paper, the topography of bare Au and rGO-coated Quartz Pro QCM chips are presented in **Fig. S4.19**. Surface roughness for each sample was measured to assess its impact on protein adsorption. The  $R_{rms}$  values for all samples are statistically similar, at 1.4 nm, thus we infer that surface roughness should not have a major effect on the protein adsorption.



**Fig. S4.19** AFM profile from a) bare Au sensors and b) rGO-coated sensors. Scan area in all images is  $2 \mu\text{m}^2$ .

#### 4.9. Sauerbrey Model

Sauerbrey was the first who derived that the relationship between  $\Delta f$  and  $\Delta m$  is linear in the limit of small  $\Delta m$  and is expressed by a simple relationship,

$$\frac{\Delta f}{f_0} = -\frac{\Delta m}{m_Q} \quad (\text{Eq. S13})$$

where  $m_Q$  is the mass of the unloaded resonator. From Eq. S13 one can introduce the mass sensitivity factor  $C_r$ , and depends only on the fundamental resonant frequency  $f_0$  and the material properties of the crystal used [336].

Hence:

$$C_r = \frac{m_Q}{f_0} \quad (\text{Eq. S14})$$

where the mass of the resonator can be expressed as the product of the average density of quartz crystal,  $\rho_Q$  and its thickness  $h_Q$ . Thus,  $C_r$  can be expressed in terms of an appropriate dimensional analysis:

$$C_r = \frac{m_Q}{f_0} = \frac{\rho_Q h_Q}{f_0} = \frac{\left[ \frac{ng}{cm^3} \cdot cm \right]}{[Hz]} = [ngcm^{-2}Hz^{-1}] \quad (\text{Eq. S15})$$

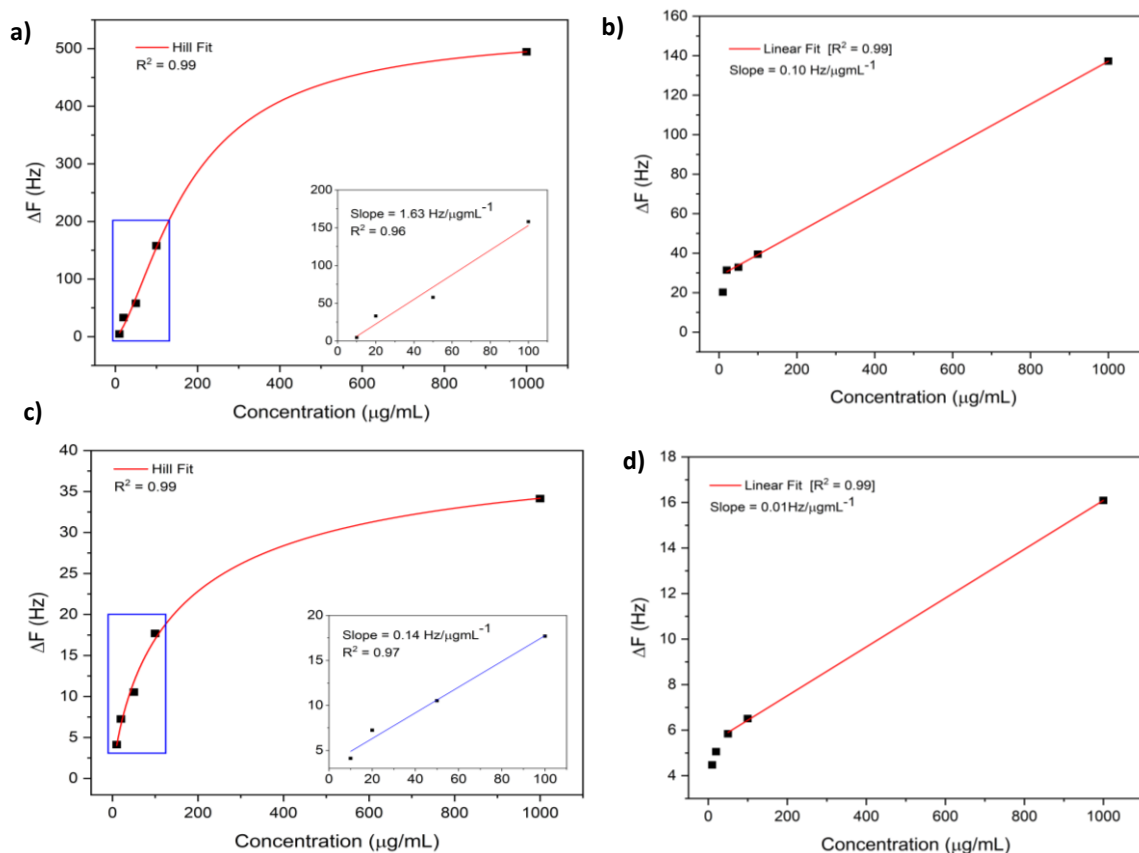
For 10 MHz quartz crystals,  $C_r$  equals  $4.5 ngcm^{-2}Hz^{-1}$  if only one side is covered [303]. For crystals with  $f_0 = 5$  MHz, the density is  $\rho_Q = 2.648 g/cm^3$  and the average thickness is  $h_Q \approx 300 \mu m$ , thus  $C_r \approx 18 ngcm^{-2}Hz^{-1}$ .

Assuming rigid adsorption to the substrate enables the use of Sauerbrey modelling to approximate the mass adsorbed on Au electrodes. To obtain the aerial mass density, the values captured for  $\Delta f$  can be plugged in the Sauerbrey equation (Eq. S13). Rearranging terms, we obtain.

$$\frac{\Delta m}{A} = -\frac{\sqrt{\rho_Q \mu_Q}}{2f_0^2} \Delta f \quad [g/cm^2] \quad (\text{Eq. S16})$$

where  $A = 0.2043 cm^2$ ,  $\mu_Q = 2.947 \times 10^{11} gcm^{-1}s^{-2}$  and  $f_0 = 10 MHz$  for the crystals used in all cQCM instrument experiments.

#### 4.10. Calibration curves



**Fig. S4.20** cQCM and QSense calibration curves. **a)** cQCM-Au response with Hill fitting. **b)** cQCM-rGO response and linear fit. **c)** QSense-Au response with Hill fitting. **d)** QSense-rGO response curve and linear fit. Inset plots **a)** and **c)** show the linear fits from the highlighted regions (rectangle)

## REFERENCES

- [1] KDE The Oxygen Team (<https://kde.org>), "Oxygen15.04.1-computer-laptop.svg." Free to copy under the GNU LGPLv3 (<http://www.gnu.org/copyleft/lesser.html>).
- [2] A. K. Geim and K. S. Novoselov, "The rise of graphene," *Nat. Mater.*, vol. 6, no. 3, pp. 183–191, 2007.
- [3] K. Wang *et al.*, "Biocompatibility of Graphene Oxide.," *Nanoscale Res. Lett.*, vol. 6, no. 1, p. 8, Dec. 2011.
- [4] S. Xu *et al.*, "Real-time reliable determination of binding kinetics of DNA hybridization using a multi-channel graphene biosensor," *Nat. Commun.*, vol. 8, p. 14902, 2017.
- [5] Y. Wang, Z. Li, J. Wang, J. Li, and Y. Lin, "Graphene and graphene oxide: biofunctionalization and applications in biotechnology," *Trends Biotechnol.*, vol. 29, no. 5, pp. 205–212, May 2011.
- [6] D. A. Melendrez *et al.*, "Adsorption and binding dynamics of graphene-supported phospholipid membranes using the QCM-D technique," *Nanoscale*, vol. 10, no. 5, pp. 2555–2567, 2018.
- [7] M. Hirtz, A. Oikonomou, T. Georgiou, H. Fuchs, and A. Vijayaraghavan, "Multiplexed biomimetic lipid membranes on graphene by dip-pen nanolithography," *Nat. Commun.*, vol. 4, no. 1, pp. 1–8, 2013.
- [8] W. Gao, "The Chemistry of Graphene Oxide," in *Graphene Oxide*, Cham: Springer International Publishing, 2015, pp. 61–95.
- [9] H. Liu and T. J. Webster, "Nanomedicine for implants: A review of studies and necessary experimental tools," *Biomaterials*, vol. 28, no. 2, pp. 354–369, Jan. 2007.
- [10] Q. He, S. Wu, Z. Yin, and H. Zhang, "Graphene-based electronic sensors," *Chem. Sci.*, vol. 3, no. 6, p. 1764, May 2012.
- [11] W. R. Sanhai, J. H. Sakamoto, R. Canady, and M. Ferrari, "Seven challenges for nanomedicine," *Nat. Nanotechnol.*, vol. 3, no. 5, pp. 242–244, May 2008.
- [12] Z. Li, M. He, D. Xu, and Z. Liu, "Graphene materials-based energy acceptor systems and sensors," *J. Photochem. Photobiol. C Photochem. Rev.*, vol. 18, pp. 1–17, Mar. 2014.
- [13] T. Krummel and T. Hannedouche, "Clinical potentials of adsorptive dialysis membranes.," *Blood Purif.*, vol. 35 Suppl 2, no. Suppl. 2, pp. 1–4, 2013.
- [14] W. Gao *et al.*, "A novel electrochemiluminescence ethanol biosensor based on tris(2,2'-bipyridine) ruthenium (II) and alcohol dehydrogenase immobilized in graphene/bovine serum albumin composite film," *Biosens. Bioelectron.*, vol. 41, pp. 776–782, 2013.
- [15] Y. L. Jeyachandran, E. Mielczarski, B. Rai, and J. A. Mielczarski, "Quantitative and qualitative evaluation of adsorption/desorption of bovine serum albumin on hydrophilic and hydrophobic surfaces," *Langmuir*, vol. 25, no. 19, pp. 11614–11620, 2009.
- [16] S. Hideshima, R. Sato, S. Inoue, S. Kuroiwa, and T. Osaka, "Detection of tumor marker in blood serum using antibody-modified field effect transistor with optimized BSA blocking," *Sensors Actuators, B Chem.*, vol. 161, no. 1, pp. 146–150, 2012.

- [17] M. Seredych, L. Mikhalovska, S. Mikhalovsky, and Y. Gogotsi, "Adsorption of Bovine Serum Albumin on Carbon-Based Materials," *C*, vol. 4, no. 1, p. 3, 2018.
- [18] B. Sengupta *et al.*, "Influence of carbon nanomaterial defects on the formation of protein corona," *RSC Adv.*, vol. 5, no. 100, pp. 82395–82402, 2015.
- [19] A. de Marco, "Recombinant expression of nanobodies and nanobody-derived immunoreagents," *Protein Expression and Purification*, vol. 172. Academic Press Inc., 01-Aug-2020.
- [20] S. Vigneshvar, C. C. Sudhakumari, B. Senthilkumaran, and H. Prakash, "Recent Advances in Biosensor Technology for Potential Applications – An Overview," *Front. Bioeng. Biotechnol.*, vol. 4, no. February, pp. 1–9, 2016.
- [21] "Biosensors Market Size, Growth, Share | Industry Analysis Report, 2020." [Online]. Available: <https://www.grandviewresearch.com/industry-analysis/biosensors-market/toc>. [Accessed: 14-Aug-2018].
- [22] V. Naresh and N. Lee, "A review on biosensors and recent development of nanostructured materials-enabled biosensors," *Sensors (Switzerland)*, vol. 21, no. 4, pp. 1–35, 2021.
- [23] L. Lan, Y. Yao, J. Ping, and Y. Ying, "Recent advances in nanomaterial-based biosensors for antibiotics detection," *Biosens. Bioelectron.*, vol. 91, pp. 504–514, May 2017.
- [24] B. D. Malhotra and M. A. Ali, "Nanomaterials in Biosensors: Fundamentals and Applications," *Nanomater. Biosens.*, p. 1, 2018.
- [25] F. De Leo, A. Magistrato, and D. Bonifazi, "Interfacing proteins with graphitic nanomaterials: from spontaneous attraction to tailored assemblies," *Chem. Soc. Rev.*, vol. 44, no. 19, pp. 6916–6953, Sep. 2015.
- [26] A. Ambrosi, C. K. Chua, A. Bonanni, and M. Pumera, "Electrochemistry of Graphene and Related Materials," *Chem. Rev.*, vol. 114, no. 14, pp. 7150–7188, Jul. 2014.
- [27] C. I. L. Justino, T. A. P. Rocha-Santos, S. Cardoso, A. C. Duarte, and S. Cardoso, "Strategies for enhancing the analytical performance of nanomaterial-based sensors," *TrAC Trends Anal. Chem.*, vol. 47, pp. 27–36, Jun. 2013.
- [28] S. Gul, S. B. Khan, I. U. Rehman, M. A. Khan, and M. I. Khan, "A Comprehensive Review of Magnetic Nanomaterials Modern Day Theranostics," *Front. Mater.*, vol. 6, p. 179, Jul. 2019.
- [29] A. P. F. Turner, "Biosensors: sense and sensibility," *Chem. Soc. Rev.*, vol. 42, no. 8, p. 3184, Apr. 2013.
- [30] Ö. Ertekin, S. Öztürk, and Z. Z. Öztürk, "Label Free QCM Immunobiosensor for AFB1 Detection Using Monoclonal IgA Antibody as Recognition Element," *Sensors 2016, Vol. 16, Page 1274*, vol. 16, no. 8, p. 1274, Aug. 2016.
- [31] B. Cai, S. Wang, L. Huang, Y. Ning, Z. Zhang, and G.-J. Zhang, "Ultrasensitive Label-Free Detection of PNA-DNA Hybridization by Reduced Graphene Oxide Field-Effect Transistor Biosensor," 2014.
- [32] Z. Huang *et al.*, "Simple and effective label-free electrochemical immunoassay for carbohydrate antigen 19-9 based on polythionine-Au composites as enhanced sensing signals for detecting different clinical samples," *Int. J. Nanomedicine*, vol. 12, pp. 3049–3058, Apr. 2017.

- [33] D. Xu, D. Xu, X. Yu, Z. Liu, W. He, and Z. Ma, "Label-free electrochemical detection for aptamer-based array electrodes," *Anal. Chem.*, vol. 77, no. 16, pp. 5107–5113, Aug. 2005.
- [34] P. Sun, Y. Jiang, G. Xie, X. Du, and J. Hu, "A room temperature supramolecular-based quartz crystal microbalance (QCM) methane gas sensor," *Sensors Actuators, B Chem.*, vol. 141, no. 1, pp. 104–108, 2009.
- [35] M. Kikuchi, K. Omori, and S. Shiratori, "Quartz crystal microbalance (QCM) sensor for ammonia gas using clay/polyelectrolyte layer-by-layer selfassembly film," in *Proceedings of IEEE Sensors, 2004.*, pp. 718–721.
- [36] H. Huang, J. Zhou, S. Chen, L. Zeng, and Y. Huang, "A highly sensitive QCM sensor coated with Ag<sup>+</sup>-ZSM-5 film for medical diagnosis," *Sensors Actuators, B Chem.*, vol. 101, no. 3, pp. 316–321, 2004.
- [37] T. Y. Lin, C. H. Hu, and T. C. Chou, "Determination of albumin concentration by MIP-QCM sensor," *Biosens. Bioelectron.*, vol. 20, no. 1, pp. 75–81, 2004.
- [38] Z. peng Yang and C. jing Zhang, "Designing of MIP-based QCM sensor for the determination of Cu(II) ions in solution," *Sensors Actuators, B Chem.*, vol. 142, no. 1, pp. 210–215, 2009.
- [39] A. Afzal *et al.*, "Gravimetric Viral Diagnostics: QCM Based Biosensors for Early Detection of Viruses," *Chemosensors*, vol. 5, no. 1, p. 7, Feb. 2017.
- [40] I. A. M. Frías, K. Y. P. S. Avelino, R. R. Silva, C. A. S. Andrade, and M. D. L. Oliveira, "Trends in Biosensors for HPV: Identification and Diagnosis," *J. Sensors*, vol. 2015, pp. 1–16, Sep. 2015.
- [41] P. Prakrankamanant *et al.*, "The development of DNA-based quartz crystal microbalance integrated with isothermal DNA amplification system for human papillomavirus type 58 detection," *Biosens. Bioelectron.*, vol. 40, no. 1, pp. 252–257, Feb. 2013.
- [42] S. K. Vashist and P. Vashist, "Recent advances in quartz crystal microbalance-based sensors," *J. Sensors*, vol. 2011, p. 571405, 2011.
- [43] Biolin Scientific, "Qsensor QSX 301 Gold."
- [44] "Digital microbalance - QCM200 - Stanford Research Systems." [Online]. Available: <https://www.directindustry.com/prod/stanford-research-systems/product-7218-54640.html>. [Accessed: 17-Dec-2021].
- [45] "Quartz Crystal Microbalance: the first scientific QCM entirely Open Source | About openQCM | Quartz Crystal Microbalance QCM-D with Dissipation Monitoring: the first scientific QCM entirely Open Source." [Online]. Available: <https://openqcm.com/openqcm>. [Accessed: 17-Dec-2021].
- [46] M. Kaisti, "Detection principles of biological and chemical FET sensors," *Biosens. Bioelectron.*, vol. 98, no. July, pp. 437–448, 2017.
- [47] M. Choudhary and K. Arora, "Chapter 8 - Electrochemical biosensors for early detection of cancer," R. Khan, A. Parihar, and S. K. B. T.-B. B. A. C. D. Sanghi, Eds. Academic Press, 2022, pp. 123–151.
- [48] A. Chaubey and B. D. Malhotra, "Mediated biosensors," *Biosens. Bioelectron.*, vol. 17, no. 6–7, pp. 441–456, Jun. 2002.

- [49] Y. Wang, H. Xu, J. Zhang, and G. Li, "Electrochemical Sensors for Clinic Analysis.," *Sensors (Basel)*, vol. 8, no. 4, pp. 2043–2081, Mar. 2008.
- [50] J. Lin and H. Ju, "Electrochemical and chemiluminescent immunosensors for tumor markers," *Biosens. Bioelectron.*, vol. 20, no. 8, pp. 1461–1470, Feb. 2005.
- [51] D. Manoj, I. Auddy, S. Nimbkar, S. Chittibabu, and S. Shanmugasundaram, "Development of Screen-Printed Electrode Biosensor for Rapid Determination of Triglyceride Content in Coconut Milk," *Int. J. Food Sci.*, vol. 2020, p. 1696201, 2020.
- [52] M. Pohanka, "Screen Printed Electrodes in Biosensors and Bioassays. A Review," *Int. J. Electrochem. Sci.*, vol. 15, pp. 11024–11035, Nov. 2020.
- [53] U. Tamer, A. İ. Seçkin, E. Temur, and H. Torul, "Fabrication of Biosensor Based on Polyaniline/Gold Nanorod Composite," *Int. J. Electrochem.*, vol. 2011, p. 869742, 2011.
- [54] R. Pei, Z. Cheng, E. Wang, and X. Yang, "Amplification of antigen–antibody interactions based on biotin labeled protein–streptavidin network complex using impedance spectroscopy," *Biosens. Bioelectron.*, vol. 16, no. 6, pp. 355–361, Aug. 2001.
- [55] M. Zhou, Y. Zhai, and S. Dong, "Electrochemical Sensing and Biosensing Platform Based on Chemically Reduced Graphene Oxide," *Anal. Chem.*, vol. 81, no. 14, pp. 5603–5613, Jul. 2009.
- [56] W.-J. Lin, C.-S. Liao, J.-H. Jhang, and Y.-C. Tsai, "Graphene modified basal and edge plane pyrolytic graphite electrodes for electrocatalytic oxidation of hydrogen peroxide and  $\beta$ -nicotinamide adenine dinucleotide," *Electrochem. commun.*, vol. 11, no. 11, pp. 2153–2156, Nov. 2009.
- [57] A. J. S. Ahammad, T. Islam, and M. M. Hasan, "Chapter 12 - Graphene-Based Electrochemical Sensors for Biomedical Applications," in *Micro and Nano Technologies*, M. Nurunnabi and J. R. B. T.-B. A. of G. and 2D N. McCarthy, Eds. Elsevier, 2019, pp. 249–282.
- [58] D. Grieshaber *et al.*, "Electrochemical Biosensors - Sensor Principles and Architectures," *Sensors*, vol. 8, no. 3, pp. 1400–1458, Mar. 2008.
- [59] A. Lerf, H. He, A. Michael Forster, and J. Klinowski, "Structure of Graphite Oxide Revisited," *Phys. Chem B*, vol. 102, no. 23, pp. 4477–4482, 1998.
- [60] C. Andronesco and W. Schuhmann, "Graphene-based field effect transistors as biosensors," *Curr. Opin. Electrochem.*, vol. 3, no. 1, pp. 11–17, 2017.
- [61] K. S. Kim *et al.*, "Highly sensitive and selective electrochemical cortisol sensor using bifunctional protein interlayer-modified graphene electrodes," *Sensors Actuators, B Chem.*, vol. 242, pp. 1121–1128, 2017.
- [62] J. Shi *et al.*, "A graphene oxide based fluorescence resonance energy transfer (FRET) biosensor for ultrasensitive detection of botulinum neurotoxin A (BoNT/A) enzymatic activity," *Biosens. Bioelectron.*, vol. 65, pp. 238–244, 2015.
- [63] A. Pattammattel and C. V. Kumar, "Kitchen Chemistry 101: Multigram Production of High Quality Biographene in a Blender with Edible Proteins," *Adv. Funct. Mater.*, vol. 25, no. 45, pp. 7088–7098, 2015.
- [64] I. W. Frank, D. M. Tanenbaum, A. M. van der Zande, and P. L. McEuen, "Mechanical properties of suspended graphene sheets," *J. Vac. Sci. Technol. B Microelectron. Nanom. Struct.*, vol. 25, no. 6, p. 2558, Dec. 2007.

- [65] P. Suvarnaphaet and S. Pechprasarn, "Graphene-based materials for biosensors: A review," *Sensors (Switzerland)*, vol. 17, no. 10, pp. 2161–2185, 2017.
- [66] D. A. Dikin *et al.*, "Preparation and characterization of graphene oxide paper," *Nature*, vol. 448, no. 7152, pp. 457–460, Jul. 2007.
- [67] Chemical Society (Great Britain), *Chemical Society reviews*. Royal Society of Chemistry, etc.].
- [68] D. W. Boukhvalov and M. I. Katsnelson, "Chemical functionalization of graphene," *J. Phys. Condens. Matter*, vol. 21, p. 12, 2009.
- [69] F. Perreault, A. Fonseca De Faria, and M. Elimelech, "Environmental applications of graphene-based nanomaterials," *Chem. Soc. Rev.*, vol. 44, no. 16, pp. 5861–5896, 2015.
- [70] S. Viswanathan *et al.*, "Graphene-protein field effect biosensors: Glucose sensing," *Mater. Today*, vol. 18, no. 9, pp. 513–522, 2015.
- [71] D. Li, W. Zhang, X. Yu, Z. Wang, Z. Su, and G. Wei, "When biomolecules meet graphene: From molecular level interactions to material design and applications," *Nanoscale*, vol. 8, no. 47, pp. 19491–19509, 2016.
- [72] C. McCallion, J. Burthem, K. Rees-Unwin, A. Golovanov, and A. Pluen, "Graphene in therapeutics delivery: Problems, solutions and future opportunities," *Eur. J. Pharm. Biopharm.*, vol. 104, pp. 235–250, 2016.
- [73] N. A. Hussien, N. Işıklan, and M. Türk, "Aptamer-functionalized magnetic graphene oxide nanocarrier for targeted drug delivery of paclitaxel," *Mater. Chem. Phys.*, vol. 211, pp. 479–488, 2018.
- [74] L. Zhang *et al.*, "High strength graphene oxide/polyvinyl alcohol composite hydrogels," *J. Mater. Chem.*, vol. 21, no. 28, pp. 10399–10406, Jul. 2011.
- [75] J. Berger, M. Reist, J. Mayer, O. Felt, R. G.-E. journal of, and undefined 2004, "Structure and interactions in chitosan hydrogels formed by complexation or aggregation for biomedical applications," *Elsevier*.
- [76] M. Hussain, F. Rupp, H. P. Wendel, and F. K. Gehring, "Bioapplications of acoustic crystals, a review," *TrAC Trends Anal. Chem.*, vol. 102, pp. 194–209, May 2018.
- [77] L. Zhang, J. Xia, Q. Zhao, L. Liu, and Z. Zhang, "Functional graphene oxide as a nanocarrier for controlled loading and targeted delivery of mixed anticancer drugs," *Small*, vol. 6, no. 4, pp. 537–544, Feb. 2010.
- [78] N. Willems *et al.*, "Biomimetic Phospholipid Membrane Organization on Graphene and Graphene Oxide Surfaces: A Molecular Dynamics Simulation Study," *ACS Nano*, vol. 11, no. 2, pp. 1613–1625, Feb. 2017.
- [79] M. Quintana, K. Spyrou, M. Grzelczak, W. R. Browne, P. Rudolf, and M. Prato, "Functionalization of graphene via 1,3-dipolar cycloaddition," *ACS Nano*, vol. 4, no. 6, pp. 3527–3533, Jun. 2010.
- [80] V. C. Sanchez, A. Jachak, R. H. Hurt, and A. B. Kane, "Biological Interactions of Graphene-Family Nanomaterials: An Interdisciplinary Review," *Chem. Res. Toxicol.*, vol. 25, no. 1, pp. 15–34, Jan. 2012.
- [81] N. Patra, B. Wang, and P. Král, "Nanodroplet Activated and Guided Folding of Graphene Nanostructures," *Nano Lett.*, vol. 9, no. 11, pp. 3766–3771, Nov. 2009.



- [82] E. P. Bellido and J. M. Seminario, "Molecular Dynamics Simulations of Folding of Supported Graphene," *J. Phys. Chem. C*, vol. 114, no. 51, pp. 22472–22477, Dec. 2010.
- [83] S. A. Hasan *et al.*, "Transferable Graphene Oxide Films with Tunable Microstructures," *ACS Nano*, vol. 4, no. 12, pp. 7367–7372, Dec. 2010.
- [84] A. Bagri, C. Mattevi, M. Acik, Y. J. Chabal, M. Chhowalla, and V. B. Shenoy, "Structural evolution during the reduction of chemically derived graphene oxide," *Nat. Chem.*, vol. 2, no. 7, pp. 581–587, Jul. 2010.
- [85] S. Kumar and S. H. Parekh, "Linking graphene-based material physicochemical properties with molecular adsorption, structure and cell fate," *Commun. Chem.*, vol. 3, no. 1, p. 8, 2020.
- [86] V. Georgakilas *et al.*, "Noncovalent Functionalization of Graphene and Graphene Oxide for Energy Materials, Biosensing, Catalytic, and Biomedical Applications," *Chem. Rev.*, vol. 116, no. 9, pp. 5464–5519, 2016.
- [87] M. Hassan, M. Walter, and M. Moseler, "Interactions of polymers with reduced graphene oxide: van der Waals binding energies of benzene on graphene with defects," *Phys. Chem. Chem. Phys.*, vol. 16, no. 1, pp. 33–37, Nov. 2013.
- [88] Y. Kamiya, K. Yamazaki, and T. Ogino, "Protein adsorption to graphene surfaces controlled by chemical modification of the substrate surfaces," *J. Colloid Interface Sci.*, vol. 431, pp. 77–81, Oct. 2014.
- [89] J. H. Park, T. N. Sut, J. A. Jackman, A. R. Ferhan, B. K. Yoon, and N. J. Cho, "Controlling adsorption and passivation properties of bovine serum albumin on silica surfaces by ionic strength modulation and cross-linking," *Phys. Chem. Chem. Phys.*, vol. 19, no. 13, pp. 8854–8865, 2017.
- [90] J. Liu *et al.*, "Understanding flocculation mechanism of graphene oxide for organic dyes from water: Experimental and molecular dynamics simulation," *AIP Adv.*, vol. 5, no. 11, 2015.
- [91] W.-R. Zhuang *et al.*, "Applications of  $\pi$ - $\pi$  stacking interactions in the design of drug-delivery systems," *J. Control. Release*, vol. 294, pp. 311–326, 2019.
- [92] H. Shen *et al.*, "PEGylated Graphene Oxide-Mediated Protein Delivery for Cell Function Regulation," *ACS Appl. Mater. Interfaces*, vol. 4, no. 11, pp. 6317–6323, Nov. 2012.
- [93] T. Chen, M. Li, and J. Liu, " $\pi$ - $\pi$  Stacking Interaction: A Nondestructive and Facile Means in Material Engineering for Bioapplications," *Cryst. Growth Des.*, vol. 18, no. 5, pp. 2765–2783, May 2018.
- [94] V. Georgakilas *et al.*, "Functionalization of Graphene: Covalent and Non-Covalent Approaches, Derivatives and Applications," *Chem. Rev.*, vol. 112, no. 11, pp. 6156–6214, Nov. 2012.
- [95] J. Shen *et al.*, "Covalent attaching protein to graphene oxide via diimide-activated amidation," *Colloids Surfaces B Biointerfaces*, vol. 81, no. 2, pp. 434–438, Dec. 2010.
- [96] C. Shan, H. Yang, D. Han, Q. Zhang, A. Ivaska, and L. Niu, "Water-Soluble Graphene Covalently Functionalized by Biocompatible Poly-L-lysine," *Langmuir*, vol. 25, no. 20, pp. 12030–12033, Oct. 2009.
- [97] H. Li *et al.*, "Spontaneous Protein Adsorption on Graphene Oxide Nanosheets Allowing Efficient Intracellular Vaccine Protein Delivery," *ACS Appl. Mater. Interfaces*, vol. 8, no.

2, pp. 1147–1155, Jan. 2016.

- [98] A. Heydari and H. Mansouri-Torshizi, "Design, synthesis, characterization, cytotoxicity, molecular docking and analysis of binding interactions of novel acetylacetonatopalladium( ii ) alanine and valine complexes with CT-DNA and BSA," *RSC Adv.*, vol. 6, no. 98, pp. 96121–96137, 2016.
- [99] M. L. Ferrer, R. Duchowicz, B. Carrasco, J. G. De La Torre, and A. U. Acuña, "The Conformation of Serum Albumin in Solution: A Combined Phosphorescence Depolarization-Hydrodynamic Modeling Study," *Biophys. J.*, vol. 80, no. 5, pp. 2422–2430, May 2001.
- [100] R. F. Atmeh, I. M. Arafa, and M. Al-Khateeb, "Albumin Aggregates: Hydrodynamic Shape and Physico-Chemical Properties," *Jordan J. Chem.*, vol. 2, no. 2, pp. 169–182, 2007.
- [101] A. K. Wright and M. R. Thompson, "Hydrodynamic structure of bovine serum albumin determined by transient electric birefringence," *Biophys. J.*, vol. 15, no. 2 Pt 1, pp. 137–141, Feb. 1975.
- [102] H. Durchschlag and P. Zipper, "Calculation of hydrodynamic parameters of biopolymers from scattering data using whole-body approaches," *Prog. Colloid Polym. Sci.*, vol. 107, pp. 43–57, 1997.
- [103] V. S. Raghuwanshi, B. Yu, C. Browne, and G. Garnier, "Reversible pH Responsive Bovine Serum Albumin Hydrogel Sponge Nanolayer," *Front. Bioeng. Biotechnol.*, vol. 8, p. 573, Jun. 2020.
- [104] X. M. He and D. C. Carter, "Atomic structure and chemistry of human serum albumin," *Nat. 1992 3586383*, vol. 358, no. 6383, pp. 209–215, Jul. 1992.
- [105] D. C. Carter and J. X. Ho, "Structure of Serum Albumin," *Adv. Protein Chem.*, vol. 45, no. C, pp. 153–203, Jan. 1994.
- [106] H. T. M. Phan, S. Bartelt-Hunt, K. B. Rodenhausen, M. Schubert, and J. C. Bartz, "Investigation of bovine serum albumin (BSA) attachment onto self-assembled monolayers (SAMs) using combinatorial quartz crystal microbalance with dissipation (QCM-D) and spectroscopic ellipsometry (SE)," *PLoS One*, vol. 10, no. 10, 2015.
- [107] M. Tencer, R. Charbonneau, N. Lahoud, and P. Berini, "AFM study of BSA adlayers on Au stripes," *Appl. Surf. Sci.*, vol. 253, no. 23, pp. 9209–9214, 2007.
- [108] T. Wangkam *et al.*, "Adsorption of bovine serum albumin (BSA) on polystyrene (PS) and its acid copolymer," *Curr. Appl. Phys.*, vol. 12, no. 1, pp. 44–52, Jan. 2012.
- [109] N. Dasgupta, S. Ranjan, D. Patra, P. Srivastava, A. Kumar, and C. Ramalingam, "Bovine serum albumin interacts with silver nanoparticles with a 'side-on' or 'end on' conformation," *Chem. Biol. Interact.*, vol. 253, pp. 100–111, Jun. 2016.
- [110] M. E. Wiseman and C. W. Frank, "Antibody adsorption and orientation on hydrophobic surfaces," *Langmuir*, vol. 28, no. 3, pp. 1765–1774, 2012.
- [111] M.-B. Gholivand, A. R. Jalalvand, and H. C. Goicoechea, "Developing a novel computationally designed impedimetric pregabalin biosensor," *Electrochim. Acta*, vol. 133, pp. 123–131, 2014.
- [112] M. M. Ouberai, K. Xu, and M. E. Welland, "Effect of the interplay between protein and surface on the properties of adsorbed protein layers," *Biomaterials*, vol. 35, no. 24, pp. 6157–6163, 2014.

- [113] J. G. G. Vilhena, P. Rubio-Pereda, P. Velloso, P. A. A. Serena, and R. Pérez, "Albumin (BSA) Adsorption over Graphene in Aqueous Environment: Influence of Orientation, Adsorption Protocol, and Solvent Treatment," *Langmuir*, vol. 32, no. 7, pp. 1742–1755, 2016.
- [114] F. Yilmaz, Y. Saylan, A. Derazshamzir, S. Atay, and A. Denizli, "Quartz Crystal Microbalance Based Hydrophobic Nanosensor for Lysozyme Detection," *World Acad. Sci. Eng. Technol. Int. J. Chem. Mol. Nucl. Mater. Metall. Eng.*, vol. 9, no. 3, pp. 451–454, 2015.
- [115] S. Y. Tan and Y. Tatsumura, "Alexander Fleming (1881–1955): Discoverer of penicillin," *Singapore Med. J.*, vol. 56, no. 7, pp. 366–367, 2015.
- [116] D. Goodsell, "Structure of Lysozyme," *Molecule of the month*, 2000. .
- [117] N. C. J. Strynadka and M. N. G. James, "Lysozyme revisited: crystallographic evidence for distortion of an N-acetylmuramic acid residue bound in site D," *J. Mol. Biol.*, vol. 220, no. 2, pp. 401–424, Jul. 1991.
- [118] G. Sener, E. Ozgur, E. Yilmaz, L. Uzun, R. Say, and A. Denizli, "Quartz crystal microbalance based nanosensor for lysozyme detection with lysozyme imprinted nanoparticles," *Biosens. Bioelectron.*, vol. 26, no. 2, pp. 815–821, 2010.
- [119] D. R. Davies and G. H. Cohen, "Interactions of protein antigens with antibodies," *Proc. Natl. Acad. Sci. U. S. A.*, vol. 93, no. 1, pp. 7–12, 1996.
- [120] A. K. H. Cheng, B. Ge, and H. Z. Yu, "Aptamer-based biosensors for label-free voltammetric detection of lysozyme," *Anal. Chem.*, vol. 79, no. 14, pp. 5158–5164, Jul. 2007.
- [121] C. Chothia *et al.*, "Conformations of immunoglobulin hypervariable regions," *Nature*, vol. 342, no. 6252, pp. 877–883, 1989.
- [122] K. A. Xavier and R. C. Willson, "Association and Dissociation Kinetics of Anti-Hen Egg Lysozyme Monoclonal Antibodies HyHEL-5 and HyHEL-10," *Biophys. J.*, vol. 74, no. 4, pp. 2036–2045, Apr. 1998.
- [123] M. R. J. Salton, "THE PROPERTIES OF LYSOZYME AND ITS ACTION ON MICROORGANISMS."
- [124] M. S. Weiss, G. J. Palm, and R. Hilgenfeld, "Crystallization, structure solution and refinement of hen egg-white lysozyme at pH 8.0 in the presence of MPD," *Acta Crystallogr. Sect. D Biol. Crystallogr.*, vol. 56, no. 8, pp. 952–958, 2000.
- [125] "Proteins: 6.3 Lysozyme - OpenLearn - Open University - S377\_2." [Online]. Available: <https://www.open.edu/openlearn/science-maths-technology/science/biology/proteins/content-section-6.3>. [Accessed: 15-Jan-2022].
- [126] V. B. Abdul-Salam *et al.*, "Identification and assessment of plasma lysozyme as a putative biomarker of atherosclerosis," *Arterioscler. Thromb. Vasc. Biol.*, vol. 30, no. 5, pp. 1027–1033, 2010.
- [127] C. Serra *et al.*, "Expression and prognostic significance of lysozyme in male breast cancer," *Breast Cancer Res.*, vol. 4, no. 6, p. R16, Dec. 2002.
- [128] H. Tomita *et al.*, "Serum lysozyme levels and clinical features of sarcoidosis," *Lung*, vol. 177, no. 3, pp. 161–167, 1999.

- [129] D. Santoriello, L. M. Andal, R. Cox, V. D. D'Agati, and G. S. Markowitz, "Lysozyme-Induced Nephropathy," *Kidney Int. Reports*, vol. 2, no. 1, pp. 84–88, Jan. 2017.
- [130] H. I. Glueck, M. R. MacKenzie, and C. J. Glueck, "Crystalline IgG protein in multiple myeloma: Identification effects on coagulation and on lipoprotein metabolism," *J. Lab. Clin. Med.*, vol. 79, no. 5, pp. 731–744, May 1972.
- [131] E. E. Perez *et al.*, "Update on the use of immunoglobulin in human disease: A review of evidence," *J. Allergy Clin. Immunol.*, vol. 139, no. 3, pp. S1–S46, 2017.
- [132] B. Mietzner *et al.*, "Autoreactive IgG memory antibodies in patients with systemic lupus erythematosus arise from nonreactive and polyreactive precursors," *Proc. Natl. Acad. Sci. U. S. A.*, vol. 105, no. 28, pp. 9727–9732, Jul. 2008.
- [133] I. N. Van Schaik *et al.*, "European Federation of Neurological Societies/Peripheral Nerve Society Guideline on management of multifocal motor neuropathy. Report of a Joint Task Force of the European Federation of Neurological Societies and the Peripheral Nerve Society - first revis," *J. Peripher. Nerv. Syst.*, vol. 15, no. 4, pp. 295–301, Dec. 2010.
- [134] R. Hughes, "The role of IVIg in autoimmune neuropathies: The latest evidence," in *Journal of Neurology*, 2008, vol. 255, no. SUPPL.3, pp. 7–11.
- [135] C. J. van Oss, R. J. Good, and M. K. Chaudhury, "Nature of the antigen-antibody interaction: Primary and secondary bonds: Optimal conditions for association and dissociation," *J. Chromatogr. B Biomed. Sci. Appl.*, vol. 376, no. C, pp. 111–119, Apr. 1986.
- [136] B. Armstrong, "Antigen-antibody reactions," *ISBT Sci. Ser.*, vol. 3, no. 2, pp. 21–32, Jun. 2008.
- [137] R. Porrozzi, A. Teva, V. F. Amaral, M. V. Santos Da Costa, and G. Grimaldi, "Cross-immunity experiments between different species or strains of *Leishmania* in rhesus macaques (*Macaca mulatta*)," *Am. J. Trop. Med. Hyg.*, vol. 71, no. 3, pp. 297–305, Sep. 2004.
- [138] M. Mandelboim *et al.*, "Significant cross reactive antibodies to influenza virus in adults and children during a period of marked antigenic drift," *BMC Infect. Dis.*, vol. 14, no. 1, p. 346, Jun. 2014.
- [139] V. Kasproicz *et al.*, "Defining the directionality and quality of influenza virus-specific CD8+ T cell cross-reactivity in individuals infected with hepatitis C virus," *J. Clin. Invest.*, vol. 118, no. 3, pp. 1143–1153, 2008.
- [140] C. Cornaby, L. Gibbons, V. Mayhew, C. S. Sloan, A. Welling, and B. D. Poole, "B cell epitope spreading: Mechanisms and contribution to autoimmune diseases," *Immunology Letters*, vol. 163, no. 1. Elsevier B.V., pp. 56–68, 01-Jan-2015.
- [141] K. Imkeller and H. Wardemann, "Assessing human B cell repertoire diversity and convergence," *Immunol. Rev.*, vol. 284, no. 1, pp. 51–66, Jul. 2018.
- [142] E. Cozzani, M. Drosera, G. Gasparini, and A. Parodi, "Serology of lupus erythematosus: Correlation between immunopathological features and clinical aspects," *Autoimmune Diseases*, vol. 2014. 2014.
- [143] C. Castro and M. Gourley, "Diagnostic testing and interpretation of tests for autoimmunity," *J. Allergy Clin. Immunol.*, vol. 125, no. 2 SUPPL. 2, pp. S238–S247, Feb.

2010.

- [144] B. Huang *et al.*, “A novel Time-resolved Fluoroimmunoassay for the quantitative detection of Antibodies against the Phospholipase A2 Receptor,” *Sci. Rep.*, vol. 7, no. March, pp. 1–8, 2017.
- [145] M. Fresquet *et al.*, “Identification of a major epitope recognized by PLA2R autoantibodies in primary membranous nephropathy,” *J. Am. Soc. Nephrol.*, vol. 26, no. 2, pp. 302–313, 2015.
- [146] M. Fresquet *et al.*, “PLA2R binds to the annexin A2-S100A10 complex in human podocytes,” *Sci. Rep.*, vol. 7, no. 1, pp. 1–11, 2017.
- [147] R. J. Glassock, “The Pathogenesis of Idiopathic Membranous Nephropathy: A 50-Year Odyssey,” *Am. J. Kidney Dis.*, vol. 56, no. 1, pp. 157–167, Jul. 2010.
- [148] J. B. Hanko, R. N. Mullan, D. M. O’Rourke, P. T. McNamee, A. P. Maxwell, and A. E. Courtney, “The changing pattern of adult primary glomerular disease,” *Nephrol. Dial. Transplant.*, vol. 24, no. 10, pp. 3050–3054, Oct. 2009.
- [149] W. Qin *et al.*, “Anti-Phospholipase A2 Receptor Antibody in Membranous Nephropathy,” *J. Am. Soc. Nephrol.*, vol. 22, no. 6, pp. 1137–1143, Jun. 2011.
- [150] M. Waldman and H. A. A. III, “Controversies in the treatment of idiopathic membranous nephropathy,” *Nat. Rev. Nephrol.*, vol. 5, no. 8, p. 469, 2009.
- [151] A. McGrogan, C. F. M. Franssen, and C. S. de Vries, “The incidence of primary glomerulonephritis worldwide: a systematic review of the literature,” *Nephrol. Dial. Transplant.*, vol. 26, no. 2, pp. 414–430, Feb. 2011.
- [152] C. Ponticelli, “Membranous nephropathy,” *J. Nephrol.*, vol. 20, no. 3, pp. 268–87, 1997.
- [153] S. Muyldermans, T. Atarhouch, J. Saldanha, J. A. R. G. Barbosa, and R. Hamers, “Sequence and structure of VH domain from naturally occurring camel heavy chain immunoglobulins lacking light chains,” *Protein Eng.*, vol. 7, no. 9, pp. 1129–1135, Sep. 1994.
- [154] S. Muyldermans, “Nanobodies: Natural single-domain antibodies,” *Annu. Rev. Biochem.*, vol. 82, pp. 775–797, 2013.
- [155] A. Monegal *et al.*, “Immunological applications of single-domain llama recombinant antibodies isolated from a naïve library,” *Protein Eng. Des. Sel.*, vol. 22, no. 4, pp. 273–280, Apr. 2009.
- [156] V. J. Hruby, “Biologically active peptides: Design, synthesis and utilization,” *Trends Biotechnol.*, vol. 12, no. 3, pp. 104–105, Mar. 1994.
- [157] D. Schumacher, J. Onas Helma, A. F. L. Schneider, and C. P. R. Hackenberger, “Nanobodies: Chemical Functionalization Strategies and Intracellular Applications.”
- [158] S. Muyldermans, “Applications of Nanobodies,” *Annu. Rev. Anim. Biosci.*, vol. 9, no. 1, pp. 401–421, Feb. 2021.
- [159] M. Liu, L. Li, D. Jin, and Y. Liu, “Nanobody—A versatile tool for cancer diagnosis and therapeutics,” *Wiley Interdisciplinary Reviews: Nanomedicine and Nanobiotechnology*. Wiley-Blackwell, 2021.
- [160] G. Hassanzadeh-Ghassabeh, N. Devoogdt, P. De Pauw, C. Vincke, and S. Muyldermans,

- "Nanobodies and their potential applications," *Nanomedicine*, vol. 8, no. 6. Future Medicine Ltd., pp. 1013–1026, 04-Jun-2013.
- [161] J. Fares, D. Kanojia, A. Rashidi, A. U. Ahmed, I. V. Balyasnikova, and M. S. Lesniak, "Diagnostic Clinical Trials in Breast Cancer Brain Metastases: Barriers and Innovations," *Clinical Breast Cancer*, vol. 19, no. 6. Elsevier Inc., pp. 383–391, 01-Dec-2019.
- [162] I. J. G. Burvenich *et al.*, "Molecular imaging of T cell co-regulator factor B7-H3 with 89Zr-DS-5573a," *Theranostics*, vol. 8, no. 15, pp. 4199–4209, 2018.
- [163] C. Xavier *et al.*, "Synthesis, preclinical validation, dosimetry, and toxicity of 68Ga-NOTA-anti-HER2 nanobodies for iPET imaging of HER2 receptor expression in cancer," *J. Nucl. Med.*, vol. 54, no. 5, pp. 776–784, May 2013.
- [164] Y. Xiang *et al.*, "Versatile and multivalent nanobodies efficiently neutralize SARS-CoV-2," *Science (80-. )*, vol. 370, no. 6523, pp. 1479–1484, Dec. 2021.
- [165] L. I. Ibañez *et al.*, "Nanobodies with in vitro neutralizing activity protect mice against H5N1 influenza virus infection," *J. Infect. Dis.*, vol. 203, no. 8, pp. 1063–1072, Apr. 2011.
- [166] T. Fang *et al.*, "Targeted antigen delivery by an anti-class II MHC VHH elicits focused  $\alpha$ UC1(Tn) immunity," *Chem. Sci.*, vol. 8, no. 8, pp. 5591–5597, 2017.
- [167] M. Rudh, "The Sauerbrey Relation," *Development*, vol. 2, no. 3, p. 2, 2006.
- [168] Biolin Scientific, "Q-Sense Analyser - ATA Scientific." [Online]. Available: <https://www.atascientific.com.au/products/q-sense-analyser/>. [Accessed: 17-Oct-2021].
- [169] M. V. Voinova, M. Rodahl, M. Jonson, and B. Kasemo, "Viscoelastic acoustic response of layered polymer films at fluid-solid interfaces: Continuum mechanics approach," *Phys. Scr.*, vol. 59, no. 5, p. 391, 1998.
- [170] Y. A. Cheon, J. H. Bae, and B. G. Chung, "Reduced Graphene Oxide Nanosheet for Chemo-photothermal Therapy," *Langmuir*, vol. 32, no. 11, pp. 2731–2736, 2016.
- [171] L. M. Pandey, S. K. Pattanayek, and D. Delabouglise, "Properties of adsorbed bovine serum albumin and fibrinogen on self-assembled monolayers," *J. Phys. Chem. C*, vol. 117, no. 12, pp. 6151–6160, 2013.
- [172] F. Taherian, V. Marcon, N. F. A. Van Der Vegt, F. Fr  d  , and F. Leroy, "What Is the Contact Angle of Water on Graphene?," 2013.
- [173] N. Yang *et al.*, "Effect of Graphene-Graphene Oxide Modified Anode on the Performance of Microbial Fuel Cell," *Nanomaterials*, vol. 6, no. 9, p. 174, Sep. 2016.
- [174] P. Nemes-Incze, Z. Osv  th, K. Kamar  s, and L. P. Bir  , "Anomalies in thickness measurements of graphene and few layer graphite crystals by tapping mode atomic force microscopy," *Carbon N. Y.*, vol. 46, no. 11, pp. 1435–1442, 2008.
- [175] C. J. Shearer, A. D. Slattery, A. J. Stapleton, J. G. Shapter, and C. T. Gibson, "Accurate thickness measurement of graphene," *Nanotechnology*, vol. 27, no. 12, p. 125704, 2016.
- [176] K. S. Novoselov *et al.*, "Electric field effect in atomically thin carbon films," *Science (80-. )*, vol. 306, no. 5696, pp. 666–669, 2004.
- [177] G. Shao, Y. Lu, F. Wu, C. Yang, F. Zeng, and Q. Wu, "Graphene oxide: The mechanisms of

- oxidation and exfoliation," *J. Mater. Sci.*, vol. 47, no. 10, pp. 4400–4409, 2012.
- [178] Y. Okamoto, K. Tsuzuki, S. Iwasa, R. Ishikawa, A. Sandhu, and R. Tero, "Fabrication of Supported Lipid Bilayer on Graphene Oxide," in *Journal of Physics: Conference Series*, 2012, vol. 352, no. 1, p. 012017.
- [179] A. Aliano *et al.*, "AFM in Liquids," *Encycl. Nanotechnol.*, pp. 83–89, 2012.
- [180] M. T. Hwang *et al.*, "Highly specific SNP detection using 2D graphene electronics and DNA strand displacement," *Proc. Natl. Acad. Sci.*, vol. 113, no. 26, pp. 7088–7093, Jun. 2016.
- [181] Y. L. Lyubchenko, L. S. Shlyakhtenko, and T. Ando, "Imaging of nucleic acids with atomic force microscopy," *Methods*, vol. 54, no. 2, pp. 274–283, Jun-2011.
- [182] H. G. Hansma *et al.*, "Reproducible imaging and dissection of plasmid DNA under liquid with the atomic force microscope," *Science (80-. )*, vol. 256, no. 5060, pp. 1180–1184, 1992.
- [183] J. Mou, J. Yang, and Z. Shao, "Atomic force microscopy of cholera toxin B-oligomers bound to bilayers of biologically relevant lipids," *Journal of Molecular Biology*, vol. 248, no. 3, pp. 507–512, 05-May-1995.
- [184] E. Henderson, P. G. Haydon, and D. S. Sakaguchi, "Actin filament dynamics in living glial cells imaged by atomic force microscopy," *Science (80-. )*, vol. 257, no. 5078, pp. 1944–1946, 1992.
- [185] M. Acik *et al.*, "The Role of Oxygen during Thermal Reduction of Graphene Oxide Studied by Infrared Absorption Spectroscopy," *J. Phys. Chem. C*, vol. 115, no. 40, pp. 19761–19781, Oct. 2011.
- [186] M. R. L. Cody V. Cushman, Shiladitya Chatterjee, George H. Major, Nicholas J. Smith, Adam Roberts, "Trends in Advanced XPS Instrumentation. 1. Overview of the Technique, Automation, High Sensitivity, Imaging, Snapshot Spectroscopy, Gas Cluster Ion Beams, and Multiple Analytical Techniques on the Instrument," *Vac. Technol. Coat.*, no. November, pp. 1–9, 2016.
- [187] J. T. Titantah and D. Lamoen, "Carbon and nitrogen 1s energy levels in amorphous carbon nitride systems: XPS interpretation using first-principles," *Diam. Relat. Mater.*, vol. 16, no. 3, pp. 581–588, 2007.
- [188] V. Jain, M. C. Biesinger, and M. R. Linford, "The Gaussian-Lorentzian Sum, Product, and Convolution (Voigt) functions in the context of peak fitting X-ray photoelectron spectroscopy (XPS) narrow scans," *Appl. Surf. Sci.*, vol. 447, pp. 548–553, 2018.
- [189] T. Susi, T. Pichler, and P. Ayala, "X-ray photoelectron spectroscopy of graphitic carbon nanomaterials doped with heteroatoms," *Beilstein J. Nanotechnol.*, vol. 6, no. 1, pp. 177–192, 2015.
- [190] "Art of curve fitting or black magic of curve fitting spectra." .
- [191] "XPS Fitting on Adventitious Carbon," *XPS Fitting*, 2019. .
- [192] Thermo Scientific, "Adventitious Carbon Contamination," *XPS Simplified*, 2019. .
- [193] A. Ganguly, S. Sharma, P. Papakonstantinou, and J. Hamilton, "Probing the thermal deoxygenation of graphene oxide using high-resolution in situ X-ray-based spectroscopies," *J. Phys. Chem. C*, vol. 115, no. 34, pp. 17009–17019, 2011.

- [194] A. C. Ferrari and J. Robertson, "Raman spectroscopy in carbons: from nanotubes to diamond," *R. Soc.*, 2004.
- [195] A. C. Ferrari, "Raman spectroscopy of graphene and graphite: disorder, electron-phonon coupling, doping and nonadiabatic effects," *Solid State Commun.*, vol. 143, no. 1, pp. 47–57, 2007.
- [196] A. C. Ferrari *et al.*, "Raman spectrum of graphene and graphene layers," *Phys. Rev. Lett.*, vol. 97, no. 18, pp. 1–4, 2006.
- [197] J. E. Proctor, D. A. M. Armada, and A. Vijayaraghavan, "6 Phonons in Graphene and Single-Walled Carbon Nanotubes (SWCNTs)," in *An Introduction to Graphene and Carbon Nanotubes*, CRC Press, 2016, pp. 89–98.
- [198] R. P. Vidano, D. B. Fischbach, L. J. Willis, and T. M. Loehr, "Observation of Raman band shifting with excitation wavelength for carbons and graphites," *Solid State Commun.*, vol. 39, no. 2, pp. 341–344, 1981.
- [199] D. R. Dreyer, S. Park, C. W. Bielawski, and R. S. Ruoff, "The chemistry of graphene oxide," *Chem. Soc. Rev.*, vol. 39, no. 1, pp. 228–240, 2010.
- [200] P. Hampitak *et al.*, "Protein interactions and conformations on graphene-based materials mapped using quartz-crystal microbalance with dissipation monitoring (QCM-D)," *Carbon N. Y.*, vol. 165, pp. 317–327, 2020.
- [201] Bio-Rad, "Bio-Dot SF Apparatus Assembly | Bio-Rad Laboratories," 2022. [Online]. Available: [https://www.bio-rad.com/en-th/life-science-research/overlay/bio-dot-sf-apparatus-assembly?ID=Bio-Dot-SF-Assembly\\_0921120359123](https://www.bio-rad.com/en-th/life-science-research/overlay/bio-dot-sf-apparatus-assembly?ID=Bio-Dot-SF-Assembly_0921120359123). [Accessed: 20-Feb-2022].
- [202] W. S. Hummers and R. E. Offeman, "Preparation of Graphitic Oxide," *J. Am. Chem. Soc.*, vol. 80, no. 6, pp. 1339–1339, Mar. 1958.
- [203] M. Brugnara, C. Della Volpe, S. Siboni, and D. Zeni, "Contact angle analysis on polymethylmethacrylate and commercial wax by using an environmental scanning electron microscope," *Scanning*, vol. 28, no. 5, pp. 267–273, Mar. 2007.
- [204] P. Yang *et al.*, "Bovine Serum Albumin-Coated Graphene Oxide for Effective Adsorption of Uranium(VI) from Aqueous Solutions," *Ind. Eng. Chem. Res.*, vol. 56, no. 13, pp. 3588–3598, 2017.
- [205] Y. J. Oh *et al.*, "Oxygen functional groups and electrochemical capacitive behavior of incompletely reduced graphene oxides as a thin-film electrode of supercapacitor," *Electrochim. Acta*, vol. 116, pp. 118–128, 2014.
- [206] H. P *et al.*, "Peptide GAM Immunoabsorption Therapy in Primary Membranous Nephropathy (PRISM): Phase II Trial Investigating the Safety and Feasibility of Peptide GAM Immunoabsorption in anti-PLA 2 R Positive Primary Membranous Nephropathy," *J. Clin. Apher.*, vol. 33, no. 3, 2018.
- [207] W. Norde, T. A. Horbett, and J. L. Brash, "Proteins at Interfaces III: Introductory Overview," 2012, pp. 1–34.
- [208] C. Chung, Y.-K. Kim, D. Shin, S.-R. Ryoo, B. H. Hong, and D.-H. Min, "Biomedical Applications of Graphene and Graphene Oxide," *Acc. Chem. Res.*, vol. 46, no. 10, pp. 2211–2224, 2013.
- [209] C. Mas-Moruno, "Surface functionalization of biomaterials for bone tissue regeneration



and repair,” in *Peptides and Proteins as Biomaterials for Tissue Regeneration and Repair*, Woodhead Publishing, 2018, pp. 73–100.

- [210] A. M. Pinto, I. C. Gonçalves, and F. D. Magalhães, “Graphene-based materials biocompatibility: A review,” *Colloids Surfaces B Biointerfaces*, vol. 111, pp. 188–202, Nov. 2013.
- [211] Y. Wang, Z. Li, J. Wang, J. Li, and Y. Lin, “Graphene and graphene oxide: Biofunctionalization and applications in biotechnology,” *Trends Biotechnol.*, vol. 29, no. 5, pp. 205–212, 2011.
- [212] F. De Leo, A. Magistrato, and D. Bonifazi, “Interfacing proteins with graphitic nanomaterials: from spontaneous attraction to tailored assemblies,” *Chem. Soc. Rev.*, vol. 44, no. 19, pp. 6916–6953, Sep. 2015.
- [213] S. Wang, Y. Zhang, N. Abidi, and L. Cabrales, “Wettability and Surface Free Energy of Graphene Films,” *Langmuir*, vol. 25, no. 18, pp. 11078–11081, Sep. 2009.
- [214] O. Leenaerts, B. Partoens, and F. M. Peeters, “Water on graphene: Hydrophobicity and dipole moment using density functional theory,” *Phys. Rev. B*, vol. 79, no. 23, p. 235440, Jun. 2009.
- [215] N. Wei, C. Lv, and Z. Xu, “Wetting of Graphene Oxide: A Molecular Dynamics Study,” *Langmuir*, vol. 30, no. 12, pp. 3572–3578, Apr. 2014.
- [216] D. Li, W. Zhang, X. Yu, Z. Wang, Z. Su, and G. Wei, “When biomolecules meet graphene: from molecular level interactions to material design and applications,” *Nanoscale*, vol. 8, no. 47, pp. 19491–19509, Dec. 2016.
- [217] C. I. Cheng, Y.-P. Chang, and Y.-H. Chu, “Biomolecular interactions and tools for their recognition: focus on the quartz crystal microbalance and its diverse surface chemistries and applications,” *Chem. Soc. Rev.*, vol. 41, no. 5, pp. 1947–1971, Feb. 2012.
- [218] B. D. Vogt, E. K. Lin, W. I. Wu, and C. C. White, “Effect of film thickness on the validity of the sauerbrey equation for hydrated polyelectrolyte films,” *J. Phys. Chem. B*, vol. 108, no. 34, pp. 12685–12690, 2004.
- [219] J. RENART, M. M. BEHRENS, M. FERNÁNDEZ-RENART, and J. L. MARTINEZ, “IMMUNOBLOTTING TECHNIQUES,” *Immunoassay*, pp. 537–554, Jan. 1996.
- [220] M. Soler, M.-C. Estevez, M. Alvarez, M. Otte, B. Sepulveda, and L. Lechuga, “Direct Detection of Protein Biomarkers in Human Fluids Using Site-Specific Antibody Immobilization Strategies,” *Sensors*, vol. 14, no. 2, pp. 2239–2258, Jan. 2014.
- [221] O. M. Slobodian *et al.*, “Low-Temperature Reduction of Graphene Oxide: Electrical Conductance and Scanning Kelvin Probe Force Microscopy,” *Nanoscale Res. Lett.*, vol. 13, no. 1, p. 139, Dec. 2018.
- [222] R. Seevaratnam, B. P. Patel, and M. J. Hamadeh, “Comparison of total protein concentration in skeletal muscle as measured by the Bradford and Lowry assays,” *J. Biochem.*, vol. 145, no. 6, pp. 791–797, 2009.
- [223] M. I. Knight and P. J. Chambers, “Problems associated with determining protein concentration: A comparison of techniques for protein estimations,” *Appl. Biochem. Biotechnol. - Part B Mol. Biotechnol.*, vol. 23, no. 1, pp. 19–28, Jan. 2003.
- [224] N. Ayawei, A. N. Ebelegi, and D. Wankasi, “Modelling and Interpretation of Adsorption

Isotherms," *J. Chem.*, vol. 2017, pp. 1–11, Sep. 2017.

- [225] C. Buttersack, "Modeling of type IV and V sigmoidal adsorption isotherms," *Phys. Chem. Chem. Phys.*, vol. 21, no. 10, pp. 5614–5626, Mar. 2019.
- [226] P. Kao, D. L. Allara, and S. Tadigadapa, "Study of adsorption of globular proteins on hydrophobic surfaces," *IEEE Sens. J.*, vol. 11, no. 11, pp. 2723–2731, 2011.
- [227] C. N. Pace, B. A. Shirley, M. McNutt, and K. Gajiwala, "Forces contributing to the conformational stability of proteins," *FASEB J.*, vol. 10, no. 1, pp. 75–83, Jan. 1996.
- [228] T. McArdle, T. P. McNamara, F. Fei, K. Singh, and C. F. Blanford, "Optimizing the Mass-Specific Activity of Bilirubin Oxidase Adlayers through Combined Electrochemical Quartz Crystal Microbalance and Dual Polarization Interferometry Analyses," *ACS Appl. Mater. Interfaces*, vol. 7, no. 45, pp. 25270–25280, 2015.
- [229] H. T. Aiyelabegan and E. Sadroddiny, *Fundamentals of protein and cell interactions in biomaterials*, vol. 88. Elsevier Ltd., 2017.
- [230] S. J. McClellan and E. I. Franses, "Effect of concentration and denaturation on adsorption and surface tension of bovine serum albumin," vol. 28, pp. 63–75, 2003.
- [231] Z. Ding, H. Ma, and Y. Chen, "Interaction of graphene oxide with human serum albumin and its mechanism," *RSC Adv.*, vol. 4, no. 98, pp. 55290–55295, 2014.
- [232] H. Zhang, Z. Zhu, Y. Wang, Z. Fei, and J. Cao, "Changing the activities and structures of bovine serum albumin bound to graphene oxide," *Appl. Surf. Sci.*, vol. 427, pp. 1019–1029, 2018.
- [233] A. A. Dombkowski, K. Z. Sultana, and D. B. Craig, "Protein disulfide engineering," *FEBS Lett.*, vol. 588, no. 2, pp. 206–212, Jan. 2014.
- [234] J. Charles A Janeway, P. Travers, M. Walport, and M. J. Shlomchik, "The Immune System in Health and Disease," 2001.
- [235] N. G. Welch, J. A. Scoble, B. W. Muir, and P. J. Pigram, "Orientation and characterization of immobilized antibodies for improved immunoassays (Review)," *Biointerphases*, vol. 12, no. 2, p. 02D301, 2017.
- [236] H. L. Birchenough, M. J. Swann, E. Zindy, A. J. Day, and T. A. Jowitt, "Enhanced avidin binding to lipid bilayers using PDP-PE lipids with PEG-biotin linkers," *Nanoscale Adv.*, vol. 2, no. 4, pp. 1625–1633, Apr. 2020.
- [237] Y. Zhang, C. Wu, and J. Zhang, "Interactions of graphene and graphene oxide with proteins and peptides," *Nanotechnol. Rev.*, vol. 2, no. 1, pp. 27–45, 2013.
- [238] Z. Gu, Z. Yang, L. Wang, H. Zhou, C. A. Jimenez-Cruz, and R. Zhou, "The role of basic residues in the adsorption of blood proteins onto the graphene surface," *Sci. Rep.*, vol. 5, pp. 1–11, 2015.
- [239] C. Zhao, X. Lu, C. Zanden, and J. Liu, "The promising application of graphene oxide as coating materials in orthopedic implants: preparation, characterization and cell behavior," *Biomed. Mater.*, vol. 10, no. 1, p. 015019, Feb. 2015.
- [240] B. Sarmiento and J. das Neves, *Biomedical applications of functionalized nanomaterials : concepts, development and clinical translation*. William Andrew, 2018.
- [241] R. Capomaccio *et al.*, "Determination of the structure and morphology of gold

- nanoparticle–HSA protein complexes,” *Nanoscale*, vol. 7, no. 42, pp. 17653–17657, 2015.
- [242] T. Alava *et al.*, “Control of the Graphene–Protein Interface Is Required To Preserve Adsorbed Protein Function,” *Anal. Chem*, vol. 85, p. 22, 2013.
- [243] J. A. Mann, T. Alava, H. G. Craighead, and W. R. Dichtel, “Preservation of antibody selectivity on graphene by conjugation to a tripod monolayer,” *Angew. Chem. Int. Ed. Engl.*, vol. 52, no. 11, pp. 3177–3180, Mar. 2013.
- [244] C. Lin, M. Zhao, G. Xi, X. Wang, and T. Chen, “Evaluation on covalent and noncovalent linking of peptide to graphene oxide for MMP-9 detection,” *Fullerenes Nanotub. Carbon Nanostructures*, vol. 26, no. 1, pp. 38–41, 2018.
- [245] N. M. Andoy, M. S. Filipiak, D. Vetter, Ó. Gutiérrez-Sanz, and A. Tarasov, “Graphene-Based Electronic Immunosensor with Femtomolar Detection Limit in Whole Serum,” *Adv. Mater. Technol.*, vol. 3, no. 12, p. 1800186, 2018.
- [246] S. K. Jang, J.-R. Jang, W.-S. Choe, and S. Lee, “Harnessing denatured protein for controllable bipolar doping of a monolayer graphene,” *ACS Appl. Mater. Interfaces*, vol. 7, no. 2, pp. 1250–6, 2015.
- [247] S. Liu, Y. Fu, C. Xiong, Z. Liu, L. Zheng, and F. Yan, “Detection of Bisphenol A Using DNA-Functionalized Graphene Field Effect Transistors Integrated in Microfluidic Systems,” *ACS Appl. Mater. Interfaces*, vol. 10, no. 28, pp. 23522–23528, 2018.
- [248] S. K. Tuteja, C. Ormsby, and S. Neethirajan, “Noninvasive Label-Free Detection of Cortisol and Lactate Using Graphene Embedded Screen-Printed Electrode,” *Nano-Micro Lett.*, vol. 10, no. 3, p. 41, 2018.
- [249] L. Zhou *et al.*, “Novel Graphene Biosensor Based on the Functionalization of Multifunctional Nano-bovine Serum Albumin for the Highly Sensitive Detection of Cancer Biomarkers,” *Nano-Micro Lett.*, vol. 11, no. 1, p. 20, 2019.
- [250] R. Forsyth, A. Devadoss, and O. J. Guy, “Graphene Field Effect Transistors for Biomedical Applications: Current Status and Future Prospects,” *Diagnostics*, vol. 7, no. 3, p. 45, 2017.
- [251] T. Goda and Y. Miyahara, “Interpretation of protein adsorption through its intrinsic electric charges: A comparative study using a field-effect transistor, surface plasmon resonance, and quartz crystal microbalance,” *Langmuir*, vol. 28, no. 41, pp. 14730–14738, 2012.
- [252] G. Sauerbrey, “Verwendung von Schwingquarzen zur Wägung dünner Schichten und zur Mikrowägung,” *Zeitschrift für Phys.*, vol. 155, no. 2, pp. 206–222, 1959.
- [253] L. Jason-Moller, M. Murphy, and J. Bruno, “Overview of Biacore Systems and Their Applications,” *Curr. Protoc. Protein Sci.*, vol. 45, no. 1, Aug. 2006.
- [254] J. Su *et al.*, “An ultrasensitive micropillar-based quartz crystal microbalance device for real-time measurement of protein immobilization and protein-protein interaction,” *Biosens. Bioelectron.*, vol. 99, pp. 325–331, 2018.
- [255] S. K. Vashist and J. H. T. Luong, “Immunoassays : An Overview,” pp. 1–18, 2018.
- [256] J. Malmström, H. Agheli, P. Kingshott, and D. S. Sutherland, “Viscoelastic modeling of highly hydrated laminin layers at homogeneous and nanostructured surfaces: Quantification of protein layer properties using QCM-D and SPR,” *Langmuir*, vol. 23, no.

19, pp. 9760–9768, 2007.

- [257] R. Huang, P. Yi, and Y. Tang, “Probing the interactions of organic molecules, nanomaterials, and microbes with solid surfaces using quartz crystal microbalances methodology, advantages, and limitations,” *Environ. Sci. Process. Impacts*, vol. 19, no. 6, pp. 793–811, 2017.
- [258] M. Mauro, A. A. Zainuddin, A. N. Nordin, and R. A. Rahim, “openQCM verification test using Impedance and Network Analyzer,” no. August, p. 5, 2016.
- [259] R. Mauchauffé, M. Moreno-Couranjou, N. D. Boscher, C. Van De Weerd, A. S. Duwez, and P. Choquet, “Robust bio-inspired antibacterial surfaces based on the covalent binding of peptides on functional atmospheric plasma thin films,” *J. Mater. Chem. B*, vol. 2, no. 32, pp. 5168–5177, 2014.
- [260] L. Rodriguez-Pardo, J. Farina, C. Gabrielli, H. Perrot, and R. Brendel, “Noise and resolution in 2 MHz, 6 MHz, 9 MHz and 27 MHz QCM sensors in liquid media,” in *Proceedings of IEEE Sensors 2003 (IEEE Cat. No.03CH37498)*, pp. 1189–1193.
- [261] H. Sota *et al.*, “A versatile planar QCM-based sensor design for nonlabeling biomolecule detection,” *Anal. Chem.*, vol. 74, no. 15, pp. 3592–3598, 2002.
- [262] D. Kanigicherla *et al.*, “Anti-PLA2R antibodies measured by ELISA predict long-term outcome in a prevalent population of patients with idiopathic membranous nephropathy,” *Kidney Int.*, vol. 83, no. 5, pp. 940–948, 2013.
- [263] J. E. Im *et al.*, “Electrochemical detection of estrogen hormone by immobilized estrogen receptor on Au electrode,” *Surf. Coatings Technol.*, vol. 205, no. SUPPL. 1, pp. S275–S278, 2010.
- [264] N. Psychogios *et al.*, “The Human Serum Metabolome,” *PLoS One*, vol. 6, no. 2, p. 16957, 2011.
- [265] K. Keiji Kanazawa and J. G. Gordon, “The oscillation frequency of a quartz resonator in contact with liquid,” *Anal. Chim. Acta*, vol. 175, no. C, pp. 99–105, 1985.
- [266] K. K. Kanazawa and J. G. Gordon, “Frequency of a Quartz Microbalance in Contact with Liquid,” *Anal. Chem.*, vol. 57, no. 8, pp. 1770–1771, 1985.
- [267] Q. Zhang *et al.*, “Ultrasensitive Quantitation of Anti-Phospholipase A2 Receptor Antibody as A Diagnostic and Prognostic Indicator of Idiopathic Membranous Nephropathy,” *Sci. Rep.*, vol. 7, no. 1, pp. 1–7, 2017.
- [268] EUROIMMUN AG, “Autoantibodies against phospholipase A2 receptor and THSD7A - EUROIMMUN,” 2019. [Online]. Available: <https://www.euroimmun.com/products/indications/autoantikrper-diagnostik/nephrology/primary-membranous-nephropathy/aak-gegen-pla2r.html>. [Accessed: 14-Jul-2020].
- [269] A. Y. Lam, E. Pardon, K. V. Korotkov, W. G. J. Hol, and J. Steyaert, “Nanobody-aided structure determination of the EpsI:EpsJ pseudopilin heterodimer from *Vibrio vulnificus*,” *J. Struct. Biol.*, vol. 166, no. 1, pp. 8–15, Apr. 2009.
- [270] S. Massa *et al.*, “Site-specific labeling of cysteine-tagged camelid single-domain antibody-fragments for use in molecular imaging,” *Bioconjug. Chem.*, vol. 25, pp. 979–988, May 2014.
- [271] D. Schumacher, C. P. R. Hackenberger, H. Leonhardt, and J. Helma, “Current Status:

- Site-Specific Antibody Drug Conjugates," *Journal of Clinical Immunology*, vol. 36. Springer New York LLC, pp. 100–107, 01-May-2016.
- [272] C. Leduc *et al.*, "A highly specific gold nanoprobe for live-cell single-molecule imaging," *Nano Lett.*, vol. 13, no. 4, pp. 1489–1494, Apr. 2013.
- [273] L. Ma, Y. Sun, X. Kang, and Y. Wan, "Development of nanobody-based flow injection chemiluminescence immunoassay for sensitive detection of human prealbumin," *Biosens. Bioelectron.*, vol. 61, pp. 165–171, Nov. 2014.
- [274] S. C. Reddington, A. J. Baldwin, R. Thompson, A. Brancale, E. M. Tippmann, and D. D. Jones, "Directed evolution of GFP with non-natural amino acids identifies residues for augmenting and photoswitching fluorescence," *Chem. Sci.*, vol. 6, no. 2, pp. 1159–1166, Jan. 2015.
- [275] W. H. Zhang, G. Otting, and C. J. Jackson, "Protein engineering with unnatural amino acids," *Curr. Opin. Struct. Biol.*, vol. 23, no. 4, pp. 581–587, Aug. 2013.
- [276] A. Yamaguchi *et al.*, "Incorporation of a Doubly Functionalized Synthetic Amino Acid into Proteins for Creating Chemical and Light-Induced Conjugates," *Bioconjug. Chem.*, vol. 27, no. 1, pp. 198–206, Jan. 2016.
- [277] D. Virant *et al.*, "A peptide tag-specific nanobody enables high-quality labeling for dSTORM imaging," *Nat. Commun.* 2018 91, vol. 9, no. 1, pp. 1–14, Mar. 2018.
- [278] G. C. Girt *et al.*, "The use of nanobodies in a sensitive ELISA test for SARS-CoV-2 Spike 1 protein," *R. Soc. Open Sci.*, vol. 8, no. 9, Sep. 2021.
- [279] P. Hampitak *et al.*, "A Point-of-Care Immunosensor Based on a Quartz Crystal Microbalance with Graphene Biointerface for Antibody Assay," *ACS Sensors*, vol. 5, no. 11, pp. 3520–3532, Nov. 2020.
- [280] D. Meléndrez, P. Hampitak, T. Jowitt, M. Iliut, and A. Vijayaraghavan, "Development of an open-source thermally stabilized quartz crystal microbalance instrument for biomolecule-substrate binding assays on gold and graphene," *Anal. Chim. Acta*, vol. 1156, p. 338329, Apr. 2021.
- [281] M. S. Filipiak *et al.*, "Highly sensitive, selective and label-free protein detection in physiological solutions using carbon nanotube transistors with nanobody receptors," *Sensors Actuators, B Chem.*, vol. 255, pp. 1507–1516, 2018.
- [282] Q. Zhou, G. Li, Y. Zhang, M. Zhu, Y. Wan, and Y. Shen, "Highly Selective and Sensitive Electrochemical Immunoassay of Cry1C Using Nanobody and  $\pi$ - $\pi$  Stacked Graphene Oxide/Thionine Assembly," *Anal. Chem.*, vol. 88, no. 19, pp. 9830–9836, 2016.
- [283] G. Y. Chen *et al.*, "Graphene Oxide Nanosheets Modified with Single-Domain Antibodies for Rapid and Efficient Capture of Cells," *Chem. - A Eur. J.*, vol. 21, no. 48, pp. 17178–17183, 2015.
- [284] H. L. Birchenough, H. D. R. Nivia, and T. A. Jowitt, "Interaction standards for biophysics: anti-lysozyme nanobodies," *Eur. Biophys. J.*, no. 0123456789, 2021.
- [285] T. Nezu, T. Masuyama, K. Sasaki, S. Saitoh, M. Taira, and Y. Araki, "Effect of pH and addition of salt on the adsorption behavior of lysozyme on gold, silica, and titania surfaces observed by quartz crystal microbalance with dissipation monitoring," *Dent. Mater. J.*, vol. 27, no. 4, pp. 573–580, 2008.
- [286] P. D. Bank, "Molecular Explorations Through Biology and Medicine."

- [287] Fortebio, "Biotinylation of Protein for Immobilization onto Streptavidin Biosensors | Molecular Devices."
- [288] J. Y. Lichtenberg, Y. Ling, and S. Kim, "Non-specific adsorption reduction methods in biosensing," *Sensors (Switzerland)*, vol. 19, no. 11. MDPI AG, 01-Jun-2019.
- [289] H. J. Motulsky and R. R. Neubig, "Analyzing Binding Data."
- [290] S. Pasche, J. Vo, H. J. Griesser, N. D. Spencer, and M. Textor, "Effects of Ionic Strength and Surface Charge on Protein Adsorption at PEGylated Surfaces," 2005.
- [291] "Albumin-lysozyme interactions: Cooperative adsorption on titanium and enzymatic activity | Elsevier Enhanced Reader." [Online]. Available: <https://reader.elsevier.com/reader/sd/pii/S0927776516307020?token=96938569F763CF3B657CC41F87BE6DE6FFEACOC7577D234F951386A37E5F672C30CBF4F0F575A3C0C59008B3BFB5F770&originRegion=eu-west-1&originCreation=20210608132744>. [Accessed: 08-Jun-2021].
- [292] V. R. Moorman, K. G. Valentine, and A. J. Wand, "The dynamical response of hen egg white lysozyme to the binding of a carbohydrate ligand," *Protein Sci.*, vol. 21, no. 7, pp. 1066–1073, Jul. 2012.
- [293] G. Xu *et al.*, "Electrophoretic and field-effect graphene for all-electrical DNA array technology," *Nat. Commun.*, vol. 5, no. January 2015, pp. 1–9, 2014.
- [294] M. J. Li, C. M. Liu, Y. B. Xie, H. Bin Cao, H. Zhao, and Y. Zhang, "The evolution of surface charge on graphene oxide during the reduction and its application in electroanalysis," *Carbon N. Y.*, vol. 66, pp. 302–311, 2014.
- [295] Y. D. Han, H. J. Chun, and H. C. Yoon, "Low-cost Point-of-Care Biosensors Using Common Electronic Components as Transducers," *Biochip J.*, vol. 14, no. 1, pp. 32–47, 2020.
- [296] D. Battal, S. Akgönüllü, M. S. Yalcin, H. Yavuz, and A. Denizli, "Molecularly imprinted polymer based quartz crystal microbalance sensor system for sensitive and label-free detection of synthetic cannabinoids in urine," *Biosens. Bioelectron.*, vol. 111, no. March, pp. 10–17, 2018.
- [297] A. Fatoni, A. N. Aziz, and M. D. Anggraeni, "Low-cost and real-time color detector developments for glucose biosensor," *Sens. Bio-Sensing Res.*, vol. 28, no. January, p. 100325, 2020.
- [298] W. Senbua, J. Mearnchu, and J. Wichitwechkarn, "Easy-to-use and reliable absorbance-based MPH-GST biosensor for the detection of methyl parathion pesticide," *Biotechnol. Reports*, vol. 27, p. e00495, 2020.
- [299] V. Puri, R. Kumar, D. Nhung Le, S. S. Jagdev, and N. Sachdeva, *BioSenHealth 2.0—a low-cost, energy-efficient Internet of Things–based blood glucose monitoring system*. Elsevier Inc., 2020.
- [300] J. M. Moon, N. Thapliyal, K. K. Hussain, R. N. Goyal, and Y. B. Shim, "Conducting polymer-based electrochemical biosensors for neurotransmitters: A review," *Biosens. Bioelectron.*, vol. 102, no. December 2017, pp. 540–552, 2018.
- [301] S. P. Mohanty, "Biosensors : A Tutorial Review Biosensors : A Tutorial Review," *IEEE Potentials*, vol. 25, no. APRIL 2006, pp. 35–40, 2015.
- [302] J. W. Thies, P. Kuhn, B. Thürmann, S. Dübel, and A. Dietzel, "Microfluidic quartz-crystal-

- microbalance (QCM) sensors with specialized immunoassays for extended measurement range and improved reusability," *Microelectron. Eng.*, vol. 179, pp. 25–30, 2017.
- [303] M. Rodahl *et al.*, "Quartz crystal microbalance setup for frequency and Q-factor measurements in gaseous and liquid environments," *Rev. Sci. Instrum.*, vol. 66, no. 7, pp. 3924–3930, 1995.
- [304] Z. Zhang *et al.*, "Hybrid hydrogel films with graphene oxide for continuous saliva-level monitoring," *J. Mater. Chem. C*, vol. 8, no. 28, pp. 9655–9662, 2020.
- [305] P. M. Wolny, J. P. Spatz, R. P. Richter, B. Unit, P. Miramon, and D. Sebastian, "On the Adsorption Behavior of Biotin-Binding Proteins on Gold and Silica," vol. 26, no. 20, pp. 1029–1034, 2010.
- [306] J. T. Marquês, R. F. M. De Almeida, and A. S. Viana, "Lipid bilayers supported on bare and modified gold - Formation, characterization and relevance of lipid rafts," *Electrochim. Acta*, vol. 126, pp. 139–150, 2014.
- [307] M. Pohanka, "QCM immunosensor for the determination of Staphylococcus aureus antigen," *Chem. Pap.*, vol. 74, no. 2, pp. 451–458, 2020.
- [308] L. Newton, T. Slater, N. Clark, and A. Vijayaraghavan, "Self assembled monolayers (SAMs) on metallic surfaces (gold and graphene) for electronic applications," *J. Mater. Chem. C*, vol. 1, no. 3, pp. 376–393, 2013.
- [309] C. A. Keller and B. Kasemo, "Surface specific kinetics of lipid vesicle adsorption measured with a quartz crystal microbalance," *Biophys. J.*, vol. 75, no. 3, pp. 1397–1402, 1998.
- [310] R. Hajiraissi *et al.*, "Adsorption and Fibrillization of Islet Amyloid Polypeptide at Self-Assembled Monolayers Studied by QCM-D, AFM, and PM-IRRAS," *Langmuir*, vol. 34, no. 11, pp. 3517–3524, 2018.
- [311] L. Xu *et al.*, "Graphene-based biosensors for the detection of prostate cancer protein biomarkers: A review," *BMC Chem.*, vol. 13, no. 1, pp. 1–12, 2019.
- [312] C. I. L. Justino, A. R. Gomes, A. C. Freitas, A. C. Duarte, and T. A. P. Rocha-Santos, "Graphene based sensors and biosensors," *TrAC - Trends Anal. Chem.*, vol. 91, pp. 53–66, 2017.
- [313] D. Susilo, T. Mujiono, and Darminto, "QCM Coating with rGO Material as a Platform Developing Piezoelectric Biosensor," *Proc. - 2019 Int. Semin. Intell. Technol. Its Appl. ISITIA 2019*, pp. 52–55, 2019.
- [314] S. Afsahi *et al.*, "Novel graphene-based biosensor for early detection of Zika virus infection," *Biosens. Bioelectron.*, vol. 100, no. June 2017, pp. 85–88, 2018.
- [315] M. B. Lerner *et al.*, "Large scale commercial fabrication of high quality graphene-based assays for biomolecule detection," *Sensors Actuators, B Chem.*, vol. 239, pp. 1261–1267, 2017.
- [316] M. H. Mat Zaid *et al.*, "PNA biosensor based on reduced graphene oxide/water soluble quantum dots for the detection of Mycobacterium tuberculosis," *Sensors Actuators, B Chem.*, vol. 241, pp. 1024–1034, 2017.
- [317] D. P. Singh, C. E. Herrera, B. Singh, S. Singh, R. K. Singh, and R. Kumar, "Graphene oxide: An efficient material and recent approach for biotechnological and biomedical

- applications," *Mater. Sci. Eng. C*, vol. 86, no. November 2017, pp. 173–197, 2018.
- [318] J. N. Dash and R. Jha, "On the Performance of Graphene-Based D-Shaped Photonic Crystal Fibre Biosensor Using Surface Plasmon Resonance," *Plasmonics*, vol. 10, no. 5, pp. 1123–1131, 2015.
- [319] X. Deng *et al.*, "A Highly Sensitive Immunosorbent Assay Based on Biotinylated Graphene Oxide and the Quartz Crystal Microbalance," *ACS Appl. Mater. Interfaces*, vol. 8, no. 3, pp. 1893–1902, 2016.
- [320] M. Edvardsson, M. Rodahl, B. Kasemo, and F. Ho, "A Dual-Frequency QCM-D Setup Operating at Elevated Oscillation Amplitudes," vol. 77, no. 15, pp. 4918–4926, 2005.
- [321] N. Chandrasekaran, S. Dimartino, and C. J. Fee, "Study of the adsorption of proteins on stainless steel surfaces using QCM-D," *Chem. Eng. Res. Des.*, vol. 91, no. 9, pp. 1674–1683, 2013.
- [322] B. Salih, M. Y. Arica, U. Guler, V. C. Ozalp, G. Bayramoglu, and M. Yilmaz, "Lysozyme specific aptamer immobilized MCM-41 silicate for single-step purification and quartz crystal microbalance (QCM)-based determination of lysozyme from chicken egg white," *Microporous Mesoporous Mater.*, vol. 207, pp. 95–104, 2015.
- [323] M. C. Dixon, "Quartz crystal microbalance with dissipation monitoring: Enabling real-time characterization of biological materials and their interactions," *J. Biomol. Tech.*, vol. 19, no. 3, pp. 151–158, 2008.
- [324] X. Sha, C. Sun, X. Xu, L. Alexander, P. J. Loll, and L. S. Penn, "Quartz crystal microbalance (QCM): Useful for developing procedures for immobilization of proteins on solid surfaces," *Anal. Chem.*, vol. 84, no. 23, pp. 10298–10305, 2012.
- [325] X. Huang, Q. Bai, J. Hu, and D. Hou, "A practical model of quartz crystal microbalance in actual applications," *Sensors (Switzerland)*, vol. 17, no. 8, pp. 1–9, 2017.
- [326] A. A. Feiler, A. Sahlholm, T. Sandberg, and K. D. Caldwell, "Adsorption and viscoelastic properties of fractionated mucin (BSM) and bovine serum albumin (BSA) studied with quartz crystal microbalance (QCM-D)," *J. Colloid Interface Sci.*, vol. 315, no. 2, pp. 475–481, 2007.
- [327] B. Jachimska, K. Tokarczyk, M. Łapczyńska, A. Puciul-Malinowska, and S. Zapotoczny, "Structure of bovine serum albumin adsorbed on silica investigated by quartz crystal microbalance," *Colloids Surfaces A Physicochem. Eng. Asp.*, vol. 489, pp. 163–172, 2016.
- [328] B. Beykal, M. Herzberg, Y. Oren, and M. S. Mauter, "Influence of surface charge on the rate, extent, and structure of adsorbed Bovine Serum Albumin to gold electrodes," *J. Colloid Interface Sci.*, vol. 460, pp. 321–328, 2015.
- [329] K. Kubiak-Ossowska, K. Tokarczyk, B. Jachimska, and P. A. Mulheran, "Bovine Serum Albumin Adsorption at a Silica Surface Explored by Simulation and Experiment," *J. Phys. Chem. B*, vol. 121, no. 16, pp. 3975–3986, 2017.
- [330] D. H. Tsai *et al.*, "Adsorption and conformation of serum albumin protein on gold nanoparticles investigated using dimensional measurements and in situ spectroscopic methods," *Langmuir*, vol. 27, no. 6, pp. 2464–2477, 2011.
- [331] S. Dominguez-Medina, S. McDonough, P. Swanglap, C. F. Landes, and S. Link, "In Situ Measurement of Bovine Serum Albumin Interaction with Gold Nanospheres," 2012.
- [332] J. Guo, X. Yao, L. Ning, Q. Wang, and H. Liu, "The adsorption mechanism and induced



- conformational changes of three typical proteins with different secondary structural features on graphene," *RSC Adv.*, vol. 4, no. 20, pp. 9953–9962, 2014.
- [333] S. Wang, X. Ou, Y. Wutthinitikornkit, M. Yi, and J. Li, "Effects of the surface polarity of nanomaterials on their interaction with complement protein gC1q," *RSC Adv.*, vol. 10, no. 69, pp. 41993–42000, 2020.
- [334] A. M. Davidson, M. Brust, D. L. Cooper, and M. Volk, "Sensitive Analysis of Protein Adsorption to Colloidal Gold by Differential Centrifugal Sedimentation," *Anal. Chem.*, vol. 89, no. 12, pp. 6807–6814, 2017.
- [335] Marco Brugnara, "Contact Angle." [Online]. Available: <https://imagej.nih.gov/ij/plugins/contact-angle.html>. [Accessed: 23-Jan-2020].
- [336] I. Reviakine, D. Johannsmann, and R. P. Richter, "Hearing what you cannot see and visualizing what you hear: Interpreting quartz crystal microbalance data from solvated interfaces," *Anal. Chem.*, vol. 83, no. 23, pp. 8838–8848, 2011.
- [337] X. Díez-Betriu *et al.*, "Raman spectroscopy for the study of reduction mechanisms and optimization of conductivity in graphene oxide thin films," *J. Mater. Chem. C*, vol. 1, no. 41, p. 6905, Oct. 2013.
- [338] B. Ma, R. D. Rodriguez, A. Ruban, S. Pavlov, and E. Sheremet, "The correlation between electrical conductivity and second-order Raman modes of laser-reduced graphene oxide," *Phys. Chem. Chem. Phys.*, vol. 21, no. 19, pp. 10125–10134, May 2019.
- [339] S. Beißner *et al.*, "Low-cost, in-liquid measuring system using a novel compact oscillation circuit and quartz-crystal microbalances (QCMs) as a versatile biosensor platform," *J. Sensors Sens. Syst.*, vol. 6, no. 2, pp. 341–350, 2017.
- [340] B. A. Narayana, K. V. L., & Rao, "A novel method of linearizing thermistor characteristic using voltage controlled oscillator," *Sensors & Transducers*, vol. 136, no. 1, pp. 1–11, 2012.
- [341] J. S. Steinhart and S. R. Hart, "Calibration curves for thermistors," *Deep. Res. Oceanogr. Abstr.*, vol. 15, no. 4, pp. 497–503, 1968.
- [342] Jimblom (Sparkfun Electronics), "Arduino Pro Micro V3 Hookup Guide," *Sparkfun Electronics*, 2020. .
- [343] M. Mauro, "openQCM File Repositories," 2015. .
- [344] B. Beauregard, "Improving the Beginner's PID – Introduction," 2011. .
- [345] B. Beauregard, "Arduino PID Library," 2011. .